Comparison between time-dependent and time-independent methods for the calculation of inter-system crossing rates: Application to uracil and its derivatives

Inaugural-Dissertation

zur

Erlangung des Doktorgrades der

Mathematisch-Naturwissenschaftlichen Fakultät

der Heinrich-Heine-Universität Düsseldorf

vorgelegt von

Mihajlo Etinski

aus Novi Sad (Serbien)

Düsseldorf 2010

Aus dem Institut für Theoretische Chemie und Computerchemie
der Heinrich-Heine-Universität Düsseldorf

Gedruckt mit Genehmigung der
Mathematisch-Naturwissenschaftlichen Fakultät
der Heinrich-Heine-Universität Düsseldorf

Referent:	Prof. Dr. Christel M. Marian
Korreferent:	Jun.-Prof. Dr. Jörg Tatchen

Tag der mündlichen Prüfung:

Hiermit versichere ich, die hier vorgelegte Arbeit eigenständig und ohne unerlaubte Hilfe angefertigt zu haben. Die Dissertation wurde in der vorgelegten oder in ähnlicher Form noch bei keiner Institution eingereicht. Ich habe keine erfolglosen Promotionsversuche unternommen.

Düsseldorf, den

(Mihajlo Etinski)

List of papers included in the thesis

- **Paper 1**
  Electronic and vibrational spectroscopy of 1-methylthymine and its water clusters: The dark state survives hydration
  Matthias Busker, Michael Nispel, Thomas Häber, Karl Kleinermanns , Mihajlo Etinski, and Timo Fleig, Chem. Phys. Chem., **9** (2008) 1570-1577

- **Paper 2**
  Intersystem crossing and characterization of dark states in the pyrimidine nucleobases uracil, thymine, and 1-methylthymine
  Mihajlo Etinski, Timo Fleig, and Christel M. Marian, J. Phys. Chem. A **113**, (2009) 11809-11816

- **Paper 3**
  Ab initio investigation of the methylation and hydration effects on the electronic spectrum of uracil and thymine
  Mihajlo Etinski and Christel M. Marian, Phys. Chem. Chem. Phys. **12**, (2010) 4915 - 4923

- **Paper 4**
  Overruling the energy gap law: Fast triplet formation in 6-azauracil
  Mihajlo Etinski and Christel M. Marian, submitted to Phys. Chem. Chem. Phys.

List of related papers not included in the thesis

- **Paper 5**
  Theoretical investigation of the excited states of 2-nitrobenzyl and 4,5-methylendioxy-2-nitrobenzyl caging groups
  Klaus Schaper, Mihajlo Etinski, and Timo Fleig, Photochem. Photobio. **85** (2009) 1075-1081

I express my gratitude to Professor Dr. Christel Marian for her help to formulate the subject of my thesis, exploration of which brought me a lot of intellectual excitement. The collaboration with Professor Marian helped me to broaden my insights into electronic spectroscopy and photophysics. I am grateful to Junior Professor Dr. Jörg Tatchen for his support of my research. I would like to thank Professor Dr. Timo Fleig for his advice during the first part of my doctoral studies in Duesseldorf. I thank Dr. Martin Kleinschmidt for help to interface the code written in C as a subroutine to the VIBES program. Also, I am grateful to all experimentalists with whom I collaborated: Professor Dr. Karl Kleinermanns, Priv. Doz. Dr. Klaus Schaper, Dr. Matthias Busker, Dr. Michael Nispel and Dr. Thomas Häber. I would like to thank all colleagues from the Institute of Theoretical and Computational Chemistry, and especially to Dr. Susanne Salzmann, Dr. Stefan Knecht, Dr. Lasse Sørensen, Dr. Vidisha Rai-Constapel, Kathleen Gollnisch, Dr. Stephan Raub, Karin Schuck and Klaus Eifert for creating a friendly and creative atmosphere. I appreciate very much all help and continual support received from Professor Dr. Miljenko Perić and Professor Dr. Werner Jakubetz.

Zusammenfassung

Der erste Teil dieser Arbeit beschäftigt sich mit der theoretischen Formulierung des Problems, Interkombinationsraten in Molekülen effizient zu evaluieren. Dafür werden zeitunabhängige- und zeitabhängige Näherungen verwendet. Letztere wird ausführlicher diskutiert. Das zentrale Objekt der zeitabhängigen Methode ist die Korrelationsfunktion. Für die Berechnung der Korrelationsfunktion, welche sowohl spinfreie, vibronische Born-Oppenheimer-Näherungen als auch die Condon-Näherung für Spin-Bahn-Matrixelemente verwendet, wird ein geschlossener Ausdruck gefunden. Es wird ebenfalls ein Ausdruck für die Rate, die eine Kumulantenentwicklung zweiter Ordnung nutzt, präsentiert. Ein besonders einfacher Ausdruck wird bei Anwendung einer Kurzzeitentwicklung der Kumulantenentwicklung erhalten. Alle drei Ausdrücke für die Interkombinationsraten sind in einem Computerprogramm implementiert worden. Die für die Testmoleküle unter Nutzung der zeitabhängigen sowie zeitunabhängigen Näherungen erhaltenen Raten werden verglichen und diskutiert. Die zeitabhängige Näherung ist für Fälle, in denen die Franck-Condon-gewichtete Dichte der vibronischen Zustände groß ist, viel versprechend. Dies könnte sowohl auf eine große adiabatische Energielücke zwischen den elektronischen Zuständen als auch einfach auf viele Normalmoden zurückzuführen sein.
Der zweite Teil der Arbeit behandelt die Anwendungen der quantenchemischen Methoden auf die elektronische Relaxation nach Photoanregung in Uracil, seinen methylierten Derivaten und 6-Azauracil. Experimente mit Hilfe zeitaufgelöster Spektroskopie in einem Molekularstrahl haben gezeigt, dass die methylierten Uracile auf der Femto-, Piko- und Nanosekundenzeitskala relaxieren. Obwohl die ersten experimentellen Ergebnisse darauf hingedeutet haben, dass die Nanosekundenrelaxierung von dem tiefsten augeregten Singulettzustand herrührt, folgern wir in einer späteren Studie, dass sie vom tiefsten elektronischen Triplettzustand verursacht wird. Wir unterbreiten auch einen kontroversen Vorschlag, dass Hydratation Nanosekundenrelaxation löscht. Unsere Ergebnisse zeigen, dass Hydratation einen signifikanten Effekt auf die elektronischen Zustände hat, so dass diese die Photostabilität der Pyrimidinbasen modifizieren kann.
Von besonderem Interesse ist die Photorelaxierung von 6-Azauracil, da die Triplettquantenausbeute sehr viel größer als in Uracil ist. Die Azasubstitution erzeugt zusätzliche, tiefliegende Singulett- und Triplett-nπ^*-Zustände. Die Berechnung der Potenzialenergieprofile entlang linear interpolierter Pfade ergibt, dass zwischen den elektronischen Singulett- und Triplettzuständen Kreuzungen und vermiedene Kreuzungen existieren. Es werden mögliche elektronische Relaxierungsmechanismen diskutiert.

Summary

The first part of this thesis is focused on the theoretical formulation of the problem how to efficiently evaluate inter-system crossing rates in molecules. The problem is addressed by time-independent and time-dependent approaches. The latter approach is presented in a more detail. The central object in time-dependent method is the correlation function. A closed-form expression for the calculation of the correlation function using spin-free Born-Oppenheimer vibronic states and the Condon approximation for the spin-orbit matrix element is found. Also, the expression for the rate using a second-order cumulant expansion is presented. A particularly simple expression is derived employing a short-time expansion of the cumulant expansion. All three expressions for the inter-system crossing rate are implemented in a computer code. The rates obtained for test molecules using time-dependent and time-independent approaches are compared and discussed. The time-dependent approach is promising in the cases where the Franck-Condon weighted density of the vibronic states is huge. This may be due to a large adiabatic energy gap between electronic states or simply due to many normal modes.

The second part of the thesis is dedicated to applications of quantum-chemical methods to the electronic relaxation upon photoexcitation in uracil, its methylated derivatives and 6-azauracil. Time-resolved spectroscopy experiments in the molecular beam showed that methylated uracils relax on the femto, pico and nanosecond time scales. Although the first experimental results suggested that the nanosecond relaxation originates from the lowest excited singlet state, in a later study we conclude that it should be due to the lowest triplet electronic state. Also, we address a controversal proposal that hydration quenches nanosecond relaxation. Our results show that hydration has a significant effect on the electronic states, so that it can modify the photostability of the pyrimidine bases.

Photorelaxation of 6-azauracil is particularly interesting because the triplet quantum yield is much larger than in uracil. The aza-substitution creates additional low-lying singlet and triplet $n\pi^*$ states. The calculation of potential energy profiles along linearly interpolated paths reveals crossings and avoided crossings between singlet and triplet electronic states. Possible electronic relaxation mechanisms are discussed.

Contents

List of Tables

List of Figures

1 Introduction

1.1 Photochemistry of nucleic acids

Ultraviolet (UV) radiation comprises the electromagnetic spectrum from 10 to 380 nm. The sun emits ultraviolet radiation in the UV-A (320-380 nm), UV-B (290-320 nm), and UV-C (290-100) bands. On Earth ground, only radiation from 290 to 380 nm is relevant because ozone or other atmospheric gases strongly absorb radiation below 290 nm. The UV-B radiation is partially absorbed by the ozone layer while it is transparent to UV-A radiation. Depletion of the ozone layer due to chlorofluorocarbon pollution increases the exposure to UV-B radiation. This is causing danger for the living organisms on Earth. Radiation can be toxic (kills living cells), mutagenic (changes the genotype of cells) and carcinogenic (removes the normal capacity to inhibit cell growth).
Biological effects upon absorption of UV light can be examined by measuring an action spectrum. It contains the biological response to a specific radiation wavelength. An action spectrum for mouse skin in the UV-B and UV-A regions is presented in Figure 1.1. It can be seen from the Figure 1.1 that in the UV-B region an action spectrum for mutagenesis and carcinogesis is overlapping with DNA absorption while in the UV-A region where DNA absorption is low, there is still a possibility for cell killing. It is believed that although the photon is not absorbed by DNA, it can be absorbed by an intermediate molecule and then its energy could be transferred to the DNA molecule. Hence, the DNA molecule is the main chromophore for UV absorption and its photophysical and photochemical properties are important for understanding the molecular origin of carcinogenesis and mutagenesis upon UV irradiation.
Nucleic acids absorb below 300 nm with maximum at 260 nm. Nucleic bases, Figure 1.2, are the main chromophores of nucleic acids. Upon absorption of a UV photon, an excited electronic state is created and it can decay through various pathways such as internal conversion to the ground state, vibrational relaxation, inter-system crossing to reactive triplet states and chemical reactions in the excited state. In the case of nucleic bases, the largest part of the excited electronic-state population decays to the ground state indicating a significant photostability. But a part of the population goes into chemical reactions. Major photoproducts of UV degradation of nucleic acids and their yields are given in Table 1.1.
Excited triplet electronic states live longer than singlet states due to the spin-forbidden character of their relaxation to the singlet ground electronic state. Since they are highly reactive, they present potential precursors for photochemical reactions. As can be seen from Table 1.1 the main mechanism of photodegradation is a dimerization of two pyrimidine bases yielding cyclobutyl structure. The detailed mechanism of this photoreaction is still under discussion: an ultrafast reaction in the singlet excited state [9] or a reaction in the triplet state [1].

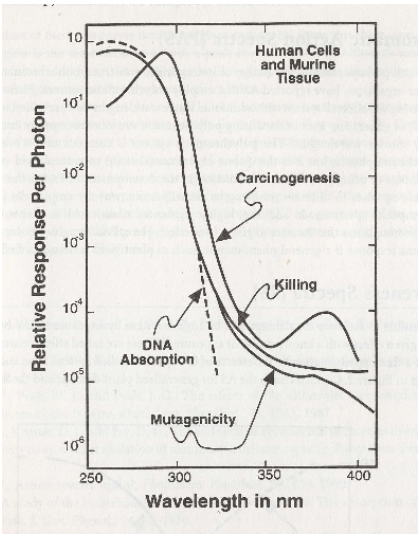

Figure 1.1: UV action spectra for human cell killing and mutagenesis and carcinogenic action spectrum for mouse skin. Figure taken from reference [4]

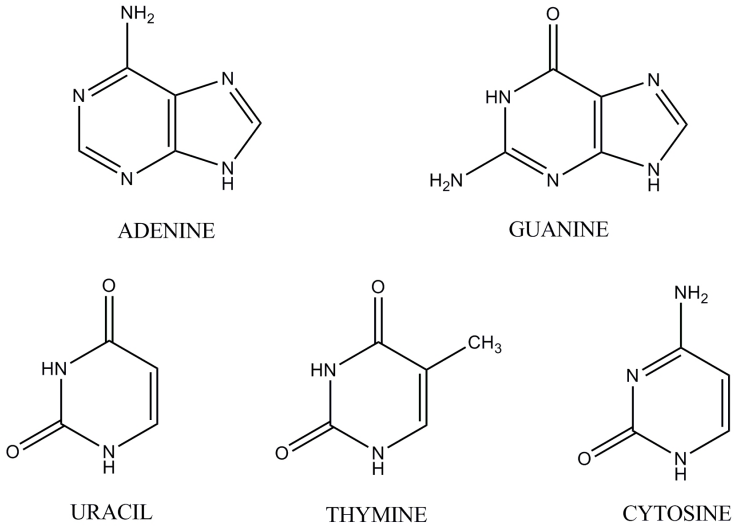

Figure 1.2: Nucleic bases

Table 1.1: Relative induction frequencies of the major photoproducts induced by UV radiation. Adapted from reference [1]

Photoproducts	Lesions/10^8 Da J/m^2		% of total photoproducts	
	UV-C	UV-B	UV-C	UV-B
Cyclobutyl pyrimidine dimer	2.3	0.30	77	78
Pyrimidine pyrimidinone [6-4]-photoproduct	0.6	0.04	20	10
Dewar Pyrimidinone	$2.3 \cdot 10^{-2}$	$\sim 4 \cdot 10^{-2}$	0.8	10
Adenine-thymine heterodimer	$6 \cdot 10^{-3}$	nd	0.2	nd
Cytosine photohydrate	$5 \cdot 10^{-2}$	$6.6 \cdot 10^{-3}$	~ 2	~ 2
Single-strand break	$\sim 5 \cdot 10^{-4}$	$\sim 4 \cdot 10^{-6}$	<0.1	<0.1
DNA-protein crosslink	$\sim 3 \cdot 10^{-4}$	$\sim 1 \cdot 10^{-6}$	< 0.1	<0.1

1.2 Motivation

This work is embedded into the Sonderforschungsbereich (Collaborative research center) 663 "Molekulare Antwort nach electronischer Anregung" (Molecular response to electronic excitation). Within this center, several experimental and theoretical groups work on the understanding of photostability of biologically relevant molecules.
The group of Professor Kleinermanns was interested in the problem of the photostability of the pyrimidine bases uracil and thymine. They wanted to investigate whether their photostability is an intristic property or a consequences of the interaction with the solvent. They chose 1-methylthymine as a molecule for the experiment. 1-Methylthymine is a model system for the DNA-base thymine, since thymine is covalently bound to the phosphate backbone in the 1-position in DNA double helices. Electronic relaxation of 1-methylthymine involves an electronic state that lives about two hundred nanoseconds in the gas phase. This electronic state could be a precursor for the creation a cyclobutyl dimer. In order to characterize the structure and lifetimes, Professor Kleinermanns and his coworkers use resonance enhanced multi photon ionization (REMPI) and IR/UV double resonance spectroscopy in combination with time of flight mass spectrometry. Throughout expansion of the molecules in supersonic gas jets is employed. In order to interpret their experimental result a theoretical analysis was needed. My work started out as an ab initio examination of the electronic relaxation of 1-methylthymine [10]. As a next step we wanted to calculate inter-system crossing rates in uracil, thymine and 1-methylthymine [7]. For the vibrational contributions to the Fermi Golden Rule formula a method based on the summation of Franck-Condon integrals was used. It is implemented in the program VIBES [11]. During our work, we realized that the method we used for the calculation of inter-system rates is difficult to apply in situations where there are many normal modes and when the adiabatic electronic energy gap is large. In those cases it takes much time to sum all Franck-Condon integrals and to obtain a rate constant. Due to that, Professor Marian proposed to develop a new method that can be applied in situations when molecules have no symmetries and therefore all normal modes should be taken into account. A natural choice is to try to base the method in the time domain in order to avoid tedious summation of Franck-Condon integrals.

2 The molecular Hamiltonian and its approximations

In order to describe molecular processes it is of fundamental importance to specify a molecular Hamiltonian. The complete molecular Hamiltonian contains three space and one spin degree of freedom per particle (an electron or a nucleus). The biggest problem concerning the description of the electronic and nuclear motion lies in the fact that electronic and nuclear degrees of freedom are coupled mutually through their interaction. Hence, the numerical solution of the Schrödinger equation for the complete Hamiltonian is usually not desirable and an analytical solution is impossible [12,13]. In fact, what we want to have is a clever choice of the important degrees of freedom that are involved in the concerned process. Then, we expect that the rest of the degrees of freedom will not significantly influence the dynamics of the selected ones, otherwise their influence can be included using effective Hamiltonian.
In the absence of an external field, the complete molecular Hamiltonian is given by [13]:

$$H = \hat{T}_{CM} + \hat{T} + \hat{T}' + \hat{V} + \hat{H}_{es} + \hat{H}_{hfs}. \tag{2.1}$$

The first term $\hat{T}_{CM}$ is a kinetic energy operator of the molecular center of mass. The next two terms are related to the relative motion around the center of mass, $\hat{T} = \hat{T}_n + \hat{T}_e$ is a sum of the kinetic energy operators of the relative motion of nuclei and electrons and $\hat{T}' =$ is a term that couples the nuclear and electron momentum operators in their relative motion. $\hat{V} = \hat{V}_{nn} + \hat{V}_{ee} + \hat{V}_{ne}$ is an electrostatic potential operator due to the Coulomb interaction between nuclei, electrons, and between electrons and nuclei. $\hat{H}_{es} = \hat{H}_{SO} + \hat{H}_{sr} + \hat{H}_{ss}$ is a Hamiltonian operator related to the interaction of each electron spin magnetic moment with the magnetic moments generated by the orbital motions of the electrons (for instance, interaction with its own orbital moment is spin-same orbit interaction and that is a part of total spin-orbit interaction $\hat{H}_{SO}$), the magnetic moments generated by the orbital motions of the nuclei ($\hat{H}_{sr}$) and the spin magnetic moments of the other electrons ($\hat{H}_{ss}$). The last term in the molecular Hamiltonian $\hat{H}_{hfs}$ is related to the interaction of the magnetic and electric moments of the nuclei with the other electric and magnetic moments in the molecule. It gives very small energies compared to the other terms, so that its contribution can be freely neglected in the present context.
Motion of the center of mass is not relevant for internal motion, so that the operator $\hat{T}_{CM}$ can be excluded. Also, the operator $\hat{T}'$ is weighted by the total mass of the molecule, so that its contribution is negligible. Therefore, the Hamiltonian of interest is given by:

$$\hat{H} = \hat{T} + \hat{V} + \hat{H}_{es}. \tag{2.2}$$

Concerning the $\hat{H}_{es}$ operator, in this thesis only the spin-orbit Hamiltonian will be considered.

2.1 Separation of electron and nuclear coordinates

In order to simplify the Hamiltonian we will consider the spin-free part and the influence of the electronic spin will be treated later. The basic approximation in treating molecules is the adiabatic or Born-Oppenheimer approximation [14]. It is based on the fact that electrons and nuclei have significantly different masses. If the nuclei do not have large kinetic energies it is possible to separate electronic and nuclear motion.
Let us label the electron coordinates with r and the nuclear coordinates with R. Then, the spin-free Schrödinger equation related to equation 2.2 is

$$(\hat{T}_n(R) + \hat{T}_e(r) + \hat{V}_{nn}(R) + \hat{V}_{ne}(R,r) + \hat{V}_{ee}(r))\Psi(R,r) = E\Psi(R,r). \tag{2.3}$$

The total wavefunction depends on the nuclear and electronic coordinates. In the Born-Oppenheimer approximation, it is separated into an electronic wavefunction $\psi_i(r;R)$ and a nuclear wavefunction $\chi_i(R)$, so that it is:

$$\Psi(R,r) = \sum_i \chi_i(R)\psi_i(r;R). \tag{2.4}$$

The former explicitly depends on the electron coordinates and parametrically on the nuclear coordinates. It is a solution of the electronic Schrödinger equation:

$$(\hat{T}_e(r) + \hat{V}_{ne}(R,r) + \hat{V}_{ee}(r))\psi_i(r;R) = E_i(R)\psi_i(r;R). \tag{2.5}$$

$E_i(R)$ is the energy of the electrons for a certain configuration of nuclei. Collecting its value for all configurations of nuclei we obtain the potential energy (hyper) surface (PES). Its significance is tremendous because it completely determines the motion of the nuclei. The nuclear wavefuntion $\chi_i(R)$ is a solution of the nuclear Schrödinger equation:

$$(\hat{T}_n(R) + E_n(R) - E)\chi_i(R) = \sum_j \Lambda_{ij}\chi_j(R) \tag{2.6}$$

where E is the total energy of the nuclei and Λ_{ij} is defined as

$$\Lambda_{ij} = -\int \psi_i(r;R)^\star T_n(R)\psi_j(r;R). \tag{2.7}$$

It represents non-adiabatic coupling in the adiabatic electronic representation and contains the first and second-order derivative coupling:

$$\Lambda_{ij} = -\sum_p \frac{1}{M_p} f_{ij}^{(p)} \frac{\partial}{\partial R_p} - \sum_p \frac{1}{2M_p} h_{ij}^{(p)}(R) \tag{2.8}$$

$$f_{ij}^{(p)} = \int \psi_i^*(r;R)\frac{\partial}{\partial R_p}\psi_j(r;R)\mathrm{d}r \tag{2.9}$$

$$h_{nm}^{(p)} = \int \psi_i^*(r;R)\frac{\partial^2}{\partial R_p^2}\psi_j(r;R)\mathrm{d}r. \tag{2.10}$$

In the case where the non-adiabatic coupling is small, we can neglect it. This leads to uncoupled equations for the nuclear wavefunctions $\chi_i(R)$:

$$(\hat{T}_n(R) + E_n(R) - E)\chi_i(R) = 0, \quad i = 1, 2, ... \tag{2.11}$$

This can be always done when the difference between the potential energy surfaces is much larger than the spacing between the energy levels related to the nuclear motion. In cases when the electronic potential surfaces are not well-separated, the non-adiabatic coupling can become very strong and even singular.

2.2 The solution of the electronic Schrödinger equation

The theoretical examination of molecular processes always starts with the construction of potential surfaces, based on equation 2.5. There are plenty of methods for the solution of the electronic Schrödinger equation, like density functional theory, molecular-orbital based methods, valence-bond based methods. For an overview of the molecular orbital methods there is an excellent monograph Molecular Electronic-Structure Theory by T. Helgaker, P. Jørgensen and J. Olsen [15].
The molecular orbital based method CC2 that was primarily used in this thesis will be explained here. The CC2 theory is built upon the Hartree-Fock method. The next section gives a short explanation of the Hartree-Fock method.

2.2.1 The Hartree-Fock method

The Hartree-Fock theory is the most elementary way for obtaining a molecular orbital basis while taking into account the Pauli exclusion principle [16]. It is a mean-field theory where the two-particle Coulomb interaction is substituted with an effective one-particle interaction. The electrons move in their spin orbitals independently of each other. The effective interaction represents an average field created by all other electrons and nuclei that interact with a given electron.
The orbitals which optimally represent the many-electron wavefunction are the orbitals that minimize the total electronic energy. They are found by employing a variational procedure to the Slater determinant:

$$\Psi(x_1, x_2, ..., x_N) = (N!)^{-\frac{1}{2}} det|\psi_1(x_1)\psi_2(x_2)...\psi_N(x_N)| \tag{2.12}$$

where $\psi_i(x_i)$ is the i-th occupied spin-orbital. The total energy related to the Slater determinant is:

$$E = \sum_i \langle\psi_i|\hat{h}(1)|\psi_i\rangle + \frac{1}{2}\sum_{i,j}(\langle\psi_i\psi_j|\hat{g}(1,2)|\psi_i\psi_j\rangle - \langle\psi_i\psi_j|\hat{g}(1,2)|\psi_j\psi_i\rangle). \tag{2.13}$$

$\hat{h}(1)$ is a one-electron operator that contains the electron kinetic energy and the interaction between electron 1 and all nuclei, $\hat{h}(1) = -\frac{1}{2}\nabla_1^2 - \sum_A \frac{Z_A}{R_{1A}}$. $\hat{g}(1,2)$ is a two-electron

operator that represents the interaction between two electrons, $\hat{g}(1,2) = \frac{1}{|\boldsymbol{r}_1 - \boldsymbol{r}_2|}$. It is useful to define the Coulomb $\hat{J}_i$ and the exchange operator $\hat{K}_i$ in the following manner:

$$\hat{J}_i(x_1)\psi_j(x_1) = [\int \hat{g}(1,2)\psi_i^\star(x_2)\psi_i(x_2)d^3x_2]\psi_j(x_1) \tag{2.14}$$

$$\hat{K}_i(x_1)\psi_j(x_1) = [\int \hat{g}(1,2)\psi_i^\star(x_2)\psi_j(x_2)d^3x_2]\psi_i(x_1). \tag{2.15}$$

The Coulomb operator represents an average local potential at x_1 arising from an electron in ψ_i. The exchange operator is a space non-local operator that exchanges the electrons 1 and 2 with respect to their spin-orbitals. It is a manifestation of the Pauli principle. It is convenient to introduce the total Coulomb and exchange operators: $\hat{J} = \sum_i \hat{J}_i$, $\hat{K} = \sum_i \hat{K}_i$ where the summation runs over all occupied spin-orbitals.
From the definition of the operators $\hat{J}$ and $\hat{K}$ it follows that the total electronic energy is:

$$E = \sum_i \langle\psi_i|\hat{h} + \frac{1}{2}(\hat{J} - \hat{K})|\psi_i\rangle. \tag{2.16}$$

Using the variational principle, $\delta E = 0$, one can derive the Hartree-Fock equations:

$$\hat{F}\psi_i = \epsilon_i\psi_i \tag{2.17}$$

where the Fock operator is given by $\hat{F} = \hat{h} + \hat{J} - \hat{K}$. Spin-orbitals that diagonalize the Fock operator are called canonical spin-orbitals. The Fock operator is an effective one-electron operator that contains no explicit two-electron interactions.
Expressed with the Fock operator, the total Hartree-Fock energy is:

$$E_{HF} = \frac{1}{2}\sum_i (\langle\psi_i|\hat{F}|\psi_i\rangle + \langle\psi_i|\hat{h}|\psi_i\rangle). \tag{2.18}$$

To solve the Hartree-Fock equations is equivalent to diagonalizing the Fock matrix. But because the latter depends on the occupied orbitals the equations have to be solved iteratively. This iterative procedure is known as the self-consistent-field method. In practice, molecular spin orbitals are expanded as combinations of atomic orbitals. This defines the LCAO procedure.
Although the Hartree-Fock method gives typically more than 99% of the total electronic energy, we usually have a need to accurately compute the remaining 1%. The difference between the total electronic energy and the Hartree-Fock energy (in a complete basis set) is the correlation energy. It presents the energy due to instantaneous electron interactions in the molecule. Usually it is divided into dynamic and static correlation energy. The former is a consequence of the fact that the Fock operator does not represent the complete electronic Hamiltonian. The difference between the complete electronic Hamiltonian and the Fock operator is a fluctuating potential. It produces virtual excitations from occupied to unoccupied orbitals. The static part is a consequence of the inadequacy of one Slater determinant to represent the electronic wavefunction. It is usually considered as a long-range effect. Static correlation

is important in bond-breaking regions of nuclear configuration space but also for many excited states. Approaches to solve the correlation problem are divided into single- or multi-reference methods. Single-reference methods are based on one Slater determinant for subsequent perturbational or variational calculation and primary account for the dynamical correlation. Multi-reference methods are based on a linear combination of several Slater determinants and can address static as well as dynamic correlation.

2.2.2 The coupled-cluster method

The coupled-cluster method is a single-reference method that successfully solves the problem of dynamic electron correlation. It is employed in many benchmark calculations of electronic energies. Dynamic correlations due to the fluctuating potential manifest themselves as virtual excitations from occupied to unoccupied orbitals. According to the number of the occupied virtual orbitals, excitations can be divided into single (S), double (D), triple (T), ... These excitations have a certain amplitude and associated probability to occur. The Rayleigh-Schrödinger perturbation theory, where the fluctuating potential is a perturbation, accounts only for excitations up to a given order. For instance, the second-order perturbation produces double excitations from the occupied orbitals to unoccupied orbitals. But the perturbation expansion converges slowly. In order to speed up convergence it is possible to use an exponential ansatz for the wavefunction:

$$|CC\rangle = e^{\hat{T}}|\Phi_{HF}\rangle \tag{2.19}$$

where the cluster operator

$$\hat{T} = \hat{T}_1 + \hat{T}_2 + \hat{T}_3 + ... + \hat{T}_N \tag{2.20}$$

is a sum of operators that produce single ($\hat{T}_1$), double ($\hat{T}_2$), and higher excitations. Using second quantization formalism they can be written as:

$$\hat{T}_1 = \sum_{AI} t_I^A a_A^\dagger a_I \tag{2.21}$$

$$\hat{T}_2 = \sum_{A>B,I>J} t_{IJ}^{AB} a_A^\dagger a_I a_B^\dagger a_J. \tag{2.22}$$

Indices I and J are used for occupied orbitals and A and B for unoccupied orbitals. t_{IA} and t_{IJAB} are cluster amplitudes for single and double excitations, respectively. The cluster operator can be written in shorthand notation as $T = t\tau = \sum_\mu t_\mu \tau_\mu$, where t denotes the cluster amplitudes, τ the corresponding excitation operator and μ cover single, double and higher-order excitations. Retaining only certain classes of excitations creates a hierarchy of approximations. The ansatz for coupled-cluster singles (CCS) contains only the T_1 operator, for singles and doubles (CCSD) it contains $\hat{T}_1 + \hat{T}_2$, for singles, doubles and triples (CCSDT) it contains $\hat{T}_1 + \hat{T}_2 + \hat{T}_3$ etc. An advantage of using the exponential ansatz is that the wavefunction contains contributions from all states that can be created by excitations from occupied to unoccupied orbitals even

at the truncated level. This can be shown by expanding the exponential ansatz into a Taylor expansion. For example, double excitations from the Hartree-Fock state can be obtained by acting with the double-excitation operator $\hat{T}_2$ or by acting twice with the single-excitation operator $\hat{T}_1$. Those different excitation processes have different amplitudes. So, the exponential ansatz represents some kind of a resummation of ordinary perturbation theory. The most used coupled-cluster approximation is singles and doubles (CCSD). The energy for that approximation is obtained from:

$$E = \langle \Phi_{HF} | \hat{H} | CCSD \rangle = \langle \Phi_{HF} | \hat{H} e^{\hat{T}_1 + \hat{T}_2} | \Phi_{HF} \rangle. \tag{2.23}$$

The CCSD cluster amplitudes are obtained by solving the amplitude equations:

$$\langle \mu_1 | e^{-\hat{T}_1 - \hat{T}_2} \hat{H} e^{\hat{T}_1 + \hat{T}_2} | \Phi_{HF} \rangle = 0 \tag{2.24}$$

$$\langle \mu_2 | e^{-\hat{T}_1 - \hat{T}_2} \hat{H} e^{\hat{T}_1 + \hat{T}_2} | \Phi_{HF} \rangle = 0 \tag{2.25}$$

where $|\mu_1\rangle$ and $|\mu_2\rangle$ denote the single and double excitation manifold. It is useful to define the $\hat{T}_1$ transformed operator as

$$\hat{\tilde{O}} = e^{-\hat{T}_1} \hat{O} e^{\hat{T}_1} \tag{2.26}$$

so that the amplitude equations can be rewritten in the form:

$$\langle \mu_1 | \hat{\tilde{H}} + [\hat{\tilde{H}}, \hat{T}_2] | \Phi_{HF} \rangle = 0 \tag{2.27}$$

$$\langle \mu_2 | \hat{\tilde{H}} + [\hat{\tilde{H}}, \hat{T}_2] + \frac{1}{2} [[\hat{\tilde{H}}, \hat{T}_2], \hat{T}_2] | \Phi_{HF} \rangle = 0. \tag{2.28}$$

If we retain the singles equations but approximate the doubles equations to first order we obtain:

$$\Omega_{\mu_1} = \langle \mu_1 | \hat{\tilde{H}} + [\hat{\tilde{H}}, \hat{T}_2] | \Phi_{HF} \rangle = 0 \tag{2.29}$$

$$\Omega_{\mu_2} = \langle \mu_2 | \hat{\tilde{H}} + [\hat{F}, \hat{T}_2] | \Phi_{HF} \rangle = 0. \tag{2.30}$$

In the doubles equations, the Fock operator is introduced. These equations define the CC2 model [17]. The ground-state energy for a closed-shell molecule is:

$$E_{CC2} = E_{SCF} + \sum_{IJAB} (t_{IJ}^{AB} + t_I^A t_J^B)(2(IA|JB) - (JA|IB)). \tag{2.31}$$

The CC2 excitation energies are obtained using a response theory. Here, the energies are obtained as eigenvalues of a Jacobian matrix, which contains derivatives of the vector function Ω_{μ_i} with respect to the cluster amplitudes [18]:

$$A_{\mu_i \nu_j} = \frac{\delta \Omega_{\mu_i}}{\delta t_{\nu_i}} = \begin{pmatrix} \langle \mu_1 | [[\hat{\tilde{H}} + [\hat{\tilde{H}}, \hat{T}_2], \tau_{\nu_1}] | HF \rangle & \langle \mu_1 | [\hat{\tilde{H}}, \tau_{\nu_2}] | HF \rangle \\ \langle \mu_2 | [\hat{\tilde{H}}, \tau_{\nu_1}] | HF \rangle & \langle \mu_2 | [\hat{F}, \tau_{\nu_2}] | HF \rangle \end{pmatrix}. \tag{2.32}$$

The CC2 method is usually employed with the RI (resolution of identity) approximation [19]. This approximation simplifies the calculation of the two-electron integrals in

an atomic basis. Particularly computationally demanding are four-index integrals. They are substituted by three-center integrals using an auxiliary basis set in the RI method. Products of the atomic orbitals pq and rs are expanded in the auxiliary basis set of atom-centered Gaussian functions. Hence, the two-electron integrals can be approximated by:

$$(pr|rs) \approx \sum_{\alpha} b_{pq}^{\alpha} b_{rs}^{\alpha} \tag{2.33}$$

$$b_{pq}^{\alpha} = \sum_{\beta} (pq|\beta) V_{\alpha\beta}^{-1/2} \tag{2.34}$$

where α and β are the auxiliary basis functions and $V_{\alpha\beta} = \iint \frac{\alpha(r_1)\beta(r_2)}{r_{12}} dr_1 dr_2$. The RI approximation greatly speeds up CC2 calculations, particularly for large molecules, i. e. for a large number of basis functions.

2.3 The nuclear Schrödinger equation and the normal mode Hamiltonian

After we have solved the electronic Schrödinger equation for a set of nuclear configurations and therefore have obtained the potential energy surface, we can study the nuclear motion on it. The nuclear Schrödinger equation can be simplified by introducing a rotating reference frame. In this way, rotations and vibrations can be separated. If we are interested in the nuclear motion in the vicinity of the potential minimum then the normal model Hamiltonian is a natural choice.
Let us start from the nuclear Schrödinger equation in Cartesian coordinates in the center of mass system, equation 2.11. We will consider rigid molecules, that is molecules that have a well defined minimum of the potential energy surface. The coordinates of the nuclei in the minimum are $(x_i^{eq}, y_i^{eq}, z_i^{eq})$. We want to separate vibrational from rotational motion. The motion in the center-of-mass system has an angular momentum $\boldsymbol{J}$. In order to decouple vibrational and rotational motion, we should minimize $\boldsymbol{J}$. It is given by:

$$\boldsymbol{J} = \sum_i m_i \boldsymbol{r}_i \times \dot{\boldsymbol{r}}_i = \sum_i m_i (\boldsymbol{r}_i^{eq} + \Delta \boldsymbol{r}_i) \times (\dot{\boldsymbol{r}}_i^{eq} + \Delta \dot{\boldsymbol{r}}_i). \tag{2.35}$$

In a rigid molecule at low energies the nuclei move in the vicinity of the potential energy minimum, so that $\boldsymbol{J}$ can be approximated by:

$$\boldsymbol{J} \approx \sum_i m_i \boldsymbol{r}_i^{eq} \times \Delta \dot{\boldsymbol{r}}_i. \tag{2.36}$$

This vector equation defines the Eckart condition:

$$\sum_i m_i \boldsymbol{r}_i^{eq} \times \Delta \boldsymbol{r}_i = 0. \tag{2.37}$$

that is employed in defining the body-fixed rotating molecular coordinate system. The three equations for the components give the three Euler angles θ, ϕ and χ that define the relative orientation of the rotating molecular system in comparison with the center of mass system.
In the vicinity of the potential energy minimum, the kinetic and potential energy operators can be diagonalized by introducing normal-mode coordinates. Thus, for a nonlinear molecule, the Cartesian body-fixed coordinate k of the i-th nucleus are related to the normal mode coordinate Q_l by an orthogonal transformation $\mathbf{L}$ defined by:

$$r_{ik} = r_{ik}^{eq} + m_i^{-\frac{1}{2}} \sum_l L_{il} Q_l. \tag{2.38}$$

In nonlinear molecules, six normal modes correspond to translation and rotation and the rest correspond to vibrations. If we put the body-fixed frame in an orientation such that its axes are parallel to the principal axes of the molecular moment of inertia and assume that the angular momenta of vibrations are small, then we can separate the rotational and vibrational motion and write a rovibrational Hamiltonian as:

$$\hat{H}_{rv} = \hat{H}_{rot} + \hat{H}_{vib} \tag{2.39}$$

$$\hat{H}_{rot} = \tfrac{1}{2}(\tfrac{L_x^2}{I_x^0} + \tfrac{L_y^2}{I_y^0} + \tfrac{L_z^2}{I_z^0}) \tag{2.40}$$

$$\hat{H}_{vib} = \tfrac{1}{2}\textstyle\sum_i (P_i^2 + \omega_i^2 Q_i^2) + \tfrac{1}{3!}\sum_{klm} \Phi_{klm} Q_k Q_l Q_m + ... \tag{2.41}$$

where I_x^0, I_y^0 and I_z^0 are principal moments of inertia, ω_i are normal-mode frequencies and Φ_{klm}, ... are anharmonic coupling constants.
Often, it is sufficient to consider a harmonic vibrational Hamiltonian as the first approximation:

$$\hat{H}_{vib} = \frac{1}{2} \sum_i (P_i^2 + \omega_i^2 \Omega_i^2). \tag{2.42}$$

Electronic transitions are usually followed by a change in normal modes. This change was first examined by Duschinsky [20] and the transformation is called Duschinsky transformation. The normal modes of the final electronic state are not orthonormal to the normal modes of the initial electronic state (for a two-dimensional case see Figure 2.1).
Consider, for instance, the ground- and some excited-state PES. In the ground state, the potential energy surface in the vicinity of the potential minimum can be represented as $E_g = \frac{1}{2}\sum_i \omega_i^2 Q_i^2 + ...$ while the excited state surface for the same nuclear geometry is $E_e = E_e(0) + \sum_i \kappa_i^e Q_i + \frac{1}{2}\sum_{i,j} \eta_{ij}^e Q_i Q_j + ...$ where $E_e(0)$ is the vertical electronic excitation energy, κ_i^e are the first-order intrastate coupling constants and η_{ij}^e are the second-order intrastate coupling constants. The body-fixed system in each electronic state is defined by the Eckart condition with respect to the equilibrium structure for that state. A calculation that involves both electronic states requires a common body frame, which is as the first approximation obtained by an affine transformation that

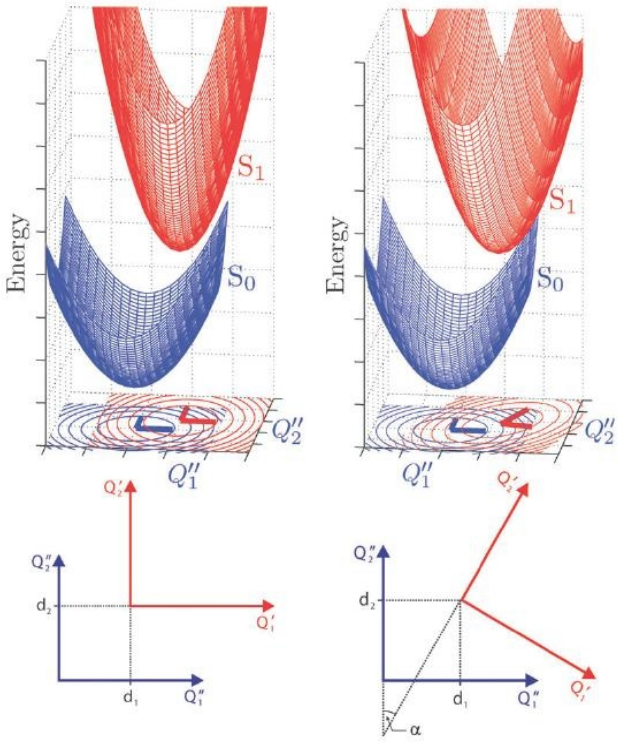

Figure 2.1: Schematic two-dimensional (Q_1, Q_2) ground (lower, blue) and excited (upper, red) state PES. Left panel: Displaced-distorted harmonic potential energy surfaces with (i) $\mathbf{D} \neq 0$, (ii) $d'_{Q_1} \neq d''_{Q_1}$ and $d'_{Q_2} \neq d''_{Q_2}$, and (iii) $\mathbf{J} = 1$, i. e. the excited state PES is (i) displaced, (ii) distorted, but (iii) not rotated relative to the ground state PES. Right panel: Displaced-distorted-rotated harmonic potential energy surfaces with (i) $\mathbf{D} \neq 0$ (ii) $d'_{Q_1} \neq d''_{Q_1}$ and $d'_{Q_2} \neq d''_{Q_2}$, and (iii) $\mathbf{J} \neq 1$. For an explanation of the terms see text. Taken from ref. [5]

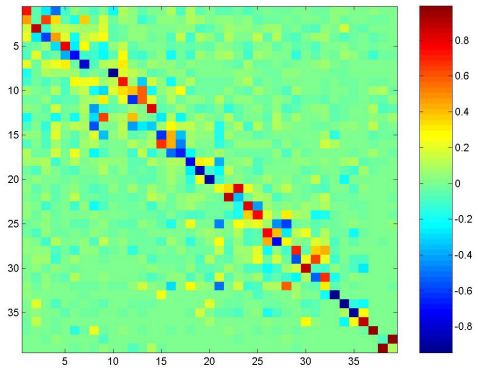

Figure 2.2: Duschinsky matrix J for thymine: It is an orthogonal matrix close to a unit matrix with the dimension equal to the number of normal modes (for discussion about translation and rotation see text); nondiagonal elements clearly show coupling between normal modes

removes the first-order intrastate coupling and diagonalizes the second-order intrastate coupling:

$$\bar{Q}_i = \sum_j J_{ij} Q_j + D_i \tag{2.43}$$

where Q_i are normal modes of the final electronic state and Q_j are normal modes of the initial electronic state. The Duschinsky matrix J is an orthogonal matrix and it produces a rotation of the normal modes. The rotation is followed by the translation D. If L' and L are orthogonal matrices that transform Cartesian coordinates of the final and initial electronic states to the normal modes, then:

$$J = L'^T L \tag{2.44}$$

$$D = L'^T m^{\frac{1}{2}} (r^{eq} - r^{eq\prime}) \tag{2.45}$$

where r^{eq} and $r^{eq\prime}$ are Cartesian coordinates of the respective electronic minima, $m^{\frac{1}{2}}$ is a diagonal matrix with square roots of the atomic masses. The two electronic states must be orientated such that they have the largest number of symmetry elements in common. The Duschinsky matrix J for thymine is shown in Figure 2.2
There are some possible complications for the determination of the Duschinsky matrix due to mixing of rotational and vibrational motion. In a case when the equilibrium geometries of the two electronic states are significantly different, then the Duschinsky matrix given by the product of the two normal mode transformation matrices cannot be decomposed into a vibrational and a rotational part. That is depicted as:

$$J = \begin{pmatrix} J_{vib} & J_{vr} & 0 \\ J_{vr} & J_{rot} & 0 \\ 0 & 0 & J_{tr} \end{pmatrix}. \tag{2.46}$$

The transformation between normal modes of two electronic states given by equation 2.43 is an approximation. In the most general case it should be nonlinear. Those nonlinearities occur due to axis-switching [21–23].

2.4 Coupling of the electron spin and angular momentum

The electron spin is a relativistic effect. The first theory that successfully explained the origin of the electron spin is Dirac's fully relativistic one-particle theory. In this theory, the electron spin and angular momentum are not conserved separately but the resulting total angular momentum is conserved. A fully relativistic two-body equation for electrons is unknown. Hence, approximate equations are used for relativistic electronic structure calculations [24]. Usually the starting point for further approximations is a four-component Dirac-Coulomb-Breit Hamiltonian that contains a sum of Dirac-like terms (kinetic energy and one-electron interaction), the Coulomb and Breit interaction (retardation effect for the Coulomb interaction and magnetic interactions). Then, it is reduced to two components and split into separate spin-independent and spin-dependent parts in order to obtain the spin-orbit Hamiltonian. The most important transformations are: Foldy-Wouthuysen and Douglas-Kroll. Using Foldy-Wouthuysen transformation, one can derive the Breit-Pauli spin-orbit Hamiltonian:

$$\begin{aligned}\hat{H}^{SO}_{BP} &= \tfrac{e^2\hbar}{2m^2c^2}\Big(\textstyle\sum_i \sum_A Z_A \boldsymbol{s}_i\big(\frac{\boldsymbol{R}_{iA}}{R^3_{iA}} \times \boldsymbol{p}_i\big) - \sum_{i\neq j}\big(\frac{\boldsymbol{r}_{ij}}{r^3_{ij}} \times \boldsymbol{p}_i\big)\cdot(\boldsymbol{s}_i + 2\boldsymbol{s}_j)\Big) \\ &= \textstyle\sum_i \hat{H}^{SO}(i) + \sum_{i,j} \hat{H}^{SO}(i,j) \end{aligned} \tag{2.47}$$

where Z_A is the charge of the A-th nucleus, $\boldsymbol{R}_{iA}$ is the position vector between electron i and nucleus A, $\boldsymbol{r}_{ij}$ is the position vector between electrons i and j, $\boldsymbol{s}_i$ is the spin of the i-th electron and $\boldsymbol{p}_i$ is its linear momentum. The Breit-Pauli Hamiltonian is the sum of the one-electron term $\hat{H}^{SO}(i)$ and the two-electron term $\hat{H}^{SO}(i,j)$. It has the drawback that it contains terms coupling electronic and positronic states. When, positron-electron pair creation is excluded from the beginning, we arrive at no-pair approximations. This can be accomplished by a unitary transformation or an expansion in the coupling strength Ze^2. The only difference between the Breit-Pauli spin-orbit Hamiltonian and the corresponding no-pair Hamiltonian is the presence of kinematic factors that damp the $1/r^3_{iA}$ and $1/r^3_{ij}$ singularities.
The matrix element of the spin-orbit operator between a pair of Slater determinants differing by a single valence spin-orbital excitation $i \rightarrow j$ is given by:

$$\begin{aligned}\hat{H}^{SO}_{ij} = \langle i|H^{SO}(1)|j\rangle &+ \tfrac{1}{2}\textstyle\sum_k n_k(\langle ik|H^{SO}(1,2)|jk\rangle \\ &-\langle ik|H^{SO}(1,2)|kj\rangle - \langle ki|H^{SO}(1,2)|jk\rangle).\end{aligned} \tag{2.48}$$

Hess et *al.* [25] defined a mean-field spin-orbit Hamiltonian by:

$$\begin{aligned}\hat{H}^{mf}_{ij} = \langle i|H^{SO}(1)|j\rangle &+ \tfrac{1}{2}\textstyle\sum_{k,fixed\,n_k} n_k(\langle ik|H^{SO}(1,2)|jk\rangle \\ &-\langle ik|H^{SO}(1,2)|kj\rangle - \langle ki|H^{SO}(1,2)|jk\rangle).\end{aligned} \tag{2.49}$$

Here, k runs over the core and valence shells. Occupation numbers of the core shells are always 2, while occupation numbers of the valence shells may vary between 0 and 2, depending on the reference determinant. In this way the two-electron contributions of the valence shells are averaged. Averaging over spin component is done as well. This

approximation works well for one- and many-center terms. For the platinum atom the deviation is less than 0.1 % and for light molecules it is about 1 %. A further approximation can be obtained by replacing the molecular mean field by a sum of atomic mean fields. In this way, only the two-electron integrals for basis functions located at the same center have to be evaluated.
The calculation of the spin-orbit integrals in the atomic basis set based on the mean-field spin-orbit Hamiltonian is implemented in the AMFI code [26]. The evaluation of the spin-orbit matrix elements in the basis of the correlated DFT/MRCI wavefunctions was implemented in the SPOCK program [27].

3 Decay of the excited electronic state

Absorption of UV radiation creates an excited electronic state. The electronically excited state will eventually decay to the ground electronic state through radiative or nonradiative processes [2, 3, 28, 29]. The electronic relaxation can be an unimolecular or bimolecular process. Bimolecular processes are important under higher pressure gas-phase or under condensed-phase conditions. Collisions with other molecules can cause energy transfer or quenching of the excited electronic state. The result of the unimolecular decay can be the same molecular species. This defines a photophysical process. Otherwise, creation of a new chemical species defines a photochemical process. The difference between photophysical and photochemical processes in the nuclear configuration space is presented schematically in Figure 3.1. The former process returns to the starting point and the latter arrives at a different point in the nuclear configuration space, corresponding to the equilibrium geometry of a photochemical product.

In this work only unimolecular photophysical processes will be examined. They are depicted in Figure 3.2 using a Jablonski diagram and their time scales are represented in Table 3.1. Figure 3.2 shows typical molecular energy levels of a closed-shell organic molecule. The energy levels are presented in a spin-free Born-Oppenheimer approximation that defines vibronic states. These vibronic states are products $\chi_m(R)\psi_n(r;R)$ of nuclear and electronic wavefunctions. The vibronic density of states (VDOS) is lowest in the vicinity of the first vibrational ground electronic state. To higher energies, the VDOS increases rapidly and that facilitates relaxation processes. The photophysical relaxation includes radiative and nonradiative processes depending whether an electromagnetic field is the driving force or not. During the electronic relaxation the total

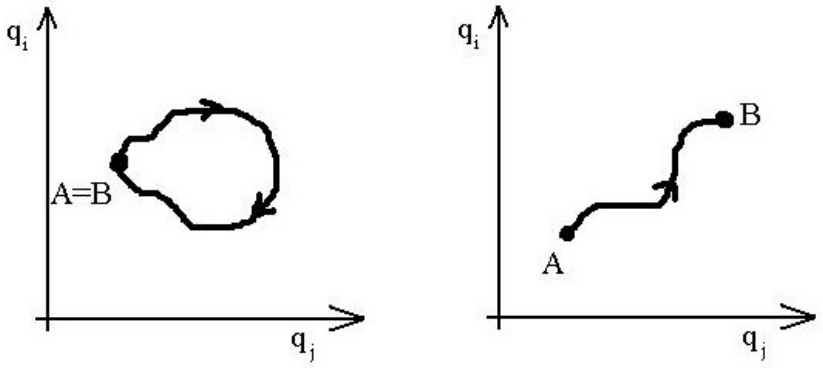

Figure 3.1: Photophysical (left) and photochemical path (right) in configuration space

Table 3.1: Typical time scales of molecular photophysical processes [2, 3].

Process	Time scale [s^{-1}]
Fluoroscence	10^6 - 10^9
Phosphorescence	10^{-2} - 10^4
Internal conversion	10^{-6} - 10^{14}
Inter-system crossing $S_1 \rightsquigarrow T_1$	10^6 - 10^{11}
Inter-system crossing $T_1 \rightsquigarrow S_0$	10^{-1} - 10^4
Intermolecular vibrational redistribution	$< 10^{13}$

electronic spin can be changed. The radiative processes are fluorescence (F) and phosphorescence (P). In a molecule with closed-shell electronic ground state fluorescence is an emission of light from an excited singlet electronic state to the ground state. According to Kasha's rule, only the first excited state exhibits detectable luminescence but there are exceptions, for example azulene where the second excited state emits. Phosphorescence is an emission of light from the excited triplet to the ground electronic state. In the spin-free Born-Oppenheimer approximation this is a spin-forbidden process. It is therefore much slower than fluorescence, at least in molecules composed of light elements. The nonradiative processes can also be spin-allowed or spin-forbidden. Internal conversion (IC) is a spin-allowed process occurring between electronically excited singlet or triplet states as well as between the first excited singlet state and the ground state. IC can be very fast, even faster than the period of the molecular vibration. Inter-system crossing (ISC) is a spin-forbidden process occurring between electronic states of different multiplicity. ISC is usually slower than internal conversion but there are exceptions. For example, inter-system crossing in thymine, thymidine, 4-thiothymidine and nitrobenzaldehydes is completed in approximately 10 ps [8,30,31]. In the condensed phase, it is possible to have vibrational relaxation (VR) as a consequence of collisions with solvent molecules. In low-pressure gas phase, the total energy of the molecule remains conserved for a long time. Internal vibrational redistribution (IVR) represents an energy flow between normal modes due to anharmonicity in the molecule.

3.1 Weak vibronic coupling

In this section the Wigner-Weisskopf model for irreversible decay [32–34] will be explained. The level coupling scheme for the model is shown in Figure 3.3. It contains a level $|s\rangle$ that is coupled to a set of levels $|l\rangle$. The level $|s\rangle$ is initially prepared at $t = 0$. Because of the coupling V_{sl}, $|s\rangle$ is not an eigenstate of the total Hamiltonian and population will be transfered to levels $|l\rangle$. If there is a sufficient density of $|l\rangle$-levels, the transfer is irreversible, hence there is a decay. Otherwise the population oscillate back and forth. The Hamiltonian for the model is:

$$\hat{H} = \hat{H}_0 + \hat{V} = E_s|s\rangle\langle s| + \sum_l E_l|l\rangle\langle l| + \sum_l V_{sl}(|s\rangle\langle l| + |l\rangle\langle s|) \tag{3.1}$$

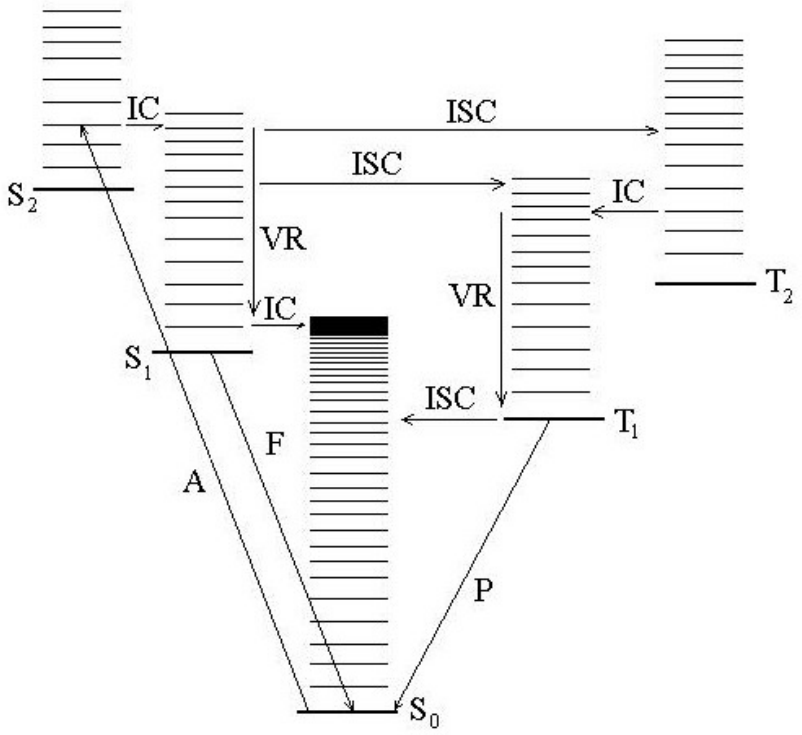

Figure 3.2: Jablonski diagram: radiative processes - absorption (A), fluorescence (F) phosphorescence (P); radiationless processes: internal conversion (IC), intersystem crossing (ISC), vibrational relaxation (VR)

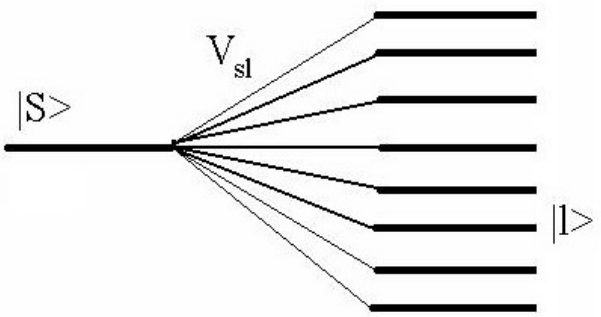

Figure 3.3: Level coupling scheme for the Wigner-Weisskopf model

It is sufficient to consider only the time-independent Schrödinger equation since all couplings in the model are time-independent:

$$(E - \hat{H})|\psi\rangle = 0 \tag{3.2}$$

The Green function for this equation is defined as:

$$(E - \hat{H})\hat{G}(E) = 0 \tag{3.3}$$

$$\hat{G}(E) = \frac{1}{E - \hat{H} + i\epsilon} \tag{3.4}$$

The Green function for the zero-order Hamiltonian $\hat{H}_0$ is:

$$\hat{G}_0(E) = \frac{1}{E - \hat{H}_0 + i\epsilon} \tag{3.5}$$

Using the identity

$$\frac{1}{\hat{A}} = \frac{1}{\hat{B}} + \frac{1}{\hat{B}}(\hat{B} - \hat{A})\frac{1}{\hat{A}} \tag{3.6}$$

with $\hat{A} = E - \hat{H} + i\epsilon$ and $\hat{B} = E - \hat{H}_0 + i\epsilon$ we obtain the Dyson equation:

$$\hat{G}(E) = \hat{G}_0(E) + \hat{G}_0(E)\hat{V}\hat{G}(E) \tag{3.7}$$

We are interested in the time development of the population of the state $|s\rangle$, $P_s(t) = |\langle s|\hat{G}(t)|s\rangle|^2$. $\hat{G}(t)$ is the Fourier transform of $\hat{G}(E)$, $\hat{G}(t) = \frac{1}{2\pi}\int_{-\infty}^{\infty} e^{iEt}\hat{G}(E)\mathrm{d}t$. Hence, let us insert the Dyson equation between $\langle s|$, $|s\rangle$ and $\langle l|$, $|s\rangle$:

$$G_{ss}(E) = \tfrac{1}{E-E_s+i\epsilon} + \tfrac{1}{E-E_s+i\epsilon}\textstyle\sum_l V_{sl}G_{ls}(E) \tag{3.8}$$

$$G_{ls}(E) = \tfrac{1}{E-E_l+i\epsilon}V_{ls}G_{ss}(E) \tag{3.9}$$

Substituting the second into the first equation, we obtain:

$$G_{ss}(E) = \frac{1}{E - E_s - \Sigma(E)} \tag{3.10}$$

where $\Sigma(E)$ is the so-called self-energy:

$$\Sigma(E) = \sum_l \frac{|V_{ls}|^2}{E - E_l + i\epsilon}. \tag{3.11}$$

It has a real and an imaginary part:

$$\Sigma(E) = \Delta_s(E) - i\Gamma_s(E) = P\sum_l \frac{|V_{ls}|^2}{E - E_l} - 2i\pi \sum_l |V_{ls}|^2 \delta(E - E_l). \tag{3.12}$$

P denotes the principal value of the integral, $\Delta_s(E)$ is the level shift due to coupling, and $\Gamma_s(E)$ is the resonance width. In principle, the energy dependence of the self-energy can be complicated. But if we assume that the coupling constants V_{ls} do not strongly depend on the energy levels l then the variation of the self-energy in the vicinity of $E = E_s$ will be small. Thereby, the frequency dependence is dominated by the resonance at $E = E_s$ and the energy dependence of self-energy $\Sigma(E)$ can be replaced with the value $\Sigma(E_s)$.
The population of the energy level s is given by:

$$P_s(t) = \left| \tfrac{1}{2\pi} \int_{-\infty}^{\infty} e^{iEt} G_{ss}(E) \mathrm{d}t \right|^2 \tag{3.13}$$

$$= \left| \tfrac{1}{2\pi} \int_{-\infty}^{\infty} e^{iEt} \tfrac{1}{E - (E_s + \Delta_s(E_s)) + i\Gamma_s(E_s)} \right|^2 = e^{-\Gamma t} \tag{3.14}$$

where the decay rate is

$$\Gamma = 2\pi \sum_l |V_{ls}|^2 \delta(E_s - E_l). \tag{3.15}$$

This expression is known as the Fermi Golden Rule of quantum mechanics. So, the population of the initially excited vibronic level decays exponentially with the rate constant Γ.

3.2 Strong vibronic coupling

Strong vibronic coupling occurs in the nuclear coordinate space in regions where two Born-Oppenheimer potential-energy surfaces are very close or even intersect each other. According to the topology of the potential surfaces, there exist two types of intersections: Jahn-Teller (conical) and Renner-Teller (glancing) [35]. Both types are induced by symmetry reasons, because when a molecule has a high symmetry there can exist degenerate electronic states. But there are also nonsymmetry-induced conical intersections or accidental conical intersections. They are more common than symmetry-induced ones.
Vibronic coupling is so strong in the vicinity of the conical intersections that sometimes potential energy intersections are called molecular funnels. That means that the electronic population in one electronic state (n) is immediately transferred to the other

electronic state (m). This is the consequence of the fact that non-adiabatic coupling Λ_{nm} is very large or even singular in the intersection.
If the vibronic coupling is strong, it is not possible to apply pertubation theory in order to obtain internal conversion or inter-system crossing rates. In this case, the Born-Oppenheimer approximation breaks down and the complete time-dependent Schrödinger equation for the coupled surfaces has to be solved.

3.3 The time-independent method for the calculation of the inter-system crossing rate

There are several possibilities for partitioning the molecular Hamiltonian into a zero-order Hamiltonian and a perturbation. From the standpoint of quantum chemical calculations the most convenient partitioning is to use pure-spin Born-Oppenheimer states as the zero-order basis and spin-orbit coupling as the perturbation. According to Henry and Siebrand [36,37] the coupling operator is a sum of the spin-orbit coupling $\hat{H}_{SO}$ and the nuclear kinetic energy operator $\hat{T}_N$, $\hat{V} = \hat{H}_{SO} + \hat{T}_N$ if the zero-order Hamiltonian $\hat{H}_0$ is built from pure-spin Born-Oppenheimer states. The matrix elements of the perturbation operator expanded up to the second order in Rayleigh-Schrödinger perturbation theory are:

$$\begin{aligned} V_{nm} &= \langle S_n|\hat{H}_{SO}|T_m^\alpha\rangle \\ &+ \textstyle\sum_i \frac{\langle S_n|\hat{H}_{SO}|T_i^\alpha\rangle\langle T_i^\alpha|\hat{T}_N|T_m^\alpha\rangle}{E_i - E_m} \\ &+ \textstyle\sum_i \frac{\langle S_n|\hat{T}_N|S_i\rangle\langle S_i|\hat{H}_{SO}|T_m^\alpha\rangle}{E_i - E_m} \end{aligned} \tag{3.16}$$

where n, m and i represent the vibronic quantum numbers, S is a singlet electronic state, T^α is an α sublevel of a triplet electronic state. At low temperature, the spin relaxation between the different components of a triplet electronic state is slow. In this case, the three states are not equally populated. At higher temperatures, spin relaxation is fast and causes transitions between the sublevels so that the three components are equally populated. If the spin-orbit coupling can be approximated by a Taylor expansion around an appropriate reference point, (similar to the Herzberg-Teller expansion of the transition dipole moment), $\hat{H}_{SO} = \hat{H}_{SO}(0) + \sum_j \frac{\partial \hat{H}_{SO}}{\partial Q_j} Q_j + ...$ then the three lowest-order terms of V_{nm} are:

$$\begin{aligned} V_{nm} &= \langle S_n|\hat{H}_{SO}(0)|T_m^\alpha\rangle \\ &+ \langle S_n|\textstyle\sum_j \frac{\partial \hat{H}_{SO}}{\partial Q_j} Q_j|T_m^\alpha\rangle \\ &+ \textstyle\sum_i \frac{\langle S_n|\hat{H}_{SO}(0)|T_i^\alpha\rangle\langle T_i^\alpha|\hat{T}_N|T_m^\alpha\rangle}{E_i - E_m} + \sum_i \frac{\langle S_n|\hat{T}_N|S_i\rangle\langle S_i|\hat{H}_{SO}(0)|T_m^\alpha\rangle}{E_i - E_m}. \end{aligned} \tag{3.17}$$

These three terms determine three mechanisms of coupling which may contribute to inter-system crossing: a direct spin-orbit coupling (spin-orbit coupling in the Condon approximation), vibronic spin-orbit coupling, and spin-vibronic coupling. The direct spin-orbit coupling is determined by the El-Sayed rule [38] that claims that the spin-orbit coupling is larger between states of different orbital angular momentum than

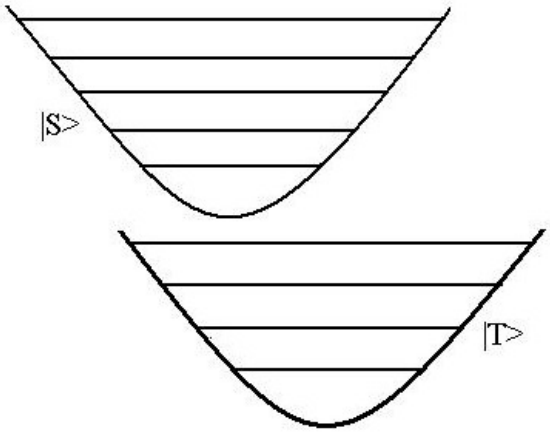

Figure 3.4: The singlet $|S\rangle$ and triplet $|T\rangle$ potential energy surfaces

between states of the same orbital angular momentum. In the case where the direct spin-orbit coupling is large, the other two mechanism are less important. Otherwise they may be important. In this thesis only the direct spin-orbit coupling will be examined, and we will neglect the other mechanisms.

Let us specify the vibronic problem in more detail. We assume that the zero-order Hamiltonian is built up from two pure-spin harmonic electronic states of different multiplicities with N vibrational degrees of freedom (an energy scheme for a one-dimensional case is given in Figure 3.4). Let us consider the transition between the singlet S and the triplet T electronic state. In this case, the zero-order Hamiltonian is in atomic units:

$$\hat{H}_0 = \left(E_S^0 + \hat{H}_S\right)|S\rangle\langle S| + \left(E_T^0 + \hat{H}_T\right)|T\rangle\langle T| \tag{3.18}$$

where $\hat{H}_S = \frac{1}{2}\left(\mathbf{P}_S^T\mathbf{P}_S + \mathbf{Q}_S^T\mathbf{\Lambda}_S^2\mathbf{Q}_S\right)$ and $\hat{H}_T$ a similar expression for the T electronic state. E_S^0 and E_T^0 are electronic energies at the equilibrium geometries, $\mathbf{Q}$ and $\mathbf{P}$ are vectors that represent normal-mode coordinates and their conjugated momenta. $\mathbf{\Lambda}_S$ is a diagonal matrix that contains normal-mode frequencies of the singlet state. In most cases, the normal modes of the two electronic states S and T will be different because electronic transitions are accompanied by a change in the equilibrium geometries. The transformation between the normal coordinates is in general nonlinear. Nonlinearity arises because of the axis-switching effect, that is because each nuclear configuration has its own molecule-fixed axis system [21, 22]. Usually nonlinearities are small and it is sufficient to consider a linear transformation known as Duschinsky transformation [20]: $\mathbf{Q}_T = \mathbf{J}\mathbf{Q}_S + \mathbf{D}$. Here, $\mathbf{J}$ is the Duschinsky matrix and $\mathbf{D}$ is the normal mode displacement vector.

The Wigner-Weisskopf model from the previous section can be applied to the inter-system crossing. If density of the final states is sufficiently high, as is expected in large molecules, then the decay rate from the initially excited singlet vibronic level $|S, \{s_i\}\rangle$

is given by the Golden Rule:

$$k_{ISC} = 2\pi \sum_{\{t_i\}} |\langle S, \{s_i\}|\hat{H}_{SO}|T, \{t_i\}\rangle|^2 \delta(E_s - E_t) \tag{3.19}$$

In the Condon approximation, that is assuming only direct spin-orbit coupling, the rate is:

$$k_{ISC} = 2\pi |\langle S|\hat{H}_{SO}|T\rangle|^2 \sum_{\{t_i\}} |\langle \{s_i\}|\{t_i\}\rangle|^2 \delta(E_s - E_t). \tag{3.20}$$

In this case, the calculation of the rate is reduced to the calculation of the spin-orbit coupling $\langle S|\hat{H}_{SO}|T\rangle$ and the Franck-Condon (FC) integrals $\langle \{s_i\}|\{t_i\}\rangle$. In the case of displaced, distorted and rotated potential energy surfaces, FC integrals cannot be represented as products of one-dimensional integrals, but are highly complex quantities. Sharp and Rosenstock [39] developed a general expression for calculating multidimensional FC integrals using the method of generating functions. Doktorov et *al*. [40, 41] found recurrence relations for multidimensional FC integrals employing the coherent state method. Dierksen and Grimme [42] exploited the sparse structure of the Duschinsky matrix in order to ease the calculation of the FC integrals in large molecules. Lin et *al*. [43] derived a closed-form expression for the multidimensional FC integrals. Domcke and coworkers [44] concluded that for vertical electronic transitions from the vibrationally cold ground state, the FC integrals depend in the first place on the properties of the final state potential energy surface within the FC zone. Using a short-time expansion they derived an expression for FC integrals which involves only the gradient of the final state at the geometry of the initial state. Jankowiak et *al*. [45] developed conditions that enable to reduce the number of FC integrals needed to be calculated by employing sum rules obtained from a coherent state generating function for the FC integrals. On the other hand, Borrelli and Peluso [46] developed a pertubative method for the calculation of FC integrals.
The VIBES program for the calculation of inter-system crossing rates employing the explicit calculation of FC integrals was implemented in our laboratory [11]. It determines the ISC rate, based on the method developed by Toniolo and Persico [47]. Here the delta function from equation 3.20 is approximated by a step function of width η centered about E_s. The program calculates the inter-system crossing rate from the lowest vibronic level of the singlet manifold. The FC integrals are evaluated analytically applying a generalized version of the recursive method of Doktorov et *al*. [40, 41]. The overlap between vibronic states is calculated only if the states belong to the selected energy interval. The VIBES program has an option to restrict the number of quanta that a certain normal modes can have at most. It also includes a possibility for accounting of vibronic spin-orbit coupling using the first-order Herzberg-Teller expansion. In the situations where the density of final states is very high due to a large adiabatic energy gap or a large number of vibrational degrees of freedom, the application of this method can be time-demanding. This was our motivation to develop a method that can be used in these situations.

3.4 The time-dependent method for the calculation of the inter-system crossing rate

At this place I would like to explain what is the meaning of time in the time-dependent approach. In quantum mechanics there are different ways to deal with time dependence: Schrödinger and Heisenberg pictures. In the Schrödinger picture, the state vectors are time dependent but operators do not necessarily carry time dependence. The time dependence of the expectation value of some operator $\hat{A}$, $\langle\hat{A}\rangle(t) = \langle\psi(t)|\hat{A}|\psi(t)\rangle$ can also be obtained by using the unitary transformation $e^{-it\hat{H}}$. In that case, the expectation value becomes $\langle\hat{A}\rangle(t) = \langle\psi(0)|e^{it\hat{H}}\hat{A}e^{-it\hat{H}}|\psi(0)\rangle$. Now, the operator is time dependent $\hat{A}(t) = e^{it\hat{H}}\hat{A}e^{-it\hat{H}}$ and the state vector $|\psi(0)\rangle$ is time independent. This defines the Heisenberg picture.

Here, three expressions for the calculation of the inter-system crossing rates are derived using the time-dependent approach. The time dependence of the spin-orbit operator in the Heisenberg picture naturally introduces the correlation function into the expression for the Golden Rule. Using a closed form expression for the sum of the Hermite polynomials, an exact expression for the rate was derived. The correlation function approach leaves room for semi-classical approximations that can be used to go to anharmonic electronic potential surfaces, similar to Heller's approach to spectroscopy [48].

The other two expressions contain approximations. We applied the cumulant expansion method [49] to the correlation function. Retaining the expansion up to the second order we found an expression for the rate. Performing a short-time expansion of this expression an interesting closed-form expression was found.

The correlation function approach to the calculation of relaxation rates is a well-established method [50]. Calculations in time domain were previously employed for the absorption of light by a trapped electron in a crystals [51,52], electronic absorption spectra [53–56], internal conversion [57–59], resonance Raman spectra [60] and electron transfer rates [61–63].

3.4.1 The correlation function

We will use the same Hamiltonian as in the time-independent approach. Let us express the delta function in equation 3.19 as the Fourier integral:

$$\delta(E_s - E_t) = \frac{1}{2\pi}\int_{-\infty}^{\infty} e^{it(E_s-E_t)}dt. \tag{3.21}$$

Substituting this back and slightly rearranging the square of the spin-orbit matrix elements, we find:

$$k_{ISC} = \int_{-\infty}^{\infty}\sum_{\{t_i\}}\langle S,\{s_i\}|\hat{H}_{SO}|T,\{t_i\}\rangle\langle S,\{s_i\}|\hat{H}_{SO}|T,\{t_i\}\rangle^* e^{it(E_s-E_t)}dt. \tag{3.22}$$

Using properties of the conjugation and the resolution of identity $\sum_{\{t_i\}} |T,\{t_i\}\rangle\langle T,\{t_i\}| = \hat{I}$, we obtain the ISC rate constant expressed as an integral of the correlation function:

$$k_{ISC} = \int_{-\infty}^{\infty} \langle S,\{s_i\}|H_{SO}(0)H_{SO}(t)|S,\{s_i\}\rangle \,\mathrm{d}t \tag{3.23}$$

where $H_{SO}(t) = e^{iH_0t}H_{SO}e^{-iH_0t}$ is a spin-orbit operator in the Heisenberg picture. Previous expression is still exact up to first-order of time-dependent perturbation theory. It is not necessarily limited to harmonic potentials or the Condon approximation for the spin-orbit matrix element.
We will consider the decay rate from the lowest vibrational level $\{s_i = 0\}$ of the singlet electronic state. Employing the Condon approximation we obtain,

$$k_{ISC} = |\langle S|H_{SO}|T\rangle|^2 \int_{-\infty}^{\infty} G\left(t\right) e^{it\left(\Delta E^0_{ST}+E_{\{s_i=0\}}\right)} \,\mathrm{d}t \tag{3.24}$$

where

$$\begin{gathered} G\left(t\right) = \textstyle\sum_{\{t_i\}} |\langle\{s_i=0\}\,|\,\{t_i\}\rangle|^2 e^{-itE_{\{t_i\}}} = \\ \textstyle\sum_{\{t_i\}} \int \chi_{\{s_i=0\}}\left(\{Q_{S_i}\}\right)\chi_{\{s_i=0\}}\left(\{\bar{Q}_{S_i}\}\right)\chi_{\{t_i\}}\left(\{Q_{T_i}\}\right) \\ \times\chi_{\{t_i\}}\left(\{\bar{Q}_{T_i}\}\right) e^{-it\sum_i (t_i+\frac{1}{2})\omega_i^T} \mathrm{d}Q_{S1}...\mathrm{d}Q_{SN}\mathrm{d}\bar{Q}_{T1}...\mathrm{d}\bar{Q}_{TN} \end{gathered} \tag{3.25}$$

is a generating function and E^0_{ST} is the singlet-triplet electronic energy gap. It is possible to find a closed analytic form of the generating function, that is to perform the summation over all vibrational quantum numbers $\{t_i\}$. This sum can be obtained using Mehler's formula [64, 65] for Hermite polynomials:

$$\sum_{n=0}^{\infty} \frac{e^{-\left(n+\frac{1}{2}\right)\xi}}{\sqrt{\pi}2^n n!} H_n\left(x\right) H_n\left(\bar{x}\right) e^{-\frac{1}{2}\left(x^2+\bar{x}^2\right)} = \frac{1}{\sqrt{2\pi\sinh\xi}} e^{-\frac{1}{4}\left((x+\bar{x})^2\tanh\left(\frac{\xi}{2}\right)+(x-\bar{x})^2\coth\left(\frac{\xi}{2}\right)\right)} \tag{3.26}$$

Arranging Mehler's formula so to include harmonic oscillator eigenfunctions $\chi_n(Q)$, we obtain:

$$\sum_{n=0}^{\infty} e^{-\left(n+\frac{1}{2}\right)i\omega t}\chi_n\left(Q\right)\chi_n\left(\bar{Q}\right) = \sqrt{\frac{\omega}{2\pi\sinh\left(i\omega t\right)}} e^{-\frac{\omega}{4}\left(\left(Q+\bar{Q}\right)^2\tanh\left(\frac{i\omega t}{2}\right)+\left(Q-\bar{Q}\right)^2\coth\left(\frac{i\omega t}{2}\right)\right)} \tag{3.27}$$

Equation 3.27 resembles the trace of the density matrix for the harmonic oscillator. In N dimensions, the previous expression can be generalized to:

$$\sum_{\{n_1,...,n_N\}} e^{-\sum_{\{n_i\}}\left(n_i+\frac{1}{2}\right)it\omega_i}\chi_{n_1}\left(Q_1\right)...\chi_{n_N}\left(Q_N\right)\chi_{n_1}\left(\bar{Q}_1\right)...\chi_{n_N}\left(\bar{Q}_N\right) \tag{3.28}$$

$$= \left(2\pi\right)^{-\frac{N}{2}}\left(\det\left(\mathbf{S}^{-1}\mathbf{\Omega}\right)\right)^{\frac{1}{2}} e^{-\frac{1}{4}\left(\left(\mathbf{Q}+\bar{\mathbf{Q}}\right)^T\mathbf{\Omega B}\left(\mathbf{Q}+\bar{\mathbf{Q}}\right)+\left(\mathbf{Q}-\bar{\mathbf{Q}}\right)^T\mathbf{\Omega B}^{-1}\left(\mathbf{Q}-\bar{\mathbf{Q}}\right)\right)} \tag{3.29}$$

where the matrices $\mathbf{\Omega}$, $\mathbf{S}$ and $\mathbf{B}$ are diagonal with elements $\Omega_{ii} = \omega_i$, $S_{ii} = \sinh\left(i\omega_i t\right)$ and $B_{ii} = \tanh\left(i\omega_i t/2\right)$. After substitution of Mehler formula into the generating function we obtain:

$$\begin{gathered} G\left(t\right) = \left(\sqrt{2}\pi\right)^{-N}\left(\det\left(\mathbf{S}^{-1}\mathbf{\Omega}_S\mathbf{\Omega}_T\right)\right)^{\frac{1}{2}}\int e^{-\frac{1}{4}\left(\left(\mathbf{Q}_T+\bar{\mathbf{Q}}_T\right)^T\mathbf{\Omega}_T\mathbf{B}\left(\mathbf{Q}_T+\bar{\mathbf{Q}}_T\right)\right)}\times \\ e^{-\frac{1}{4}\left(\left(\mathbf{Q}_T-\bar{\mathbf{Q}}_T\right)^T\mathbf{\Omega}_T\mathbf{B}^{-1}\left(\mathbf{Q}_T-\bar{\mathbf{Q}}_T\right)+2\mathbf{Q}_S^T\mathbf{\Omega}_S\mathbf{Q}_S+2\bar{\mathbf{Q}}_S^T\mathbf{\Omega}_S\bar{\mathbf{Q}}_S\right)}\mathrm{d}Q_{S_1}...\mathrm{d}Q_{S_1}\mathrm{d}\bar{Q}_{S_1}...\mathrm{d}\bar{Q}_{S_1} \end{gathered} \tag{3.30}$$

Now, we can transform the normal coordinates $\mathbf{Q}_T$ into $\mathbf{Q}_S$ employing the Duschinsky transformation $\mathbf{Q}_T = \mathbf{J}\mathbf{Q}_S + \mathbf{D}$:

$$\begin{aligned} G(t) = \left(\sqrt{2}\pi\right)^{-N} \left(\det\left(\mathbf{S}^{-1}\mathbf{\Omega}_S\mathbf{\Lambda}_T\right)\right)^{\frac{1}{2}} \int e^{-\frac{1}{4}\left(2\mathbf{Q}_S^T\mathbf{\Omega}_S\mathbf{Q}_S + 2\bar{\mathbf{Q}}_S^T\mathbf{\Omega}_S\bar{\mathbf{Q}}_S\right)} \\ \times e^{-\frac{1}{4}\left(\left(\mathbf{Q}_S+\bar{\mathbf{Q}}_S\right)^T\mathbf{J}^T\mathbf{\Omega}_T\mathbf{B}\mathbf{J}\left(\mathbf{Q}_S+\bar{\mathbf{Q}}_S\right) + 2\mathbf{D}^T\mathbf{\Omega}_T\mathbf{B}\mathbf{J}\left(\mathbf{Q}_S+\bar{\mathbf{Q}}_S\right) + 2\left(\mathbf{Q}_s+\bar{\mathbf{Q}}_s\right)^T\mathbf{J}^T\mathbf{\Omega}_T\mathbf{B}\mathbf{D} + 4\mathbf{D}^T\mathbf{\Omega}_T\mathbf{B}\mathbf{D}\right)} \\ \times e^{-\frac{1}{4}\left(\left(\mathbf{Q}_s-\bar{\mathbf{Q}}_s\right)^T\mathbf{J}^T\mathbf{\Omega}_T\mathbf{B}^{-1}\mathbf{J}\left(\mathbf{Q}_s-\bar{\mathbf{Q}}_s\right)\right)} \mathrm{d}Q_{S_1}...\mathrm{d}Q_{S_1}\mathrm{d}\bar{Q}_{S_1}...\mathrm{d}\bar{Q}_{S_1} \end{aligned} \tag{3.31}$$

In order to ease integration, let us substitute: $\mathbf{X} = \mathbf{Q}_s + \bar{\mathbf{Q}}_s$ and $\mathbf{Y} = \mathbf{Q}_s - \bar{\mathbf{Q}}_s$. The related Wronskian for this coordinate transformation is: $W = |\frac{\partial\left(Q_S,\bar{Q}_S\right)}{\partial(X,Y)}| = 2^{-N}$. Substituting this transformation into the generating function we obtain:

$$\begin{aligned} G(t) &= \left(2\sqrt{2}\pi\right)^{-N} \left(\det\left(\mathbf{S}^{-1}\mathbf{\Omega}_S\mathbf{\Omega}_T\right)\right)^{\frac{1}{2}} \int e^{-\frac{1}{4}\left(\mathbf{X}^T\mathbf{\Omega}_s\mathbf{X} + \mathbf{Y}^T\mathbf{\Omega}_S\mathbf{Y}\right)} \\ &\times e^{-\frac{1}{4}\left(\mathbf{X}^T\mathbf{J}^T\mathbf{\Omega}_T\mathbf{B}\mathbf{J}\mathbf{X} + 2\mathbf{X}^T\mathbf{J}^T\left(\mathbf{\Omega}_T\mathbf{B} + \mathbf{B}^T\mathbf{\Omega}_T^T\right)\mathbf{D} + 4\mathbf{D}^T\mathbf{\Omega}_T\mathbf{B}\mathbf{D}\right)} \\ &\times e^{-\frac{1}{4}\left(\mathbf{Y}^T\mathbf{J}^T\mathbf{\Omega}_T\mathbf{B}^{-1}\mathbf{J}\mathbf{Y}\right)} \mathrm{d}X_1...\mathrm{d}X_N\mathrm{d}Y_1...\mathrm{d}Y_N \\ &= \left(2\sqrt{2}\pi\right)^{-N} \left(\det\left(\mathbf{S}^{-1}\mathbf{\Lambda_a}\mathbf{\Lambda_b}\right)\right)^{\frac{1}{2}} \int e^{D^T\mathbf{\Lambda_b}\mathbf{B}\mathbf{D}} I_x I_y \end{aligned} \tag{3.32}$$

where:

$$\begin{aligned} I_x = \int e^{-\frac{1}{4}\mathbf{X}^T\left(\mathbf{J}^T\mathbf{\Omega}_T\mathbf{B}\mathbf{J} + \mathbf{\Omega}_S\right)\mathbf{X} - \frac{1}{2}\mathbf{X}^T\mathbf{J}^T\left(\mathbf{\Omega}_T\mathbf{B} + \mathbf{B}^T\mathbf{\Omega}_T^T\right)\mathbf{D}} \mathrm{d}X_1...\mathrm{d}X_N \\ I_y = \int e^{-\frac{1}{4}\mathbf{Y}^T\left(\mathbf{J}^T\mathbf{\Omega}_T\mathbf{B}^{-1}\mathbf{J} + \mathbf{\Omega}_S\right)\mathbf{Y}} \mathrm{d}Y_1...\mathrm{d}Y_N \end{aligned} \tag{3.33}$$

This way, the evaluation of the generating function is reduced to two N-dimensional integrals. They have a standard Gaussian form so that we can use the tabulated Gaussian integral:

$$\int e^{-\mathbf{X}^T\mathbf{A}\mathbf{X} + 2\mathbf{X}^T\mathbf{B}} \mathrm{d}X_1...\mathrm{d}X_N = \sqrt{\frac{\pi^N}{\det\mathbf{A}}} e^{\mathbf{B}^T\mathbf{A}^{-1}\mathbf{B}} \tag{3.34}$$

and obtain the closed-form expressions:

$$I_x = \pi^{\frac{N}{2}} 2^N \left(\det\left(\mathbf{J}^T\mathbf{\Omega}_T\mathbf{B}\mathbf{J} + \mathbf{\Omega}_S\right)\right)^{-\frac{1}{2}} e^{\mathbf{D}^T\mathbf{\Omega}_T\mathbf{B}\mathbf{J}\left(\mathbf{J}^T\mathbf{\Omega}_T\mathbf{B}\mathbf{J} + \mathbf{\Omega}_S\right)^{-1}\mathbf{J}^T\mathbf{\Omega}_T\mathbf{B}\mathbf{D}} \tag{3.35}$$

$$I_y = \pi^{\frac{N}{2}} 2^N \left(\det\left(\mathbf{J}^T\mathbf{\Omega}_T\mathbf{B}^{-1}\mathbf{J} + \mathbf{\Omega}_S\right)\right)^{-\frac{1}{2}}. \tag{3.36}$$

Substituting back these integrals, the final form of the generating function is obtained:

$$\begin{aligned} G(t) = 2^{\frac{N}{2}} \sqrt{\frac{\det\left(\mathbf{S}^{-1}\mathbf{\Omega}_S\mathbf{\Omega}_T\right)}{\det\left(\left(\mathbf{J}^T\mathbf{\Omega}_T\mathbf{B}\mathbf{J} + \mathbf{\Omega}_S\right)\det\left(\mathbf{J}^T\mathbf{\Omega}_T\mathbf{B}^{-1}\mathbf{J} + \mathbf{\Omega}_S\right)\right)}} \\ \times e^{\mathbf{D}^T\left(\mathbf{\Omega}_T\mathbf{B}\mathbf{J}\left(\mathbf{J}^T\mathbf{\Omega}_T\mathbf{B}\mathbf{J} + \mathbf{\Omega}_S\right)^{-1}\mathbf{J}^T\mathbf{\Omega}_T\mathbf{B} - \mathbf{\Omega}_T\mathbf{B}\right)\mathbf{D}} \end{aligned} \tag{3.37}$$

For evaluating the inter-system crossing rate, a time integration has to be performed:

$$k_{ISC} = |\langle S|\hat{H}_{SO}|T\rangle|^2 \int_{-\infty}^{\infty} G(t)\, e^{\frac{it}{\hbar}\left(\Delta E_{ST}^0 + \frac{1}{2}Tr\mathbf{\Omega}_S\right)} \mathrm{d}t \tag{3.38}$$

In practice, this time integration is done numerically

3.4.2 Cumulant expansion

Cumulants or semi-invariants are used often in probability theory. Cumulants of a probability distribution can be employed to determine the nature of a random variable. They are related to the cluster expansion in statistical and quantum mechanics [49]. In this section they will be used in connection to the ordered exponential function. After substitution of the delta function with the Fourier integral we obtain from equation 3.20:

$$k_{ISC} = |\langle S|\hat{H}_{SO}|T\rangle|^2 \int_{-\infty}^{\infty} \langle \{s_i = 0\} \left| e^{it\hat{H}_S} e^{-it\hat{H}_T} \right| \{s_i = 0\}\rangle e^{it\Delta E^0_{ST}} \mathrm{d}t \tag{3.39}$$

It is possible to use the cumulant expansion to approximate the average in the previous equation. Using Feynman's theorem [66] about ordered exponential functions, we write:

$$G'(t) = \langle \{s_i = 0\} \left| e^{it\hat{H}_S} e^{-it\hat{H}_T} \right| \{s_i = 0\}\rangle = \langle \{s_i = 0\} \left| e_-^{i\int_0^t \Delta\hat{H}(t)\,\mathrm{d}t} \right| \{s_i = 0\}\rangle \tag{3.40}$$

where we used the negative time-ordered exponential and

$$\Delta\hat{H}(t) = e^{i\hat{H}_S t} \left(\hat{H}_T - \hat{H}_S\right) e^{-i\hat{H}_S t} \tag{3.41}$$

is the time-dependent energy gap. The last expression can be written using the cumulant expansion:

$$G'(t) = e^{\sum_{n=1}^{\infty} i^n \kappa_n(t)} \tag{3.42}$$

where the n-th order cumulant is defined by

$$\kappa_n = \int_0^t dt_n \int_0^{t_n} dt_{n-1} ... \int_0^{t_2} dt_1 \langle \{s_i = 0\} \left| \Delta\hat{H}(t_1)\, \Delta\hat{H}(t_2) ... \Delta\hat{H}(t_n) \right| \{s_i = 0\}\rangle_c \tag{3.43}$$

As was previously mentioned, the time integration is ordered negatively so that $t > t_n > t_{n-1} > ... > t_2 > t_1$. The first two cumulants are:

$$\begin{gathered} \kappa_1 = \int_0^t dt_1 \langle \{s_i = 0\} | \Delta\hat{H}(t_1) | \{s_i = 0\}\rangle_c = \\ \int_0^t dt_1 \langle \{s_i = 0\} | \Delta\hat{H}(t_1) | \{s_i = 0\}\rangle \\ \kappa_2 = \int_0^t dt_2 \int_0^{t_2} dt_1 \langle \{s_i = 0\} | \Delta\hat{H}(t_1)\, \Delta\hat{H}(t_2) | \{s_i = 0\}\rangle_c = \\ \int_0^t dt_2 \int_0^{t_2} dt_1 \left(\langle \{s_i = 0\} | \Delta\hat{H}(t_1)\, \Delta\hat{H}(t_2) | \{s_i = 0\}\rangle - \langle \{s_i = 0\} | \Delta\hat{H}(t) | \{s_i = 0\}\rangle^2 \right) \end{gathered} \tag{3.44}$$

We will not consider higher cumulants furthermore. Using the Duschinsky transformation between the coordinates $\mathbf{Q}_S$ and $\mathbf{Q}_T$, the time-dependent energy gap $\Delta H(t)$ is:

$$\Delta\hat{H}(t) = \frac{1}{2} \sum_{i,j=1}^{N} Q_{S_i}(t)\, M_{ij} Q_{S_j}(t) + \sum_{i=1}^{N} A_i Q_{S_i}(t) + C \tag{3.45}$$

where $\mathbf{M} = \mathbf{J}^T\mathbf{\Omega}_T^2\mathbf{J} - \mathbf{\Omega}_S^2$, $\mathbf{A} = \mathbf{J}^T\mathbf{\Omega}_T^2\mathbf{D}$, $C = \frac{1}{2}\mathbf{D}^T\mathbf{\Omega}_T^2\mathbf{D}$ and N is the number of normal modes. It is not difficult to find the following averages:

$$\langle\{s_i = 0\}|\Delta\hat{H}\left(t\right)|\{s_i = 0\}\rangle = \frac{1}{4}\sum_{i=1}^{N}\frac{M_{ii}}{\omega_{S_i}} + C \tag{3.46}$$

$$\begin{gathered}\langle\{s_i = 0\}|\Delta\hat{H}\left(t_1\right)\Delta\hat{H}\left(t_2\right)|\{s_i = 0\}\rangle = \frac{1}{16}\sum_{i,j=1}^{N}\frac{M_{ii}M_{jj}}{\omega_{S_i}\omega_{S_j}} \\ +\frac{1}{8}\sum_{i,j=1}^{N}\frac{M_{ij}^2}{\omega_{S_i}\omega_{S_j}}e^{i\left(\omega_{S_i}+\omega_{S_j}\right)\left(t_2-t_1\right)} + \frac{1}{2}C\sum_{i=1}^{N}\frac{M_{ii}}{\omega_{S_i}} + \frac{1}{2}\sum_{i=1}^{N}\frac{A_i^2}{\omega_{S_i}}e^{i\omega_{S_i}\left(t_2-t_1\right)} + C^2\end{gathered} \tag{3.47}$$

$$\begin{gathered}\langle\{s_i = 0\}|\Delta\hat{H}\left(t_1\right)\Delta\hat{H}\left(t_2\right)|\{s_i = 0\}\rangle_c = \\ \langle\{s_i = 0\}|\Delta\hat{H}\left(t_1\right)\Delta\hat{H}\left(t_2\right)|\{s_i = 0\}\rangle - \langle\{s_i = 0\}|\Delta\hat{H}\left(t\right)|\{s_i = 0\}\rangle^2 = \\ \frac{1}{8}\sum_{i,j=1}^{N}\frac{M_{ij}^2}{\omega_{S_i}\omega_{S_j}}e^{i\left(\omega_{S_i}+\omega_{S_j}\right)\left(t_2-t_1\right)} + \frac{1}{2}\sum_{i=1}^{N}\frac{A_i^2}{\omega_{S_i}}e^{i\omega_{S_i}\left(t_2-t_1\right)}\end{gathered} \tag{3.48}$$

Substituting these into the first and second-order cumulants, we find:

$$\kappa_1 = \frac{1}{4}\sum_{i=1}^{N}\frac{M_{ii}}{\omega_{S_i}} + Ct \tag{3.49}$$

$$\kappa_2 = \frac{1}{8}\sum_{i,j=1}^{N}\frac{M_{ij}^2}{\omega_{S_i}\omega_{S_j}}\left(\frac{it}{\omega_{S_i}+\omega_{S_j}} + \frac{1-e^{i\left(\omega_{S_i}+\omega_{S_j}\right)t}}{\left(\omega_{S_i}+\omega_{S_j}\right)^2}\right) + \frac{1}{2}\sum_{i=1}^{N}\frac{A_i^2}{\omega_{S_i}}\left(\frac{it}{\omega_{S_i}} + \frac{1-e^{i\omega_{S_i}t}}{\omega_{S_i}^2}\right)$$

This gives the inter-system crossing rate within the second-order cumulant expansion:

$$\begin{gathered}k_{ISC} = |\langle S|\hat{H}_{SO}|T\rangle|^2\int_{-\infty}^{\infty}e^{it\left(\Delta E_{ST}^0+\frac{1}{4}\sum_{i=1}^{N}\frac{M_{ii}}{\omega_{S_i}}+C\right)} \\ \times e^{-\frac{1}{8}\sum_{i,j=1}^{N}\frac{M_{ij}^2}{\omega_{S_i}\omega_{S_j}}\left(\frac{it}{\omega_{S_i}+\omega_{S_j}}+\frac{1-e^{i\left(\omega_{S_i}+\omega_{S_j}\right)t}}{\left(\omega_{S_i}+\omega_{S_j}\right)^2}\right)-\frac{1}{2}\sum_{i=1}^{N}\frac{A_i^2}{\omega_{S_i}}\left(\frac{it}{\omega_{S_i}}+\frac{1-e^{i\omega_{S_i}t}}{\omega_{S_i}^2}\right)}\mathrm{d}t\end{gathered} \tag{3.50}$$

3.4.3 Short-time approximation

It is possible to obtain short-time approximation from the second-order cumulant expansion by keeping the time-dependent terms up to the second order in time:

$$G'\left(t\right) = e^{it\left(\frac{1}{4}\sum_{i=1}^{N}\frac{M_{ii}}{\omega_{S_i}}+C\right)-t^2\left(\frac{1}{8}\sum_{i,j=1}^{N}\frac{M_{ij}^2}{\omega_{S_i}\omega_{S_j}}+\frac{1}{2\hbar}\sum_{i=1}^{N}\frac{A_i^2}{\omega_{S_i}}\right)} \tag{3.51}$$

Using the tabulated integral $\int_{-\infty}^{\infty}e^{iat-bt^2}\,\mathrm{d}t = \sqrt{\frac{\pi}{b}}e^{-\frac{a^2}{4b}}$ we obtain:

$$k_{ISC} = |\langle S|\hat{H}_{SO}|T\rangle|^2\sqrt{\frac{\pi}{\frac{1}{8}\sum_{i,j=1}^{N}\frac{M_{ij}^2}{\omega_{S_i}\omega_{S_j}}+\frac{1}{2\hbar}\sum_{i=1}^{N}\frac{A_i^2}{\omega_{S_i}}}}e^{-\frac{\left(\frac{1}{4}\sum_{i=1}^{N}\frac{M_{ii}}{\omega_{S_i}}+\frac{C}{\hbar}+\Delta E^0\right)^2}{\frac{1}{2}\sum_{i,j=1}^{N}\frac{M_{ij}^2}{\omega_{S_i}\omega_{S_j}}+2\sum_{i=1}^{N}\frac{A_i^2}{\omega_{S_i}}}} \tag{3.52}$$

This expression is interesting because it expresses the rate in a closed-form. No numerical time-integration is needed, here.

4 Implementation and testing of the time-dependent method for inter-system crossing rates

4.1 Implementation

The time-dependent approach for the calculation of inter-system crossing rates presented in the previous chapter is implemented in MATLAB and the C language. The code written in C is also interfaced as a subroutine to the VIBES program. The computer implementation of the equations does not present a difficult problem because the calculation of the correlation function and the cumulant expansion involves only time integration, multiplication of the matrices, and calculation of a matrix inverse, and a determinant. This clearly is an advantage of the time-dependent over the time-independent approach for the calculation of inter-system crossing rates. The real parts of the correlation function and the cumulant expansion are even functions of time. It is only needed to calculate their values for positive times. Imaginary part of these functions are odd functions of time. Their net contributions to the rate are zero.

In order to ensure convergence of the correlation function and the cumulant expansion, a damping factor η is introduced. Its physical role is to include all possible additional dampings that vibronic states subject to, such as radiative damping or damping due to coupling between normal modes or due to vibrational relaxation. The damping function has a Gaussian form. In order to correlate the damping parameter with the value of the window function width in the time-independent approach, its value is represented in the energy unit cm^{-1}. The calculated rate will weakly depend on the actual choice of the damping parameter. Due to this, it is recommended that inter-system crossing rates are calculated for several different damping values.

Here the input needed to start a time-dependent calculation of the inter-system crossing rate using the VIBES program will be explained. It is presented in Figure 4.1. Compared to a VIBES input for a time-independent calculation, it contains new keywords: $method, $damping, $interval, and $npoints. These keywords are mandatory for the time-dependent approach. The input file starts with the keyword $method that can have two values, static and dynamic. The former is for the time-independent and the latter is for the time-dependent calculation. $deltae specifies the adiabatic electronic energy gap in cm^{-1}. The Gaussian damping in cm^{-1} should be specified in $damping. Once the damping value is determined, the next step is to fix the time interval for the integration (in femtoseconds) and the number of points in it. This can be done with the keywords $interval and $npoints. The time interval should be

```
$method=dynamic
$deltae=6652.182
$damping=1.0
$npoints=1000
$interval=5.0
$elec=2319.0
$eta=0.10
$vibs mopac
s1_mopac.out
t1_mopac.out
$coord-files
s1_mopac.out
t1_mopac.out
$end
```

Figure 4.1: An example input file to start a time-dependent calculation of an inter-system crossing rate with the VIBES program

sufficiently large to ensure that at its end the values of the correlation function and cumulant expansion are almost completely dampted. Also, the number of the integration points should be sufficiently high to guarantee numerical accuracy. Further discussion about the optimal value of the damping parameter, the time interval and the number of points for the integration is given in the following section where test results are presented. The keyword $elec specifies the value of the square of the electronic spin-orbit matrix element (in cm^{-2}). $eta is a "dummy" keyword because it is not needed for the time-dependent calculation, but it should be present in order to start the VIBES program. The end of the input file contains information about what types files are used for coordinate ($coord-files) and frequencies and related normal modes ($vibs). The coordinates, frequencies and normal modes, the adiabatic electronic energy gap and the electronic spin-orbit matrix element are obtained from the quantum-chemical calculations.

The pseudocode related to the program is presented in Figure 4.2. After the input data are read, the subroutine from VIBES program that calculates the displacement vector **B** and the Duschinsky matrix **J** is started. **B** and **J** together with the damping, the time interval, the number of points, the adiabatic electronic energy gap and the spin-orbit matrix element are transferred to a subroutine *ika_gsl* written in C that performs the calculation of the inter-system crossing rate based on the time-dependent approach. Here, all input data are transformed into atomic units. This finishes the preparation of the data needed for the subsequent calculations.

The first quantities that are calculated are the matrix **M**, the vector **A** and the scalar C needed for the rate calculation using the cumulant expansion. After this, the loop that calculates the correlation function and the cumulant expansion for every point in the time interval starts. The values of the correlation function and the cumulant expansion are placed in vectors. The calculation of the correlation function is more difficult than the calculation of the cumulant expansion because it involves the evaluation of

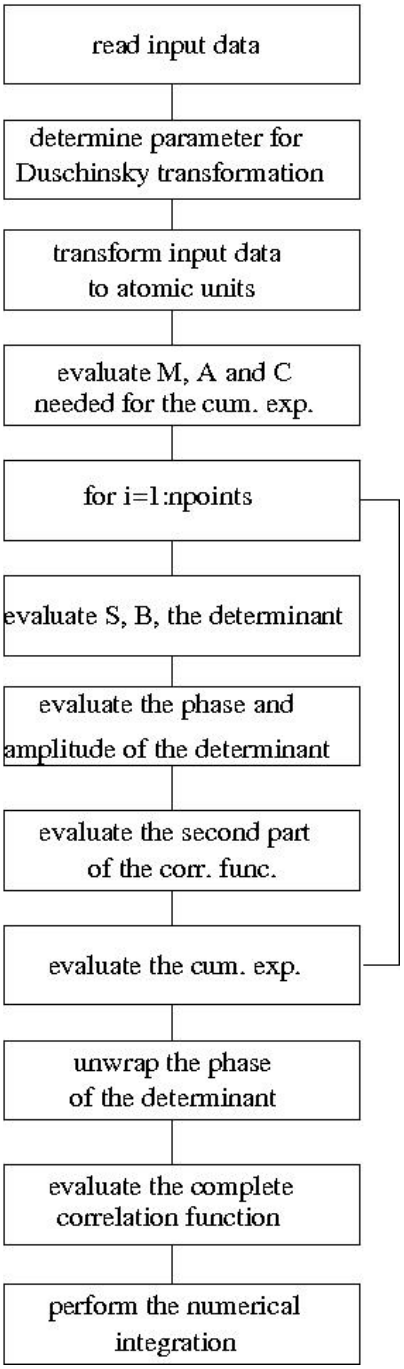

Figure 4.2: The pseudocode of the program. For explanation see text.

square roots of complex determinant (see the equation 3.37). The ratio of the three determinants is calculated as a determinant of the ratio of matrices. Because the determinant has a complex value, the determination of its root contains some subtleties. The problem is that the phase of the complex number comes out in the interval $(-\pi, \pi)$. With the increase of time, the phase of the determinant will be larger than π and then its value will have a jump of 2π. In order to avoid these jumps, there should be an unwrapping of the phase so that the phase has a continuous dependence on time. Therefore, in the loop the matrices $\mathbf{B}$ and $\mathbf{S}$ are evaluated and subsequently the determinant is obtained. The phase and amplitude of the determinant are stored in separate vectors. They are used later. The second part of the function G from the equation 3.37 is calculated and multiplied with the phase factor due to adiabatic electronic energy gap and the zero-order vibrational energy of the initial state. Also, the cumulant expansion is evaluated. The loop stops after all points are computed. Now, the phase of the determinant is unwrapped so that it becomes a continuous function of time. Together with the square root of the amplitude of the determinant, it is used to obtain the complete correlation function. At the end of the program, there is a numerical integration and also the calculation of the inter-system crossing rate in the short-time approximation which does not require time integration (according to equation 3.52). The integration is performed using Simpson's one-third rule.
The program prints the rates calculated with the three different approaches to standard output. One such output reads:

```
complete correlation function= 2452256345.593507 (1/s)
cumulant expansion = 10291385105.363094 (1/s)
short time approximation = 27152082130.970325 (1/s)
```

To relate the output to the underlying theory, we specify one more time the formulas that were used. The correlation function is calculated using equation 3.38, the cumulant expansion using equation 3.50 and the short-time expansion using equation 3.52. Also, the program writes two files *correlation.out* and *cumulant.out* that contain the time (in a.u.) and real and imaginary parts of the correlation function and cumulant expansion, respectively.

4.2 Test results

In the previous Chapter, three different formulas were derived. The first one, expressing the correlation function using Mehler's formula for the sum of the Hermite polynomials is exact. The second is based on the second-order cumulant expansion and the third is a short-time approximation of it. Both are approximations to the first formula. Here, a comparison of the results from the three formulas with the values obtained from the time-independent approach is given.
As was mentioned in the previous section, a more detailed discussion about the influence of the input parameters on the results will be given.

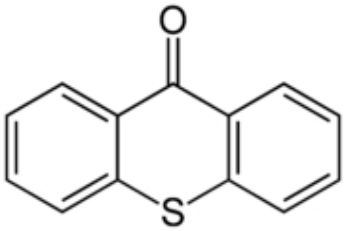

Figure 4.3: Chemical structure of thioxanthone

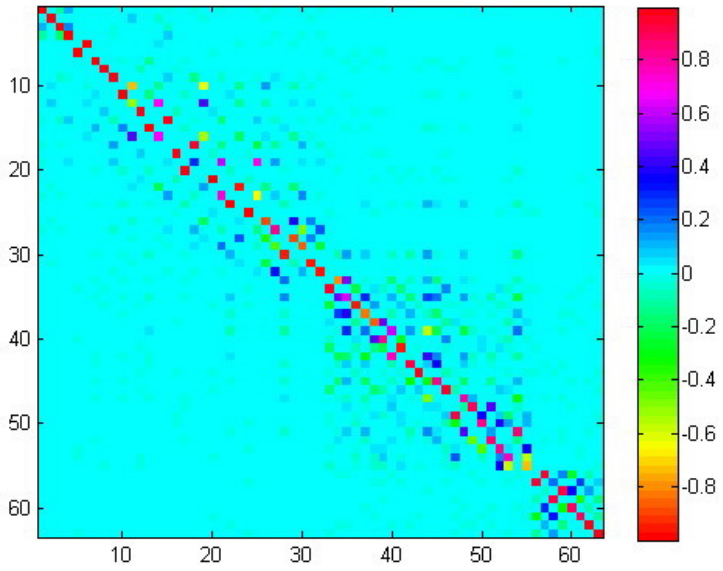

Figure 4.4: Graphical representation of the Duschinsky matrix for the $S_0 \rightarrow S_2$ transition in thioxanthone

4.2.1 Absorption spectrum of thioxanthone

In order to gain confidence about the correctness of our approach, we applied the correlation function approach to the calculation of a vibronic spectrum. For that purpose, we chose thioxanthone, a heterocycle with a sulfur atom and a keto group. Its ground state structure formula is presented in Figure 4.3. It is well known that thioxanthone exhibits strong dependence of the electronic relaxation on the polarity and hydrogen-bonding of the solvent.
Rai-Constapel et al. [67] examined the electronic absorption spectrum of thioxanthone. They optimized the ground and excited states geometries at the DFT/B3-LYP/TZVP level with a TZVPP basis set on the sulfur atom. The ground state is planar with C_{2v} symmetry. There are 63 normal modes. The adiabatic energy gap between the ground and the second excited singlet state is 26947 cm^{-1}. The Duschinsky matrix for the transition from the ground to the second excited singlet electronic state ($^1\pi\pi^*$) is presented in Figure 4.4. It shows noticeable mixing between the normal modes. The calculated correlation function of the transition dipole moment according to equation 3.38 is presented in Figure 4.5. The related absorption spectrum is shown in Figure 4.6.

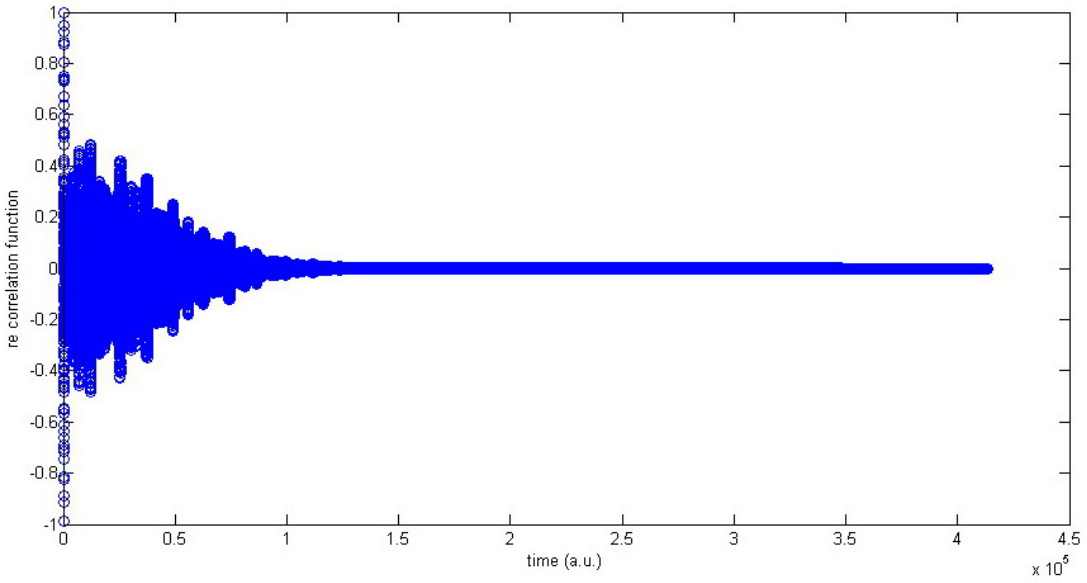

Figure 4.5: Real part of the correlation function related to the absorption spectrum of thioxanthone

Figure 4.6 also contains the absorption spectrum obtained from the time-independent approach. Here, the Franck-Condon factors are evaluated explicitly using the VIBES program. There is an excellent agreement between the two calculated spectra with the time-dependent and the time-independent approaches, respectively.

4.2.2 Inter-system crossing rates

Four molecules were selected as test cases for the calculation of inter-system crossing rates: thymine, flavone, porphyrin, and phenalenone, see Figure 4.7. They are chosen to include examples with large Duschinsky mixing (thymine), fast inter-system crossing rates (flavone), slow inter-system crossing rates (porphyrin), and large numbers of normal modes (phenalenone, flavone and porphyrine). For all these molecules inter-system crossing rates were previously obtained by using the time-independent approach as implemented in the VIBES program.

4.2.2.1 Thymine

Thymine or 5-methyluracil is a pyrimidine basis and it is the smallest molecule for which the inter-system crossing rate was obtained using the time-dependent approach. Its most significant photophysical property is the ultrafast relaxation to the electronic ground state due to strong non-adiabatic coupling [68]. Despite that, it is observed that the triplet quantum yield depends on the solvent [69,70]. The solvent dependence of the triplet quantum yield is a consequence of the strong shift of the $n\pi^*$ states due to solvation [71]. In acetonitrile solution, Hare et al. [8] using time-resolved infra-red spectroscopy estimated that the triplet state is formed within 10 ps after excitation to

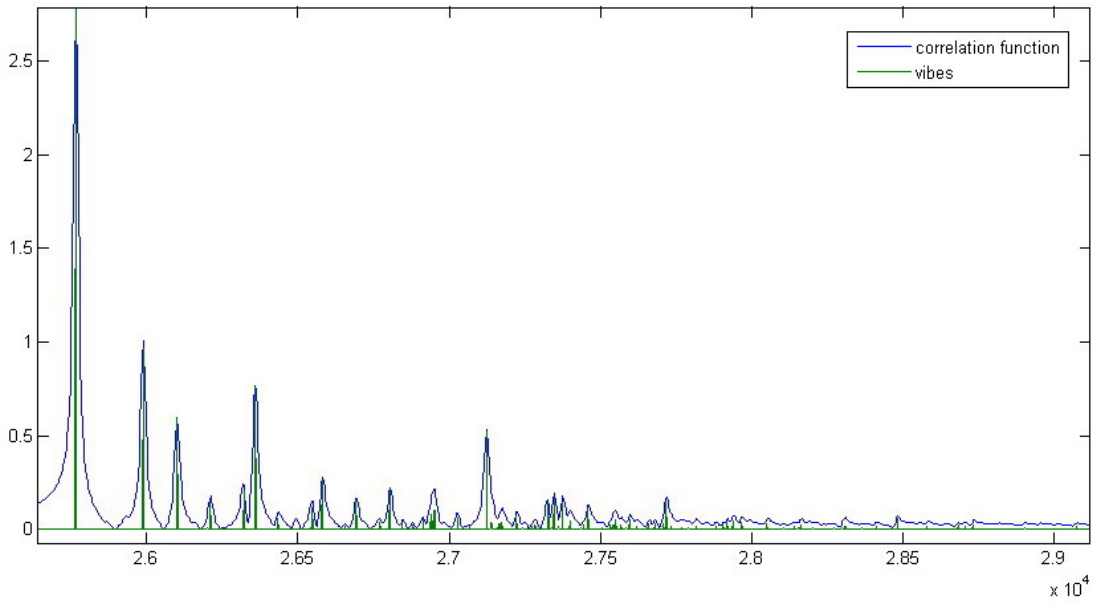

Figure 4.6: Absorption spectrum for the $S_2 \leftarrow S_0$ transition in thioxanthone obtained from the time-dependent and the time-independent (VIBES) approaches

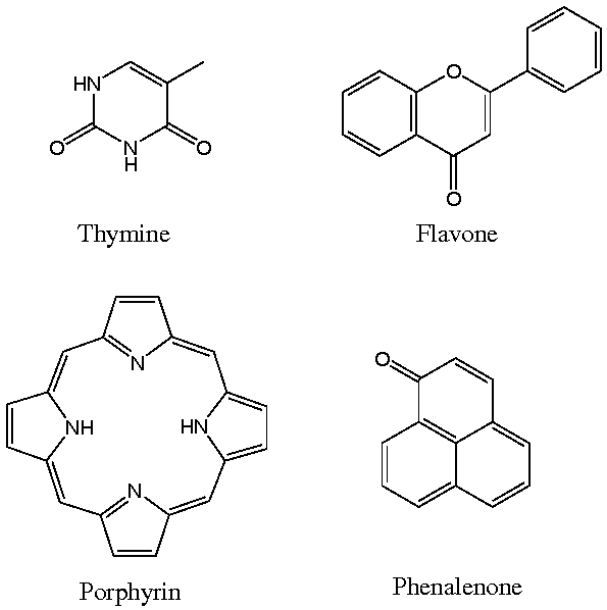

Figure 4.7: The ground state structures of the test molecules.

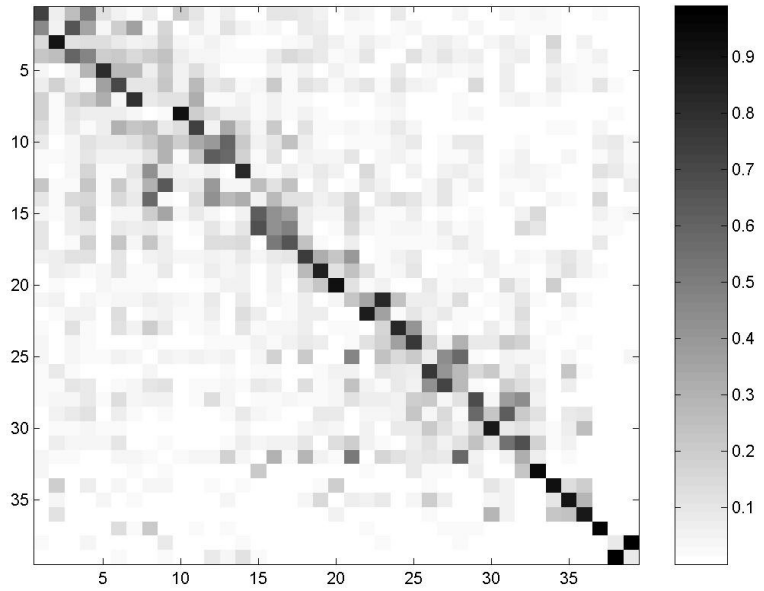

Figure 4.8: Duschinsky matrix related to the transition between the S_1 and T_1 states of thymine. In order to visualize the normal mode mixing, absolute values of the matrix elements J_{ij} are shown.

the first bright electronic state. Understanding the mechanism and time-scale of the triplet formation in thymine could give insight into the mechanism of the formation of a cyclobutane dimer, the prevailing photoproduct upon UV excitation of nucleic acids. In the work of Etinski et al. [7], the inter-system crossing between the S_1 and T_1 states in thymine was examined. For the test purposes of this thesis, we will use the RI-CC2/cc-pVDZ optimized geometries of the S_1 ($n\pi^*$) and T_1 ($\pi\pi^*$) states from reference [7]. The equilibrium nuclear geometries of both electronic states were obtained without symmetry constrains. There are 39 normal modes. The adiabatic electronic energy gap between the S_1 and T_1 states is 6652 cm^{-1}. The sum of squares of all electronic spin-orbit matrix elements is 2319 cm^{-1}. The S_1 state is planar exhibiting an elongated C_4-O_4 bond while the T_1 state is significantly V shaped. As a result, the normal modes are strongly displaced and there is a large mixing of the normal modes. There are only 5 normal modes that have displacements less than 0.1. 11 normal modes have displacements larger than 1.0. The Duschinsky matrix related to the $S_1 \rightarrow T_1$ transition is presented in Figure 4.8. The mixing is particularly large among the low-frequency modes.

It was found that the ISC rate constant is 1.3×10^9 s^{-1} using all RI-CC2 vibrational modes, 5 quanta per mode were allowed and the search interval was 0.01 cm^{-1}. Interestingly, the ISC rate constant obtained using DFT/B3-LYP/TZVP geometries was two order of magnitude larger. This was explained by a better vibrational overlap due to a larger similarity of the DFT optimized S_1 and T_1 geometries.

The correlation function, cumulant expansion and short-time expansion for thymine are presented in Figure 4.8. No damping was used in this case, that is $\eta = 0$. This is because there were many normal modes with large displacement so that both the

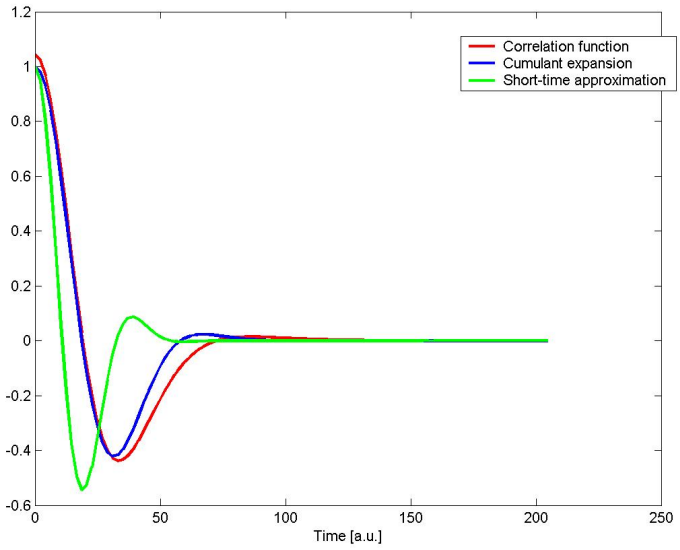

Figure 4.9: The real parts of the correlation function, second-order cumulant expansion and short-time approximation as functions of time for thymine

complete correlation function and the cumulant expansion perform only two oscillations and then remain zero. It is interesting to note that the functions decay to zero with only 5 fs. On the other hand, the short-time approximation is a product of a cosine and an exponentially decreasing function as can be seen from equation 3.51. It will always have the same time dependence. Here it is plotted only to compare its time dependence with the other functions. Within the program, it is never actually calculated. Instead, the expression obtained by analytical integration (equation 3.51) is used.

The rates obtained by numerical integration are 2.5×10^9, 1.0×10^{10} and 2.7×10^{10} s^{-1} using the correlation function, cumulant expansion and short-time approximation respectively. The closest value as compared to the time-independent approach is the one from the exact correlation function. In this case, the cumulant expansion and the short-time approximation give a result which is one order of magnitude larger. It should be kept in mind that the rate obtained with the time-independent approach is only an approximation to the full harmonic result because it was evaluated using at most 5 quanta per mode in the final vibronic states. It is interesting that the shape of the correlation function and cumulant expansion are similar to each other but that the rate obtained from the cumulant expansion is 4 times larger. This is because the correlation function has the more negative values than the cumulant expansion. The short-time approximation decays faster than the other functions, yielding the largest value for the rate.

It can be seen in Figure 4.8 that the value of the correlation function for $t = 0$ is greater than one, although it should be exactly one. This is the consequence of the fact that the determinant of the Duschinsky matrix is 0.96. If the Duschinsky matrix is orthogonal, its determinant should be always one. This disagreement is due to the impossibility to separate the vibrational and rotational parts of the Duschinsky matrix,

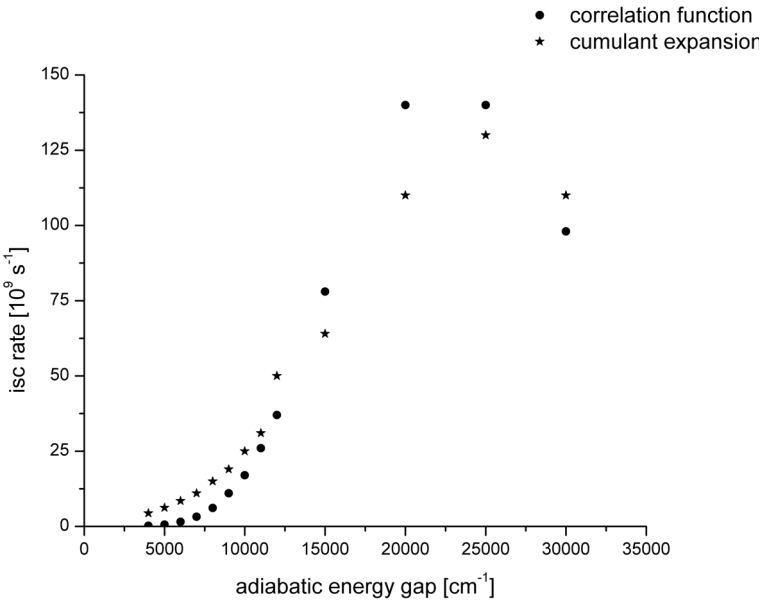

Figure 4.10: Dependence of the inter-system crossing rate on the adiabatic electronic energy gap in thymine

as explained in the Chapter about the molecular Hamiltonian.
The time-dependent approach is ideally suited to calculate inter-system crossing rates for large adiabatic electronic energy gaps. This is almost computationally impossible to obtain with the time-independent approach due to extremely large vibronic density of final states. Rates obtained for various adiabatic energy gaps are presented in Figure 4.9. Shown are values obtained using the correlation function and the second-order cumulant expansion. For energy gaps between 4000 and 15000 cm^{-1}, the rate increases almost exponentially. For energy gaps above 25000 cm^{-1}, there is a decrease in the rates probably due to a smaller vibrational overlap. The time needed for their calculation was the same regardless of the adiabatic energy gap. The computational time was about 5 s. This clearly shows a great advantage of the time-dependent over the time-independent approach.

4.2.2.2 Phenalenone

Phenalenone or 1H-phenalen-1-one is an aromatic ketone with triplet quantum yield close to 100% in variety of solvents. Due to that it is employed as a reference for the determination of singlet oxygen sensitization [72]. There is evidence that compounds that include the phenalenone skeleton are involved in a defence mechanism of plants against microorganisms [73, 74].
The photophysics of phenalenone was examined by quantum chemical methods in the work of Daza et al. [75]. The equilibrium geometries of the S_1 ($n\pi^*$) and T_1 ($\pi\pi^*$) electronic states were optimized at the DFT/B3-LYP/TZVP level using C_s symmetry. The adiabatic energy gap between the S_1 and T_1 states is 3599 cm^{-1}. There are 60 normal modes. The squares of the electronic spin-orbit matrix elements between the S_1

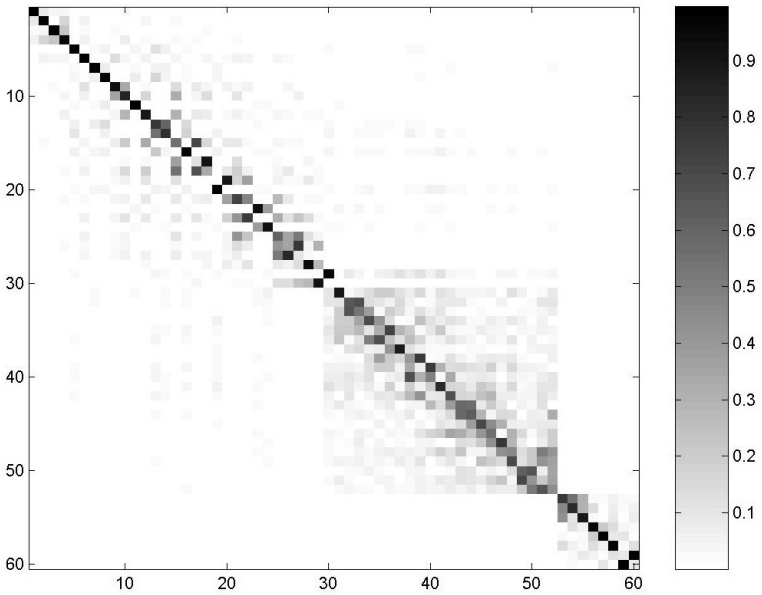

Figure 4.11: Duschinsky matrix related to transition between the S_1 and T_1 states of phenalenone. In order to visualize the normal mode mixing, absolute values of the matrix elements J_{ij} are shown.

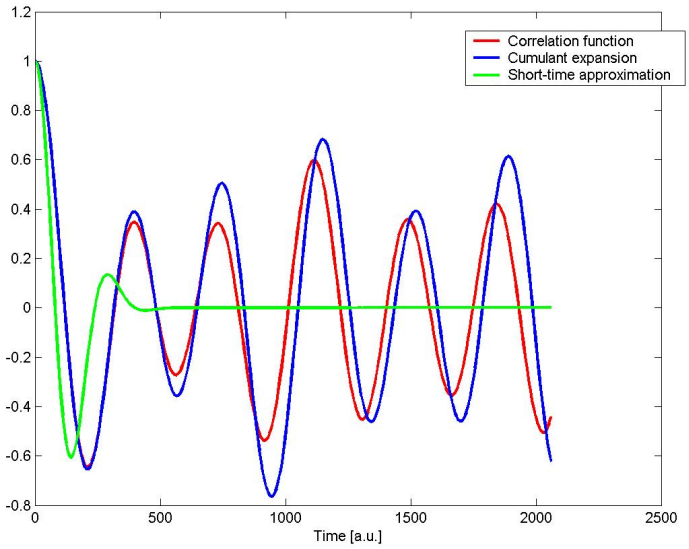

Figure 4.12: The real parts of the correlation function, the second-order cumulant expansion and the short-time approximation as functions of time for phenalenone (presented only the first 50 fs)

and the x, y and z sublevels of the T_1 state are 1823, 234, and <1, cm^{-1} respectively. The Duschinsky matrix for the transition between the S_1 and T_1 states is presented in Figure 4.11. It contains several blocks in which normal modes are mixed. The existence of the blocks is due to the symmetry constraints imposed on the electronic states. Using the time-independent approach, the following rates were found: 1.1×10^{11} s^{-1} ($S_1 \rightsquigarrow T_{1x}$), 1.4×10^{11} s^{-1} ($S_1 \rightsquigarrow T_{1y}$) 8.1×10^{10} s^{-1} ($S_1 \rightsquigarrow T_{1z}$). Due to symmetry only 41 totally symmetric in-plane vibational modes were used. The search interval was 0.5 cm^{-1}.

Phenalenone was a test case where the parameters (the time interval and the number of points for the integration, and the damping factor η) for the numerical calculations were fully tested. It has a reasonably large number of normal modes. In combination with the noticeable adiabatic energy gap makes the time-independent approach severely time-consuming. The time-dependent calculations that were performed including all normal modes. The correlation function, the second-order cumulant expansion, and the short-time approximation from a test calculation for phenalenone are presented in Figure 4.12. Only the first 50 fs were plotted in order to present the oscillations of the functions in a more transparent way. As in thymine, the short-time approximation decreases faster than the other two functions. Oscillations that the correlation function and cumulant expansion perform seem to will never cease. Because of this, η was introduced, to damp those oscillations with the Gaussian function so to ensure convergence of the integration. Test calculations for different values of the numerical integration parameters and the damping factor are summed up in Table 4.1. The purpose of having different damping factors is to build the vibronic density of the final states (VDOS) with different resolution. In the large molecule (statistical) limit, the VDOS should be a continuous function of the electronic adiabatic energy gap. But in real molecules, it is not and contains small discontinuities due to a sudden change of the number of the vibronic state. These discontinuities depend on the resolution, so there is a systematic way how to refine the VDOS by taking smaller and smaller values for the η. Seven different values for the η were used: 10.0, 5.0, 3.0, 2.0, 1.0, 0.5 and 0.1 cm^{-1}. Those values are selected because they are usually used in the time-independent approach as the search interval. For every η value, several integration limits (time interval) and numbers of grid points are used. The goal of this examination was to find how numerical parameters influence the final result. As can be seen from Table 4.1, taking a longer time intervals does not change the rate. Also, in the cases $\eta = 1.0$ and $\eta = 0.1$ cm^{-1}, an increase in the number of grid points did not change the rate. It seems that the optimal number of points per one picosecond depends on the value η. For the large η (10.0-2.0 cm^{-1}), it is sufficient to take 1500 points/1 ps but for smaller η (1.0-0.1 cm^{-1}) it is necessary to use more points, i. e. 2000-2500. This prescription can depend on the number of normal modes. Concerning the dependence of the rate on the damping parameter, we see that using smaller and smaller values gives systematically smaller values of the rates obtained by the correlation function method. The exception is the smallest value of damping parameter, 0.1 that gives the largest rate. This is the due to the previously explained dependence of the final state vibrational density of states that is not continuous. On the other side, rates obtained by the cumulant expansion are more robust to the variation of the damping factor.

Table 4.1: Calculated inter-system crossing rates $S_1 \rightsquigarrow T_{1y}$ for phenalenone in s^{-1}

time interval [ps]	# points	correlation function	cumulant expansion	η cm^{-1}
3	4500	5.7 10^9	2.9 10^9	10.0
200	500000	5.7 10^9	2.9 10^9	10.0
6	9000	3.9 10^9	2.8 10^9	5.0
200	500000	3.9 10^9	2.8 10^9	5.0
20	30000	3.1 10^9	2.9 10^9	3.0
200	500000	3.1 10^9	2.9 10^9	3.0
20	30000	3.0 10^9	3.0 10^9	2.0
200	500000	3.0 10^9	3.0 10^9	2.0
20	20000	2.6 10^9	2.1 10^9	1.0
20	30000	2.6 10^9	2.1 10^9	1.0
200	500000	2.6 10^9	2.1 10^9	1.0
44	66000	2.3 10^9	1.7 10^9	0.5
200	500000	7.3 10^9	2.5 10^9	0.1
200	1000000	7.3 10^9	2.5 10^9	0.1
400	2000000	7.3 10^9	2.5 10^9	0.1

Taking the same value of the damping as for the search interval in the time-independent calculations performed by Daza et al., the following rates are obtained using the correlation function, the cumulant expansion and the short-time approximation, respectively: for $S_1 \rightsquigarrow T_{1x}$, 1.8×10^{10}, 1.3×10^{10} and 8.6×10^{10} s^{-1}, for $S_1 \rightsquigarrow T_{1y}$, 2.3×10^9, 1.7×10^9 and 1.1×10^{10} s^{-1}. As for thymine, the rates from the complete correlation function method are closest to the rates obtained using time-independent approach. But in this case, the cumulant expansion method also gives good results. The short-time approximation gives an order of magnitude larger rates.
Sometimes in the current implementation, negative rates are obtained under certain circumstances for some choice of the input parameters. In this case, it can be seen from the plot of the correlation function that every second point has a wrong phase. This is related to the way how calculation of the square root of determinants in equation 3.37 is implemented. The determinants are not calculated separately but the ratio of the matrices is calculated and then the determinant is found. This is done, because otherwise there would be a arithmetic overflow. Although the two ways are mathematically equivalent, the calculation using one determinant brings the phase problem. The phase problem is due to the way the unwrapping is done. It can be solved by increasing a number of the integration points.

4.2.2.3 Flavone

Flavone belongs to the class of flavonoids also known as Vitamin P. Its photophysics depends on the acidity of the solvent [76]. In neutral and alkaline solvents, almost quantitative triplet formation is observed upon UV irradiation [77, 78]. A very fast ISC transition was observed causing a build-up time for $T_n \leftarrow T_1$ absorption of 30-40 ps [79].

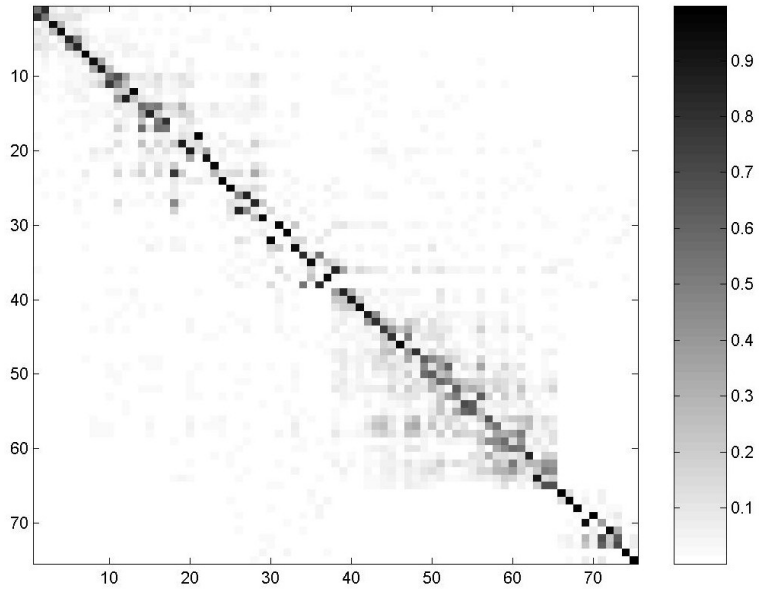

Figure 4.13: Duschinsky matrix related to transition between the S_1 and T_1 states of flavone. In order to visualize the normal mode mixing, absolute values of the matrix elements J_{ij} are shown.

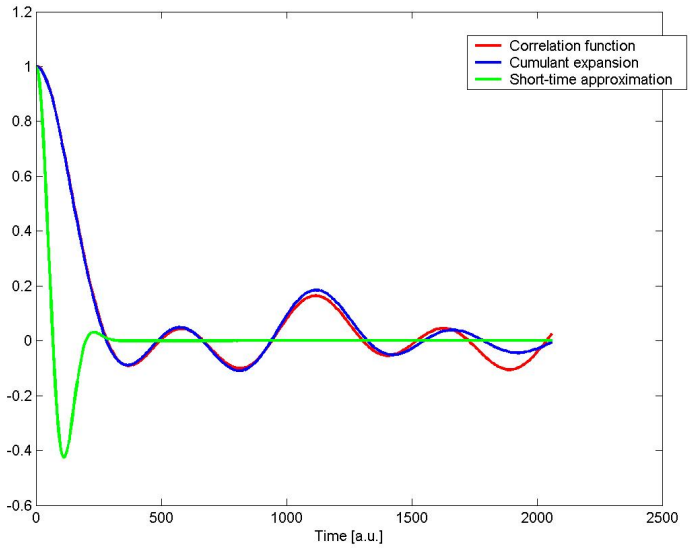

Figure 4.14: The real parts of the correlation function, the second-order cumulant expansion and the short-time approximation as functions of time for flavone (presented only the first 50 fs)

Table 4.2: Calculated inter-system crossing rates $S_1 \rightsquigarrow T_{1x}$ for flavone in s^{-1}

time interval [ps]	# points	correlation function	cumulant expansion	η cm^{-1}
20	20000	5.3 10^{11}	2.6 10^{11}	1.0
20	30000	5.3 10^{11}	2.6 10^{11}	1.0
44	66000	3.8 10^{11}	3.3 10^{11}	0.5
200	1000000	9.5 10^{10}	2.0 10^{11}	0.1

Marian [80] examined spin-forbidden transitions in flavone theoretically. The S_1 ($n\pi^*$) and T_1 ($\pi\pi^*$) electronic states were optimized at the B3-LYP/TZVP level without symmetry constraints. The adiabatic energy gap is 2782 cm^{-1}. There are 75 normal modes. The squares of the electronic spin-orbit matrix elements between S_1 and the x, y and z sublevels of the T_1 state are 695.38, 857.32, and 509.87 cm^{-1} respectively. The Duschinsky matrix related to the $S_1 \rightsquigarrow T_1$ electronic transition is shown in Figure 4.13. Overall, the normal mode mixing is less pronounced in the thymine but it is still pronounced. ISC rates between S_1 and x, y, and z sublevel of T_1 states were calculated to be 1.1×10^{11}, 1.4×10^{11} and 8.1×10^{10} s^{-1}. These results are in good agreement with the experimental results. All normal modes were used and the search interval was 0.1 cm^{-1}.
The first 50 fs of the correlation function, cumulant expansion and short-time expansion for flavone are presented in Figure 4.14. It can be seen that there is even better agreement of the correlation function and cumulant expansion than in phenalenone. Also, oscillations have smaller amplitude than in phenalenone.
Test calculations for different values of the numerical integration parameters and damping factor are presented in Table 4.2. Three different values of the damping parameters were used: 1.0 , 0.5 and 0.1 cm^{-1}. Upon using smaller damping values the rates obtained by the correlation function become systematically smaller. This is not the case for the rate obtained using the cumulant expansion but that rate does not change significantly with the damping parameter.
Taking the same value of the damping as for the search interval in the time-independent calculations performed by Marian, the following rates are obtained respectively using the correlation function, cumulant expansion and short-time approximation: for $S_1 \rightsquigarrow T_{1x}$, 9.5×10^{10}, 2.0×10^{11} and 1.4×10^{11} s^{-1}, for $S_1 \rightsquigarrow T_{1y}$, 1.2×10^{11}, 2.5×10^{11} and 1.7×10^{11} s^{-1}, for $S_1 \rightsquigarrow T_{1z}$ 7.1×10^{10}, 1.5×10^{11} and 1.0×10^{11} s^{-1}. In this case, all three methods give good results. The closest results give calculations based on the correlation function.

4.2.2.4 Free base porphyrin

Porhyrins are involved in various chemical processes in living organisms like oxygen transformation and storage, metabolism of H_2O_2, electron transfer and photosyntetic light-harvesting. Also it is used in phototherapy for oxidation of a tumor [81].
The free-base porphyrin is a heterocycle that does not contain a metal atom in its cavity. Its absorption spectrum is dominated by two major bands, the weak Q band (500-650 nm) and the strong B (Soret) band (350-400 nm). Upon excitation to the

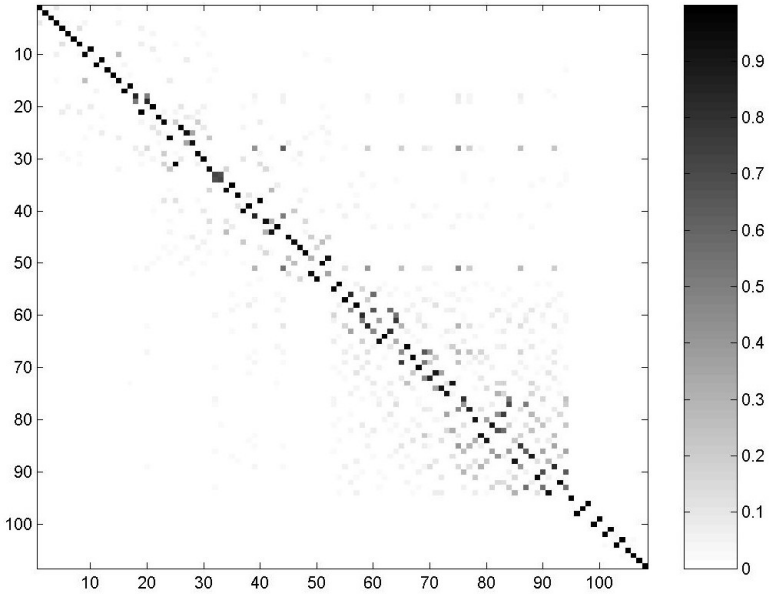

Figure 4.15: Duschinsky matrix related to transition between the S_1 and T_1 states of porphyrin. In order to visualize the normal mode mixing, absolute values of the matrix elements J_{ij} are shown.

B band, the majority of the population (90 %) goes to the lowest triplet state by inter-system crossing.

Perun et al. [82] theoretically examined the inter-system crossing in free-base porphyrin. They optimized the nuclear geometries of the S_1 ($n\pi^*$) and T_1 ($\pi\pi^*$) states at B3-LYP/def-SV(P) level using D_{2h} symmetry constraint. The adiabatic energy between the S_1 and T_1 states is 2420 cm^{-1}. Spin-orbit coupling is very small due to the same electronic character of the S_1 and T_1 states ($\pi\pi^*$) and its square is 0.004 for the z triplet sublevel. There are 108 normal modes in total, making free-base porphyrin a very challenging molecule for the application of the time-independent method. The Duschinsky matrix related to the $S_1 \rightsquigarrow T_1$ transition is given in Figure 4.15. Because the symmetry constraints were used, the Duschinsky matrix is significantly diagonal indicating small normal mode mixing. There are many normal modes that have a small displacement. Using the time-independent approach, the $S_1 \rightsquigarrow T_{1z}$ rate was calculated to be 5.4×10^5 s^{-1} using 10.0 cm^{-1} for the search interval. Only the 19 totally symmetric normal modes were used.

The first 50 fs of the correlation function, cumulant expansion, and short-time expansion for free base porhyrin are presented in Figure 4.16. In this case, the overlapping between the correlation function and cumulant expansion is not so good as for flavone. The oscillations are also larger than in flavone. Test calculations for different values of the numerical integration parameters and the damping factor are presented in Table 4.3. Four different damping parameters were used: 100.0, 10.0, 1.0 and 0.5 cm^{-1}. The values of the rates depende on the used damping. This is due to the small adiabatic energy gap and many normal modes that have small displacement.

Performing the time-dependent calculation of the inter-system crossing rate with the

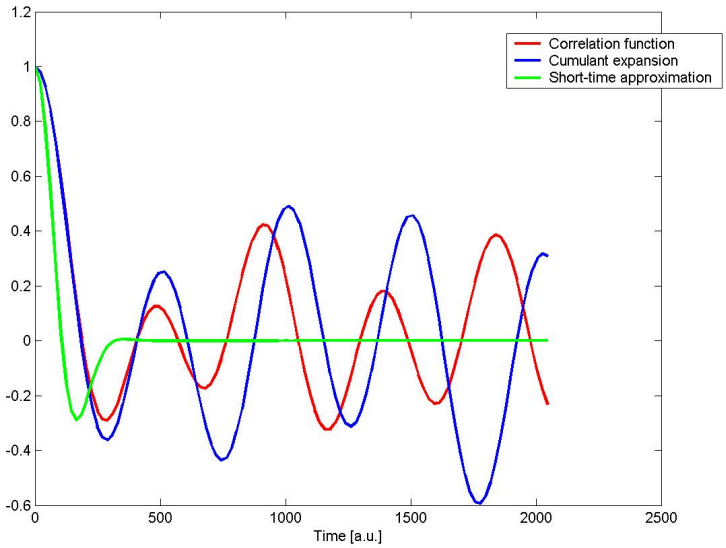

Figure 4.16: The real parts of the correlation function, the second-order cumulant expansion and the short-time approximation as functions of time for porphyrin (presented only the first 50 fs)

Table 4.3: Calculated inter-system crossing rates $S_1 \rightsquigarrow T_{1x}$ for porphyrin in s^{-1}

time interval [ps]	# points	correlation function	cumulant expansion	η cm^{-1}
0.4	2000	7.9 10^5	5.9 10^5	100.0
3	12000	1.1 10^6	6.8 10^5	10.0
20	30000	4.1 10^4	1.3 10^4	1.0
44	200000	1.3 10^5	1.6 10^5	0.5

same value of the damping as for the search interval in the time-independent calculations done by Perun et al. we found the following $S_1 \rightsquigarrow T_{1z}$ rates: 1.1×10^6, 6.8×10^6, and 7.0×10^5 s^{-1} respectively using the correlation function, cumulant expansion, and short-time approximation. In this case, the closest value to time-independent method is obtained by using the short-time approximation.

5 Applications

All electronic-structure calculations in this chapter were performed using the TURBOMOLE [83], MOLPRO [84] and DFT/MRCI program packages [85]. In the DFT/MRCI method, dynamical electron correlation is mainly taken into account by DFT. Static electron correlation is obtained from multi-reference configuration interaction expansions employing a one-particle basis of BH-LYP Kohn-Sham molecular orbitals. The SNF program [86] was employed for numerical calculations of vibrational frequencies in the harmonic approximation. Spin-orbit matrix elements were evaluated using the SPOCK program [27] where a one-center mean-field approximation to the Breit-Pauli Hamiltonian is employed. Here, an overview of the most important results is given. More detailed discussions can be found in the publications and the supplementary information attached to this thesis.

5.1 Dark electronic state in the pyrimidine bases uracil, thymine, and their methylated derivatives

Because of the fundamental importance of the photostability of DNA for all life on the Earth, the study of the excited-state relaxation of the nucleobases is a very active field of research. Both, spectroscopists and theoreticians, have put numerous efforts in clarifing the relaxation dynamics of the nucleobases after irradiation with UV light. Electronic relaxation is usually monitored by the decrease in steady-state emission quantum yields of an excited state or by time-resolved spectroscopy that is able to resolve electronic and nuclear motion. But sometimes, an ordinary spectroscopic technique cannot detect dark electronic states (states that do not radiate) that are created during the electronic relaxation. Those states are important because of the possibility that a molecule remains in an excited electronic state increases the probability for a chemical reaction. There is a new method, namely ultrafast electron diffraction [87,88] that is able to study the dark states at high space and time resolution (0.01 Å and 1 ps). Its application to pyrimidine bases looks promising.

When this thesis was started, it was believed that nucleic bases are highly photostable because of the ultrafast internal conversion to the ground state [68]. In the course of time it became clear that in addition to the internal conversion to the ground state, intermediate electronic dark states were populated. The following work shines some light on the possible explanation of the formation and character of the dark states.

5.1.1 Overview of the experimental and theoretical results

It has been shown that thymine does not have a sharp REMPI spectrum [89]. This fact was attributed either to mixing of the states or to a large geometrical change between ground- and excited-state structures.
In molecular beams, pump-probe experiments on the pyrimidine bases uracil and thymine showed that the electronic relaxation kinetics following the primary photoexcitation is complex and that it has components of femto, pico and nanosecond time scales [6, 10, 90–94]. The interpretation of the experimental results is sometimes difficult and depends on the fitting procedure. Hence, sometimes different decay time constants are obtained.

Table 5.1: Wavelengths of the pump and probe pulses, resolution and relaxation time constants obtained in femtosecond pump-probe experiments in molecular beams

Experimental group	pump/probe wavelength [nm]	resolution [fs]	time constants
Kang et *al.* [90]	267/3×800	400	uracil 2.4 ps thymine 6.4/>100 ps
Canuel at *al.* [93]	267/2×400	80	uracil 130 fs/1.05 ps thymine 105 ps/ 5.12 fs
Ullrich et *al.* [92]	267/200	160	uracil 530 fs/2.4 ps thymine 490 fs/6.4 ps

Wavelengths of the pump and probe pulses, resolution and relaxation time constants obtained in femtosecond pump-probe experiments in molecular beams are presented in Table 5.1. Kang et *al.* performed a pump-probe transient ionization experiment to examine the electronic relaxation dynamics of nucleic acids [90]. In this experiment, the excitation was at 267 nm and the ionization was performed by three photons from the laser fundamental at 800 nm. The time resolution of the experiment was 400 fs. They used a single-exponential curve to fit the pump-probe transient ionization signal with the exception of thymine where they used a double-exponential curve. The fitted time constant for uracil was 2.4 ps and for thymine the first one was 6.4 ps and the second was larger than 100 ps. Using energetic considerations they assigned the larger time constant to the lifetime of a triplet electronic state.
Canuel et *al.* [93] performed a similar experiment as Kang et *al.* but used a higher time resolution of 80 fs for their experiment. Because of this resolution they were able to fit the transient signal with a double-exponential function. Their pump pulse had a wavelength of 267 nm and the probe pulse had 2×400 nm. The fitted time constants were 130 fs and 1.05 ps for uracil and 105 fs and 5.12 ps for thymine.
Ullrich et *al.* [92] obtained femtosecond time-resolved photoelectron spectra of DNA and RNA bases in a molecular beam. An excitation wavelength of 250 nm was employed. Using a two-dimensional global fit procedure they found decay time constants of 530 fs and 2.4 ps for uracil and 490 fs and 6.4 ps for thymine.

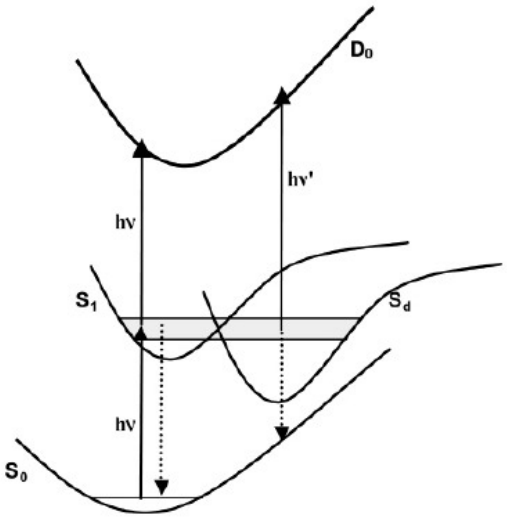

Figure 5.1: Proposed potential energy surfaces and processes for the pyrimidine bases. Ionization from the S_1 state and the dark state S_d sample different Franck-Condon regions of the ionic state, resulting in different ionization energies for these two states. From reference [6]

Experiments that were performed on a nanosecond time-scale showed that in methylated uracils and thymines, transient decay could be observed indicating a long-lived electronically excited state. He et *al.* [6, 91] performed an interesting spectroscopic experiment on methylated uracils and thymines and their water complexes at low-pressure gas phase conditions. They used resonantly enhanced multiphoton ionization as the experimental setup. The energy scheme of the relaxation model that they proposed is presented in Figure 5.1. It was found that after excitation to the first bright state S_1, bare molecules were trapped in a dark electronic state S_d via fast internal conversion. The lifetime of this dark state was determined to be tens to hundreds of nanoseconds and to depend on the degree of methylation and internal energy. This dependence is presented in Figure 5.2. The dark state was assigned to the low-lying $^1n\pi^\star$ state. Also, they found that a gradual increase in microhydration quenches the dark state.

Contrary to them, Busker et *al.* [10] were able to detect the dark state of microhydrated 1-methylthymine and 1-methyluracil via resonant two-photon delayed ionization under careful control of the applied water-vapor pressure. Their experiments demonstrated that hydration did not accelerate the internal conversion to the ground state to such a degree that the dark state was quenched. This is in agreement with the observation of the long-lived dark state upon excitation of thymine and uracil nucleotides in aqueous solution [95]. It was even observed that hydration increases the lifetime of the dark state of 1-methylthymine in the gas phase. In order to examine the nature of the dark state, Busker et *al.* tried to quench the dark state by oxygen coexpansion and by crossing molecular beam with an oxygen beam. They could not detect any significant quenching of the dark state. Due to that they attributed the dark state to the low-lying $^1n\pi^\star$ state.

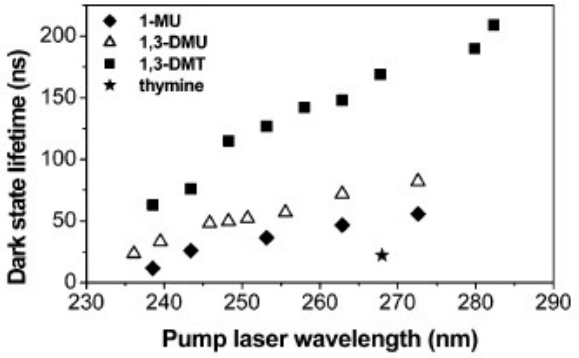

Figure 5.2: Lifetimes of 1-methyluracil, 1,3-dimethyluracil, 1,3-dimethylthymine, and thymine at different excitation wavelengths. From reference [6]

Recently, González-Vázquez et *al*. [94] reexamined the dark electronic state in thymine. They used a femtosecond pump-probe ionization experiment to observe the relaxation dynamics in isolated thymine monomers and small thymine-water clusters. Three transients with lifetimes of ≤ 100 fs, 7 ps and > 1 ns were observed. Their experiment showed that the long-lived transient was weak or absent in thymine-water complexes. They could not assign the dark state, but proposed that it was a triplet electronic state or the transient signal came from the local minimum on the S_1 potential energy surface.

Schneider et *al*. [96] used two-color photofragment Doppler spectroscopy and one-color slice imaging in order to monitor the photodissociation dynamics of thymine. They found that after photoexcitation to the first optically bright state, the H atom photofragment spectra are dominated by a two-photon excitation processes with a subsequent statistical dissociation. The second photon was absorbed by the dark long-lived state resulting in a formation of a highly excited state that quickly deactivates to the electronic ground state. Schneider et *al*. found no evidence that the dark state was a $^1\pi\sigma^\star$ electronic state.

In the liquid phase, Hare et *al*. [70, 95] found using femtosecond transient absorption spectroscopy two decay channels in uracil, direct internal conversion to the ground state and decay to the $^1\mathrm{n}\pi^*$ state which was also proposed as a gateway for the triplet state. In a later study, Hare et *al*. [8] used time-resolved infrared (TRIR) spectroscopy in the excited state and compared the results with a simulated S_0-T_1 difference spectrum to identify the long-lived dark state. They concluded that the triplet state is formed within 10 ps after excitation and that the vibrationally relaxed $^1n\pi$ state is not the precursor for the triplet formation.

Concerning theoretical calculations in general, vertical and adiabatic excitation energies as well as different relaxation pathways are reported. Using DFT/MRCI method Marian et *al*. [97] found that the diketo tautomer of uracil is more stable than the enol tautomers. They also calculated electronic spin-orbit coupling matrix elements and phosphorence lifetimes. Fleig et *al*. [98] performed benchmark calculations of vertical excitation spectra using coupled cluster theory. They found that uracil and thymine are the only nucleic acid bases that have a $^1\mathrm{n}\pi^*$ state as the lowest singlet state. Perun

et *al*. [99] found three conical intersections between singlet electronic states in thymine with the Complete-Active-Space Self-Consistent-Field (CASSCF) approach. Using the ab initio multiple spawning (AIMS) method Hudock et *al*. [100] proposed that the first step in the relaxation dynamics of uracil and thymine is nuclear motion to the minimum of the $^1\pi\pi^*$ state. The picosecond dynamics is related to barrier crossing and subsequent motion to the $^1\pi\pi^*/^1\mathrm{n}\pi^*$ conical intersection. Merchán et *al*. found a barrierless path from the Franck-Condon region to the conical intersection between the $^1\pi\pi^*$ and the ground state [101] in the pyrimidine bases. Also, they proposed that the longer lifetime component of the decay signal and fluorescence emission are related to the presence of a $^1\pi\pi^*$ planar minimum and to the barrier to access other conical intersections. They concluded that the $^1\mathrm{n}\pi^*$ state does not play a significant role in the primary photochemical event. Gustavsson et *al*. [102] used the PCM/TD-DFT(PBE0) method to analyze the $^1\pi\pi^*$ potential energy surface. They found that in water uracil and thymine will go through a $^1\pi\pi^*/\mathrm{S}_0$ conical intersection. Although they obtain a conical intersection between the $^1\mathrm{n}\pi^*$ and $^1\pi\pi^*$ states in vacuum and nonpolar solvents, in water the $^1\mathrm{n}\pi^*$ state is seen to be significantly blue shifted and does not appear to play any role. Using MRCI Matsika found a conical intersection between the $^1\pi\pi^*$ and $^1\mathrm{n}\pi^*$ states and also a three-state conical intersection between the $^1\pi\pi^*$, $^1\mathrm{n}\pi^*$ and the ground state in uracil [103, 104].
Triplet electronic states and inter-system crossing processes in uracil and thymine were theoretically examined much less than singlet states and internal conversions. Serrano-Andrés and coworkers employed CASSCF/CASPT2 methods in order to explain how the lowest triplet state $^3\pi\pi$ is formed in uracil [105] and thymine [106]. They propose three pathways for populating the $^3\pi\pi$ state from the initially excited $^1\pi\pi$ state. The first one proceeds via the intermediate $^3n\pi$ state whereas the second is a direct spin-forbidden transition from $^1\pi\pi$ to $^3\pi\pi$ at the intersection of their potential energy surfaces. The third mechanism includes internal conversion to the $^1n\pi$ state followed by inter-system crossing to the $^3\pi\pi$ state.

5.1.2 Electronic spectroscopy of 1-methylthymine and its water clusters

The work on the electronic relaxation of the 1-methylthymine and 1-methylthymine-water clusters was done in collaboration with the experimental group of Professor Kleinermanns [10]. To gain further insight into the electronic relaxation of 1-methylthymine, ab initio calculation using the CASSCF/CASPT2 and CC2 methods were performed. The goal of the calculations was to find relaxation paths from the first bright electronic state to the ground electronic state. Only singlet electronic states were taken into account and hence only internal conversion processes were considered.
In accordance with previous calculations [99, 101, 103] we found two conical intersections $^1\pi\pi^\star/^1\mathrm{n}\pi^\star$ (CI_1) and $^1\pi\pi^\star/\mathrm{S}_0$ (CI_2) at the CASSCF level. The geometries of the conical intersections are shown in Figure 5.3. In order to examine the accessibility of the conical intersections, linearly interpolated in internal coordinates (LIIC) paths were constructed connecting stationary points on the potential surfaces with the conical intersections. Potential energy profiles along such paths are presented in Figure

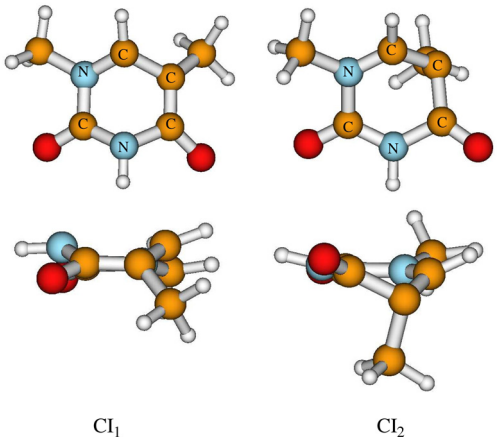

Figure 5.3: Geometries of the conical intersection in 1-methylthymine: $^1\pi\pi^\star/^1n\pi^\star$ (CI_1), $^1\pi\pi^\star/S_0$ (CI_2).

5.4. Our investigation suggests that after excitation to the S_2 ($\pi\pi^*$) state, the molecule can either propagate to the CI_1 or to a local minimum on the $\pi\pi^*$ hypersurface. Subsequently, the molecule may pass CI_1 and go to the minimum of the S_1 ($n\pi^*$) state or through CI_2 to the electronic ground state. As was previously concluded [96] for thymine, the $^1\pi\sigma^*$ state is not involved in the relaxation mechanism from the first $\pi\pi^*$ state in methylated thymine either. We found that the $^1\pi\sigma^*$ state comes to lie 0.8 eV vertically above the S_2 ($\pi\pi^*$) state at the CC2/aug-cc-pVTZ level.
Also, the influence of one water molecule on the relaxation paths of 1-methylthymine was investigated. We found that the investigated paths are similar to those of 1-methylthymine. Therefore, we concluded that photostability is intrinsic properties of pyrimidine basis itself. This conclusion was questioned in the following work.
One of the relaxation paths of 1-methylthymine to the ground state includes intermediate $^1n\pi^\star$ state. This $^1n\pi^\star$ state could be a good initial state for inter-system crossing to the triplet manifold according to the El-Sayed rules [38]. This possibility was considered in subsequent work [7].

5.1.3 Effects of hydration and methylation on the electronic states of uracil and thymine

It was shown in the work of Kong and coworkers [6, 91] that the degree of methylation plays an important role for the lifetime of the dark state. In order to examine this effect, a theoretical analysis of the influence of the methylation and hydration on the electronic states of uracil and thymine was performed [71]. Excited electronic states of the following molecules were examined: uracil (U), 1-methyluracil (1MU), 3-methyluracil (3MU), thymine (T), 1-methylthymine (1MT), 3-methylthymine (3MT), 1,3-dimethyluracil (1,3DMU), and 1,3-dimethylthymine (1,3DMT). Their ground state chemical structures are presented in Figure 5.5.
The vertical excitation energies of the lowest three singlet and triplet vertical electronic states were calculated at the RI-CC2/aug-cc-pVDZ level. The order of the states is

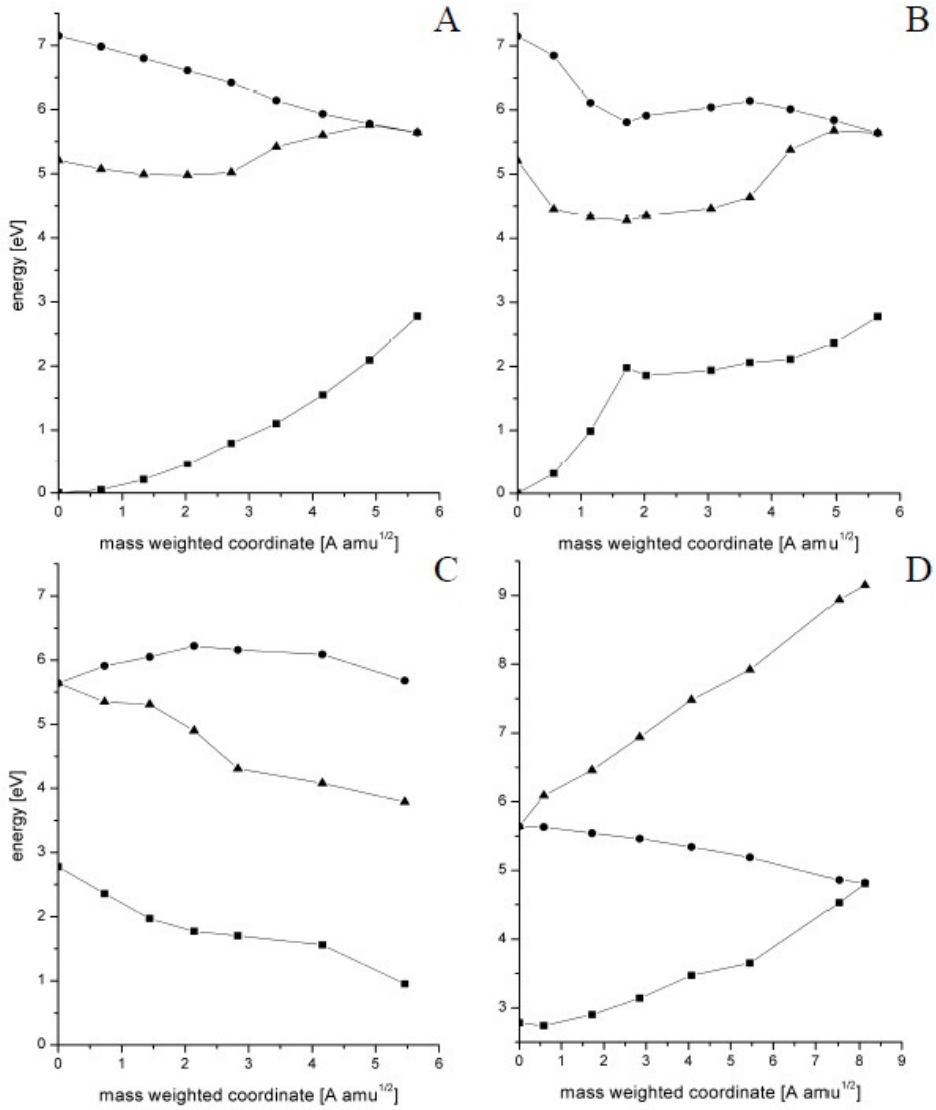

Figure 5.4: Potential energy profiles of the ground (squares), ^{1}nπ^* (triangles) and $^1\pi\pi^*$ state (circles) of 1-methylthymine, calculated at the CASSCF(10,8)/6-31G* level of theory along the LIIC reaction path. A: from the equilibrium geometry of the ground state to the CI_1; B: from the equilibrium geometry of the ground state to the minimum of the $^1\pi\pi^*$ state and to the CI_1; C: from the CI_1 to the minimum of the ^{1}nπ^* state; D: from the CI_1 to the CI_2.

the same in all compounds. The first singlet state is an $n\pi^\star$, the second is a $\pi\pi^\star$ and the third is a Rydberg state. The first triplet state is a $\pi\pi^\star$ the second is an $n\pi^\star$ and the third is a $\pi\pi^\star$ state. It was found that methylation did not shift $n\pi^\star$ states but shifted $\pi\pi^\star$ and Rydberg states.

Methylation effects are position dependent and hence they are not due to basis set superposition errors because some compounds have the same atom numbers but show different effects. The most pronounced effects concerning singlet states were found in

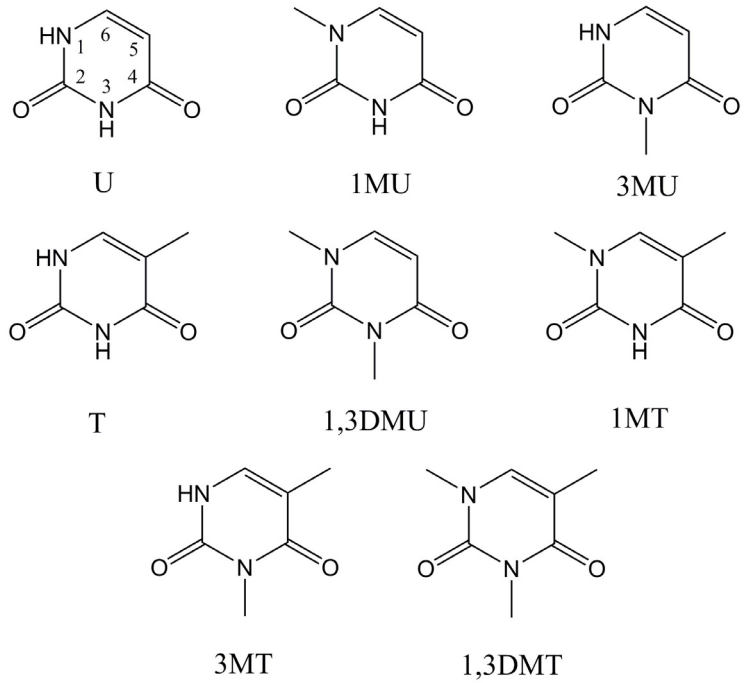

Figure 5.5: Chemical structures of methylated uracils and thymines. Atom labels are given for uracil.

the position N_1 for the $\pi\pi^\star$ state and in position C_5 for the Rydberg state (for the atom labels see Figure 5.5). Substitution at position C_5 had a smaller effect for the $\pi\pi^\star$ state than in position N_1, while effects were negligible in position N_3. In the triplet states, the substitution effects were smaller. Adiabatic energies behave similar to vertical excitation energies but the largest shift of the $\pi\pi^\star$ state is found for methylation in the position C_5. Also, it was found that methylation effects are additive.

In order to rationalize the position dependence of the energy shifts upon methylation, the density distributions of the Hartree-Fock frontier molecular orbitals of all compounds are presented in Figure 5.6. The highest three occupied molecular orbitals are: π (HOMO), π (HOMO-1) and n (HOMO-2). The electron density of the HOMO orbital is located on the atoms in positions 1 and 5 of the ring and over the oxygen atoms while the electron density of the HOMO-1 orbital is located on the oxygen atoms and the nitrogen atom in position 3. The major contribution to nonbonding orbital stems from the oxygen atom in position 4. The LUMO orbital has Rydberg character. The first unoccupied π orbital is LUMO+4 (in uracil). Because the second singlet state is mainly an excitation from the π (HOMO) orbital, it can be (de)stabilized by substitution at the atoms N_1 and C_5 . The same is true for the first triplet electronic state.

In 1-methylthymine and 1,3-dimethylthymine, the singlet $n\pi^\star$ and $\pi\pi^\star$ electronic states lie vertically so close in energy that they most probably exhibit strong non-adiabatic interactions which in turn are expected to increase significantly the population of the $^1n\pi^\star$ state. That might explain the strong dependence of the lifetime of 1-methyluracil, 1,3-dimethyluracil, thymine and 1,3-dimethylthymine on the excitation wavelength as

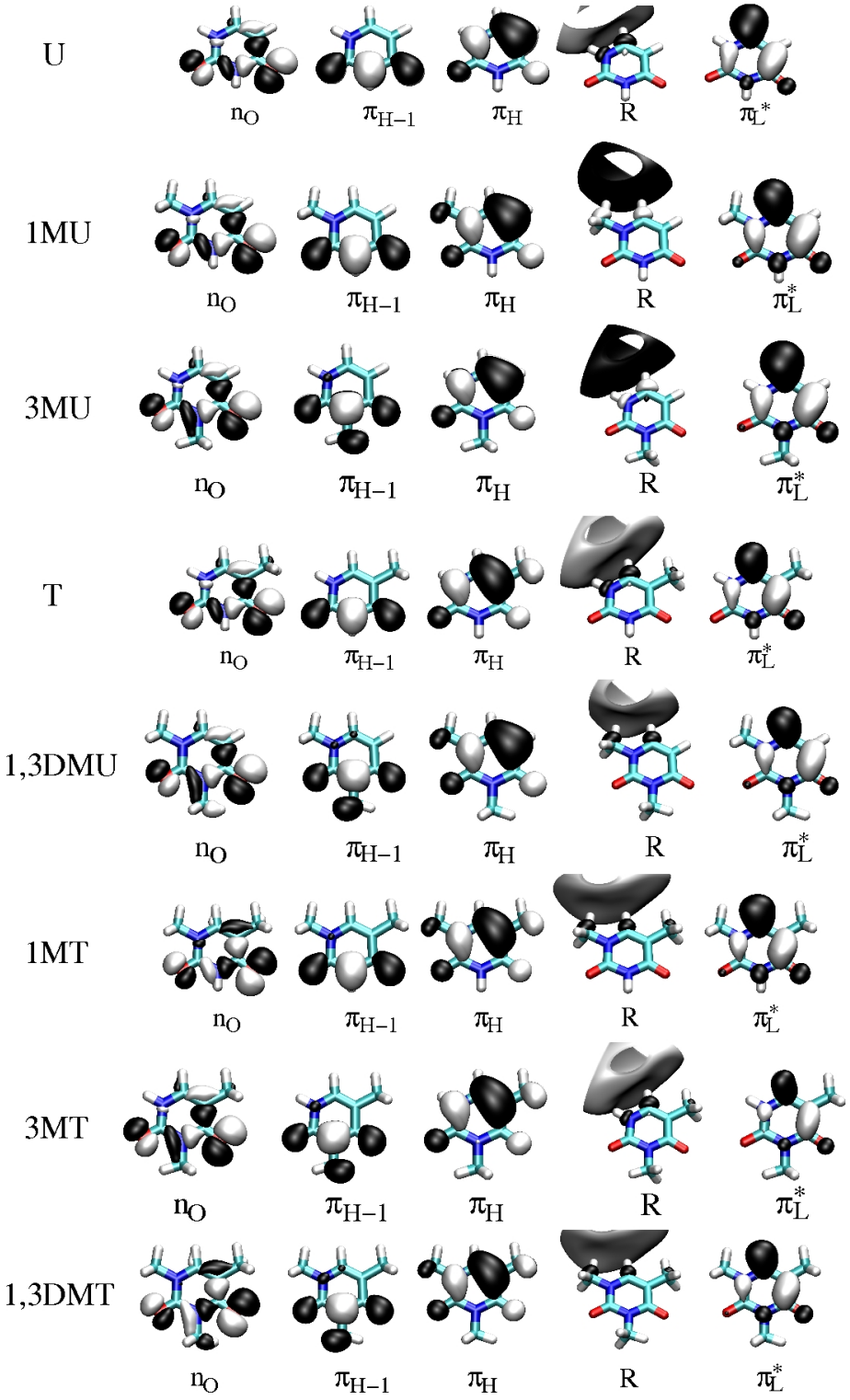

Figure 5.6: Density distribution of the Hartree-Fock frontier molecular orbitals which contribute to the lowest excited electronic states of methylated uracils and thymines (aug-cc-pVDZ basis set, isovalue=0.03).

shown in Figure 5.2.
In order to examine the influence of microhydration on the electronic states of methylated uracils and thymines, ground state clusters with six water molecules were optimized at the B3-LYP level. Contrary to the previous calculation, where five water molecules were involved [10] this time it was found that the first two singlet states changed their order, so that the $\pi\pi^\star$ state became the lowest singlet electronically excited state. This flipping of states is due to the fact that the $n\pi^\star$ state was destabilized through hydrogen bonds. Methylation and hydration effects partially cancel each other so that the variation of the $\pi\pi^\star$ excitation energies is much smaller than in the bare chromophores.
In order to estimate the vertical excitation energies in bulk water, the dielectric continuum model COSMO was used in addition to microhydration with six water molecules. Bulk solvation strongly destabilizes the ^{1}n$\pi^\star$ state. Due to the bulk solvation the energy gap between the first two singlet electronic states increases from 0.29 eV in uracil to 0.48 eV in 1,3-dimethylthymine. The blue shift of the ^{1}n$\pi^\star$ state has a strong impact on the photostability of uracils and thymines because it can decrease the population in the lowest triplet $\pi\pi^\star$ state that is formed via the intermediate singlet $n\pi^\star$ state. Because triplet states are usually highly reactive, this means that solvation can enhance the photostability of the pyrimidine bases.

5.1.4 Inter-system crossing in uracil, thymine and 1-methylthymine

Inter-system crossing rates between the lowest vibrational level of the S_1 electronic state and the T_1 electronic state were calculated for uracil, thymine and 1-methylthymine using DFT and RI-CC2 optimized geometries [7]. Also, rates for the transitions between the S_2 and T_2 and the S_2 and T_3 electronic states for uracil were calculated using DFT optimized geometries. The goal of this work was to examine the possibility that the dark state seen in the nanosecond spectroscopy experiments [6, 10, 91] is the lowest triplet electronic state.
Triplet states can in principle be investigated by ultrafast spectroscopy but in the pyrimidine bases the triplet states are difficult to study because triplet and ^{1}nπ^* absorption bands are overlapping. Another method to study triplet states is time-resolved infrared (TRIR) spectroscopy. It captures the transient infra-red difference spectra of the excited electronic states. Hare et *al.* [8] applied TRIP spectroscopy with femtosecond pump and probe pulses to monitor triplet states of thymine in argon-purged deuterated acetonitrile. The region of 1300-1800 cm^{-1} was recorded from femtosecond to microsecond time scales. They monitored in particular the shifts in the C=O stretching frequencies upon electronic excitation to the first bright electronic state. To understand their experiment better, we calculated vibrational spectra of the ground, S_1 and T_1 electronic states using the CC2 and DFT methods. Difference vibrational spectra of the S_0-T_1 and S_0-S_1 states together with the experimental results of Hare et *al.* are represented in Figure 5.7. The dip with the highest wavenumber and the neighbouring maximum result from a red shift of the C_2=O_2 stretching frequency in the excited state. The second dip can be assigned to the disappearance of the C_4=O_4 stretching band in the electronic ground state. The comparison shows that the time-

Figure 5.7: Calculated difference IR spectra of thymine. Upper row: RI-CC2/cc-pVDZ, middle row: B3-LYP/DFT/TZVP frequency calculations, The line spectra were broadened by Gaussian functions with a with of 50 cm^{-1} at half maximum, from ref. [7]. Lower row: TRIR spectrum of thymine in argon-purged acetonitrile-d_3 at a delay of 0-1 μs (solid curve). Also shown is the inverted and scaled steady-state IR absorption spectrum (dashed curve). The inset compares the TRIR spectra of thymine (solid) and thymine-d_2 (dashed) at the same time delay, from ref. [8].

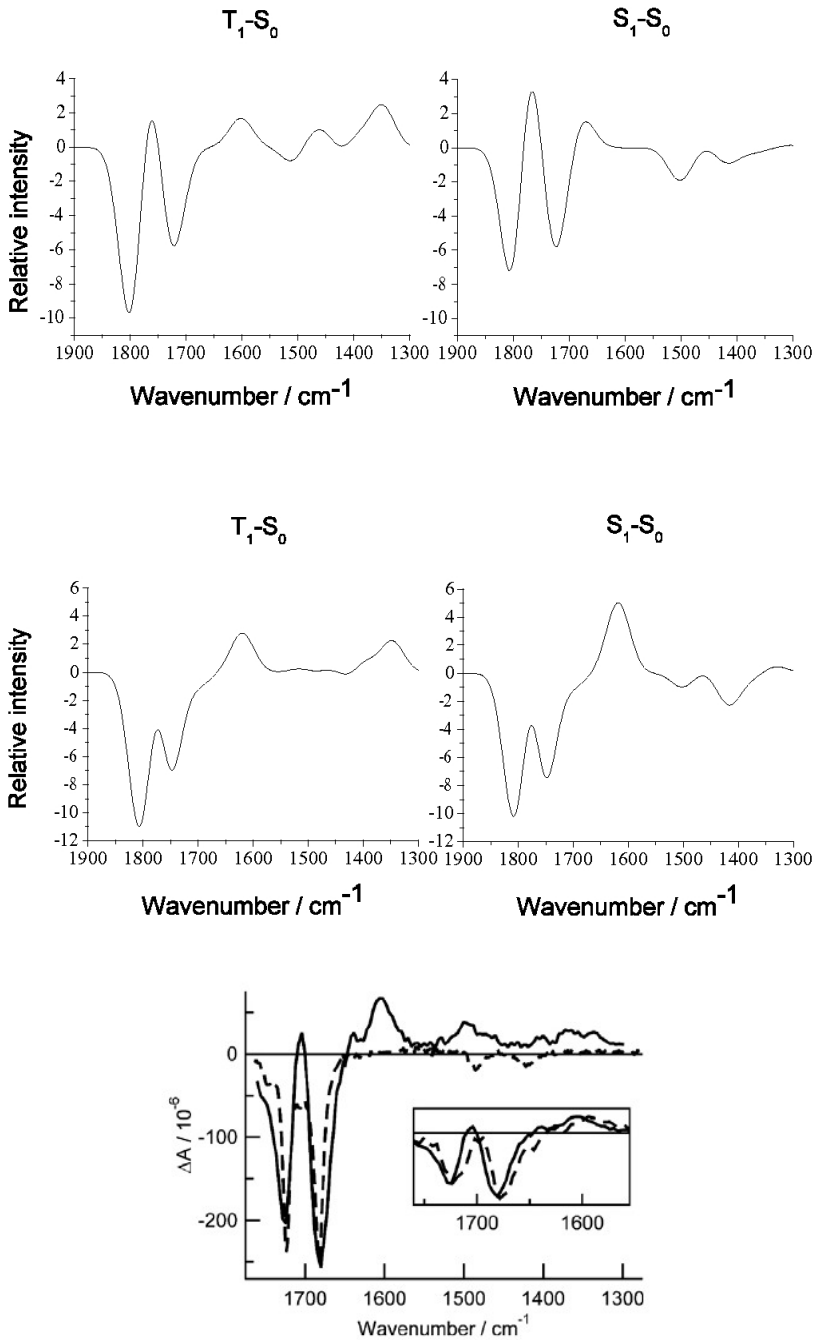

resolved infrared spectrum recorded by Hare et *al.* is due to the T_1 ($^3\pi\pi^*$) but not from the S_1 ($^1n\pi^*$) electronic state.
Spin-orbit matrix elements (SOME) at the optimized geometries of the S_1 and S_2 electronic states calculated using DFT/MRCI wavefunctions are presented in Tables 5.2 and 5.3, respectively. Test results of the influence of various parameters on the values of the spin-orbit matrix elements are given in the Table 5.2. Individual components of H_{SO} depend on the orientation of the molecule. It can be seen that the sum of squares of the components is to a large extent independent of the basis set. As the S_1 and T_1 states have different electronic character, the SOME between them are large. The same is true for the SOME between the S_2 and T_2 states. Opposite to that, the SOME for S_2 and T_1 and the one for S_2 and T_3 are small. The values for thymine in Table 5.2 are in agreement with the values found in the recent theoretical work by Serrano-Pérez et *al.* [106]. However, these authors did not determine inter-system crossing rates.
The calculated inter-system crossing rates in the Condon approximation between the S_1 and T_1 states in uracil, thymine and 1-methylthymine are shown in Table 5.4. There is a discrepancy of two orders of magnitude between rates calculated with RI-CC2 and DFT geometries. It is a consequence not of SOME values but from different values of Franck-Condon overlaps. Due to differences between the geometries optimized at the RI-CC2 level and DFT levels, the vibrational overlap is larger in the latter case and accordingly rates are larger. Calculated inter-system crossing rates of thymine and 1-methylthymine are smaller than those of uracil but the order of magnitude remains.

Table 5.2: Spin-orbit matrix elements $\langle S_1|\hat{H}_{SO}|T_1\rangle$ in cm^{-1} calculated at the S_1 state geometry

Component	DFT/MRCI/cc-pVDZ// RI-CC2/cc-pVDZ[a]	DFT/MRCI/aug-cc-pVTZ// RI-CC2/cc-pVDZ[a]	DFT/MRCI/TZVP// TDDFT B3-LYP/TZVP[a]
		Uracil	
$\hat{H}_{SO,x}$	38.95	36.96	7.70
$\hat{H}_{SO,y}$	29.37	32.74	46.25
$\hat{H}_{SO,z}$	–3.39	4.71	–0.04
Sum of squares	2391	2460	2198
		Thymine	
$\hat{H}_{SO,x}$	42.46	44.00	44.13
$\hat{H}_{SO,y}$	–20.59	–21.49	10.40
$\hat{H}_{SO,z}$	9.59	9.73	–0.62
Sum of squares	2319	2493	2056
		1-Methylthymine	
$\hat{H}_{SO,x}$	–35.78	–36.96	44.75
$\hat{H}_{SO,y}$	–31.65	–32.73	–10.10
$\hat{H}_{SO,z}$	–4.68	4.71	–0.02
Sum of squares	2304	2460	2110

[a]Method used for spin–orbit calculation // method used for geometry optimization of state

Inter-system crossing rates between the S_2 and T_2 and the S_2 and T_3 electronic states in uracil are shown in Table 5.5. All geometries used were obtained at the DFT level. As was previously shown, the SOME between the S_2 and T_1 states are small and consequently the transition is slow. This relaxation channel can thus be ruled out. Similarly, the rate of inter-system crossing between S_2 and T_3 states is small even in the Herzberg-Teller approximation. Only the channel connecting the S_2 and T_2 states gives a rate that can be compared with other spin-forbidden channels like the $S_1 \rightsquigarrow T_1$

Table 5.3: Spin-orbit matrix elements in cm^{-1} calculated at the TDDFT optimized S_2 geometry of uracil using the DFT/MRCI/TZVP method for generating the wave function

$\langle S_2\|\hat{H}_{SO,x}\|T_1\rangle$	–0.59
$\langle S_2\|\hat{H}_{SO,y}\|T_1\rangle$	–0.73
$\langle S_2\|\hat{H}_{SO,z}\|T_1\rangle$	–0.01
sum of squares	< 1
$\langle S_2\|\hat{H}_{SO,x}\|T_2\rangle$	–18.98
$\langle S_2\|\hat{H}_{SO,y}\|T_2\rangle$	12.47
$\langle S_2\|\hat{H}_{SO,z}\|T_2\rangle$	0.83
sum of squares	516
$\langle S_2\|\hat{H}_{SO,x}\|T_3\rangle$	–3.43
$\langle S_2\|\hat{H}_{SO,y}\|T_3\rangle$	0.78
$\langle S_2\|\hat{H}_{SO,z}\|T_3\rangle$	0.12
sum of squares	12

Table 5.4: Calculated rate constants k_{ISC} [s^{-1}] for the ($S_1 \rightsquigarrow T_1$) ISC channels in uracil, thymine and 1-methylthymine. ΔE^{ad} [cm^{-1}] denotes the adiabatic electronic energy difference.

Method	ΔE^{ad}	k_{ISC}
Uracil		
RI-CC2/cc-pVTZ//RI-CC2/cc-pVTZ	5150	0.93×10^{10}
DFT/MRCI/TZVP//DFT B3-LYP/TZVP	6704	0.23×10^{12}
Thymine		
RI-CC2/cc-pVDZ//RI-CC2/cc-pVDZ	6652	0.13×10^{10}
DFT/MRCI/TZVP//DFT B3-LYP/TZVP	8426	0.11×10^{12}
1-Methylthymine		
RI-CC2/cc-pVDZ//RI-CC2/cc-pVDZ	6724	0.49×10^{10}

channel. However it is known that internal conversion is the faster relaxation process for the S_2 state. The spin-forbidden $S_2 \rightsquigarrow T_2$ transition cannot compete.

Table 5.5: Rate constants k_{ISC} [s^{-1}] for the ($S_2 \rightsquigarrow T_2$) and ($S_2 \rightsquigarrow T_3$) ISC channels in uracil calculated at the DFT/MRCI/TZVP//DFT B3-LYP/TZVP level. ΔE^{ad} [cm^{-1}] denotes the adiabatic electronic energy difference.

Channel	ΔE^{ad}	Approximation	k_{ISC}
($S_2 \rightsquigarrow T_2$)	11391	FC	$\simeq 0.2 \times 10^{12}$
($S_2 \rightsquigarrow T_3$)	5355	FC	0.32×10^{9}
($S_2 \rightsquigarrow T_3$)	5355	FC+HT	0.36×10^{9}

In order to gain further insight into the inter-system crossing in uracil, a linearly interpolated path between the DFT-optimized T_1 (RC=0) and S_1 (RC=1.0) geometries was

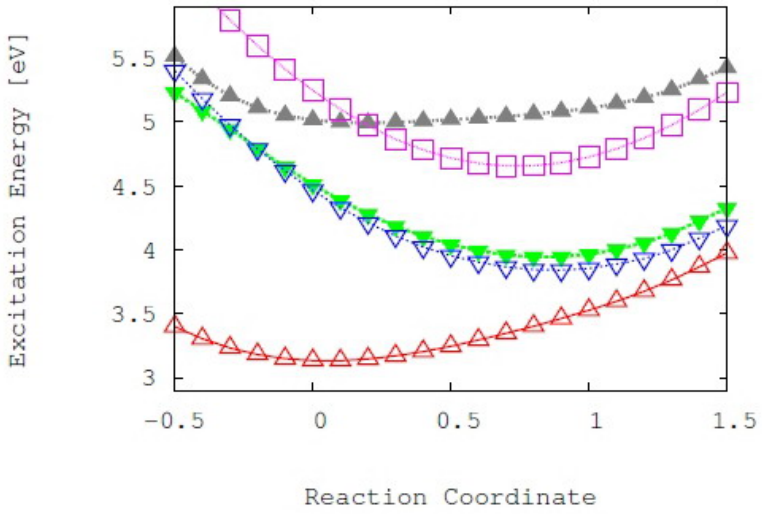

Figure 5.8: DFT/MRCI/TZVP single-point calculations along a linearly interpolated path between the UDFT-optimized T_1 geometry (RC = 0) and the TDDFT-optimized S_1 geometry (RC = 1.0) of uracil. The paths are also extrapolated on both sides. T_1 ($\pi\pi^\star$): upright open triangles; T_2 ($n\pi^\star$): upside down open triangles; S_1 ($n\pi^\star$): upside down filled triangles; T_3 ($\pi\pi^\star$): open squares; S_2 ($\pi\pi^\star$): upright filled triangles.

calculated, see Figure 5.8. There are several crossings of potential surfaces indicating possible ultrafast electronic relaxation. The energy profile shows a crossing between S_2 and S_1 states in the vicinity of the T_1 minimum in accordance with the previous theoretical findings where a conical intersection is reported in this area of the coordinate space [99–103, 107–111]. Also, there is an intersection between the S_2 and T_3 potential energy curves. The S_2 and T_1 potential energy profiles are essentially parallel.

After investigation of several pathways for inter-system crossing we proposed two fast ISC channels for the population of the T_1 ($^3\pi\pi^*$) state: the first is a nonradiative transition from the intermediate S_1 ($^1\mathrm{n}\pi^*$) state directly to the T_1 state and the second is a transition from the initially populated S_2 ($^1\pi\pi^*$) state to T_2 ($^3\mathrm{n}\pi^*$) followed by internal conversion to the T_1 state. The second pathway is probably less important because of ultrafast internal conversion from the S_2 state to the S_1 and ground states. In both cases, our calculations yield time constants for the singlet-triplet transition on the order of 10 ps. The experimental lifetime of the dark electronic state is at least 1000 times longer than our computed time-constant for the $S_1 \rightsquigarrow T_1$ transition. Therefore, the S_1 state is not a likely candidate for the dark state.

Our results therefore support the $S_2 \rightsquigarrow S_1 \rightsquigarrow T_1$ mechanism proposed by Hare et *al.* [70,95] where the intermediate S_1 state serves as a gateway for the triplet formation in uracil and its methylated derivatives.

5.2 Formation of the triplet electronic state in 6-azauracil

Analogues of nucleic bases are created by substitution of an atom or a group of atoms in bases. They could have drastically different physical and chemical properties relative to the parent nucleic basis. For instance, 2-aminopurine has a lifetime of the excited state three times longer than 6-aminopurine (adenine) [68, 112, 113]. The difference of the excited state lifetime caused by the change of the position of the amino group was rationalized by considering the accessibility of a conical intersection between the ground and the excited state [114]. Another example is 4-thiothymidine that exhibits a distinctively different electronic relaxation compared to thymidine [115]. It is dominated by fast inter-system crossing.

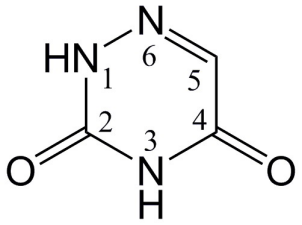

Figure 5.9: 6-azauracil: structure and numbering.

Recently Kobayashi and coworkers investigated the electronic relaxation from the first bright electronic state of 6-azauracil [30, 116, 117]. 6-azauracil is the analogue of uracil where the CH group in position 6 is replaced by an N atom, see Figure 5.9. It is a well-known compound in the pharmaceutical industry where it is employed as antiviral drug [118] and growth inhibitor for many microorganisms [119]. It was shown, similarly as in the case of the thio substitution, that the electronic relaxation after excitation to the first bright electronic state with 248 nm radiation in acetonitrile created the triplet electronic state with quantum yield of unity [116]. On the other hand, irradiation with a longer wavelength (308 nm) created the triplet state as well but weak fluoroscence was also observed.

Ab initio calculations were performed in order to gain insight into the photophysics of 6-azauracil [120]. The ground, two singlet electronically excited states and the triplet electronical state were optimized using the RI-CC2/cc-pVDZ method. The first singlet state has $n\pi^\star$ character while the second singlet and the first triplet states have $\pi\pi^\star$ character. Compared to uracil, the adiabatic energies of the first singlet and triplet electronic states of the 6-azauracil molecule are lowered by 0.3 eV. Below the first singlet $\pi\pi^\star$ state, there are three triplet states while in uracil there are two. Substitution of the carbon with nitrogen atom shifts the Rydberg states upward in energy and creates additional $n\pi^\star$ states. Solvation in acetonitrile did not change the order of the calculated vertical electronic excitation energy levels obtained in vacuum. In order to understand the electronic relaxation upon UV irradiation, energy profiles along linearly interpolated paths (LIP) between stationary points on the potential energy surfaces were calculated. Energy profiles of the excited electronic states along

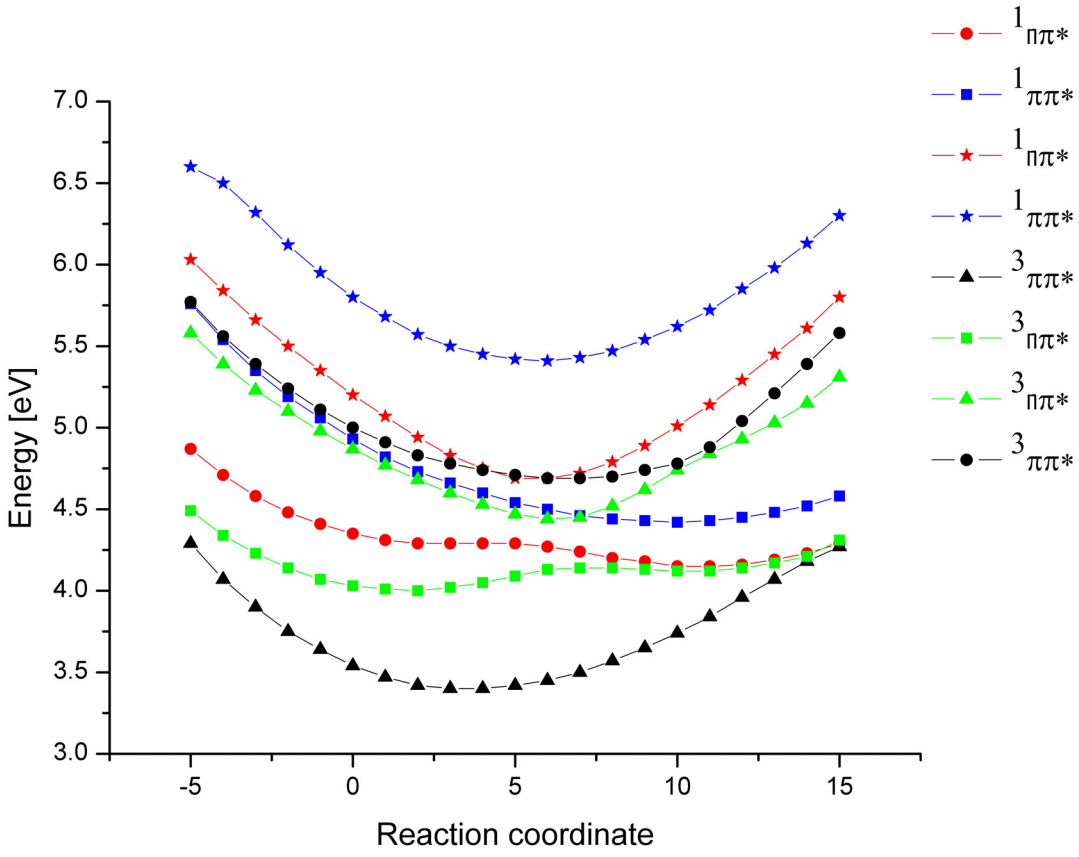

Figure 5.10: Single-point calculations along a linearly interpolated path between the FC point (RC=0) and the S_2 minimum (RC=10) of 6-azauracil. The curves are extended on both sides.

the LIP from the S_0 geometry (RC=0) toward the minimum of the S_2 state (RC=10) are displayed in Figure 5.10. There is a barrierless path from the Franck-Condon point toward the minimum of the first singlet $\pi\pi^\star$ state. Also, for the value of the reaction coordinate between RC=5 and RC=6 there is an avoided crossing of the first and second singlet and triplet $n\pi^\star$ states. There is a general rule that in the vicinity of an avoided crossing there is a conical intersection [121]. Because the lowest singlet $\pi\pi^\star$ state is located between two singlet $n\pi^\star$ states, it is expected that there is a conical intersection between the first two singlet states, resulting in an ultrafast relaxation of the electronic population to the lowest singlet excited state.

Energy profiles along a LIP between the S_2 minimum (RC=0) and the S_1 minimum (RC=10) are displayed in Figure 5.11. The avoided crossings from the Figure 5.10 are clearly seen here, too. Also, there is an avoided crossing between the two singlet $\pi\pi^\star$ states.

LIPs from the S_1 minimum towards the T_1 minimum are shown in Figure 5.12. There is an intersection between the lowest singlet and triplet states close to the S_1 minimum. This is an indication of fast inter-system crossing from the S_1 to the T_1 state. At

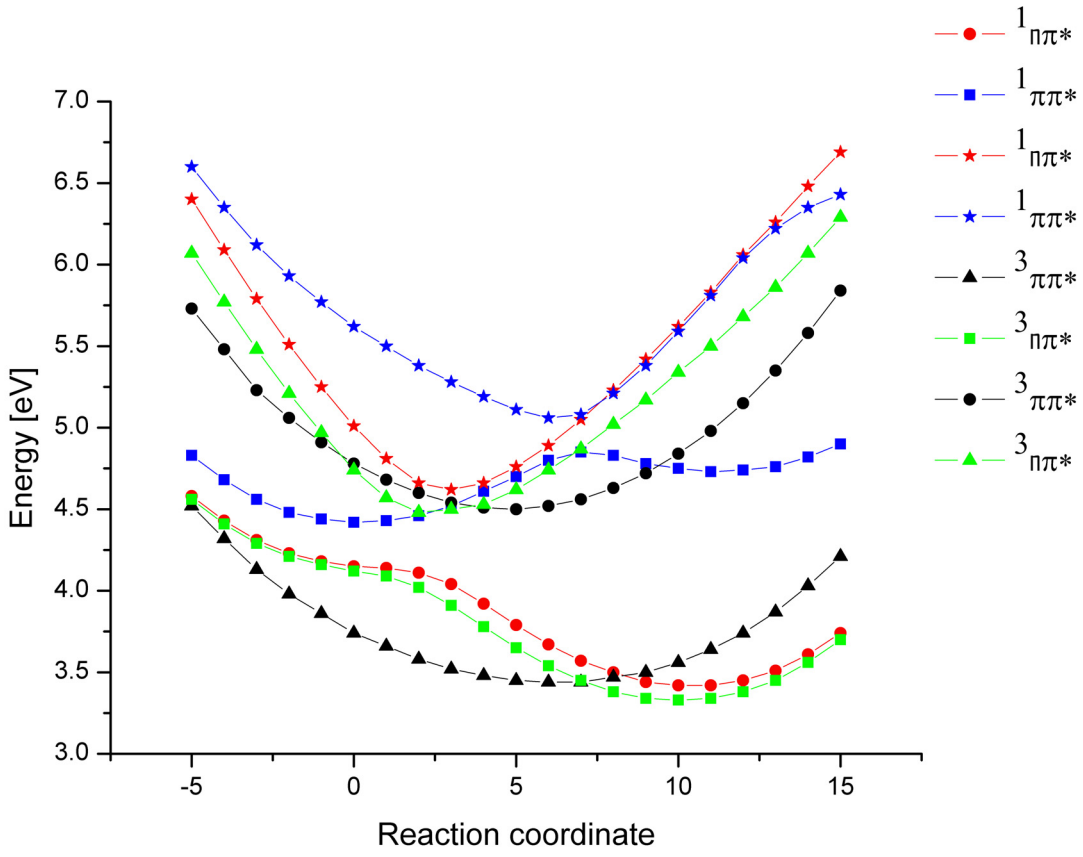

Figure 5.11: Single-point calculations along a linearly interpolated path between the S_2 minimum (RC=0) and the S_1 minimum (RC=10) of 6-azauracil. The curves are extended on both sides.

RC≈ 15, there is an intersection between T_1 and the ground state indicating possible electronic relaxation channel to the ground state.
Spin-orbit coupling matrix elements calculated at the singlet state geometries with DFT/MRCI wavefunctions are presented in Table 5.6. In accord with the El-Sayed rule [38] they are large when during a spin change there is a change in the orbital angular momentum. In the Condon approximation the inter-system crossing rate between the S_2 and T_2 states is 1.5×10^{10} s^{-1}. In acetonitrile is 0.6×10^{10} s^{-1}. Between the S_1 and T_1 states is 0.8×10^{10} s^{-1} whereas 2.9×10^{10} s^{-1} in acetonitrile. These values should be taken as a rough estimate because the spin-orbit matrix elements vary within nuclear space. Figure 5.13 presents the sum of the squares of the spin-orbit matrix elements along the LIP from S_2 minimum geometry (RC=0) towards the S_1 minimum geometry (RC=10). It can be clearly seen that the spin-orbit matrix elements are strongly coordinate dependent and there is a jump of the values in the area of the avoided crossing between the electronic states.

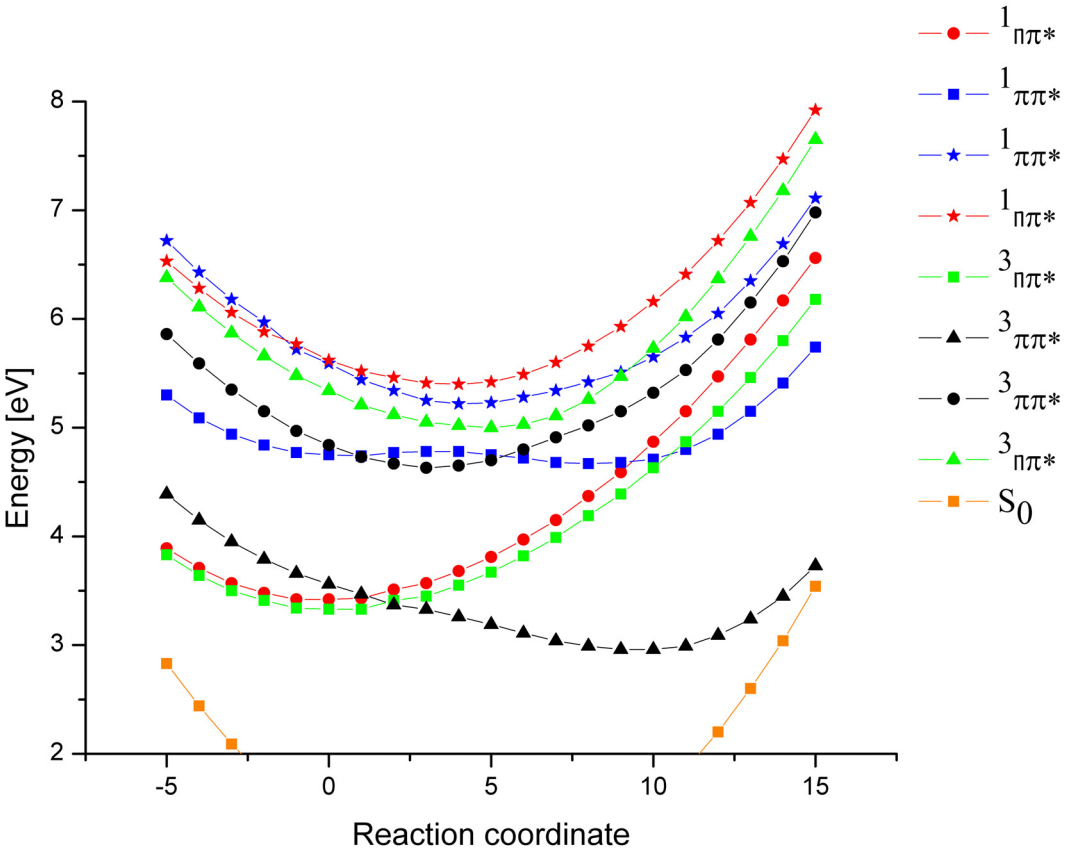

Figure 5.12: Single-point calculations along a linearly interpolated path between the S_1 minimum (RC=0) and the T_1 minimum (RC=10) of 6-azauracil. The curves are extended on both sides.

Table 5.6: Spin-orbit matrix elements calculated at the respective singlet minimum geometry of 6-azauracil

Component	Spin-orbit matrix element/cm^{-1}		
	$S_1 \rightsquigarrow T_1$	$S_2 \rightsquigarrow T_2$	$S_2 \rightsquigarrow T_3$
$\hat{H}_{\mathrm{SO},x}$	-33.56	10.22	12.02
$\hat{H}_{\mathrm{SO},y}$	36.44	19.97	31.91
$\hat{H}_{\mathrm{SO},z}$	0.22	0.01	0.01
$\sum_i \lvert\hat{H}_{\mathrm{SO},i}\rvert^2$	2454.20	503.25	1162.73

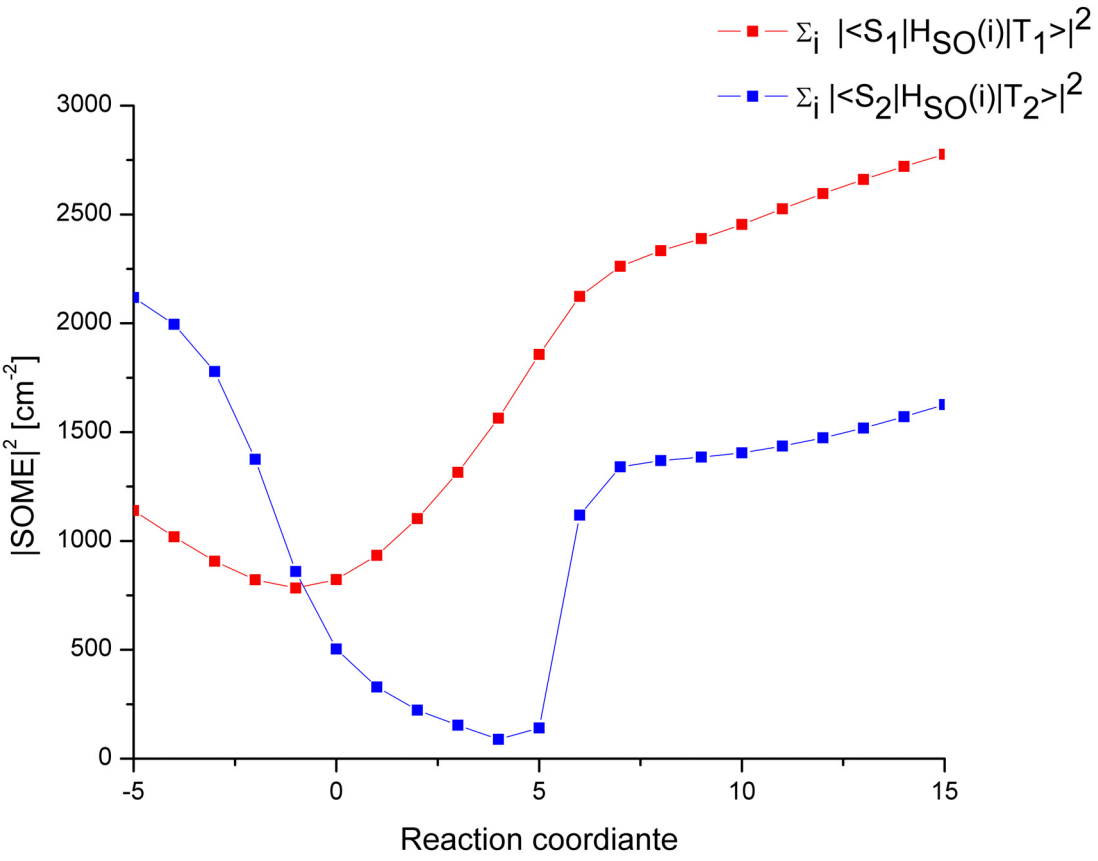

Figure 5.13: Sum of the squared spin-orbit matrix element components computed along the linearly interpolated reaction path connecting the S_2 minimum geometry (RC=0) and the S_1 minimum geometry (RC=10) of 6-azauracil.

6 Conclusions and outlook

This thesis includes both method development and application of quantum-chemical methods to the problem of electronic relaxation in uracil and its derivatives.
A new method for the calculation of inter-system crossing rates with the Condon approximation based on the time-dependent approach was developed and implemented. An exact correlation function was derived using Mehler's formula for the sum of the Hermite polynomials. Based on this, two approximate expressions were obtained. The first expression is based on the second-order cumulant expansion. The second is the short-time approximation to the first. All equations were programmed in MATLAB and C language. The C code is implemented as a subroutine to the VIBES program.
In order to test the method, four molecules were chosen: thymine, flavone, phenalenone and porphyrin. A comparison of the inter-system crossing rates obtained with the time-dependent approach and the time-independent approach as implemented in the VIBES program is given in Table 6.1. For the sake of comparison, the input parameters were chosen in a way as to make the calculations as comparable as possible. The best agreement with the time-independent method is obtained for the calculations based on the complete correlation function. The cumulant expansion formula also gives reasonably good results. The short-time formula usually gives an order of magnitude larger rates. But its simplicity is highly attractive.
For running the C-program, four input parameters in addition to the parameters needed for the time-independent calculations are needed: the keyword "$method=dynamics", the Gaussian damping, time interval for the integration and the number of points. What is the recipe for choosing the most optimal values of the integration parameters and the damping? First, the damping should be chosen. It is recommended that several values are tested every time. Next, the time interval for the integration is chosen. Our recommendation is to take at least 2, 20, or 200 ps for the dampings 10, 1.0, or 0.1 cm^{-1}. The number of points for the integration depends on the number of normal modes used. For smaller molecules, 2 points per each femtosecond are sufficient, but for larger molecules more points are needed. We conclude that similarly to calculations

Table 6.1: Comparison of calculated inter-system crossing rates with time-dependent and time-independent approach (VIBES) in s^{-1}.

molecule	correlation function	cumulant expansion	short time approximation	vibes
thymine ($S_1 \rightsquigarrow T_1$)	2.5 10^9	1.0 10^{10}	2.7 10^{10}	1.3 10^9
flavone ($S_1 \rightsquigarrow T_{1x}$)	9.5 10^{10}	2.0 10^{11}	1.4 10^{11}	1.1 10^{11}
flavone ($S_1 \rightsquigarrow T_{1y}$)	1.2 10^{11}	2.5 10^{11}	1.7 10^{11}	1.4 10^{11}
flavone ($S_1 \rightsquigarrow T_{1z}$)	7.1 10^{10}	1.5 10^{11}	1.0 10^{11}	8.1 10^{10}
phenalenone ($S_1 \rightsquigarrow T_{1x}$)	1.8 10^{10}	1.3 10^{10}	8.6 10^{10}	1.6 10^{10}
phenalenone ($S_1 \rightsquigarrow T_{1y}$)	2.3 10^9	1.7 10^9	1.1 10^{10}	2.0 10^9
porphyrin ($S_1 \rightsquigarrow T_{1z}$)	1.1 10^6	6.8 10^6	7.0 10^5	5.4 10^5

of the inter-system crossing rates with time-independent methods, the test calculation with various input parameters should be performed for each molecule.
The main area of application for the time-dependent approach are those cases where the Franck-Condon weighted density of the vibronic states is large. This may be due to a large adiabatic energy gap between electronic states or simply due to many normal modes.
There are several directions in which the method development can be continued. The next step would be to develop a time-dependent based method to go beyond the Condon approximation. This would include the vibronic spin-orbit mechanism. Inter-system crossing between states that have the same electronic character do occur in molecules but the calculation of their rates is computationally very demanding. The time-dependent approach is expected to greatly facilitate the calculations. The direct and vibronic spin-orbit mechanism can be generalized to cases when the molecule is in a heat bath. Usually vibrational relaxation is faster than electronic relaxation. Then the population distribution in the initial electronic states will obey Boltzmann statistic.
It would be interesting to go beyond the Duschinsky transformation and to include axis-switching effects. Those effects could be important in the cases where there is a large change in the equilibrium nuclear geometries of the initial and final electronic states.
As was demonstrated, the method can be used to generate an electronic absorption spectrum. With the small changes it would be possible to calculate emission spectra, resonance Raman spectra, but also rates of electron transfer. This is a consequence of the fact that all these spectra and rates include electronic states and related calculations of the Franck-Condon factors.
The application part of the thesis is concerned with electronic relaxation upon photoexcitation of uracil and its derivatives. In order to gain qualitative insight into the energetics of the excited states, state-of-the art quantum chemical methods were used. Electronic relaxation on the ultrafast time scales was discussed in 1-methylthymine. It was shown that after excitation to the S_2 ($\pi\pi^*$) state, 1-methylthymine relaxes to the ground state or to the lower S_1 ($n\pi^*$) state. In subsequent work, inter-system crossing, S_1 ($n\pi^*$) $\rightsquigarrow$ T_1 ($\pi\pi^*$) in uracil, thymine, and 1-methylthymine were discussed. Using the time-independent approach for the calculation of the inter-system crossing rates, it was found that the $S_1 \rightsquigarrow T_1$ rates are of order 10^9 - 10^{11} s^{-1}, depending on the molecule and the electronic structure method used. The experimentally observed relaxation in the nanosecond range is at least 1000 times slower than $S_1 \rightsquigarrow T_1$ transition. Therefore, the most likely candidate for the dark electronic state seen in nanosecond experiments is the T_1 electronic state.
Also, we address the controversial proposal that hydration quenches the nanosecond relaxation. Our first results showed that hydration did not influence the electronic relaxation of uracil and its methylated compounds. But a subsequent more comprehensive analysis revealed significant effects. Taking six water molecules for the microsolvation instead of five, showed that the first two electronic states change their order, so that the first electronic state became the $\pi\pi^*$ and the second the $n\pi^*$ state. Continuum solvation made the $n\pi^*$ state even more blue-shifted. As the $n\pi^*$ state is important for the triplet formation, blue-shifting the $n\pi^*$ state will significantly suppress the triplet

formation and increase the photostability of the pyrimidine nucleobases.
The electronic relaxation of 6-azauracil was examined in detail. 6-azauracil, an analogue of uracil is spectroscopically interesting because its triplet quantum yield is much larger than that of uracil. The aza-substitution creates additional low-lying singlet and triplet $n\pi^*$ states. In order to understand their role in the relaxation from the S_2 ($\pi\pi^*$) state, potential energy profiles along linearly interpolated paths (LIP) that connect stationary points on the potential surfaces were calculated. The LIPs revealed multiple crossings and avoided crossing between singlet and triplet electronic states. They are responsible for the ultrafast internal conversion, S_2 ($\pi\pi^*$) $\rightsquigarrow$ S_1 ($n\pi^*$) and subsequent the inter-system crossing, S_1 ($n\pi^*$) $\rightsquigarrow$ T_1 ($\pi\pi^*$). Using the time-independent approaches for the calculation of inter-system crossing rates, it was found that the T_1 ($\pi\pi^*$) state is formed approximately within 125 ps in isolated 6-azauracil and within 30 ps in acetonitrile solution. The enhancement of the rate is due to the increase of the adiabatic energy gap between S_1 and T_1 states.
To obtain a more detailed picture of all competing processes during electronic relaxation in molecules, it will be necessary to perform dynamical studies that include nonadiabatic coupling and spin-orbit coupling at the same time.

Bibliography

[1] D. L. Mitchell, in *Organic Photochemistry and Photobiology*, ed. W. M. Horspool and P.-S. Song, 1995, pp. 1326–1331.

[2] N. J. Turro, V. Ramamurthy and J. C. Scaiano, *Principles of Molecular Photochemistry*, University Science Books, Sausalito, CA, 2009.

[3] M. Klessinger and J. Michl, *Excited States and Photochemistry of Organic Molecules*, VCH Publishers Inc., New York, 1995.

[4] T. P. Coohill, in *Organic Photochemistry and Photobiology*, ed. W. M. Horspool and P.-S. Song, 1995, pp. 1267–1275.

[5] C. W. Müller, J. J. Newby, C.-P. Liu, C. P. Rodrigo and T. S. Zwier, *Phys. Chem. Chem. Phys.*, 2010, **12**, 2331–2343.

[6] Y. He, C. Wu and W. Kong, *J. Phys. Chem. A*, 2004, **108**, 943–949.

[7] M. Etinski, T. Fleig and C. M. Marian, *J. Phys. Chem. A*, 2009, **113**, 11809–11816.

[8] P. M. Hare, C. T. Middleton, K. I. Mertel, J. M. Herbert and B. Kohler, *Chem. Phys.*, 2008, **347**, 383–392.

[9] W. J. Schreier, T. E. Schrader, F. O. Koller, P. Gilch, C. E. Crespo-Hernández, V. N. Swaminathan, T. Carell, W. Zinth and B. Kohler, *Science*, 2007, **315**, 625–629.

[10] M. Busker, M. Nispel, T. Häber, K. Kleinermanns, M. Etinski and T. Fleig, *Chem. Phys. Chem.*, 2008, **9**, 1570–1577.

[11] J. Tatchen, *VIBES*, Universität Düsseldorf, 2005.

[12] H. Meyer, *Annu. Rev. Phys. Chem.*, 2002, **53**, 141–172.

[13] P. R. Bunker and P. Jensen, *Molecular symmetry and spectroscopy*, NRC-CNRC, Ottawa, 1998.

[14] W. Domcke, D. R. Yarkony and H. Köppel, *Conical Intersections*, World Scientific, Singapore, 2004.

[15] T. Helgaker, P. Jørgensen and J. Olsen, *Molecular Electronic-Structure Theory*, Wiley, 2004.

[16] A. Szabo and N. S. Ostlund, *Modern Quantum Chemistry*, Dover Publications, 1996.

[17] O. Christiansen, H.Koch and P. Jørgensen, *Chem. Phys. Lett.*, 1995, **243**, 409–418.

[18] H. Koch and P. Jørgensen, *J. Chem. Phys.*, 1990, **93**, 3333–3344.

[19] O. Vahtras, J. Almlöf and M. W. Feyereisen, *Chem. Phys. Lett.*, 1993, **213**, 514–518.

[20] F. Duschinsky, *Acta Physicochim.*, 1937, **7**, 551–566.

[21] J. T. Hougen and J. K. G. Watson, *Can. J. Phys.*, 1965, **43**, 298–320.

[22] İlker Özkan, *J. Mol. Spectrosc.*, 1990, **139**, 147–162.

[23] G. M. Sando and K. G. Spears, *J. Phys. Chem. A*, 2001, **105**, 5326–5333.

[24] C. Marian, in *Reviews In Computational Chemistry*, ed. K. Lipkowitz and D. Boyd, Wiley-VCH, Weinheim, 2001, vol. 17, pp. 99–204.

[25] B. A. Heß, C. M. Marian, U. Wahlgren and O. Gropen, *Chem. Phys. Lett.*, 1996, **251**, 365.

[26] B. Schimmelpfennig, 1996, Stockholms University.

[27] M. Kleinschmidt, J. Tatchen and C. M. Marian, *J. Comp. Chem.*, 2002, **23**, 824–833.

[28] E. W. Schlag, S. Schneider and S. F. Fischer, *Annu. Rev. Phys. Chem.*, 1971, **22**, 465–526.

[29] P. Avouris, W. M. Gelbart and M. A. El-Sayed, *Chem. Rev.*, 1977, **77**, 793–833.

[30] T. Kobayashi, H. Kuramochi, T. Suzuki and T. Ichimura, *Phys. Chem. Chem. Phys.*, 2010, **12**, 5140–5148.

[31] B. Heinz, T. Schmierer, S. Laimgruber and P. Gilch, *J. Photochem. Photobio. A.*, 2008, **199**, 274–281.

[32] V. F. Weisskopf and E. P. Wigner, *Z. Phys.*, 1930, **63**, 54.

[33] V. F. Weisskopf and E. P. Wigner, *Z. Phys.*, 1930, **65**, 18.

[34] S. Mukamel, *Principles of Nonlinear Optical Spectroscopy*, Oxford University Press, USA, 1999.

[35] D. R. Yarkony, *Rew. Mod. Phys.*, 1996, **68**, 985–1013.

[36] B. R. Henry and W. Siebrand, *J. Chem. Phys.*, 1971, **54**, 1072–1085.

[37] V. Lawetz, G. Orlandi and W. Siebrand, *J. Chem. Phys.*, 1972, **56**, 4058–4072.

[38] M. A. El-Sayed, *Acc. Chem. Res.*, 1968, **1**, 8–16.

[39] T. E. Sharp and H. M. Rosenstock, *J. Chem. Phys.*, 1964, **41**, 3453–3463.

[40] E. v. Doktorov, I. A. Malkin and v. I. Man'ko, *J. Mol. Spectrosc.*, 1975, **56**, 1–20.

[41] E. v. Doktorov, I. A. Malkin and v. I. Man'ko, *J. Mol. Spectrosc.*, 1977, **64**, 302–326.

[42] M. Dierksen and S. Grimme, *J. Chem. Phys.*, 2005, **122**, 244101–244101–9.

[43] R. Islampour, M. Dehestani and S. H. Lin, *J. Mol. Spectrosc.*, 1999, **194**, 179–184.

[44] W. Domcke, L. S. Cederbaum, H. Köppel and W. v. Niessen, *Mol. Phys.*, 1977, **34**, 1759–1770.

[45] H. C. Jankowiak, J. L. Stuber and R. Berger, *J. Chem. Phys.*, 2007, **127**, 234101–234101–23.

[46] R. Borrelli and A. Peluso, *J. Chem. Phys.*, 2008, **129**, 064116–064116–7.

[47] A. Toniolo and M. Persico, *J. Chem. Phys.*, 2001, **115**, 1817–1827.

[48] E. J. Heller, *Acc. Chem. Res.*, 1981, **14**, 368–375.

[49] R. Kubo, *J. Phys. Soc. Japan*, 1962, **17**, 1100–1120.

[50] D. A. McQuarrie, *Statistical Mechanics*, University Science Books, Sausalito, CA, 2000.

[51] R. C. O'Rourke, *Phys. Rev.*, 1953, **91**, 265–270.

[52] R. Kubo and Y. Toyozawa, *Prog. Theor. Phys.*, 1955, **13**, 160–182.

[53] M. Lax, *J. Chem. Phys.*, 1952, **20**, 1752–1760.

[54] S. Mukamel, S. Abe, Y. J. Yan and R. Islampour, *J. Phys. Chem.*, 1985, **89**, 201–204.

[55] R. Islampour, *Chem. Phys.*, 1989, **133**, 425–435.

[56] A. M. Mebel, M. Hayashi, K. K. Liang and S. H. Lin, *J. Phys. Chem. A*, 1999, **103**, 10674–10690.

[57] M. Hayashi, A. M. Mebel, K. K. Liang and S. H. Lin, *J. Chem. Phys.*, 1998, **108**, 2044–2055.

[58] R. Islampour and M. Miralinaghi, *J. Phys. Chem. A*, 2007, **111**, 9454–9462.

[59] Q. Peng, Y. Yi, Z. Shui and J. Shao, *J. Chem. Phys.*, 2007, **126**, 114302–1–114302–8.

[60] R. Islampour, M. Dehestani and S. H. Lin, *Mol. Phys.*, 2000, **98**, 101–110.

[61] R. Islampour and S. H. Lin, *J. Phys. Chem.*, 1991, **95**, 10261–10266.

[62] R. Islampour and S. H. Lin, *Chem. Phys. Lett.*, 1991, **179**, 147–151.

[63] K. K. Liang, A. M. Mebel, S. H. Lin, M. Hayashi, H. L. Selzle, E. W. Schlag and M. Tachiya, *Phys. Chem. Chem. Phys.*, 2003, **5**, 4656–4665.

[64] F. G. von Mehler, *J. Reine Angew. Math.*, 1866, **66**, 161–176.

[65] J. J. Markham, *Rew. Mod. Phys.*, 1959, **31**, 956–989.

[66] R. P. Feynman, *Phys. Rev.*, 1951, **84**, 108–128.

[67] V. Rai-Constapel, M. Kleinschmidt, S. Salzmann, L. Serrano-Andrés and C. M. Marian, *Phys. Chem. Chem. Phys.*, 2010, accepted.

[68] C. E. Crespo-Hernández, B. Cohen, P. M. Hare and B. Kohler, *Chem. Rev.*, 2004, **104**, 1977–2019.

[69] S. M. Bishop, M. Malone, D. Philips, A. W. Parker and M. C. R. Symons, *J. Chem. Soc., Chem. Commun.*, 1994, 871–872.

[70] P. M. Hare, C. E. Crespo-Hernández and B. Kohler, *J. Phys. Chem. B*, 2006, **110**, 18641–18650.

[71] M. Etinski and C. M. Marian, *Phys. Chem. Chem. Phys.*, 2010, **12**, 4915–4923.

[72] R. Schmidt, C. Tanielian, R. Dunsbach and C. Wolff, *J. Photochem. Photobio.*, 1994, **79**, 11–17.

[73] C. Flors, C. Prat, R. Suau, F. Najera and S. Nonell, *J. Photochem. Photobio.*, 2005, **81**, 120–124.

[74] C. F. C, P. R. Ogilby, J. G. Luis, T. A. Grillo, L. R. Izquierdo, P. L. Gentili, L. Bussotti and S. Nonell, *J. Photochem. Photobio.*, 2006, **82**, 95–103.

[75] M. C. Daza, M. Doerr, S. Salzmann, C. M. Marian and W. Thiel, *Phys. Chem. Chem. Phys.*, 2009, **11**, 1688–1696.

[76] S. Kumar, S. K. Jain, N. Sharma and R. C. Rastogi, *Spectrochim. Acta A*, 2001, **57**, 299–308.

[77] K. Bhattacharyya, D. Ramaiah, P. K. Das and M. V. George, *J. Phys. Chem.*, 1986, **90**, 5984–5989.

[78] V. Avila and C. M. Previtali, *J. Chem. Soc. Perkin Trans.*, 1995, **2**, 2281–2285.

[79] K. Hamanoue, T. Nakayama, T. Miyake and H. Teranishi, *Chem. Lett.*, 1981, **1**, 39–42.

[80] C. M. Marian, *Spectrochim. Acta A*, 2009, **73**, 1–5.

[81] C. Schweitzer and R. Schmidt, *Chem. Rev.*, 2003, **103**, 1685–1757.

[82] S. Perun, J. Tatchen and C. M. Marian, *Chem. Phys. Chem.*, 2008, **9**, 282–292.

[83] R. Ahlrichs, M. Bär, H.-P. Baron, R. Bauernschmitt, S. Böcker, N. Crawford, P. Deglmann, M. Ehrig, K. Eichkorn, S. Elliott, F. Furche, F. Haase, M. Häser, C. Hättig, H. Horn, C. Huber, U. Huniar, M.Kattannek, A. Köhn, C. Kölmel, M. Kollwitz, K. May, P. Nava, C. Ochsenfeld, H. Öhm, H. Patzelt, D. Rappoport, O. Rubner, A. Schäfer, U. Schneider, M. Sierka, O. Treutler, B. Unterreiner, M. von Arnim, F. Weigend, P. Weis and H. Weiss, *TURBOMOLE (Vers. 5.7)*, Universität Karlsruhe, 2004.

[84] H.-J. Werner, P. J. Knowles, R. Lindh, F. R. Manby, M. Schütz, P. . Celani, T. Korona, G. Rauhut, R. D. Amos, A. Bernhardsson, A. Berning, D. L. Cooper, M. J. O. Deegan, A. J. Dobbyn, F. Ecker, C. Hampel, G. Hetzer, A. W. Lloyd, S. J. McNicholas, W. Mayer, M. E. Mura, A. Nicklass, P. Palmieri, R. Pitzer, U. Schumann, H. Stoll, A. J. Stone, R. Tarroni and T. Thorsteinsson, MOLPRO *version 2006.1, A package of ab initio programs.*, 2006, http://www.molpro.net.

[85] S. Grimme and M. Waletzke, *J. Chem. Phys.*, 1999, **111**, 5645–5655.

[86] J. Neugebauer, M. Reiher, C. Kind and B. A. Hess, *J. Comp. Chem.*, 2002, **23**, 895–910.

[87] R. Srinivasan, J. S. Feenstra, S. T. Park, S. Xu and A. H. Zewail, *Scince*, 2005, **307**, 558–563.

[88] S. T. Park, A. Gahlmann, Y. He, J. S. Feenstra and A. H. Zewail, *Angew. Chem. Int. Ed.*, 2008, **47**, 9496–9499.

[89] B. B. Brady, L. A. Peteanu and D. H. Levy, *Chem. Phys. Lett.*, 1988, **147**, 538–543.

[90] H. Kang, K. T. Lee, B. Jung, Y. J. Ko and S. K. Kim, *J. Am. Chem. Soc.*, 2002, **124**, 12958–12959.

[91] Y. He, C. Wu and W. Kong, *J. Phys. Chem. A*, 2003, **107**, 5143–5148.

[92] S. Ullrich, T. Schultz, M. Z. Zgierski and A. Stolow, *Phys. Chem. Chem. Phys.*, 2004, **6**, 2796–2801.

[93] C. Canuel, M. Mons, F. Piuzzi, B. Tardivel, I. Dimicoli and M. Elhanine, *J. Chem. Phys.*, 2005, **122**, 074316–1–074316–6.

[94] J. González-Vázquez, L. González, E. Samoylova and T. Schultz, *Phys. Chem. Chem. Phys.*, 2009, **11**, 3927–3934.

[95] P. M. Hare, C. E. Crespo-Hernández and B. Kohler, *PNAS*, 2007, **104**, 435–440.

[96] M. Schneider, R. Maksimenka, F. J. Buback, T. Kitsopoulis, L. R. Lago and I. Fischer, *Phys. Chem. Chem. Phys.*, 2006, **8**, 3017–3021.

[97] C. M. Marian, F. Schneider, M. Kleinschmidt and J. Tatchen, *Eur. Phys. J. D*, 2002, **20**, 357–367.

[98] T. Fleig, S. Knecht and C. Hättig, *J. Phys. Chem. A*, 2007, **111**, 5482.

[99] S. Perun, A. L. Sobolewski and W. Domcke, *J. Phys. Chem. A*, 2006, **110**, 13238–13244.

[100] H. R. Hudock, B. G. Levine, A. L. Thompson, H. Satzger, D. Townsend, N. Gador, S. Ullrich, A. Stolow and T. J. Martinez, *J. Phys. Chem. A*, 2007, **111**, 8500–8508.

[101] M. Merchán, R. González-Luque, T. Climent, L. Serrano-Andrés, E. Rodriguez, M. Reguero and D. Peláz, *J. Phys. Chem. B*, 2006, **110**, 26471–26476.

[102] T. Gustavsson, A. Bányász, E. Lazzarotto, D. Markovitsi, G. Scalmani, M. Frisch, V. Barone and R. Improta, *J. Am. Chem. Soc.*, 2006, **128**, 607–619.

[103] S. Matsika, *J. Phys. Chem. A*, 2004, **108**, 7548.

[104] S. Matsika, *J. Phys. Chem A*, 2005, **109**, 7538.

[105] T. Climent, R. González-Luque, M. Merchán and L. Serrano-Andrés, *Chem. Phys. Lett.*, 2007, **441**, 327–331.

[106] J. J. Serráno-Perez, R. González-Luque, M. Merchán and L. Serrano-Andrés, *J. Phys. Chem. B*, 2007, **111**, 11880–11883.

[107] M. Z. Zgierski, S. Patchkovskii, T. Fujiwara and E. C. Lim, *J. Phys. Chem. A.*, 2005, **109**, 9384–9387.

[108] A. Yoshikawa and S. Matsika, *Chem. Phys.*, 2008, **347**, 393–404.

[109] G. Zechmann and M. Barbatti, *J. Phys. Chem. A*, 2008, **112**, 8273–8279.

[110] Y. Mercier, F. Santoro, M. Reguero and R. Improta, *J. Phys. Chem. B*, 2008, **112**, 10769–10772.

[111] Z. Lan, E. Fabiano and W. Thiel, *J. Phys. Chem. B*, 2009, **113**, 3548–3555.

[112] R. K. Neely, S. W. Magennis, D. T. F. Dryden and A. C. Jones, *J. Chem. Phys. B*, 2004, **108**, 17606–17610.

[113] C. Canuel, M. Mons, F. Piuzzi, B. Tardivel, I. Dimicoli and M. Elhanine, *J. Chem. Phys.*, 2005, **122**, 074316.

[114] K. A. Seefeld, C. Plützer, D. Löwenich, T. Häber, R. Linder, K. Kleinermanns, J. Tatchen and C. M. Marian, *Phys. Chem. Chem. Phys.*, 2005, **7**, 3021–3026.

[115] Y. Harada, C. Okabe, T. Kobayashi, T. Suzuki, T. Ichimura, N. Nishi and Y.-Z. Xu, *J. Phys. Chem. Lett.*, 2010, **1**, 480–484.

[116] T. Kobayashi, Y. Harada, T. Suzuki and T. Ichimura, *J. Phys. Chem. A*, 2008, **112**, 13308–13315.

[117] T. Kobayashi, H. Kurumochi, Y. Harada, T. Suzuki and T. Ichimura, *J. Phys. Chem. A*, 2009, **113**, 12088–12093.

[118] E. D. Clercq, *Antivir. Res.*, 2005, **67**, 56–75.

[119] F. Exinger and F. Lacroute, *Curr. Genet.*, 1992, **22**, 9–11.

[120] M. Etinski and C. M. Marian, *Phys. Chem. Chem. Phys.*, 2010, submitted.

[121] D. G. Truhlar and C. A. Mead, *Phys. Rev. A*, 2003, **68**, 032501.

Paper 1

Electronic and vibrational spectroscopy of 1-methylthymine and its water clusters: The dark state survives hydration

Matthias Busker, Michael Nispel, Thomas Haber, Karl Kleinermanns ,Mihajlo Etinski, and Timo Fleig

Chem. Phys. Chem., **9** (2008) 1570-1577

CHEMPHYSCHEM

DOI: 10.1002/cphc.200800111

Electronic and Vibrational Spectroscopy of 1-Methylthymine and its Water Clusters: The Dark State Survives Hydration

Matthias Busker,[a] Michael Nispel,[a] Thomas Häber,[a] Karl Kleinermanns,*[a] Mihajlo Etinski,[b] and Timo Fleig*[b]

Electronic and vibrational gas phase spectra of 1-methylthymine (1MT) and 1-methyluracil (1MU) and their clusters with water are presented. Mass selective IR/UV double resonance spectra confirm the formation of pyrimidine-water clusters and are compared to calculated vibrational spectra obtained from ab initio calculations. In contrast to Y. He, C. Wu, W. Kong; J. Phys. Chem. A, ***2004***, 108, *94 we are able to detect 1MT/1MU and their water clusters via resonant two-photon delayed ionization under careful control of the applied water-vapor pressure. The long-living dark electronic state of 1MT and 1MU detected by delayed ionization, survives hydration and the photostability of 1MT/1MU cannot be attributed solely to hydration. Oxygen coexpansions and crossed-beam experiments indicate that the triplet state population is probably small compared to the $^1n\pi^*$ and/or hot electronic ground state population. Ab initio theory shows that solvation of 1MT by water does not lead to a substantial modification of the electronic relaxation and quenching of the $^1n\pi^*$ state. Relaxation pathways via $^1\pi\pi^*$–$n\pi^*$ and $^1\pi\pi^*$–S_0 conical intersections and barriers have been identified, but are not significantly altered by hydration.*

1. Introduction

Absorption of UV radiation by DNA bases can generate mutations which mainly occur at bipyrimidine sites. The major photoproducts are cyclobutane dimers and pyrimidine-(6-4)-pyrimidone adducts. The detailed mechanism of this photoreaction is still unclear—direct reaction in the photoexcited $^1\pi\pi^*$ state,[1] a long-living $^1n\pi^*$ or triplet state[2,3] populated by relaxation of the $^1\pi\pi^*$ state and non-concerted product formation in the hot S_0 ground state come into question.

The pyrimidine bases uracil (U) and thymine (T) feature broad absorptions in the gas phase and in solution[4–10] with an onset at around 275 nm in the vapor spectrum. This first absorption band has been assigned to a $^1\pi\pi^*$ ($S_2 \rightarrow S_0$) excitation.[6,10–13] The computed oscillator strength for the $^1n\pi^*$ ($S_1 \rightarrow S_0$) transition is smaller by a factor of about 10^3, that is, the state is "dark".[12] The dominating decay channel of UV-excited thymine is subpicosecond internal conversion from the $^1\pi\pi^*$ state to S_0[14] creating $\approx$90 % vibrationally hot T which cools on the ps time scale.[15] Passage to the dark $^1n\pi^*$ state accounts for approximately 10% of T in solution.[15] Condensed phase lifetimes of the $^1n\pi^*$ state are typically 30 ps for thymine and 4× longer for thymidine monophosphates (TMP). A small fraction of the $^1n\pi^*$ population is proposed to undergo intersystem crossing to the lowest triplet state T_1 in competition with vibrational cooling.[15]

The triplet states of uracil and thymine have been characterized in considerable detail. Weak phosphorescence of U at 77 K was observed with a maximum at 450 nm (2.76 eV)[4] which compares favorably with the computed vertical $T_1 \rightarrow S_0$ deexcitation energy of $\approx$2.73 eV.[12] The adiabatic transition energy is about 3.2 eV. Phosphorescence is weak because the T_1–S_2 and T_1–S_0 spin-orbit coupling matrix elements are small whereas the significant T_1–S_1 coupling does not lead to enhanced emission because the S_1 state is dark.[12] A triplet lifetime of 75 ms was observed for T at 77 K via phosphorescence[4] in contrast to a unimolecular decay time of 32 μs in deaerated aqueous solutions as measured by nanosecond transient absorption spectroscopy (ns-TAS).[16] Triplet state formation has a low quantum yield $<$0.02 in water.[17,18,18–20] However, the triplet state is still of interest due to its long lifetime when considering excited state DNA chemistry. TMP has the lowest triplet energy of all nucleotides[21] hence interbase triplet energy transfer would lead to accumulated triplet TMP.

Ns-TAS experiments show that UV excitation of the single-stranded oligonucleotide $(dT)_{20}$ leads to cyclobutane pyrimidine dimers (CPD) in less than 200 ns, whereas the (6–4) adduct is formed within 4 ms probably via intermediate oxetane.[22] Quantum yields of 0.03 and 0.004 are determined for CPD and (6–4) formation, respectively. Femtosecond time-resolved infrared spectroscopy is used to study the formation of CPD in $(dT)_{18}$ upon 272 nm excitation.[1] The ultrafast appearance of CPD marker bands points to dimer formation in less than 1 ps. It is concluded that T dimerization in DNA is an ul-

[a] *M. Busker, Dr. M. Nispel, Dr. T. Häber, Prof. Dr. K. Kleinermanns*
Institut für Physikalische Chemie und Elektrochemie 1
Heinrich-Heine Universität-Düsseldorf, 40225 Düsseldorf (Germany)
E-mail: kleinermanns@uni-duesseldorf.de

[b] *M. Etinski, Dr. T. Fleig*
Institut für Theoretische und ComputerChemie
Heinrich-Heine Universität-Düsseldorf, 40225 Düsseldorf (Germany)

Supporting information for this article is available on the WWW under http://dx.doi.org/10.1002/cphc.200800111.

trafast photoreaction and occurs directly in the photoexcited singlet $^1\pi\pi^*$ state.[1]

Spectroscopic experiments in supersonic jets are able to study isolated nucleobases in detail and may shine more light on the puzzle of thymine's excited states. IR and microwave experiments demonstrate that the diketo tautomer of U and T is the most abundant species in the gas phase—probably the only one.[10,23,24] Resonance enhanced two-photon ionization (R2PI) experiments show broad and diffuse electronic spectra of U and T which are attributed either to mixing of electronic states or to a large geometry change between the ground and excited electronic states.[10] Kong and co-workers[25] showed that methyl-substituted uracils and thymines can be ionized with tens to hundreds of nanoseconds delay after electronic excitation pointing to the existence of a long-living dark electronically excited state of T in the gas phase which they assigned to a $^1n\pi^*$ state. The lifetime of this dark state depends on the internal energy and the degree of methyl substitution with the general trend that the lifetime increases the more substituted the ring and the longer the pump wavelength is. They observed a decrease of lifetime of the dark state of T and a gradual loss of the ion signal with increasing water content in the jet and concluded that in water solutions the dark state is not populated significantly anymore because fast internal conversion to the electronic ground states dominates. Hence Kong and co-workers infer that the photostability is not an intrinsic property of the pyrimidine DNA bases but results from their hydration.[25] The work of Kohler et al.[15] on the corresponding pyrimidine nucleotides and short DNA strands however showed that this state is clearly not quenched in water. We therefore decided to reinvestigate the photophysical behavior of methyl substituted thymine in the gas phase.

Herein we present the first IR/UV double resonance spectra of hydrated 1-methylthymine (1MT) from which we infer the structures of 1MT-water clusters. In particular we demonstrate that in 1MT (methylation where the sugar sits in the DNA) the dark state survives hydration and delayed ionization is still possible. We observe broad electronic spectra both of 1MT and its water clusters and assign their diffuse appearance to fast internal conversion of the pumped $^1\pi\pi^*$ state. Hence in the isolated and in the hydrated molecule both fast and slow channels are still observable. Extensive high level ab initio calculations are performed to understand this photophysical behavior in detail.

2. Results

2.1. Spectra

Figure 1 shows the time-of-flight mass spectra of 1MT and 1MU and their hydrated clusters at water vapor pressures of 8.2 and 12.3 mbar. Two-photon ionization is performed by using 273.2 nm as excitation wavelength and 193 nm for ionization with 40 ns delay between the two laser pulses. At low water vapor pressure (8 mbar) only the masses of the monomers and the 1:1 water clusters are discernible. We assume that the contribution from fragmenting larger water clusters

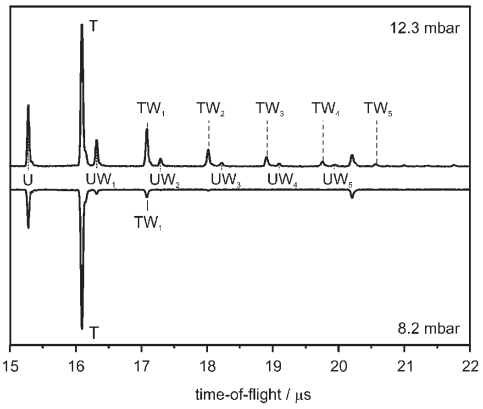

Figure 1. Mass spectra of 1MT and 1MU (abbreviated here as T and U) and their water clusters at water-vapor pressures of 12.3 mbar (top trace) and 8.2 mbar (lower trace). The ion signal of the lower spectrum has been inverted for easier comparison. Excitation at 273.2 nm, ionization at 193 nm; 40 ns delay between the excitation and ionization laser pulses.

plays only a minor role at 8 mbar H_2O pressure. The intensity of the monomer ion signal is about 18-times larger than the water cluster ion signal under these conditions. At a higher water pressure of 12.3 mbar, we observe clusters with up to five water molecules and only four times more monomer than 1:1 cluster signal pointing to extensive monomer-water aggregation and considerable fragmentation contributions to the mass spectrum. At still higher water pressures we monitored increasingly larger water clusters and a continuing decrease of monomer signal due to cluster formation down to zero monomer signal. In contrast to ref. [25], clusters with more than four water molecules were easily detected. With increasing water-vapor pressure, all ion intensities (monomer and cluster masses) decrease and finally vanish, which is probably correlated to a lower ion-detection efficiency under these conditions and the formation of "ice-balls" containing 1MT or 1MU (any traces of 1MT and 1MU are incorporated into very large clusters). As a consequence the overall ion-signal intensities on all small-cluster masses as well as the monomer mass are reduced. This may have been a problem in earlier measurements,[25] in which a water-vapor pressure of 23 mbar was used to generate thymine-water clusters.

The vibronic spectra of jet-cooled dry 1MT and 1MU detected by R2PI are displayed in Figure 2a. The spectrum of 1MT reveals a distinct peak at 35880 cm^{-1} (278.7 nm) with an onset at ~35700 cm^{-1} followed by a broad, unstructured band which extends up to 41000 cm^{-1} (~244 nm). The electronic spectrum of 1MU is essentially unstructured and blue-shifted relative to the 1MT spectrum, as expected from the lower degree of methylation, with an onset at ~36400 cm^{-1} (274.7 nm). Figure 2b shows the R2PI spectra of 1MT(H_2O) and 1MU(H_2O) clusters detected on the parent masses at low water concentration (8 mbar). As discussed above, we expect preferential formation of small clusters under these experimental conditions. The spectra are again largely unstructured and exhibit only a small shift relative to the monomer spectra. The peak at

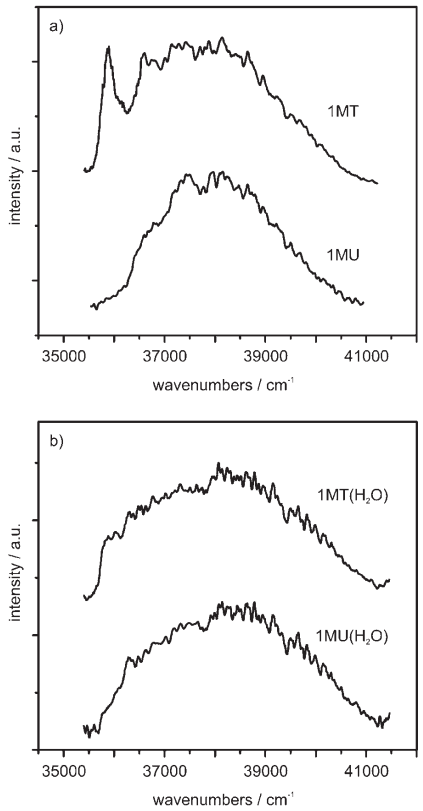

Figure 2. a) Vibronic spectra of 1MT and 1MU monomers (without addition of water) detected by R2PI. b) R2PI spectra of 1MT/1MU-water clusters detected at the 1MT/1MU$(H_2O)_1$ mass at low water concentration (8 mbar). Ionization at 193 nm; 40 ns delay between the excitation (300 μJ for clusters and 120 μJ for monomers) and ionization (30 μJ) laser pulses.

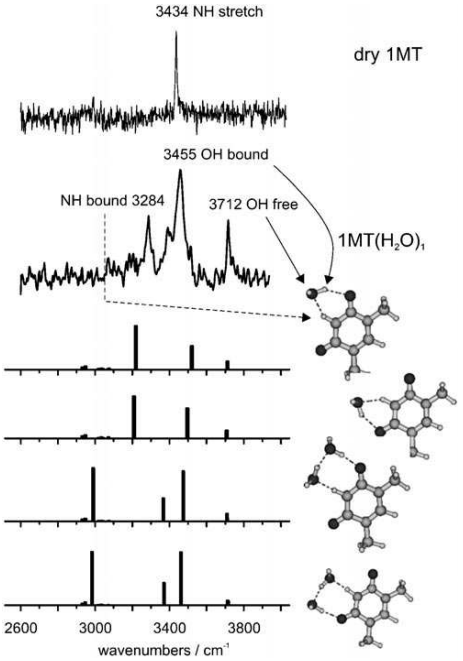

Figure 3. Top trace: IR/UV spectrum of dry 1MT. Lower trace: IR/UV spectrum of 1MT-water detected at the 1MT$(H_2O)_1$ mass at low water concentration (6 mbar vapor pressure). Excitation at 273.3 nm, ionization at 213 nm. Displayed are the most stable structures of 1MT$(H_2O)_{1,2}$ and their infrared spectra calculated at the RIMP2/ccpVDZ level. The vibrational frequencies were scaled by a factor of 0.9502 to match the calculated free NH-stretch frequency of the 1MT monomer to its experimental value.

35880 cm^{-1} (278.8 nm) in the 1MT spectrum is not discernible anymore in the 1MT/water spectrum.

The IR/UV spectrum of dry 1MT is presented in the top trace of Figure 3. The absorption at 3434 cm^{-1} is attributed to the "free" NH stretch vibration. The free NH stretch vibration of 1MU is detected at 3432 cm^{-1} (not shown here). The next trace in Figure 3 shows the IR/UV ion dip spectrum recorded at the 1MT$(H_2O)_1$ mass at a still lower water pressure of 6 mbar. Cluster structures containing one and two water molecules calculated at the RIMP2 level and their IR stick spectra are displayed for comparison and assignment of the experimental spectrum. The ground-state geometries obtained from CC2/cc-pVDZ calculations of clusters with up to five water molecules are in close agreement with the RIMP2 structures (cf. Figure 7).

Closer analysis shows that the experimental spectrum can be ascribed to the NH and OH stretch vibrations of 1MT$(H_2O)_1$ with some contributions from 1MT$(H_2O)_2$ discernible by the shoulder at 3388 cm^{-1}. The IR band of 1MT$(H_2O)_2$ calculated at $\approx$3000 cm^{-1} is readily assigned to the OH stretch vibration in the OH···O(H) hydrogen bond and can be expected to be very broad and therefore hard to detect. However, we cannot differentiate between the different isomers of 1MT$(H_2O)_1$ displayed in Figure 3 because of the close resemblance of the calculated spectra.

2.2. Lifetime Measurements

Figure 4a shows the ion-signal decay of electronically excited dry 1MT and 1MU as a function of the delay time between the excitation (273.2 nm) and ionization (193 nm) laser pulses. Decay times are 107 ns $\pm$ 30 ns for 1MU and 227 ns $\pm$ 30 ns for 1MT. As already pointed out[25] the lifetime increases with degree of methylation. This finding is supported by ab initio calculations: For bare 1MT we determine the barrier between the $^1n\pi^*$ minimum and the $^1\pi\pi^*/^1n\pi^*$ conical intersection to be 1.33 eV (details in the following), whereas this barrier is lower than 1 eV for bare uracil.[26]

Figure 4b shows the ion-signal decay curves in the presence of water, both, on the monomer masses (1MT and 1MU) and on the 1MT/1MU$(H_2O)_1$ cluster masses. The ion signals on the cluster masses show a slow, nearly linear decay. In Figure 1, ion signals of clusters with more than four water molecules are readily discernible at a delay time of 40 ns and low water content. At higher water-vapor pressures we measured ion signals for clusters with up to eight water molecules. The decay curves of the larger clusters all show the same, nearly linear decay as the 1MT/1MU(H_2O) clusters. Contrary to earlier measurements[25] we do not observe a sharp drop of the ion-signal intensities for clusters with more than four water molecules. Instead, the intensities decrease smoothly with increasing cluster size, as in a typical cluster experiment, because more collisions are required to form larger clusters. Figure 4 clearly demonstrates that delayed ionization is possible not only for the

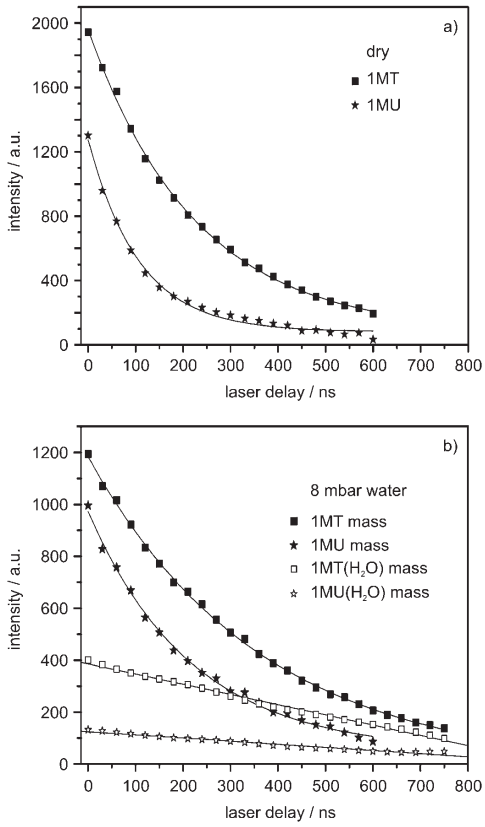

Figure 4. Ion-signal decay of dry 1MT and 1MU (a) and of hydrated 1MT and 1MU (b). Excitation at 273.2 nm (120 μJ) and ionization at 193 nm (30 μJ) with a variable time delay between the excitation and ionization laser pulses. Water-vapor pressure: 8 mbar (4 °C).

monomers, but also for their clusters with water. Identical decay curves are obtained when using 213 nm instead of 193 nm for ionization. Kong and co-workers[25] used rather high water-vapor pressures in their experiment which leads to a decrease of the ion-detection efficiency up to complete disappearance of the delayed ion signal according to our experience.

The ion-signal decay curves of the clusters in Figure 4b are limited by the time the clusters need to fly out of the ionization volume with the speed of the molecular beam. In our experiment (beam width $\approx$2 mm) it takes about 1.5 μs for all the clusters to fly out of the ionization volume. That time agrees with the extrapolated intersection between the nearly linear decay curves and the time axis in Figure 4b. We confirm this by varying the size of the ionization laser beam. Thus, the long-living dark state of the water clusters decays on a slower timescale ($>$1 μs) than the size of our observation window.

The lifetime measured on the monomer mass in the presence of water (8 mbar vapor pressure) increases to 218 ns $\pm$ 30 ns for 1MU and 363 ns $\pm$ 30 ns for 1MT which is attributed to a contribution of water clusters fragmenting to the monomer mass, either during the lifetime of the dark state or after ionization .[27,28]

2.3. Oxygen Coexpansion

The identification of the dark state still remains an open question. Possible candidates are the $^1n\pi^*$ state, a low-lying triplet state or the vibrationally hot electronic ground state populated by efficient internal conversion from the excited-singlet state. Since ground-state triplet oxygen features a low-lying singlet state, efficient 1MT triplet quenching is expected when coexpanding 1MT with oxygen or when crossing a molecular beam of excited 1MT with an oxygen beam. Indeed quenching of T and TMP triplet–triplet absorption with O_2 has been reported to be very effective so that the measurements have to be done in an aqueous solution saturated with N_2 excluding all O_2.[16] Therefore we decided to use oxygen quenching as a check of the triplet character of the dark state.

In a first step, we coexpanded dry 1MT and 1MU in a mixture of 10% oxygen and 90% helium. The lifetime did not change within the accuracy of our measurements. In a second approach we established an effusive oxygen beam (100% O_2), which propagated perpendicular to the molecular beam carrying 1MT and 1MU and again measured the lifetime of the dark state. We compared the ion-signal intensities under normal expansion and crossed-beam conditions using a delay of 40 ns between the excitation and ionization laser pulses. Crossed-beam experiments with nitrogen and argon were performed as a reference for the attenuation of the molecular beam due to elastic and inelastic collisions in the crossed-beam setup. Comparing the ion intensities gives valuable information, even if the quenching process occurs on a timescale below the detection limit of our apparatus (10 ns). In that case quenching is still observable by a decreased ion-signal intensity.

Indeed we observe a small intensity decrease. However, the effect was similarly large in collisions with nitrogen or argon and can therefore not be attributed to specific triplet quenching. The lifetime of dry 1MT/1MU did not change in the oxygen-beam experiment within the uncertainty of our measurements. Therefore the triplet-state population is probably small compared to the population of the $^1n\pi^*$ or hot vibrational ground state. Kong et al. observed weak fluorescence of 1,3-dimethyluracil with similar lifetimes as the decay times of the delayed ionization signal so that the hot S_0 state seems to us a less likely candidate for the dark state than the $^1n\pi^*$ state. Note, however, that delayed fluorescence in which a low-lying excited-singlet state becomes populated by a thermally activated radiationless transition from the first-excited triplet state is a well-known phenomenon in condensed-phase spectroscopy.[1,2]

2.4. Calculations

The variance in decay times for bare and hydrated 1MT might be related to the relative energies of the involved electronic states. To gain further insights into the change of the lowest $^1n\pi^*$ and $^1\pi\pi^*$ singlet and triplet states with hydration we performed extensive high-level ab initio calculations. We specifically focus on the following questions: Is a direct decay from the bright $^1\pi\pi^*$ state to the electronic ground state enhanced

by hydration? Does hydration significantly affect the energy barrier for an alternative decay via the dark state?

Our single-point/adiabatic CC2 and LIIC CASSCF/CASPT2 calculations (Supporting Information) enable us to construct an energy level diagram for bare 1MT as shown in Figure 5. In

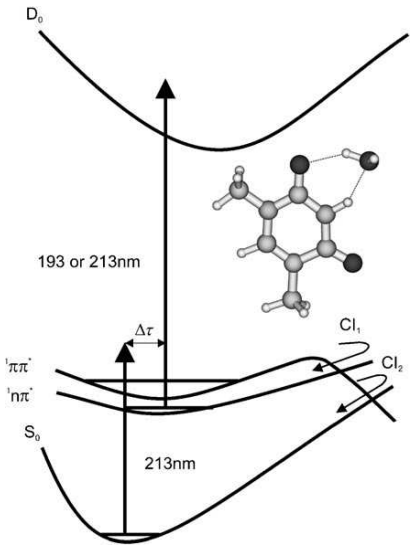

Figure 5. Schematic representation of possible relaxation pathways in 1MT $(H_2O)_1$ (triplet states excluded).

accord with previous investigations[29–31] we find conical intersections $^1\pi\pi^*/^1n\pi^*$ (CI_1) and $^1\pi\pi^*/S_0$ (CI_2). Furthermore, the two excited states in question exhibit minima on the potential hypersurfaces. The structures at the conical intersections are shown in Figure 6. The structures of the 1MT-water clusters in the electronic ground and $^1n\pi^*$ state optimized at the CC2/cc-pVDZ level are displayed in Figure 7 and in Figure 9 of the Supporting Information.

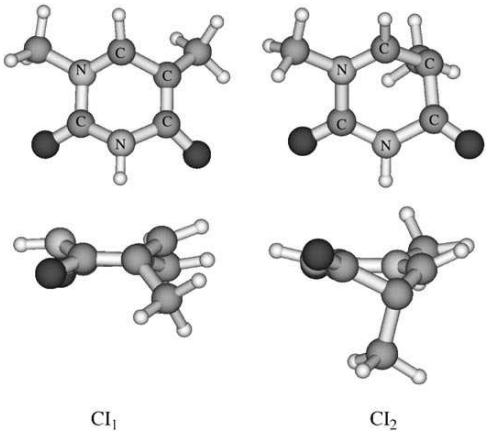

Figure 6. Geometries of the conical intersections in 1MT optimized at the CASSCF(10,8)/6-31G* level: CI_1 is the intersection between $^1\pi\pi^*$ and $^1n\pi^*$ adiabatic states and CI_2 is the intersection between $^1\pi\pi^*$ and ground adiabatic states.

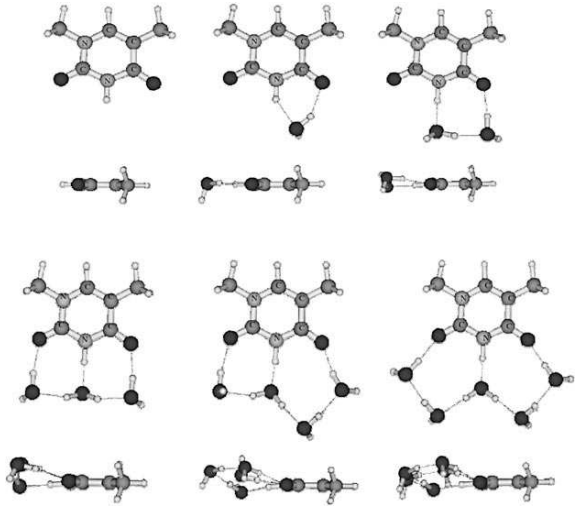

Figure 7. Geometries of ground state 1MT and 1MT-water clusters optimized at the CC2/cc-pVDZ level.

Our calculations show that LIIC paths for bare 1MT and singly-hydrated 1MT are essentially the same. Because of that, we may restrict the discussion to the variance of relative energies due to hydration at crucial points on the hypersurfaces, that is, at the respective minima and conical intersections. From our most accurate calculations (CC2/aug-cc-pVTZ) we determine a $^1n\pi^*$ adiabatic excitation energy of 3.73 eV and a barrier between the minimum of $^1n\pi^*$ and CI_1 of 1.33 eV for bare 1MT. Upon microhydration with one water molecule, this barrier is lowered to 1.09 eV and the adiabatic energy is increased to 3.88 eV. Due to these findings we expect a higher probability of $^1\pi\pi^*/^1n\pi^*$ internal conversion upon hydration with one water molecule than for bare 1MT.

To address the question of whether increased microhydration might further lower this barrier or lead to a dramatically enhanced direct relaxation from $^1\pi\pi^*$ to S_0 through CI_2 we have carried out a series of CC2/aug-cc-pVTZ single-point calculations. The results are shown in Figure 8 and Figure 10 (in the Supporting Information) for two points, the equilibrium geometry of the ground state and the equilibrium geometry of the $^1n\pi^*$ excited state. Interestingly, we observe the trend that the $^1n\pi^*$ state is destabilized energetically relative to the $^1\pi\pi^*$ state for structures with one and two water molecules. This points to both an enhanced direct relaxation and a reduced population of the $^1n\pi^*$ state. The trend, however, is broken at the time when the third and subsequent water molecules are attached to the system. In the cluster with five water molecules only a minute deviation of the relative energies from those of bare 1MT remains. We ascribe this energetic reconstitution to a recovery of partial symmetry at the substitution sites (where the hydrogen bonds perturb the electronic valence distribution) as soon as the third water molecule enters the cluster. The preferred formation of water clusters around the oxygen binding sites is shown in Figure 7 where also the symmetry argument becomes obvious. Thus, a substantial modification of the relaxation pathways of 1MT through micro-

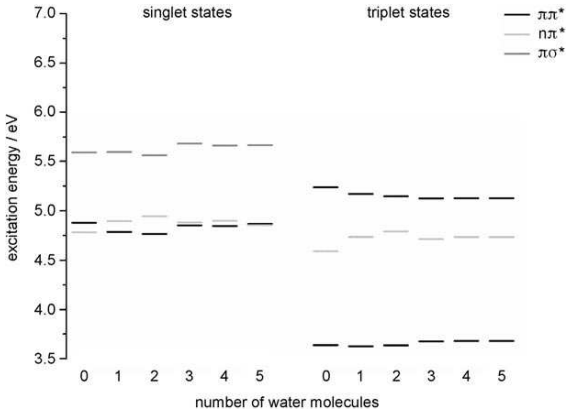

Figure 8. Vertical electronic excitation energies calculated at the ground state geometry at CC2/aug-cc-pVTZ level (the three lowest states). All structures are optimized at the CC2/cc-pVDZ level.

hydration is not observed and a claim that solvation by water would lead to a quenching of the dark state cannot be supported by ab initio theory.

3. Discussion

The decay mechanisms of 1MT/1MU have been investigated and correlated with their water aggregates. We are, to our knowledge, the first to publish R2PI spectra of 1MT/1MU and their water clusters. IR/UV double resonance experiments confirmed the formation of 1MT/1MU(H_2O) clusters, in which the water molecule forms a bridge between the NH bond and a neighboring C=O group. Ab initio calculations reproduce the experimental spectra. The infrared spectra also show that fragmentation of larger water clusters is minimized at low water concentrations in the supersonic expansion. In contrast to the work published by Kong and co-workers,[25] we were able to detect delayed ionization of 1MT/1MU-water clusters up to 1 μs after excitation under careful control of the applied water-vapor pressure. Even aggregates carrying more than five water molecules were detected. In addition, our ab initio calculations show that the energetics of the excited states and the de-excitation pathways are not significantly altered by hydration.

The decay curves of the bare monomers (1MT and 1MU) in Figure 4a show an exponential decay much faster than our upper detection limit of about 1.5 μs. We can only detect molecules (or clusters) that are ionizable at the wavelength of our ionization laser (193 or 213 nm). This means that on the timescale of our experiment 1MT and 1MU relax from a higher to a lower state, which is not ionizable anymore. The pyrimidine bases thymine and uracil and their derivatives undergo ultrafast (sub-picosecond timescale) internal conversion from the initially excited $^1\pi\pi^*$ state to the vibrationally excited ("hot") S_0 ground state and to some extent to the optically dark $^1n\pi^*$ state.[14,15] For the moment, let us assume that the ionization laser also probes the hot electronic ground state. IVR would spread the energy over the vibrational degrees of freedom on a timescale much faster than our lower detection limit of 10 ns. However, since the gas-phase experiment takes place in the collision-free region of a skimmed molecular beam, the energy will stay in the molecule as long as the radiation lifetime of the vibrational modes (>1 μs). In that case the molecule could be ionized at any time with the same probability, resulting in a linear decay as the molecules fly out of the ionization volume.

This is clearly not the case for the bare monomers in Figure 4a. After 600 ns only a small fraction of the monomers can be ionized anymore, indicating that the hot ground state either cannot be ionized at 193 nm or that the ionization probability is too low for detection due to an unfavorable Franck–Condon overlap. We therefore attribute the exponential decay of the monomer-ion signal to the true relaxation from an electronically excited state (the dark state) to the S_0 ground state.

By contrast, the 1MT- and 1MU-water clusters show a linear decay of the ion signal, meaning that the probed state has a longer lifetime than our upper detection limit. However, we have no reason to believe that the hot ground state of the clusters has a higher ionization probability than the monomer nor do the energetics change significantly between the monomer and clusters, which could have explained a faster decay to the hot ground state. To the contrary, the higher number of vibrational degrees of freedom is likely to facilitate the energy dissipation via IVR. In addition, vibrationally hot clusters tend to fragment and loose energy (evaporative cooling). Therefore we attribute the slow decay of the cluster-ion signal also to the relaxation of an electronically excited state, which is most likely the optically dark $^1n\pi^*$ state. Our upper detection limit is then only a lower limit for the dark state lifetime (>1 μs).

Kohler and co-workers[32] showed that hydrogen bonds between nucleobases and the solvent strongly enhance vibrational cooling, allowing the nucleobases to dissipate vibrational excess energy to the solvent more effectively. The additional hydrogen bonds between the ribosyl group and the water solvent are responsible for the four-fold larger lifetime of the TMP and UMP nucleotides compared to the nucleobases T and U in solution.[15] Similar effects might be responsible for the increased dark-state lifetime of the 1MT- and 1MU-water clusters compared to the isolated nucleobases in the gas phase. A more effective energy dissipation of the hydrated monomers as well as cluster fragmentation during the lifetime of the dark state (evaporative cooling) might lead to a slower passage of the $^1n\pi^*/S_0$ barrier and an increase of the dark-state lifetime.

4. Conclusions

Our experimental results demonstrate that hydration does not accelerate internal conversion to the electronic ground state to a degree that the dark state is quenched;[25] the conclusions of Kong et al.[25] which state that the photostability is not an intrinsic property of the pyrimidine bases but results from their hydration is not confirmed for 1MT and 1MU. To the contrary, we propose an increase of the dark-state lifetime of 1MT- and 1MU-water clusters in the gas phase. Our results agree with the observation of a long-living dark state upon UV excitation of T and U nucleotides in aqueous solutions.[15] Ab initio theory

shows that solvation of 1MT by water does not lead to a substantial modification of electronic relaxation and quenching of the $^1n\pi^*$ state. Coexpansions and crossed-beam experiments with oxygen showed no measurable decrease of the dark-state lifetime, so that the triplet-state population is probably small compared to the $^1n\pi^*$ population. Further experimental and theoretical work is directed towards identification of the dark state via vibrational spectroscopy and towards clarification of a possible connection of the dark state to the dimerization of thymine.

Experimental and Theoretical Section

The experimental setup has been described in detail elsewhere.[27] A mixture of helium and thymine derivatives at 150 to 170°C is expanded through the 300 μm orifice of a pulsed nozzle (General Valve). The skimmed molecular beam (Beam Dynamics Skimmer, 1 mm orifice) crosses the collinear laser beams at a right angle. The ions are extracted in a modified Wiley-McLaren type time-of-flight (TOF) spectrometer perpendicular to the molecular and laser beams.

1-Methylthymine (1MT) and 1-methyluracil (1MU) were purchased from Sigma–Aldrich and used without further purification. Water clusters were formed by bubbling helium through water prior to the expansion. The water content was controlled by the temperature dependence of the water-vapor pressure. Different vapor pressures of 6 mbar (273 K), 8.2 mbar (277 K) and 12.3 mbar (283 K) were investigated.

R2PI (resonance enhanced two-photon ionization) spectra were obtained by exciting the molecules to the first optically accessible electronic state by the frequency doubled output of a Nd:YAG (Spectra Physics, GCR 170) pumped dye laser (LAS, LDL 205) with fluorescein 27, coumarine 307 and coumarine 153. The molecules were ionized by delayed ionization using the 193 nm output of an ArF excimer laser (Neweks, PSX-501-2) or the fifth harmonic of a Nd:YAG laser (213 nm, Innolas, Spitlight 600). Longer ionization wavelengths reduce the excess energy in the ions and thus fragmentation of the 1MT clusters. For the IR/UV double resonance spectra an infrared (IR) laser pulse was fired 36 ns prior to the UV excitation laser. IR light (3000–4000 cm^{-1}) was generated by an IR-OPO/OPA setup (LaserVision), pumped by the fundamental of a Nd:YAG laser (Spectra Physics, Indi 40-10). IR laser frequencies were calibrated by recording an ammonia vapor spectrum.

All calculations were performed with the quantum chemistry program packages TURBOMOLE[33] and MOLPRO.[34] We carried out resolution-of-the-identity (RI)-coupled-cluster (CC) 2[35,36] geometry optimization[37] of ground- and excited states and RI-CC2 in combination with linear response theory for vertical single-point calculations. We used Dunning's correlation-consistent basis sets cc-pVDZ (C, N, O: 9s4p1d/3s2p1d; H: 4s1p/2s1p) for geometry optimizations and aug-cc-pVTZ (C, N, O: 11s6p3d2f/5s4p3d2f; H: 6s3p2d/4s3p2d) for excitation energies which have provided results of high accuracy in previous CC2 calculations on nucleic acid bases.[38] Geometries were optimized without symmetry constraints. The optimization of conical intersections and the calculation of linear interpolation in internal coordinates (LIIC) paths have been carried out with state-averaged CASSCF/CASPT2 (complete-active-space self-consistent-field/complete-active-space perturbation theory to 2nd order) methods[39–41] and Pople's 6-31G* (C, N, O: 10s4p1d/3s2p1d; H: 4s/2s) basis set.[42] The optimization of conical intersections was carried out with the CASSCF method with an active space of 10 electrons in 8 molecular orbitals (3π, 2n, 2π* and 1σ* orbitals) and the 6-31G* basis set. We obtained starting geometries for conical intersection optimization by slightly deforming the ring in order to destabilize the electronic ground state. In all calculations we retained a frozen core comprised by all heavy-atom 1s electrons.

Acknowledgements

The authors thank the Deutsche Forschungsgemeinschaft (SFB 663) for financial support. M.E. also thanks Mario Barbatti and Christel Marian for helpful discussions.

Keywords: ab initio calculations · DNA · photophysics · vibrational spectroscopy · water clusters

[1] W. J. Schreier, T. E. Schrader, F. O. Koller, P. Gilch, C. E. Crespo-Hernández, V. N. Swaminathan, T. Carell, W. Zinth, B. Kohler, *Science* **2007**, *315*, 625.
[2] M. J. Mantione, B. Pullman, *Biochim. Biophys. Acta* **1964**, *91*, 387.
[3] R. O. Rahn, M. H. Patrick, *Photochemistry and Photobiology Nucleic Acid, in Biologie*, (Ed.: S. Y. Wang), Academic Press, Inc., New York **1976**, *Vol. II*, pp. 97–145.
[4] R. Becker, G. Kogan, *Photochem. Photobiol.* **1980**, *31*, 5.
[5] P. R. Callis, *Annu. Rev. Phys. Chem.* **1983**, *34*, 329.
[6] L. B. Clark, G. G. Peschel, J. I. Tinoco, *J. Phys. Chem.* **1965**, *69*, 3615.
[7] M. Fujii, T. Tamura, N. Mikami, M. Ito, *Chem. Phys. Lett.* **1986**, *126*, 583–587.
[8] Y. Tsuchiya, T. Tamura, M. Fujii, M. Ito, *J. Phys. Chem.* **1988**, *92*, 1760.
[9] D. R. Voet, W. B. Gratzer, R. A. Cox, P. Doty, *Biopolymers* **1963**, *1*, 193.
[10] B. B. Brady, L. A. Peteanu, D. H. Levy, *Chem. Phys. Lett.* **1988**, *147*, 538.
[11] J. Lorentzon, M. P. Fülscher, B. O. Roos, *J. Am. Chem. Soc.* **1995**, *117*, 9265.
[12] C. M. Marian, F. Schneider, M. Kleinschmidt, J. Tatchen, *Eur. Phys. J. D* **2002**, *20*, 357.
[13] J. D. Petke, G. M. Maggiora, R. E. Christoffersen, *J. Phys. Chem.* **1992**, *96*, 6992.
[14] C. E. Crespo-Hernández, B. Cohen, P. M. Kohler, *Chem. Rev.* **2004**, *104*, 1977.
[15] P. M. Hare, C. E. Crespo-Hernández, B. Kohler, *Proc. Natl. Acad. Sci. USA* **2007**, *104*, 435.
[16] Q. Song, W. Lin, S. Yao, N. Lin, *J. Photochem. Photobiol. A* **1998**, *114*, 181.
[17] D. N. Nikogosyan, V. S. Letokhov, *Riv. Nuovo Chim.* **1983**, *6*, 1–72.
[18] M. Gueron, J. Eisinger, A. A. Lamola in *Basic Principles in Nucleic Acid Chemistry*, (Ed.: P. O. P. Ts'o) Academic Press, Inc., New York **1974**, pp. 311–398.
[19] C. Salet, R. Bensasson, *Photochem. Photobiol.* **1975**, *22*, 231.
[20] C. Salet, R. V. Bensasson, R. S. Becker, *Photochem. Photobiol.* **1979**, *30*, 325.
[21] P. D. Wood, R. W. Redmond, *J. Am. Chem. Soc.* **1996**, *118*, 4256.
[22] S. Marguet, D. Markovitsi, *J. Am. Chem. Soc.* **2005**, *127*, 5780.
[23] M. R. Viant, R. S. Fellers, R. P. McLaughlin, R. J. Saykally, *J. Chem. Phys.* **1995**, *103*, 9502–9505.
[24] R. D. Brown, P. D. Godfrey, D. McNaughton, A. P. Pierlot, *J. Am. Chem. Soc.* **1988**, *110*, 2329.
[25] Y. He, C. Wu, W. Kong, *J. Phys. Chem. A* **2004**, *108*, 943.
[26] A. Yoshikawa, S. Matsika, *Chem. Phys.* **2008**, *347*, 393–404.
[27] C. Janzen, D. Spangenberg, W. Roth, K. Kleinermanns, *J. Chem. Phys.* **1999**, *110*, 9898–9907.
[28] K. Kleinermanns, C. Janzen, D. Spangenberg, M. Gerhards, *J. Phys. Chem. A* **1999**, *103*, 5232–5239.
[29] S. Perun, A. Sobolewski, W. Domcke, *J. Phys. Chem. A* **2006**, *110*, 13238.
[30] S. Matsika, *J. Phys. Chem. A* **2005**, *109*, 7538.
[31] M. Merchán, R. González-Luque, T. Climent, L. Serrano-Andrés, E. Rodríguez, M. Reguero, D. Peláez, *Chem. Phys. Lett.* **2006**, *110*, 26471.
[32] J.-M. L. Pecourt, J. Peon, B. Kohler, *J. Am. Chem. Soc.* **2001**, *123*, 10370–10378.
[33] R. Ahlrichs, M. Bär, M. Häser, H. Horn, C. Kölmel, *Chem. Phys. Lett.* **1989**, *162*, 165–169.

[34] MOLPRO *Version 2006.1, a package of ab initio programs*, H.-J. Werner, P. J. Knowles, R. Lindh, F. R. Manby, M. Schütz, P. Celani, T. Korona, G. Rauhut, R. D. Amos, A. Bernhardsson, A. Berning, D. L. Cooper, M. J. O. Deegan, A. J. Dobbyn, F. Ecker, C. Hampel, G. Hetzer, A. W. Lloyd, S. J. McNicholas, W. Mayer, M. E. Mura, A. Nicklass, P. Palmieri, R. Pitzer, U. Schumann, H. Stoll, A. J. Stone, R. Tarroni, T. Thorsteinsson, http://www.molpro.net **2006**.
[35] C. Hättig, F. Weigend, *J. Chem. Phys.* **2000**, *113*, 5154.
[36] C. Hättig, A. Köhn, *J. Chem. Phys.* **2002**, *117*, 6939.
[37] C. Hättig, *J. Chem. Phys.* **2003**, *118*, 7751.
[38] T. Fleig, S. Knecht, C. Hättig, *J. Phys. Chem. A* **2007**, *111*, 5482.
[39] H.-J. Werner, P. J. Knowles, *J. Chem. Phys.* **1985**, *82*, 5053.
[40] P. J. Knowles, H.-J. Werner, *Chem. Phys. Lett.* **1985**, *115*, 259.
[41] P. Celani, H.-J. Werner, *J. Chem. Phys.* **2000**, *112*, 5546.
[42] W. Hehre, R. Ditchfield, J. Pople, *J. Chem. Phys.* **1972**, *56*, 2257.

Received: February 26, 2008
Published online on July 11, 2008

CHEMPHYSCHEM

Supporting Information

Supplementary Material

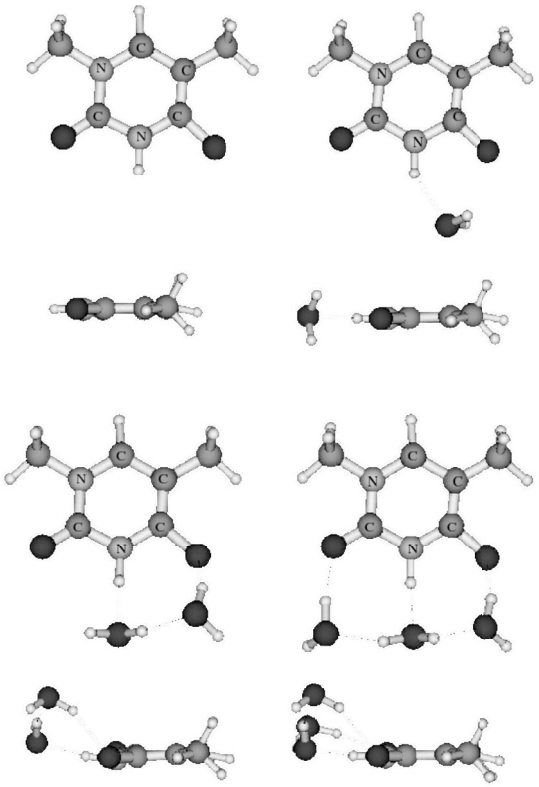

Figure 9: Geometry of the $^1n\pi^*$ state of 1MT and 1MT-water clusters optimized at the CC2/cc-pVDZ level.

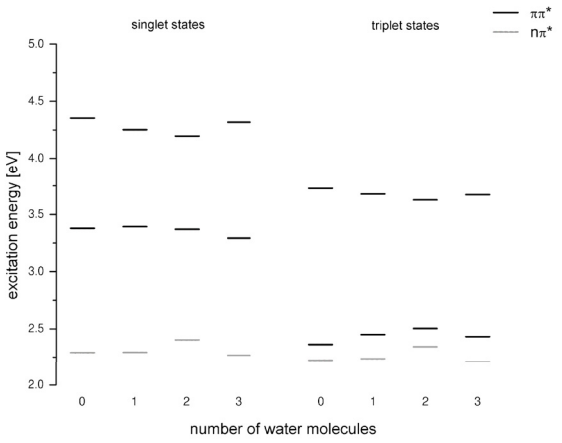

Figure 10: Vertical electronic excitation energies calculated at the geometry of the ^{1}nπ^* state at CC2/aug-cc-pVTZ level (the three lowest states). All structures are optimized at the CC2/cc-pVDZ level.

Paper 2

Intersystem Crossing and Characterization of Dark States in the Pyrimidine Nucleobases Uracil, Thymine, and 1-Methylthymine

Mihajlo Etinski, Timo Fleig, and Christel M. Marian

J. Phys. Chem. A **113**, (2009) 11809-11816

Intersystem Crossing and Characterization of Dark States in the Pyrimidine Nucleobases Uracil, Thymine, and 1-Methylthymine†

Mihajlo Etinski,‡ Timo Fleig,‡,§ and Christel M. Marian*,‡

Institute of Theoretical and Computational Chemistry, Heinrich Heine University Düsseldorf, Düsseldorf, Germany

Received: March 31, 2009; Revised Manuscript Received: July 10, 2009

The ground and low-lying excited states of the pyrimidine nucleo bases uracil, thymine, and 1-methylthymine have been characterized using ab initio coupled-cluster with approximate doubles (CC2) and a combination of density functional theory (DFT) and semiempirical multireference configuration interaction (MRCI) methods. Intersystem crossing rate constants have been determined perturbationally by employing a nonempirical one-center mean-field approximation to the Breit−Pauli spin−orbit operator for the computation of electronic coupling matrix elements. Our results clearly indicate that the $S_2(^1\pi\rightarrow\pi^*)$ ⇝ $T_2(^3n\rightarrow\pi^*)$ process cannot compete with the subpicosecond decay of the S_2 population due to spin-allowed nonradiative transitions, whereas the $T_1(^3\pi\rightarrow\pi^*)$ state is populated from the intermediate $S_1(^1n\rightarrow\pi^*)$ state on a subnanosecond time scale. Hence, it is very unlikely that the $S_1(^1n\rightarrow\pi^*)$ state corresponds to the long-lived dark state observed in the gas phase.

Introduction

The most significant photophysical property of the pyrimidine nucleo bases is their ultrafast decay to the ground state after UV irradiation,[1] both in the gas phase[2−6] and in solution.[7−11] It is agreed nowadays that this behavior is a consequence of energetically low-lying conical intersections and the concomitant strong nonadiabatic coupling between the primarily excited $^1\pi \rightarrow \pi^*$ state, the lowest $^1n \rightarrow \pi^*$ state, and the electronic ground state.[10,12−21]

Despite the ultrafast relaxation of the majority of the nucleobases, photochemical dimerization of the pyrimidine bases[22,23] is an abundant photolesion of the DNA after UV irradiation. For a long time, the mechanisms of the dimerization reactions, i.e., the formation of a cyclobutane dimer, (6−4) photoproduct, or the spore photoproduct, were believed to proceed via a transient triplet state.[24] Recently, indications were presented, however, that the thymine dimerization is an ultrafast process.[25−27] This finding does not exclude the participation of a triplet mechanism. Rather, quantum chemical studies[28−31] were able to show that two mechanisms exist: A concerted (one-step) cyclobutane formation on an excited singlet potential energy hypersurface (PEH) and a two-step ring-closure on the lowest triplet PEH.

Gas-phase experiments often can give detailed information about energy levels and relaxation dynamics. Vapor spectra of some pyrimidine bases were recorded long ago,[32] but the absorption bands were found to be broad and structureless. Vibrationally resolved electronic excitation of gaseous thymine using electron energy loss (EEL) techniques was reported,[33] revealing the absorption maxima of various singlet transitions. Furthermore, a band in the low energy regime was attributed to the lowest triplet state (T_1). However, uracil and thymine do not have sharp resonance-enhanced multiphoton ionization (REMPI) spectra.[34] Femtosecond time-resolved experiments in supersonic jets revealed that the decay signal from the first bright state of uracil and thymine exhibits a multiexponential behavior that represents different relaxation channels.[2,3,5] On the basis of quantum molecular dynamics simulations Hudock et al.[19] attributed the femtosecond component to the relaxation from the Franck−Condon (FC) region to the minimum of the $^1\pi \rightarrow \pi^*$ state. Their calculations suggest that the ionization potential increases substantially along this relaxation pathway, thus explaining the lack of REMPI spectra. The picosecond component was assigned to the process of crossing the barrier connecting the minimum of the $^1\pi \rightarrow \pi^*$ potential energy surface to the conical intersection between the $^1\pi \rightarrow \pi^*$ (S_2) and $^1n \rightarrow \pi^*$ (S_1) states. Other authors presented different interpretations of the multiexponential decay process. Lan et al.[21] using semiempirical surface-hopping molecular dynamics propose a two-step relaxation mechanism for uracil and thymine with a $^1\pi \rightarrow \pi^*$ (S2) ⇝ $^1n \rightarrow \pi^*$ (S_1) deexcitation on the femtosecond time scale and a subsequent internal conversion (IC) of the S_1 state to the electronic ground state on the picosecond time scale. In addition, these authors find a small contribution from trajectories of a direct decay of the $^1\pi \rightarrow \pi^*$ state to the ground state. Conical intersections between the S_2/S_1, the S_2/S_0, and the S_1/S_0 states of uracil and thymine were also located in numerous steady-state quantum chemical investigations.[10,12,14−18,35]

Interestingly, nanosecond time-resolved experiments in the gas phase found indications for a long-lived dark state in methylated uracils and thymines.[36−38] Kong and co-workers[36,37] found its lifetime to vary from a few tens to hundreds of nanoseconds depending on the degree of methylation and the energy of the initial excitation. They showed that methylation stabilizes the dark state whereas it is quenched by microhydration. In contrast, recently Busker et al.[38] observed the dark state also in microhydrated 1-methylthymine. Both groups characterized the dark state as $^1n \rightarrow \pi^*$.

In the condensed phase, Hare et al.,[11,39] using femtosecond transient absorption techniques, found two decay channels from the primarily excited $^1\pi \rightarrow \pi^*$ state, i.e., direct IC to the ground

† Part of the "Walter Thiel Festschrift".

* Corresponding author. E-mail: Christel.Marian@uni-duesseldorf.de.
‡ HHU Düsseldorf.
§ Current address: IRSAMC, Université Paul Sabatier, Toulouse, France.

10.1021/jp902944a CCC: $40.75
Published on Web 08/11/2009

state and decay to the $^1n \rightarrow \pi^*$ state, which was also proposed as a gateway for the triplet-state population. In a later study, Hare et al.[40] used time-resolved infrared (TRIR) spectroscopy in the excited state and comparison with a simulated S_0-T_1 spectrum to identify the long-lived dark state. They concluded that the triplet state is formed within 10 ps after excitation and that the vibrationally relaxed $^1n \rightarrow \pi^*$ state is not the precursor for the triplet formation. The triplet quantum yield φ_T ranges from 0.02 in water up to 0.54 in ethylacetate for 1-cyclohexyluracil.[39] The general trend is that φ_T increases going from polar protic solvents to nonpolar solvents.

Serrano-Andrés and co-workers performed quantum chemical calculations on the isolated pyrimidine bases to explain how the lowest triplet state $^3\pi \rightarrow \pi^*$ is formed in uracil[41] and thymine.[42] In essence, they propose three pathways for populating the $^3\pi \rightarrow \pi^*$ state from the initially excited $^1\pi \rightarrow \pi^*$ state. The first one proceeds via the intermediate $^3n \rightarrow \pi^*$ state whereas the second is a direct intersystem transition $^1\pi \rightarrow \pi^* \rightsquigarrow {}^3\pi \rightarrow \pi^*$ at the intersection of the latter potential energy surfaces. The third mechanism includes IC to the $^1n \rightarrow \pi^*$ state followed by intersystem crossing (ISC) to the $^3\pi \rightarrow \pi^*$ state. In all cases electronic spin−orbit coupling matrix elements (SOMEs) were found to be sizable. It is well-known, however, that large electronic spin−orbit coupling does not automatically bring about high ISC rates, because the latter depend crucially on the vibrational overlaps of the initial and final states.[43]

Understanding the nature of the dark state is an important issue because it can reveal how various photoproducts are formed. The purpose of the present study is to characterize the experimentally observed long-lived dark state of uracil, thymine and 1-methylthymine.[27,36−40] The paper is organized as follows: In the next section we summarize computational methods and basis sets that were used for our calculations. In the subsequent section we present ground- and excited-state structures, vibrational frequencies, and vertical and adiabatic electronic excitation energies. Furthermore, various paths for ISC are investigated and related rates are determined. Finally, we discuss the results and draw conclusions from our study.

Theoretical Methods and Computational Details

We employed the following electronic structure methods: coupled-cluster with approximate treatment of doubles (CC2), density functional theory (DFT) and the combined density functional theory/multireference configuration interaction (DFT/MRCI) approach. The CC2 method[44] is an approximation to the coupled-cluster singles and doubles (CCSD) method where the singles equations are retained in the original form and the doubles equations are truncated to first order in the fluctuating potential. We used the resolution-of-identity (RI)[45] CC2 implementation in TURBOMOLE[46] for the ground state[47] and in combination with linear response theory for excited-state optimizations,[48] vertical excitation energies and the calculation of properties.[49] We utilized DFT, unrestricted DFT (UDFT), and time-dependent DFT (TDDFT)[50] with the B3-LYP[51] functional implementation of TURBOMOLE[52] for ground-state and excited-state optimizations. The SNF[53] program was employed for numerical calculations of vibrational frequencies in harmonic approximation. In the DFT/MRCI method[54] dynamic electronic correlations are taken mainly into account by DFT. Static electronic correlations are obtained from multireference configuration interaction expansions employing a one-particle basis of BH-LYP Kohn−Sham molecular orbitals.[55,56] Double-counting of dynamic electron correlation is avoided by extensive configuration selection. In all electronic structure calculations only valence electrons were correlated.

We used Dunning's[57,58] correlation-consistent basis sets cc-pVDZ (C, N, O, 9s4p1d/3s2p1d; H, 4s1p/2s1p) and aug-cc-pVTZ (C, N, O, 11s6p3d2f/5s4p3d2f; H, 6s3p2d/4s3p2d) and the standard TZVP (C, N, O, 10s6p1d/4s3p1d; H, 5s1p/3s1p) basis sets from the TURBOMOLE library.[59] Auxiliary basis sets for the RI approximation of the two-electron integrals in the CC2 and MRCI treatments were taken from the TURBOMOLE library.[60,61]

SOMEs were evaluated for DFT/MRCI electronic wave functions using SPOCK.[62] Herein a one-center mean-field approximation to the Breit−Pauli Hamiltonian is employed.[63,64] This approximation typically reproduces results within 5% of the full treatment.[65,66] ISC rates were calculated using the methods described in detail elsewhere.[67,68] If not stated otherwise, we made use of the Condon approximation employing a constant electronic SOME evaluated at the minimum of the initial state multiplied by FC factors. For intercombination transitions of the type $^1\pi \rightarrow \pi^* \rightsquigarrow {}^3\pi \rightarrow \pi^*$, earlier work in our laboratory[67,68] had shown that it is necessary to go beyond the Condon approximation. In these cases, a Herzberg−Teller (HT) like expansion up to first order in the normal coordinates was carried out. To obtain ISC rates, matrix elements were calculated between the $\upsilon = 0$ vibrational wave function of the initial electronic state and vibrational wave functions of the final electronic state with energies in a small interval of width 2η. In test calculations, values of η ranged from 0.001 to 10 cm^{-1}. For the final ISC rates, interval widths between 0.001 and 0.01 cm^{-1} were chosen.

Results and Discussion

Ground-State Geometries and Vertical Excitation Energies. The ground-state equilibrium structures of uracil, thymine, and 1-methylthymine were optimized using the B3-LYP/DFT/TZVP and RI-CC2/cc-pVDZ levels of computation. Bond lengths obtained with these two methods are presented in Figures 1−3. As a general trend, the B3-LYP/DFT/TZVP equilibrium bond distances are somewhat shorter than the corresponding RI-CC2/cc-pVDZ values. Comparison of our RI-CC2/cc-pVDZ optimized geometries for uracil and thymine with the benchmark RI-CC2 calculations by Fleig et al.[69] reveals that improvement of the basis set leads to a slight bond contraction. The best values in that work (aug-cc-pVTZ/CC2 for thymine and aug-cc-pVQZ/CC2 for uracil) are essentially exact in comparison with experiment.[70] It should be kept in mind, however, that the X-ray structural parameters for uracil[70] were determined in the crystalline state that contains hydrogen-bonded uracil dimers. A more appropriate comparison with experimental values is possible for thymine where gas-phase electron diffraction and microwave data are available.[71] The experimentally derived bond lengths are displayed in Figure 2 in square brackets. Comparison with our B3-LYP/DFT/TZVP optimized values (given in parentheses) and RI-CC2/cc-pVDZ parameters (plain numbers) yields overall good agreement for the single bonds and shows that the DFT results for the lengths of the double bonds are closer to experiment, at least for the electronic ground state.

Computed vibrational spectra associated with the electronic ground state and available gas-phase spectral data are given in Tables S1, S7, and S11 of the Supporting Information. With the exception of a peak at 1897 cm^{-1} and a shoulder at 1356 cm^{-1} all peaks in the experimental gas-phase spectrum of uracil[72] in the mid-infrared region can be assigned unambiguously. Also for the thymine bands of very strong, strong, and medium intensity, a one-to-one correspondence between experiment[72] and theory can be established. In the wavenumber region below

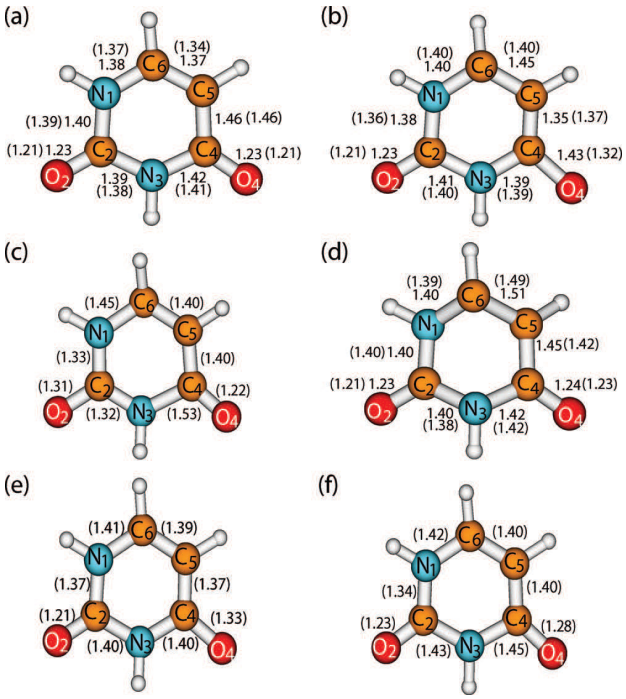

Figure 1. Stationary points of ground and excited-state PEHs of uracil, optimized at the RI-CC2/cc-pVDZ (B3-LYP/DFT/TZVP) levels: (a) ground-state minimum; (b) $S_1(n\rightarrow\pi^*)$ minimum; (c) saddle point structure of $S_2(\pi\rightarrow\pi^*)$ with one imaginary frequency; (d) $T_1(\pi\rightarrow\pi^*)$ minimum; (e) $T_2(n\rightarrow\pi^*)$ minimum; (f) $T_3(\pi\rightarrow\pi^*)$ minimum. All bond lengths are in Å.

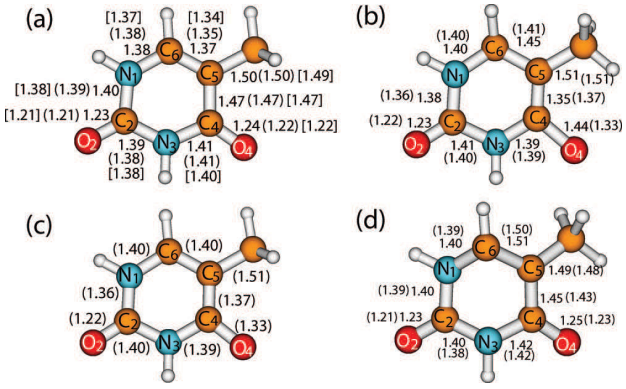

Figure 2. Stationary points of ground and excited-state PEHs of thymine, optimized at the RI-CC2/cc-pVDZ (B3-LYP/DFT/TZVP) levels: (a) ground-state minimum; (b) $S_1(n\rightarrow\pi^*)$ minimum with 60° rotated methyl group (it represents the global minimum at the RI-CC2/cc-pVDZ level whereas it is a local minimum at the B3-LYP/UDFT/TZVP level); (c) S_1-state global minimum structure obtained at the B3-LYP/UDFT/TZVP level; (d) T_1 $(\pi\rightarrow\pi^*)$ minimum. Experimental bond lengths[71] are displayed in square brackets. All bond lengths are in Å.

1000 cm^{-1}, however, calculated and measured intensities do not match well in several cases, most certainly because the harmonic approximation is too crude for soft modes. For more details see the Supporting Information.

Vertical electronic excitation energies of the lowest excited singlet and triplet states are compiled in Table 1. The S_1 state exhibits $n \rightarrow \pi^*$ character in the FC region of all three compounds whereas the first optically bright band originates from a transition to the $S_2(\pi\rightarrow\pi^*)$ state. Three triplet states are found energetically below or at least close to the S_2 state. To give a comprehensive overview over the excitation energies obtained with various quantum chemical methods and basis sets is far beyond the purpose of the present work. Suffice it to say that the orders of singlet states are identical in most of the recent theoretical works,[10,12,14−19,21,35,38,41,69,73−79] whereas the actual energy gaps vary considerably. For a comparison with our results in Table 1 we picked only a few studies that used either the same methods or basis sets.

Comparing the spectra of the three compounds for a fixed combination of method and basis set, one sees that the excitation energies of the $n \rightarrow \pi^*$ states are nearly constant whereas a marked stabilization is observed for the $S_2(\pi\rightarrow\pi^*)$ state when proceeding from uracil over thymine (=5-methyluracil) to 1-methylthymine (=1,5-dimethyluracil). A similar but less pronounced effect is found for the T_1 state. The methylation effect can be explained by the differential impact of the electron-donating methyl group that affects π orbitals (ring, delocalized) more strongly than an n orbital (which is much more localized). The magnitude of the effect in substituted uracils is, indeed, remarkable. Ongoing theoretical investigations on 1-methyl-uracil, an isomer of thymine, and 1,3-dimethyluracil, an isomer of 1-methylthymine, show that these species exhibit different electronic spectra and that the observed shifts are not artifacts of a basis set superposition error.[80]

Augmentation of the basis set at a fixed nuclear geometry lowers the CC2 excitation energies. Again, the energies of the S_2 states take the largest advantage from the improvement of the basis set. This is in line with an observation relating to CASSCF and CASPT2 excitation energies of the nucleobases[16,41,74] from which it is well-known that dynamic electron correlation effects are significantly larger for the $^1\pi \rightarrow \pi^*$ excitations than for $^1n \rightarrow \pi^*$ or triplet states. On the other hand, changing the nuclear geometry from the RI-CC2/cc-pVDZ to the B3-LYP/DFT/TZVP optimized structure while keeping the correlation method and basis set constant, leads to a nearly uniform blue shift of the $n \rightarrow \pi^*$ and $\pi \rightarrow \pi^*$ excitation energies by 0.12−0.14 eV. The geometry effect can be rationalized on the basis of bond length changes. In both, the $n \rightarrow \pi^*$ and the $\pi \rightarrow \pi^*$ states, the C_5-C_6 and the C−O double bonds are markedly extended at equilibrium (see next paragraph). The CC2- and MP2-optimized geometry parameters thus yield lower excitation energies with respect to the electronic ground state. DFT/MRCI gives larger gaps between the first two excited singlet states than the CC2 method. Also, it generally gives lower triplet-state excitation energies. Only a few experimental gas-phase data are available for comparison. It appears that the observed band maxima of the $S_2 \leftarrow S_0$ transitions in uracil and thymine are located at longer wavelengths than the vertical excitation wavelengths in the calculations.

Excited-State Properties. For uracil, we optimized the nuclear arrangements of the first two excited singlet states and the three lowest-lying triplet states. In the case of the methylated compounds, we searched only for the minimum structures of the respective S_1 and T_1 states. Bond lengths of the optimized excited-state structures are displayed in Figures 1−3. Adiabatic excitation energies are collected in Table 2 together with results of previous theoretical work.[41,42,81] Nuclear coordinates and harmonic vibrational frequencies of all optimized structures are provided in the Supporting Information.

The most outstanding characteristic of the nearly planar $S_1(n\rightarrow\pi^*)$ geometry is that the C_4-O_4 bond is significantly elongated compared to the C_2-O_2 bond by 0.20 Å (RI-CC2) or 0.11 Å (DFT). Since there are no experimental nuclear geometry data available for the S_1 state, it can presently not be decided which C_4-O_4 bond length is more realistic. Ab initio

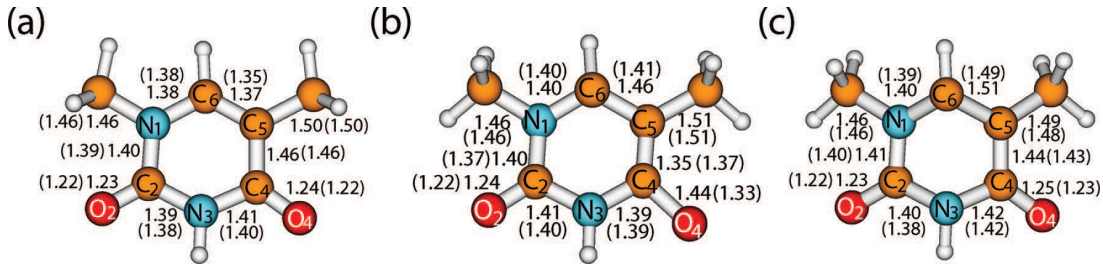

Figure 3. Minimum nuclear arrangements of 1-methylthymine optimized at the RI-CC2/cc-pVDZ (B3-LYP/DFT/TZVP) levels: (a) ground-state minimum; (b) $S_1(n\rightarrow\pi^*)$ minimum; (c) $T_1(\pi\rightarrow\pi^*)$ minimum. All bond lengths are in Å.

CASSCF[15] and MRCI singles[17] results using comparable basis sets as well as the semiempirical OM2-MRCI values[21] are much closer to the TDDFT values. RI-CC2 yields a minimum structure with the methyl group rotated by 60° with respect to the ground state (Figure 2b). This nuclear arrangement represents also a local minimum on the TDDFT PEH, the global minimum of which is found for the same orientation of the methyl group as in the ground state (Figure 2c). The subsequent DFT/MRCI calculations reverse the energetic order of these two minima. Thus, the structure displayed in Figure 2b is considered to be the global minimum at the DFT/MRCI level, too. In 1-methylthymine, both methyl groups are rotated by 60° with respect to the ground-state structure. Vibrational spectra in harmonic approximation associated with the S_1 states are given in Tables S2, S8, and S12 of the Supporting Information. In line with the larger geometry change, the energy release upon relaxation of the nuclear arrangement in the S_1 state is larger at the RI-CC2 level. Despite their considerably higher vertical absorption energies, the adiabatic excitation energies of the S_1 states of uracil, thymine, and 1-methylthymine are lower at the RI-CC2 level than the corresponding DFT/MRCI values (Table 2).

At the RI-CC2/cc-pVDZ level of calculation, stationary points for the S_2 states of the three compounds could not be located. When the planarity constraint is lifted, continued root flipping between the lowest $^1\pi\rightarrow\pi^*$ and $^1n\rightarrow\pi^*$ states occurs after a few steps of initial energy relaxation, indicating a nearby intersection of the corresponding PEHs. A similar behavior was reported by other authors.[15] The existence of a true S_2 equilibrium structure is discussed controversially in the literature.[15−17,19,21] It appears that the barrier separating the S_2 minimum from the conical intersection region diminishes upon inclusion of dynamic electron correlation. At the B3-LYP/TDDFT/TZVP level we obtained a first-order saddle point for the S_2 state of uracil. The imaginary frequency (ν = i59 cm^{-1}) is associated with a puckering mode that exhibits the largest amplitude for a pyramidalization at the N_3 center. The saddle point exhibits an almost planar geometry with the H atom attached to C_6 pointing out of plane. Compared to the ground-state geometry, the most significant bond length changes occur in the ring bonds (see Figure 1). In addition, the C_2-O_2 bond is markedly elongated, in good agreement with recent CASSCF results by Perun et al.[15] and MRCI singles results by Yoshikawa and Matsika,[17] but at variance with the CASSCF and CASPT2 optimized structures by Hudock et al.[19] Note that a single-point DFT/MRCI calculation, carried out at the saddle-point structure, yields a substantially higher excitation energy of the S_2 state (5.25 eV) than at the T_1 minimum geometry (5.01 eV).

The T_1 state results from a HOMO → LUMO excitation and exhibits $\pi\rightarrow\pi^*$ character. The geometry is slightly butterfly shaped where the CC2 optimized structure is more folded compared to the UDFT geometry. The most significant bond length change with respect to the ground-state geometry parameters occurs for the C_5-C_6 bond that is elongated by about 0.15 Å. At the B3-LYP/UDFT/TZVP and CC2/cc-pVDZ levels, the minimum is found for a structure with the methyl group rotated by 60°. In 1-methylthymine, both methyl groups are rotated with respect to the ground-state structure but have the same orientation as in the S_1 state. The adiabatic excitation energies, computed at the DFT/MRCI level, are somewhat lower than those obtained at the RI-CC2 level (see Table 2). Harmonic frequencies are given in Tables S4, S10, and S13 of the Supporting Information.

In principle, TRIR spectroscopy in the excited state can be used to identify the long-lived dark state. Such measurements were conducted by Hare et al.[40] for thymine in argon-purged deuterated acetonitrile. They monitored in particular the shifts in the C═O stretching frequencies upon electronic excitation and concluded that the transient species is the T_1 state. However, as will be outlined in more detail in the Supporting Information, the assignment of the dark state based on the shifts of the C═O stretching frequencies is not conclusive, since the simulated S_0-T_1 and S_0-S_1 difference spectra look very similar in that wavenumber region (Figure S1 of the Supporting Information). Characteristic of the S_0-T_1 difference spectrum are a peak near 1500 cm^{-1} that results from a combination of the C_4═C_5 stretching and the N_1H wagging motions and a peak near 1350 cm^{-1} that arises from a ring deformation vibration. Particularly the S_0-T_1 spectrum computed at the RI-CC2 level reproduces all experimental features excellently whereas significant deviations are noticed for the low-frequency region of the simulated S_0-S_1 spectrum. We are therefore confident that the TRIR spectrum observed by Hare et al.[40] stems from the transient T_1 state of thymine and not from the S_1 state.

The T_2 state has $n\rightarrow\pi^*$ character. As may be expected, its minimum geometry parameters are nearly indistinguishable from those of the corresponding singlet state (S_1) and the singlet−triplet splitting of the $n\rightarrow\pi^*$ states is rather small. The T_3 state originates from a single excitation of an electron from a π orbital that is located mainly at the two oxygen atoms and the intermediate N_3 atom to the LUMO. Its minimum is located energetically below the lowest point of the S_2 state and is thus of interest for ISC processes. Also this state exhibits a planar minimum geometry.

Intersystem Crossings. For uracil, transition rates for three different nonradiative singlet−triplet pathways were calculated:

(a) $S_1(^1n\rightarrow\pi^*) \rightsquigarrow T_1(^3\pi\rightarrow\pi^*)$

(b) $S_2(^1\pi\rightarrow\pi^*) \rightsquigarrow T_2(^3n\rightarrow\pi^*)$

(c) $S_2(^1\pi\rightarrow\pi^*) \rightsquigarrow T_3(^3\pi\rightarrow\pi^*)$

For thymine and 1-methylthymine only pathway (a) was taken into consideration. Our methods do not allow us to compute ISC rates for vibrationally hot states. The dependence of the ISC dynamics on the excess energy in the S_1 state, as observed by Hare et al.[39] for 1-cyclohexyluracil, was therefore not investigated in the present work.

TABLE 1: Vertical Excitation Spectrum of Uracil, Thymine, and 1-Methylthymine at the Ground-State Geometry (eV)[a]

state	CC2/cc-pVDZ// CC2/cc-pVDZ	CC2/aug-cc-pVTZ// CC2/cc-pVDZ	CC2/aug-cc-pVTZ// B3-LYP/TZVP	DFT/MRCI/TZVP// B3-LYP/TZVP	CC2/TZVP// MP2/6-31G*[b]	DFT/MRCI/TZVP// MP2/6-31G*[c]	CC2/aug-cc-pVQZ// CC2/aug-cc-pVQZ[d]	experiment
				Uracil				
$S_1(n\rightarrow\pi^*)$	4.91	4.78	4.91	4.67	4.91	4.41	4.80	
$S_2(\pi\rightarrow\pi^*)$	5.54	5.25	5.38	5.56	5.52	5.33	5.35	5.08[e]
$T_1(\pi\rightarrow\pi^*)$	3.90	3.84	3.97	3.78			3.95	3.65[f]
$T_2(n\rightarrow\pi^*)$	4.66	4.58	4.70	4.46			4.60	
$T_3(\pi\rightarrow\pi^*)$	5.44		5.50	5.16			5.42	
				Thymine				
$S_1(n\rightarrow\pi^*)$	4.96	4.80	4.94	4.59	4.94	4.48	4.82	
$S_2(\pi\rightarrow\pi^*)$	5.44	5.12	5.25	5.26	5.39	5.18	5.20	4.80,[g] 4.95[h]
$T_1(\pi\rightarrow\pi^*)$	3.82	3.72	3.86	3.54			3.82	3.60[h]
$T_2(n\rightarrow\pi^*)$	4.70	4.59	4.73	4.37			4.61	
$T_3(\pi\rightarrow\pi^*)$	5.43			4.98			5.39	
				1-Methylthymine				
$S_1(n\rightarrow\pi^*)$	4.96	4.78[i]	4.92	4.59				
$S_2(\pi\rightarrow\pi^*)$	5.23	4.88[i]	5.01	5.10				
$T_1(\pi\rightarrow\pi^*)$	3.76	3.64[i]	3.78	3.46				
$T_2(n\rightarrow\pi^*)$	4.72	4.59[i]	4.72	4.38				
$T_3(\pi\rightarrow\pi^*)$	5.37	5.24[i]		4.91				

[a] Method used for calculation of vertical spectrum//method used for geometry optimization of the ground state. [b] Schreiber et al.[78] [c] Silva-Junior et al.[79] [d] Fleig et al.[69] [e] Vapor spectrum, Clark et al.[32] [f] Electron energy loss specroscopy, Abouaf et al., cited as private communication in ref 81. [g] Gas-phase absorption of 1,3-methyluracil, Clark et al.[32] [h] Electron energy loss specroscopy, Abouaf et al.[33] [i] Busker et al.[38]

In the Condon approximation, electronic SOMEs for a pair of states are required only at a single geometry $\mathbf{q_0}$, about which the Taylor series of the interaction is expanded. Typically, the equilibrium geometry of the initial state is chosen as offset for the Taylor expansion. We made this choice for process a whereas in cases b and c the saddle point of the primarily excited $^1\pi\rightarrow\pi^*$ state was used due to the absence of a true minimum geometry. Furthermore, for computing the FC and HT matrix elements of the zero-point vibrational level of the S_2 state the harmonic frequency of the imaginary mode was set to $+100$ cm^{-1}.

In Table 3, SOMEs computed at the respective S_1 minima are collected. They are large, agreeing with recent theoretical work of Serrano-Pérez et al.[42] but contradicting the conclusions drawn by Hare et al.[39] who predicted that the relaxed $^1n\rightarrow\pi^*$ state has negligible spin−orbit coupling with the $^3\pi\rightarrow\pi^*$ state. The Cartesian components of the electronic SOMEs depend on the molecular orientation in a space-fixed coordinate system. In the Condon approximation it is sufficient to use the sum over the squared electronic matrix elements of the components (given as additional entries in Table 3) for randomly oriented molecules in the gas phase or in solution. These sums vary only slightly when proceeding from uracil to thymine and 1-methylthymine.

Calculated $S_1 \rightsquigarrow T_1$ ISC rates are shown in Table 4. Although the electronic coupling strengths are nearly identical at the RI-CC2 and TDDFT optimized geometries, the resulting rates differ by a factor of about 25 for uracil and by up to 2 orders of magnitude for thymine. At first sight, this is counterintuitive since the S_1/T_1 energy gaps are smaller in the CC2 case. For the smallest of the three systems, uracil, therefore, a series of calculations was carried out, testing—among other parameters—the dependence of the ISC rates on the electronic energy difference between the pair of coupling states. Interestingly, the computed ISC rate increases dramatically (by nearly 3 orders of magnitude) when the energy gap is varied from 4000 to 8000 cm^{-1} where a maximum evolves (see Table S17, Supporting Information, for further details). This strange behavior results from a trade-off between the vibrational density of states and the overlap of the vibrational wave functions. Using the DFT-optimized potentials shifted vertically to match the adiabatic energy difference of the RI-CC2 method (5150 cm^{-1}) yields an ISC rate of 1.4×10^{11} s^{-1}, somewhat smaller than the value (2.3×10^{11} s^{-1}) computed with the DFT/MRCI method but in the same ballpark. We interpret the much lower ISC rate (0.9×10^{10} s^{-1}) calculated for the RI-CC2 potentials as being caused mainly by a larger coordinate displacement and concomitant smaller vibrational overlap. Nevertheless, even with these uncertainties the lifetime of the S_1 state with respect to this ISC process (5−100 ps) is significantly shorter than the lifetime of the dark state in the gas-phase experiments, ranging from about 20 to 200 ns depending on the methylation and the laser excitation energy.[36−38] The calculated $S_1 \rightsquigarrow T_1$ ISC rates of thymine and 1-methylthymine are somewhat smaller than those of the corresponding process in uracil, but the order of magnitude is conserved.

To gain further insight, we calculated a linearly interpolated path between the UDFT-optimized T_1 geometry (RC = 0) of uracil and the TDDFT-optimized S_1 minimum (RC = 1.0) and extended this path on both sides. This energy profile (Figure 4) shows a crossing between the shallow PEH of the primarily excited $S_2(\pi\rightarrow\pi^*)$ state and the $S_1(n\rightarrow\pi^*)$ state in the neighborhood of the T_1 (and presumably also the S_2) minimum nuclear geometry, in accord with the findings of previous theoretical work on uracil and thymine where a conical intersection is

TABLE 2: Adiabatic Excitation Energies of Uracil, Thymine, and 1-Methylthymine (eV)[a]

state	CC2/cc-pVDZ// CC2/cc-pVDZ	CC2/aug-cc-pVTZ// CC2/cc-pVDZ	DFT/MRCI/TZVP// B3-LYP/TZVP	B3-LYP/6-311++G(3df,2p)// B3-LYP/6-311++G(3df,2p)[b]	CASPT2/ANO-S// CASSCF(14,10)/ANO-S[c]
			Uracil		
$S_1(n\rightarrow\pi^*)$	3.88	3.74	3.96		4.03
$S_2(\pi\rightarrow\pi^*)$			(5.01)[d]		4.48
$T_1(\pi\rightarrow\pi^*)$	3.24	3.31	3.13	3.02	3.15
$T_2(n\rightarrow\pi^*)$			3.84		3.91
$T_3(\pi\rightarrow\pi^*)$			4.58		
			Thymine		
$S_1(n\rightarrow\pi^*)$	3.93	3.73	4.02		4.05
$T_1(\pi\rightarrow\pi^*)$	3.10	3.16	2.96	2.84	2.87
			1-Methylthymine		
$S_1(n\rightarrow\pi^*)$	3.89	3.73	4.03		
$T_1(\pi\rightarrow\pi^*)$	3.06	3.11	2.94		

[a] Method used for calculation of adiabatic energies//method used for geometry optimization of state. [b] Reference 81. [c] References 41 and 42. S_2 minimum of uracil was optimized at the CASPT2 level. [d] TDDFT saddle point; adiabatic energy at the T_1 minimum is displayed.

TABLE 3: Spin−Orbit Matrix Elements $\langle S_1|\hat{H}_{SO}|T_1\rangle$ (cm^{-1}) Calculated at the S_1-State Geometry[a]

component	DFT/MRCI/cc-pVDZ// RI-CC2/cc-pVDZ	DFT/MRCI/aug-cc-pVTZ// RI-CC2/cc-pVDZ	DFT/MRCI/TZVP// TDDFT B3-LYP/TZVP
		Uracil	
$\hat{H}_{SO,x}$	38.95	36.96	7.70
$\hat{H}_{SO,y}$	29.37	32.74	46.25
$\hat{H}_{SO,z}$	−3.39	4.71	−0.04
sum of squares	2391	2460	2198
		Thymine	
$\hat{H}_{SO,x}$	42.46	44.00	44.13
$\hat{H}_{SO,y}$	−20.59	−21.49	10.40
$\hat{H}_{SO,z}$	9.59	9.73	−0.62
sum of squares	2319	2493	2056
		1-Methylthymine	
$\hat{H}_{SO,x}$	−35.78	−36.96	44.75
$\hat{H}_{SO,y}$	−31.65	−32.73	−10.10
$\hat{H}_{SO,z}$	−4.68	4.71	−0.02
sum of squares	2304	2460	2110

[a] Method used for spin−orbit calculation//method used for geometry optimization of state.

TABLE 4: Calculated Rate Constants k_{ISC} (s^{-1}) for the (S_1 ⇝ T_1) ISC Channels in Uracil, Thymine, and 1-Methylthymine[a]

method[b]	ΔE^{ad}	k_{ISC}
Uracil		
RI-CC2/cc-pVTZ//RI-CC2/cc-pVTZ[c]	5150	0.93×10^{10}
DFT/MRCI/TZVP//DFT B3-LYP/TZVP[d]	6704	0.23×10^{12}
Thymine		
RI-CC2/cc-pVDZ//RI-CC2/cc-pVDZ[c]	6652	0.13×10^{10}
DFT/MRCI/TZVP//DFT B3-LYP/TZVP[e]	8426	0.11×10^{12}
1-Methylthymine		
RI-CC2/cc-pVDZ//RI-CC2/cc-pVDZ[e]	6724	0.49×10^{10}

[a] ΔE^{ad} (cm^{-1}) denotes the adiabatic electronic energy difference. [b] Method used for energy calculation//method used for geometry optimization. [c] Interval width of $\eta = 0.01$ cm^{-1} used. All vibrational modes were employed and 5 quanta per mode were allowed. DFT/MRCI/cc-pVDZ wave functions were employed for computing the SOMEs. [d] Interval width of $\eta = 0.01$ cm^{-1} used. All vibrational modes were employed and an unlimited number of quanta per mode were allowed. [e] Interval width of $\eta = 0.001$ cm^{-1} used. All vibrational modes were employed and 3 quanta per mode were allowed.

reported in this area of the coordinate space.[10,12,14−19,21,35] In addition, we find an intersection between the $S_2(\pi\rightarrow\pi^*)$ and $T_3(\pi\rightarrow\pi^*)$ potential energy curves. The S_2 and T_1 potential energy profiles, on the other hand, run essentially parallel.

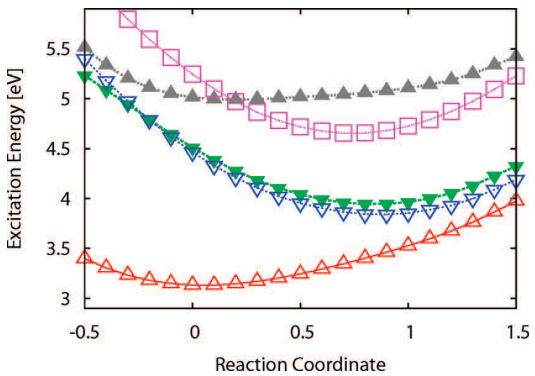

Figure 4. DFT/MRCI/TZVP single-point calculations along a linearly interpolated path between the UDFT-optimized T_1 geometry (RC = 0) of uracil and the TDDFT-optimized S_1 minimum (RC = 1.0) and extended on both sides. $T_1(\pi\rightarrow\pi^*)$: upright open triangles. $T_2(n\rightarrow\pi^*)$: upside down open triangles. $S_1(n\rightarrow\pi^*)$: upside down filled triangles. $T_3(\pi\rightarrow\pi^*)$: open squares. $S_2(\pi\rightarrow\pi^*)$: upright filled triangles.

Electronic SOMEs calculated at the S_2 saddle point are shown in Table 5. Spin−orbit coupling between the $S_2(\pi\rightarrow\pi^*)$ and $T_1(\pi\rightarrow\pi^*)$ states is found to be small as may be expected for two states with similar electronic structures. Moreover, the significant energy gap combined with a lack of substantial geometric shifts yields negligible FC factors for a radiationless transition between these states. A participation of this channel

TABLE 5: Spin−Orbit Matrix Elements (cm^{-1}) Calculated at the TDDFT Optimized S_2 Geometry of Uracil Using the DFT/MRCI/TZVP Method for Generating the Wave Function

$\langle S_2\|\hat{H}_{SO,x}\|T_1\rangle$	−0.59
$\langle S_2\|\hat{H}_{SO,y}\|T_1\rangle$	−0.73
$\langle S_2\|\hat{H}_{SO,z}\|T_1\rangle$	−0.01
sum of squares	<1
$\langle S_2\|\hat{H}_{SO,x}\|T_2\rangle$	−18.98
$\langle S_2\|\hat{H}_{SO,y}\|T_2\rangle$	12.47
$\langle S_2\|\hat{H}_{SO,z}\|T_2\rangle$	0.83
sum of squares	516
$\langle S_2\|\hat{H}_{SO,x}\|T_3\rangle$	−3.43
$\langle S_2\|\hat{H}_{SO,y}\|T_3\rangle$	0.78
$\langle S_2\|\hat{H}_{SO,z}\|T_3\rangle$	0.12
sum of squares	12

TABLE 6: Rate Constants k_{ISC} (s^{-1}) for the ($S_2 \rightsquigarrow T_2$) and ($S_2 \rightsquigarrow T_3$) ISC Channels in Uracil Calculated at the DFT/MRCI/TZVP//DFT B3-LYP/TZVP Level[a]

channel	ΔE^{ad}	approximation	k_{ISC}
($S_2 \rightsquigarrow T_2$)	11391	FC[b]	$\simeq 0.2 \times 10^{12}$
($S_2 \rightsquigarrow T_3$)	5355	FC[c]	0.32×10^{9}
($S_2 \rightsquigarrow T_3$)	5355	FC[c]+HT[d]	0.36×10^{9}

[a] ΔE^{ad} (cm^{-1}) denotes the adiabatic electronic energy difference. [b] Interval width of $\eta = 0.01$ cm^{-1} used. All vibrational modes were employed and 5 quanta per mode were allowed. An ISC rate of 0.16×10^{12} was obtained for an energy gap of 9000 cm^{-1}. The discrete summation over FC factors could not be carried out for an adiabatic energy difference as large as 11 391 cm^{-1}. [c] Interval width of $\eta = 0.01$ cm^{-1} used. All vibrational modes were employed and an unlimited number of quanta per mode were allowed. [d] Interval width of $\eta = 0.01$ cm^{-1} used. Derivative couplings for all vibrational modes were employed. The number of quanta per mode was limited to at most 1.

in the photophysics of uracil and its methylated derivatives can therefore be ruled out. Because of the admixture of $n \rightarrow \pi^*$ character into the $S_2(\pi\rightarrow\pi^*)$ wave function, the coupling matrix element with the $T_2(n\rightarrow\pi^*)$ state is somewhat reduced at this geometry whereas the $\langle S_2|\hat{H}_{SO}|T_3\rangle$ matrix elements are significantly larger than typical $^1\pi \rightarrow \pi^*/^3\pi \rightarrow \pi^*$ SOMEs that are obtained, e.g., for the S_2 and T_1 pair of states. Despite the intersection of the two PEHs, the rate constant for the $S_2 \rightsquigarrow T_3$ is rather small (Table 6), even if HT-like vibronic spin−orbit coupling is invoked. Only the ISC rate for the $S_2 \rightsquigarrow T_2$ transition is found to be substantial. It is of similar magnitude to the rate for the $S_1 \rightsquigarrow T_1$ channel. The presence or absence of a true $S_2(\pi\rightarrow\pi^*)$ minimum will have only minor influence on the ISC rate. However, it will have large impact on the rates for the spin-allowed decay processes of the S_2 population via close-by conical intersections. As long as these concurrent processes take place on a much faster time scale, the spin-forbidden $S_2 \rightsquigarrow T_2$ transition cannot compete.

Summary and Conclusion

We have studied the properties of the isolated nucleo bases uracil, thymine, and 1-methylthymine in their ground and low-lying excited states. Particular emphasis has been placed on vibrational spectra in the $T_1(^3\pi\rightarrow\pi^*)$ and $S_1(^1n\rightarrow\pi^*)$ states, since these data can be used to identify the nature of the long-lived dark state that had been observed in these pyrimidine bases.[27,36−40] We find two indications in favor of the assignment of this state to the $T_1(^3\pi\rightarrow\pi^*)$ state. The experimentally observed lifetimes of the dark state are at least 1000 times longer than our computed time constants for the $S_1 \rightsquigarrow T_1$ decay. We thus conclude that the S_1 is not a likely candidate for the dark state. Comparison of our calculated difference infrared spectra for the S_0-T_1 and S_0-S_1 states with experimental data of Hare et al.[40] clearly shows that the time-resolved infrared spectrum, recorded by these authors, is due to vibrational excitation in the $T_1(^3\pi\rightarrow\pi^*)$ state.

How is the triplet state formed? It is agreed in the literature that most of the excited-state population that is initially generated in the $S_2(^1\pi\rightarrow\pi^*)$ state decays on a subpicosecond time scale to the electronic ground state, either by a direct route or via the intermediate $S_1(^1n\rightarrow\pi^*)$ state.[1−21] Nevertheless, substantial triplet quantum yields are found in aprotic solvents.[24,39] In the present work we have investigated several pathways for singlet−triplet intersystem crossing. In agreement with earlier proposals,[11,39−42] we find two fast ISC channels for the population of the $T_1(^3\pi\rightarrow\pi^*)$ state: (a) A nonradiative transition from the intermediate $S_1(^1n\rightarrow\pi^*)$ state directly to the T_1 state and (b) a transition from the initially populated $S_2(^1\pi\rightarrow\pi^*)$ state to $T_2(^3n\rightarrow\pi^*)$ followed by internal conversion to the T_1 state. In both cases, our calculations yield time constants for the singlet−triplet transition on the order of 10 ps. Due to the presence of the ultrafast $S_2 \rightsquigarrow S_0$ and $S_2 \rightsquigarrow S_1$ decay channels, the spin-forbidden $S_2 \rightsquigarrow T_2$ transition is not competitive, however. Our results therefore support the $S_2 \rightsquigarrow S_1 \rightsquigarrow T_1$ mechanism proposed by Hare et al.[11,39] where the intermediate S_1 state serves as a gateway for the triplet formation in uracil and its methylated derivatives. The strong solvent dependence of the triplet quantum yield[24,39] could be a consequence of the relative probabilities for the $S_2 \rightsquigarrow S_0$ and $S_2 \rightsquigarrow S_1$ decay processes following the initial $S_2 \leftarrow S_0$ excitation. To derive a complete picture of all competing decay processes of the photoexcited pyrimidine bases will require dynamical studies that include nonadiabatic and spin−orbit coupling on the same footing.

Acknowledgment. Financial support of this project by the Deutsche Forschungsgemeinschaft (DFG) through SFB 663 is gratefully acknowledged.

Supporting Information Available: Harmonic vibrational frequencies and Cartesian coordinates of all stationary points, simulated S_0-T_1 and S_0-S_1 difference spectra and the dependence of the computed ISC rates on technical parameters. This material is available free of charge via the Internet at http://pubs.acs.org.

References and Notes

(1) Crespo-Hernández, C. E.; Cohen, B.; Hare, P. M.; Kohler, B. *Chem. Rev.* **2004**, *104*, 1977–2019.
(2) Kang, H.; Lee, K. T.; Jung, B.; Ko, Y. J.; Kim, S. K. *J. Am. Chem. Soc.* **2002**, *124*, 12958–12959.
(3) Ullrich, S.; Schultz, T.; Zgierski, M. Z.; Stolow, A. *Phys. Chem. Chem. Phys.* **2004**, *6*, 2796–2801.
(4) Samoylova, E.; Lippert, H.; Ullrich, S.; Hertel, I. V.; Radloff, W.; Schultz, T. *J. Am. Chem. Soc.* **2005**, *127*, 1782–1786.
(5) Canuel, C.; Mons, M.; Piuzzi, F.; Tardivel, B.; Dimicoli, I.; Elhanine, M. *J. Chem. Phys.* **2005**, *122*, 074316-1−074316-6.
(6) Schneider, M.; Maksimenka, R.; Buback, F. J.; Kitsopoulis, T.; Lago, L. R.; Fisher, I. *Phys. Chem. Chem. Phys.* **2006**, *8*, 3017–3021.
(7) Peon, J.; Zewail, A. H. *Chem. Phys. Lett.* **2001**, *348*, 255–262.
(8) Pecourt, J.-M. L.; Peon, J.; Kohler, B. *J. Am. Chem. Soc.* **2001**, *123*, 10370–10378.
(9) Gustavsson, T.; Sharonov, A.; Markovitsi, D. *Chem. Phys. Lett.* **2002**, *351*, 195–200.
(10) Gustavsson, T.; Bányász, A.; Lazzarotto, E.; Markovitsi, D.; Scalmani, G.; Frisch, M.; Barone, V.; Improta, R. *J. Am. Chem. Soc.* **2006**, *128*, 607–619.
(11) Hare, P. M.; Crespo-Hernández, C. E.; Kohler, B. *Proc. Natl. Acad. Sci. U.S.A.* **2007**, *104*, 435–440.

(12) Matsika, S. *J. Phys. Chem. A* **2004**, *108*, 7584–7590.
(13) Tomić, K.; Tatchen, J.; Marian, C. M. *J. Phys. Chem. A* **2005**, *109*, 8410–8418.
(14) Zgierski, M. Z.; Patchkovskii, S.; Fujiwara, T.; Lim, E. C. *J. Phys. Chem. A.* **2005**, *109*, 9384–9387.
(15) Perun, S.; Sobolewski, A. L.; Domcke, W. *J. Phys. Chem. A* **2006**, *110*, 13238–13244.
(16) Merchán, M.; González-Luque, R.; Climent, T.; Serrano-Andrés, L.; Rodríguez, E.; Reguero, M.; Peláez, D. *J. Phys. Chem. B* **2006**, *110*, 26471–26476.
(17) Yoshikawa, A.; Matsika, S. *Chem. Phys.* **2008**, *347*, 393–404.
(18) Zechmann, G.; Barbatti, M. *J. Phys. Chem. A* **2008**, *112*, 8273–8279.
(19) Hudock, H. R.; Levine, B. G.; Thompson, A. L.; Satzger, H.; Townsend, D.; Gador, N.; Ullrich, S.; Stolow, A.; Martínez, T. J. *J. Phys. Chem. A* **2007**, *111*, 8500–8508.
(20) Nieber, H.; Doltsinis, N. L. *Chem. Phys.* **2008**, *347*, 405–412.
(21) Lan, Z.; Fabiano, E.; Thiel, W. *J. Phys. Chem. B* **2009**, *113*, 3548–3555.
(22) Cadet, J.; Vigny, P. *Bioorganic Photochemistry*; Wiley: New York, 1990; Vol. 1, pp 1−272.
(23) Douki, T.; Cadet, J. *Photochem. Photobiol. Sci.* **2003**, *2*, 433–436.
(24) Bishop, S. M.; Malone, M.; Philips, D.; Parker, A. W.; Symons, M. C. R. *J. Chem. Soc., Chem. Commun.* **1994**, 871–872.
(25) Marguet, S.; Markovitsi, D. *J. Am. Chem. Soc.* **2005**, *127*, 5780–5781.
(26) Schreier, W. J.; Schrader, T. E.; Koller, F. O.; Gilch, P.; C. E.; Crespo-Hernández, V. N. S.; Carell, T.; Zinth, W.; Kohler, B. *Science* **2007**, *315*, 625–629.
(27) Kwok, W.-M.; Ma, C.; Phillips, D. L. *J. Am. Chem. Soc.* **2008**, *130*, 5131–5139.
(28) Zhang, R. B.; Eriksson, L. A. *J. Phys. Chem. B* **2006**, *110*, 7556–7562.
(29) Boggio-Pasqua, M.; Groenhof, G.; Schaefer, L. V.; Grubmueller, H.; Robb, M. A. *J. Am. Chem. Soc.* **2007**, *129*, 10996–10997.
(30) Blancafort, L.; Migani, A. *J. Am. Chem. Soc.* **2007**, *129*, 14540–14541.
(31) Roca-Sanjuan, D.; Olaso-González, G.; González-Ramirez, I.; Serrano-Andrés, L.; Merchán, M. *J. Am. Chem. Soc.* **2008**, *130*, 10768–10779.
(32) Clark, L. B.; Peschel, G. G.; Tinoco, I., Jr. *J. Phys. Chem.* **1965**, *69*, 3615–3618.
(33) Abouaf, R.; Pommier, J.; Dunet, H. *Chem. Phys. Lett.* **2003**, *381*, 486–494.
(34) Brady, B. B.; Peteanu, L. A.; Levy, D. H. *Chem. Phys. Lett.* **1988**, *147*, 538–543.
(35) Mercier, Y.; Santoro, F.; Reguero, M.; Improta, R. *J. Phys. Chem. B* **2008**, *112*, 10769–10772.
(36) He, Y.; Wu, C.; Kong, W. *J. Phys. Chem. A* **2003**, *107*, 5143–5148.
(37) He, Y.; Wu, C.; Kong, W. *J. Phys. Chem. A* **2004**, *108*, 943–949.
(38) Busker, M.; Nispel, M.; Häber, T.; Kleinermanns, K.; Etinski, M.; Fleig, T. *Chem. Phys. Chem.* **2008**, *9*, 1570–1577.
(39) Hare, P. M.; Crespo-Hernández, C. E.; Kohler, B. *J. Phys. Chem. B* **2006**, *110*, 18641–18650.
(40) Hare, P. M.; Middleton, C. T.; Mertel, K. I.; Herbert, J. M.; Kohler, B. *Chem. Phys.* **2008**, *347*, 383–392.
(41) Climent, T.; González-Luque, R.; Merchán, M.; Serrano-Andrés, L. *Chem. Phys. Lett.* **2007**, *441*, 327–331.
(42) Serrano-Pérez, J. J.; González-Luque, R.; Merchán, M.; Serrano-Andrés, L. *J. Phys. Chem. B* **2007**, *111*, 11880–11883.
(43) Henry, B. R.; Siebrand, W. *J. Chem. Phys.* **1971**, *54*, 1072–1085.
(44) Christiansen, O.; Koch, H.; Jørgensen, P. *Chem. Phys. Lett.* **1995**, *243*, 409–418.
(45) Vahtras, O.; Almlöf, J.; Feyereisen, M. W. *Chem. Phys. Lett.* **1993**, *213*, 514–518.
(46) Hättig, C.; Weigend, F. *J. Chem. Phys.* **2000**, *113*, 5154–5161.
(47) Hättig, C. *J. Chem. Phys.* **2003**, *118*, 7751–7761.
(48) Köhn, A.; Hättig, C. *J. Chem. Phys.* **2003**, *119*, 5021–5036.
(49) Hättig, C.; Köhn, A. *J. Chem. Phys.* **2002**, *117*, 6939–6951.
(50) Bauernschmitt, R.; Ahlrichs, R. *Chem. Phys. Lett.* **1996**, *256*, 454–464.
(51) Becke, A. D. *J. Chem. Phys.* **1993**, *98*, 5648–5652.
(52) Ahlrichs, R.; et al. *TURBOMOLE (Vers. 5.7)*; Universität Karlsruhe: Germany, 2004.
(53) Neugebauer, J.; Reiher, M.; Kind, C.; Hess, B. A. *J. Comput. Chem.* **2002**, *23*, 895–910.
(54) Grimme, S.; Waletzke, M. *J. Chem. Phys.* **1999**, *111*, 5645–5655.
(55) Becke, A. D. *J. Chem. Phys.* **1993**, *98*, 1372–1377.
(56) Lee, C.; Yang, W.; Parr, R. G. *Phys. Rev. B* **1988**, *37*, 785–789.
(57) Dunning, T. H. *J. Chem. Phys.* **1989**, *90*, 1007–1023.
(58) Kendall, R. A.; Dunning, T. H. J.; Harrison, R. J. *J. Chem. Phys.* **1992**, *96*, 6796–6806.
(59) Schäfer, A.; Huber, C.; Ahlrichs, R. *J. Chem. Phys.* **1994**, *100*, 5829–5835.
(60) Weigend, F.; Köhn, A.; Hättig, C. *J. Chem. Phys.* **2002**, *116*, 3175–3183.
(61) Eichkorn, K.; Weigend, F.; Treutler, O.; Ahlrichs, R. *Theor. Chem. Acc.* **1997**, *97*, 119–124.
(62) Kleinschmidt, M.; Tatchen, J.; Marian, C. M. *J. Comput. Chem.* **2002**, *23*, 824–833.
(63) Schimmelpfennig, B. *AMFI*; Stockholm University: Sweden, 1996.
(64) Hess, B. A.; Marian, C. M.; Wahlgren, U.; Gropen, O. *Chem. Phys. Lett.* **1996**, *251*, 365–371.
(65) Tatchen, J.; Marian, C. M. *Chem. Phys. Lett.* **1999**, *313*, 351–357.
(66) Danovich, D.; Marian, C. M.; Neuheuser, T.; Peyerimhoff, S. D.; Shaik, S. *J. Phys. Chem. A* **1998**, *102*, 5923–5936.
(67) Tatchen, J.; Gilka, N.; Marian, C. M. *Phys. Chem. Chem. Phys.* **2007**, *9*, 5209–5221.
(68) Salzmann, S.; Tatchen, J.; Marian, C. M. *J. Photochem. Photobio. A* **2008**, *198*, 221–231.
(69) Fleig, T.; Knecht, S.; Hättig, C. *J. Phys. Chem. A* **2007**, *111*, 5482–5491.
(70) Steward, R. F.; Jensen, L. H. *Acta Chrystallogr.* **1967**, *23*, 1102–1105.
(71) Vogt, N.; Khaikin, L. S.; Grikina, O. E.; Rykov, A. N.; Vogt, J. *J. Phys. Chem. A* **2008**, *112*, 7662–7670.
(72) Colarusso, P.; Zhang, K.; Guo, B.; Bernath, P. F. *Chem. Phys. Lett.* **1997**, *269*, 39–48.
(73) Petke, J. D.; Maggiora, G. M.; Christoffersen, R. E. *J. Phys. Chem.* **1992**, *96*, 6992–7001.
(74) Lorentzon, J.; Fülscher, M. P.; Roos, B. O. *J. Am. Chem. Soc.* **1995**, *117*, 9265–9273.
(75) Broo, A.; Holmén, A. *J. Phys. Chem.* **1997**, *101*, 3589–3600.
(76) Marian, C. M.; Schneider, F.; Kleinschmidt, M.; Tatchen, J. *Eur. Phys. J. D* **2002**, *20*, 357–367.
(77) Epifanovsky, E.; Kowalski, K.; Fan, P.-D.; Valiev, M.; Matsika, S.; Krylov, A. I. *J. Phys. Chem. A* **2008**, *112*, 9983–9992.
(78) Schreiber, M.; Silva-Junior, M.; Sauer, S. P. A.; Thiel, W. *J. Chem. Phys.* **2008**, *128*, 134110-1–134110-25.
(79) Silva-Junior, M. R.; Schreiber, M.; Sauer, S. P. A.; Thiel, W. *J. Chem. Phys.* **2008**, *129*, 104103-1–104103-14.
(80) Etinski, M.; Fleig, T.; Marian, C. M. Manuscript in preparation.
(81) Nguyen, M. T.; Zhang, R.; Nam, P.-C.; Ceulemans, A. *J. Phys. Chem. A* **2004**, *108*, 6554–6561.

JP902944A

Intersystem crossing and characterization of dark states in the pyrimidine nucleobases uracil, thymine, and 1-methylthymine.

Supporting Information

Mihajlo Etinski,[†] Timo Fleig,[†,‡] and Christel M. Marian[*,†]

Institute of Theoretical and Computational Chemistry, Heinrich Heine University Düsseldorf, Düsseldorf, Germany

E-mail: Christel.Marian@uni-duesseldorf.de

In this supplement, harmonic vibrational frequencies and cartesian coordinates of all stationary points are given. Furthermore, simulated S_0-T_1 and S_0-S_1 difference spectra are discussed and the dependence of the computed ISC rates on technical parameters is shown.

[†]HHU Düsseldorf
[‡]Current address: IRSAMC, Université Paul Sabatier, Toulouse, France

Figure S1: Calculated difference IR spectra of thymine. Upper panel RI-CC2/cc-pVDZ, lower panel B3-LYP/DFT/TZVP frequency calculations. The line spectra were broadened by Gaussian functions with a width of 50 cm^{-1} at half maximum.

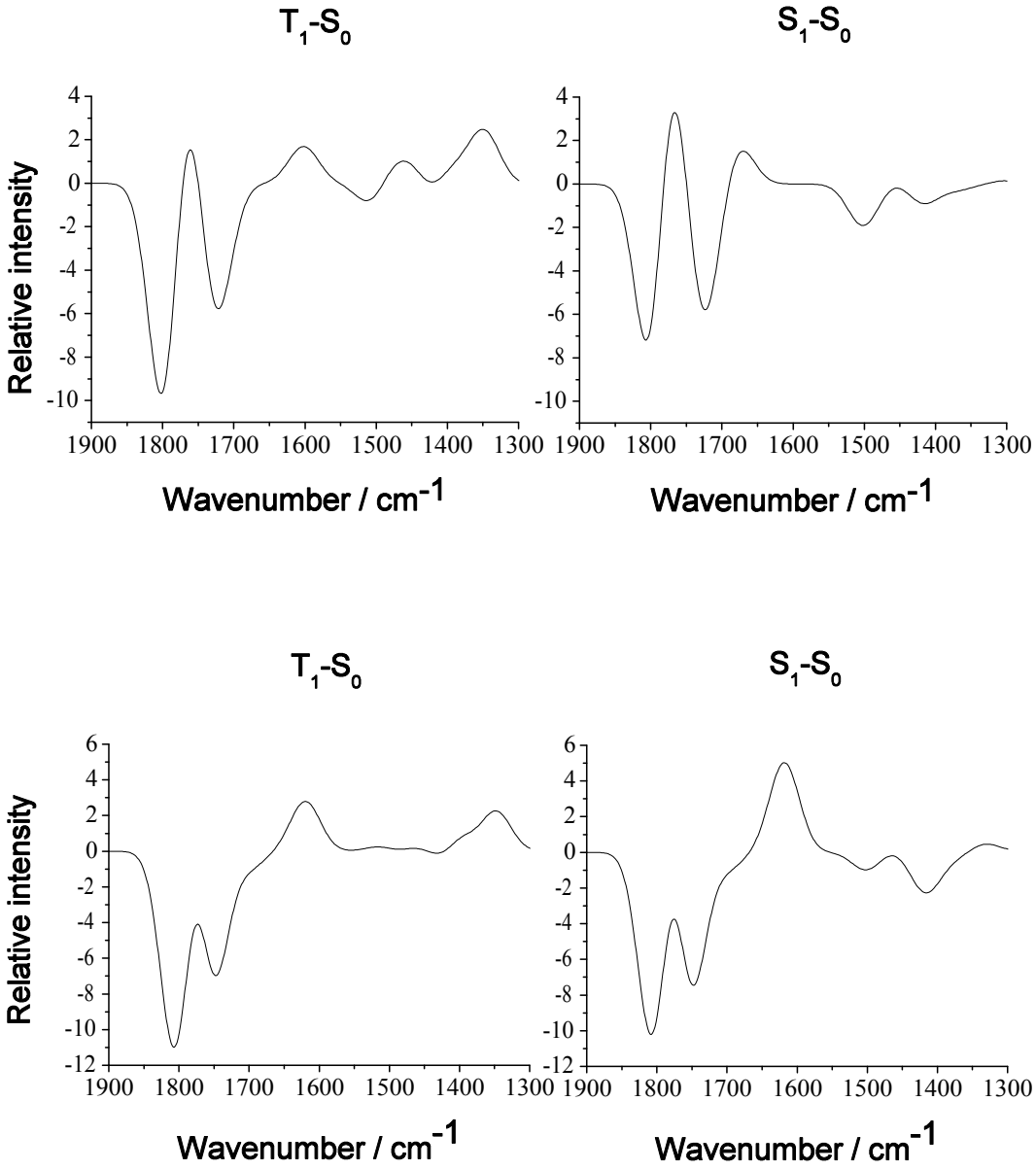

The dip with highest wavenumber in the simulated S_0-T_1 and S_0-S_1 difference spectra (Figure S1) and the neighboring maximum result from a red shift of the C_2=O_2 stretching frequency in the excited state. The second dip can be assigned to the disappearance of the C_4=O_4 stretching band in the electronic ground state. Although these three features are very prominent in the spectra, they cannot be used to distinguish between a transient S_1 or T_1 state. The maximum around 1600 cm^{-1} in the S_0-T_1 spectrum is associated with the red-shifted C_4=O_4 stretch in the T_1 state. The wavenumber of the C_4=O_4 stretching mode in the S_1 state is shifted to values of 1080 cm^{-1} (RI-CC2) and 1197 cm^{-1} (TDDFT), out of the observation region. The similar looking maximum at 1677 cm^{-1} (RI-CC2) and 1618 cm^{-1} (TDDFT) in the S_0-S_1 difference spectrum originates from the C_4=C_5 stretch that gains intensity in the S_1 state. Characteristic of the S_0-T_1 difference spectrum are the peak near 1500 cm^{-1} that results from a combination of the C_4=C_5 stretching and the N_1H wagging motions and the peak near 1350 cm^{-1} that arises from a ring deformation vibration.

Table S1: Vibrational spectrum of the uracil ground state (unscaled frequencies). Wavenumbers ν are given in cm^{-1} intensities I in km/mol.

CC2/cc-pVDZ		DFT/B3-LYP/TZVP		experiment[a]	
ν	I	ν	I	ν	I[b]
127	0.05	165	1.60		
156	0.44	175	0.04		
374	17.84	393	19.60	374	vw
375	29.60	400	22.70	395	w
506	14.05	525	19.92	512	w
522	5.89	549	10.56		
546	2.33	562	3.28	545	w
554	36.68	568	40.34	660	w
689	78.57	676	87.06	692	vw
721	1.03	725	11.28		
735	42.79	756	42.48	717	vw
761	2.21	769	3.45	757	w
800	55.57	808	67.80	802	w
940	0.73	959	0.88		
962	9.47	965	11.65	952	w
980	5.35	992	7.10	990	(sh)m
1084	5.44	1090	6.15	1082	m
1197	94.15	1191	91.28	1172	s
1226	0.37	1233	19.95	1187	s
1369	6.95	1383	102.34	1371	(sh)m
1390	45.74	1408	68.50	1387	s
1405	60.25	1426	3.28	1400	s
1500	100.96	1501	82.04	1515	m
1661	12.61	1675	73.17	1641	s
1744	386.69	1773	745.59	1703	(sh)vs
1798	587.67	1806	593.87	1756	vs
3247	3.42	3209	2.28	1897	m
3290	1.00	3251	2.10	3124	m
3594	63.74	3591	67.71	3436	s
3648	114.93	3632	104.27	3484	s

[a] gas phase[1]

[b] sh, shoulder; vs, very strong; s, strong; m, medium; w, weak; vw, very weak;

Table S2: Vibrational spectrum of the uracil S_1 state (unscaled frequencies). Wavenumbers ν are given in cm^{-1} intensities I in km/mol.

CC2/cc-pVDZ		TDDFT/B3-LYP/TZVP	
ν	I	ν	I
47	4.16	90	5.88
158	1.45	166	3.11
288	10.76	194	18.74
303	5.32	342	7.45
314	50.47	356	10.57
344	68.85	368	59.17
473	8.89	501	15.59
508	3.67	530	59.43
534	12.49	535	2.98
549	36.69	558	10.19
592	38.48	577	52.57
691	46.31	717	83.29
718	2.34	736	9.96
743	44.77	781	7.14
910	12.32	944	26.60
971	19.04	1010	10.29
1013	34.70	1040	28.98
1105	8.82	1145	49.57
1150	9.38	1208	47.65
1277	6.88	1268	3.46
1307	14.45	1356	41.41
1406	3.40	1429	11.67
1427	7.63	1448	25.73
1451	6.34	1489	5.50
1631	132.32	1642	346.56
1777	470.40	1784	515.17
3256	5.65	3246	4.17
3275	1.24	3284	0.60
3627	78.00	3631	158.54
3629	126.46	3635	38.36

Table S3: Vibrational spectrum of the uracil saddle point of the S_2 state obtained at TDDFT/B3-LYP/TZVP level (unscaled frequencies). Wavenumbers ν are given in cm^{-1} intensities I in km/mol.

ν	I
-59	3.06
189	3.57
298	4.54
338	2.05
384	57.85
452	43.53
502	97.07
516	24.96
551	20.48
579	2.98
696	131.44
726	51.00
739	19.35
818	8.92
852	31.03
956	23.04
1046	28.50
1089	25.14
1189	76.66
1221	5.02
1368	17.90
1382	7.72
1417	84.49
1535	52.63
1581	33.24
1789	387.31
3214	3.49
3239	2.55
3585	151.16
3646	110.47

Table S4: Vibrational spectrum of the uracil T_1 state (unscaled frequencies). Wavenumbers ν are given in cm^{-1} intensities I in km/mol.

CC2/cc-pVDZ		UDFT/B3-LYP/TZVP	
ν	I	ν	I
127	2.15	155	2.65
159	1.04	194	0.80
229	2.45	250	0.24
367	20.90	385	22.68
460	18.79	488	26.58
480	8.89	511	28.26
498	10.58	553	6.35
531	7.07	554	10.50
554	37.24	563	24.13
641	31.81	629	6.55
683	109.17	657	149.73
698	2.96	726	10.70
727	70.26	743	60.27
762	0.29	764	3.96
938	4.97	937	8.86
959	17.32	961	20.36
1015	8.54	1012	8.34
1145	74.01	1150	93.26
1227	32.14	1248	24.18
1354	85.20	1360	124.75
1361	55.82	1394	19.15
1379	6.24	1406	5.64
1405	61.11	1418	122.73
1457	150.99	1486	76.87
1609	82.21	1610	122.45
1769	318.67	1777	451.15
3241	10.55	3222	5.11
3255	1.92	3232	0.32
3599	101.12	3603	101.31
3600	42.43	3608	60.02

Table S5: Vibrational spectrum of the uracil T_2 state obtained at TDDFT/B3-LYP/TZVP level (unscaled frequencies). Wavenumbers ν are given in cm^{-1} intensities I in km/mol.

ν	I
103	2.25
152	5.50
268	29.66
337	8.04
375	25.43
429	7.52
498	13.33
511	25.40
530	1.27
557	125.14
563	10.90
725	47.97
776	5.40
796	26.65
946	26.80
1004	13.53
1050	22.87
1156	58.85
1232	33.28
1284	21.08
1363	61.21
1430	6.42
1477	63.97
1492	8.08
1610	185.41
1792	589.78
3240	2.04
3288	0.60
3639	153.32
3643	33.37

Table S6: Vibrational spectrum of the uracil T_3 state obtained at TDDFT/B3-LYP/TZVP level (unscaled frequencies). Wavenumbers ν are given in cm^{-1} intensities I in km/mol.

ν	I
104	7.87
202	7.36
232	19.70
350	9.57
371	14.86
476	4.83
509	3.00
511	3.06
551	7.34
577	0.44
617	163.78
733	36.24
758	14.41
776	4.26
843	49.35
944	27.53
996	31.85
1056	76.26
1164	20.72
1275	1.89
1332	6.61
1377	32.07
1421	0.58
1524	48.95
1644	105.30
1896	1863.43
3233	8.38
3289	9.04
3554	115.73
3633	92.67

Table S7: Vibrational spectrum of the thymine ground state (unscaled frequencies). Wavenumbers ν are given in cm^{-1} intensities I in km/mol.

CC2/cc-pVDZ		DFT/B3-LYP/TZVP		experiment[a]	
ν	I	ν	I	ν	I
103	0.01	108	0.01		
135	0.29	138	0.32		
147	0.04	149	1.23		
270	2.83	281	2.60		
287	0.01	290	0.33		
374	23.95	388	17.31		
377	16.66	390	19.35		
451	14.47	463	19.31	462	vw
529	6.18	548	7.93		
555	51.60	554	53.67	541	w
592	1.03	610	1.28	658	w
686	78.05	665	90.71	689	vw
732	38.07	732	5.37	755	w
737	3.65	748	25.96		
750	5.59	760	29.89	767	w
792	1.68	806	4.82	804	vw
884	16.63	903	18.65	885	w
960	11.10	964	13.82	931	vw
1013	1.21	1025	2.04	963	vw
1058	1.04	1069	0.82	1031	vw
1158	4.76	1149	8.36	1078	m
1200	106.57	1198	129.22	1178	s
1258	18.65	1219	29.65		
1367	8.80	1372	13.44		
1373	5.40	1412	41.30	1393	s
1409	18.07	1417	87.33	1409	s
1419	45.48	1429	2.39		
1465	6.29	1471	8.12		
1482	10.23	1492	32.54	1463	s
1502	103.92	1500	44.79	1518	m
1687	3.24	1697	51.13	1668	s
1725	338.46	1755	605.10	1725	vs
1797	639.59	1806	742.77	1772	vs
3079	24.56	3036	20.95	2941	
3169	8.08	3087	9.89	2984	
3183	11.30	3111	14.35	3076	m
3235	5.36	3196	4.89		
3594	63.24	3590	66.07	3437	s
3646	111.24	3633	103.04	3484	s

[a] gas phase[1]

[b] sh, shoulder; vs, very strong; s, strong; m, medium; w, weak; vw, very weak

Table S8: Vibrational spectrum of the thymine S_1 state (unscaled frequencies). Wavenumbers ν are given in cm^{-1} intensities I in km/mol.

CC2/cc-pVDZ		TDDFT/B3-LYP/TZVP	
ν	I	ν	I
50	2.95	52	0.13
93	0.06	90	2.23
154	0.35	148	0.01
189	7.48	219	1.83
237	2.35	257	31.42
303	6.95	260	5.01
315	0.77	348	5.12
344	54.89	367	38.47
369	71.18	384	16.95
454	7.92	470	14.99
485	6.31	511	7.09
551	43.21	526	77.13
553	12.50	568	54.52
589	47.27	587	2.51
693	23.91	719	36.13
715	3.19	767	4.07
776	4.69	787	15.15
909	14.47	945	32.04
967	6.70	999	2.99
1050	2.61	1064	0.17
1080	1.62	1133	57.73
1141	31.66	1168	32.86
1213	43.16	1197	30.07
1236	1.16	1259	11.74
1296	10.51	1332	25.99
1405	0.15	1424	6.56
1408	10.39	1430	1.99
1422	3.66	1468	19.80
1456	14.14	1487	8.18
1475	6.30	1497	6.06
1492	6.88	1512	6.11
1677	99.57	1618	267.51
1777	516.19	1778	541.50
3062	42.15	3031	31.55
3150	18.48	3077	17.11
3157	15.85	3113	11.46
3236	5.77	3271	0.36
3624	68.10	3635	150.57
3627	130.97	3638	48.07

Table S9: Vibrational spectrum of the thymine S_1 state with rotated methyl group obtained at TDDFT/B3-LYP/TZVP level (unscaled frequencies). Wavenumbers ν are given in cm^{-1} intensities I in km/mol.

ν	I
108	0.51
145	0.87
167	0.01
234	1.61
272	2.31
287	26.50
352	4.85
379	20.94
416	47.42
470	15.58
513	6.24
553	69.89
588	2.17
590	52.60
724	40.01
764	3.70
789	13.84
952	25.46
1004	1.77
1140	50.50
1168	37.78
1196	50.99
1259	12.17
1324	24.37
1428	7.30
1431	5.55
1469	23.58
1483	10.65
1497	2.99
1508	12.66
1641	304.02
1780	554.70
3029	47.11
3074	20.24
3122	9.52
3269	0.22
3632	158.30
3635	39.61

Table S10: Vibrational spectrum of the thymine T_1 state (unscaled frequencies). Wavenumbers ν are given in cm^{-1} intensities I in km/mol.

CC2/cc-pVDZ		UDFT/B3-LYP/TZVP	
ν	I	ν	I
75	0.54	78	0.76
140	1.45	147	2.36
152	0.77	170	0.37
180	0.66	196	0.25
275	5.69	289	4.71
309	9.38	319	6.95
376	15.58	384	18.57
437	19.20	448	26.29
484	8.69	482	35.85
547	23.84	532	7.89
575	5.84	588	2.63
633	36.75	597	5.06
679	82.79	633	150.60
691	4.35	675.	13.41
721	83.17	720	25.03
738	7.80	740	34.81
781	5.79	787	5.06
947	4.30	953	6.90
972	10.12	978	9.02
980	0.84	994	0.54
1148	61.78	1134	120.01
1151	69.35	1165	38.04
1243	7.10	1231	14.29
1348	116.77	1348	122.46
1355	13.91	1392	29.31
1379	26.98	1399	13.26
1405	56.39	1413	102.69
1421	1.28	1435	15.19
1453	47.15	1464	11.52
1466	13.49	1472	11.21
1491	85.14	1504	78.56
1602	89.85	1620	148.57
1769	346.00	1775	516.40
3041	13.82	2981	10.20
3111	10.30	3010	11.94
3197	1.91	3142	2.58
3224	11.69	3208	5.04
3594	71.75	3606	112.96
3602	71.28	3607	48.15

Table S11: Vibrational spectrum of the 1-methylthymine ground state obtained at RI-CC2/cc-pVDZ level (unscaled frequencies). Wavenumbers ν are given in cm^{-1} intensities I in km/mol.

ν	I	ν	I
56	0.01	1156	15.77
96	0.01	1205	38.34
127	0.10	1249	7.85
145	0.66	1347	31.43
195	4.45	1374	3.14
260	3.24	1391	84.81
292	0.55	1415	26.82
327	1.76	1448	2.38
379	17.76	1465	4.56
392	3.74	1468	104.67
433	19.10	1469	8.66
510	2.51	1490	14.48
634	1.02	1516	48.34
681	50.01	1682	0.22
698	6.63	1723	357.17
733	36.66	1767	613.62
744	9.85	3077	27.63
767	3.28	3096	36.24
862	3.31	3166	8.57
881	15.75	3181	11.40
1014	0.73	3192	8.56
1056	1.30	3217	1.48
1082	31.36	3224	10.39
1147	0.09	3590	64.17

Table S12: Vibrational spectrum of the 1-methylthymine S_1 state obtained at RI-CC2/cc-pVDZ level (unscaled frequencies). Wavenumbers ν are given in cm^{-1} intensities I in km/mol.

ν	I	ν	I
16	1.91	1144	2.96
86	0.13	1182	1.39
101	0.24	1216	50.85
105	0.42	1224	55.11
189	2.43	1269	4.50
231	2.50	1361	3.33
240	6.27	1404	0.67
294	1.99	1409	6.12
305	2.78	1428	14.40
359	2.66	1459	39.35
373	41.29	1474	6.26
375	109.20	1490	8.35
427	10.25	1492	7.16
484	1.05	1509	4.06
567	0.59	1687	89.80
586	3.83	1743	477.44
686	10.89	3060	44.91
703	7.97	3080	45.92
719	4.47	3148	19.30
839	1.26	3155	15.98
975	1.50	3168	20.84
1043	11.42	3211	8.83
1051	0.16	3230	0.03
1081	3.89	3626	148.13

Table S13: Vibrational spectrum of the 1-methylthymine T_1 state obtained at RI-CC2/cc-pVDZ level (unscaled frequencies). Wavenumbers ν are given in cm^{-1} intensities I in km/mol.

ν	I	ν	I
76	0.59	1139	10.33
98	0.27	1186	25.73
112	0.03	1240	31.79
150	1.61	1309	143.12
160	1.83	1351	7.17
244	5.10	1380	86.34
267	4.43	1381	12.88
316	4.48	1408	41.92
345	0.81	1437	71.23
387	17.77	1445	1.08
416	20.87	1465	8.46
469	6.80	1486	24.14
594	13.81	1493	15.12
613	2.07	1505	53.28
657	45.65	1600	90.08
687	7.48	1739	294.05
717	87.61	3042	15.04
726	3.81	3081	37.99
769	7.25	3111	11.06
822	1.47	3172	15.38
972	4.15	3195	2.49
982	0.85	3209	10.84
1067	19.33	3232	0.14
1136	46.80	3589	70.35

Table S14: Calculated ISC rate constants between S_1 and T_1 states of uracil for different parameters. The energy interval η for vibrational states search is given in cm^{-1}, # modes denotes the number of vibrational modes included in the calculation, and the entry quanta displays the maximum allowed number of vibrational quanta per mode. Geometries and vibrational frequencies were obtained at the RI-CC2/cc-pVDZ level.

η	# modes	rate[a]	# quanta	states within interval
0.01	30	0.99×10^5	1	6
0.01	30	0.12×10^7	3	173
0.01	30	0.39×10^7	5	300
0.01	30	0.39×10^7	7	387
0.1	30	0.23×10^5	1	73
0.1	30	0.51×10^7	3	1682
0.1	30	0.63×10^7	5	3131
0.1	30	0.64×10^7	7	3931
1.0	30	0.27×10^6	1	656
1.0	30	0.83×10^7	3	16614
1.0	30	0.99×10^7	5	30779
1.0	30	0.10×10^8	7	38592
1.0	30	0.10×10^8	9	42839

[a] This rate was calculated for a spin-orbit matrix element of 1 cm^{-1}.
The true rate is obtained multiplying this rate with the calculated sum over squares of SOMEs.

Table S15: Calculated ISC rate constants between S_1 and T_1 states of thymine for different parameters. The energy interval η for vibrational states search is given in cm^{-1}, # modes denotes the number of vibrational modes included in the calculation, and the entry quanta displays the maximum allowed number of vibrational quanta per mode. Geometries and vibrational frequencies were obtained at the RI-CC2/cc-pVDZ level.

η	# modes	rate[a]	# quanta	states within interval
0.01	39	0.44×10^6	5	116499
0.1	39	0.21×10^6	3	375376
0.1	39	0.54×10^6	5	1164004
1.0	39	0.24×10^3	1	35201
1.0	39	0.12×10^6	3	3754116

[a] This rate was calculated for a spin-orbit matrix element of 1 cm^{-1}.
The true rate is obtained multiplying this rate with the calculated sum over squares of SOMEs.

Table S16: Calculated ISC rate constants between S_1 and T_1 states of 1-methylthymine for different parameters. The energy interval η for vibrational states search is given in cm^{-1}, # modes denotes the number of vibrational modes included in the calculation, and the entry quanta displays the maximum allowed number of vibrational quanta per mode. Geometries and vibrational frequencies were obtained at the RI-CC2/cc-pVDZ level.

η	# modes	rate[a]	# quanta	states within interval
0.001	48	0.93×10^4	1	312
0.001	48	0.21×10^7	3	73563
0.01	48	0.31×10^6	1	3445
0.01	30	0.13×10^7	3	65613
0.1	48	0.74×10^6	1	34420
0.1	20	0.92×10^6	3	23433
0.1	20	0.76×10^7	5	132222
0.1	30	0.52×10^5	3	660366
1.0	48	0.27×10^6	1	343636

[a] This rate was calculated for a spin-orbit matrix element of 1 cm^{-1}.
The true rate is obtained multiplying this rate with the calculated sum over squares of SOMEs.

Table S17: Calculated ISC rate constants between S_1 and T_1 states of uracil for different parameters. ΔE is the adiabatic energy gap between the states. The energy interval η for vibrational states search is given in cm^{-1}, # modes denotes the number of vibrational modes included in the calculation, and the entry quanta displays the maximum allowed number of vibrational quanta per mode. Geometries and vibrational frequencies were obtained at the TDDFT/B3-LYP/TZVP and UDFT/B3-LYP/TZVP level respectively.

ΔE	η	# modes	rate[a]	# quanta	states within interval
6704	0.001	30	0.38×10^6	1	2
6704	0.001	30	0.18×10^8	3	165
6704	0.001	30	0.26×10^8	5	332
6704	0.001	30	0.33×10^8	all	538
6704	0.01	30	0.83×10^8	3	1752
6704	0.01	30	0.10×10^9	5	3651
6704	0.01	30	0.11×10^9	all	5618
6704	0.1	30	0.92×10^8	all	55443
4000	0.01	30	0.83×10^6	all	18
5000	0.01	30	0.85×10^8	all	262
5150	0.01	30	0.64×10^8	all	296
6000	0.01	30	0.25×10^9	all	1620
7000	0.01	30	0.13×10^9	all	9326
8000	0.01	30	0.47×10^9	all	45971
9000	0.01	30	0.10×10^9	all	204443

[a] This rate was calculated for a spin-orbit matrix element of 1 cm^{-1}.
The true rate is obtained multiplying this rate with the calculated sum over squares of SOMEs.

Table S18: Calculated ISC rate constants between S_2 and T_2 states of uracil for different parameters. ΔE is the adiabatic energy gap between the states. The energy interval η for vibrational states search is given in cm^{-1}, # modes denotes the number of vibrational modes included in the calculation, and the entry quanta displays the maximum allowed number of vibrational quanta per mode. Geometries and vibrational frequencies were obtained at the TDDFT/B3-LYP/TZVP level.

ΔE	η	# modes	rate[a]	# quanta	states within interval
11391	0.01	30	0.20×10^6	1	575
5000	0.01	30	0.88×10^7	5	587
6000	0.01	30	0.12×10^7	5	3485
7000	0.01	30	0.11×10^9	5	17100
8000	0.01	30	0.23×10^9	5	75656
9000	0.01	30	0.32×10^9	5	294950

[a] This rate was calculated for a spin-orbit matrix element of 1 cm^{-1}.
The true rate is obtained multiplying this rate with the calculated sum over squares of SOMEs.

Table S19: Calculated ISC rate constants between S_2 and T_3 states of uracil for different parameters. ΔE is the adiabatic energy gap between the states. The energy interval η for vibrational states search is given in cm^{-1}, # modes denotes the number of vibrational modes included in the calculation, and the entry quanta displays the maximum allowed number of vibrational quanta per mode. Geometries and vibrational frequencies were obtained at the TDDFT/B3-LYP/TZVP level.

ΔE	η	# modes	rate[a]	rate[b]	# quanta	states within interval
5355	0.01	30	0.33×10^6	0.33×10^8	1	18
5355	0.01	30	0.27×10^8		3	639
5355	0.01	30	0.27×10^8		5	1303
5355	0.01	30	0.27×10^8		all	2270

[a] This rate was calculated for a spin-orbit matrix element of 1 cm^{-1} in Condon approximation. The true rate is obtained multiplying this rate with the calculated sum over squares of SOMEs.
[b] Calculated in Herzberg-Teller approximation.

Table S20: Calculated ISC rate constants between S_1 and T_1 states of thymine for different parameters. ΔE is the adiabatic energy gap between the states. The energy interval η for vibrational states search is given in cm^{-1}, # modes denotes the number of vibrational modes included in the calculation, and the entry quanta displays the maximum allowed number of vibrational quanta per mode. Geometries and vibrational frequencies were obtained at the TDDFT/B3-LYP/TZVP level.

ΔE	η	# modes	rate[a]	# quanta	states within interval
8495	0.001	39	0.31×10^4	1	258
8495	0.001	39	0.18×10^7	3	87999
8495	0.01	39	0.35×10^4	1	2779
8495	0.1	39	0.41×10^4	1	27155

[a] This rate was calculated for a spin-orbit matrix element of 1 cm^{-1}.
The true rate is obtained multiplying this rate with the calculated sum over squares of SOMEs.

Table S21: Calculated ISC rate constants between the local minimum of the S_1 state and the T_1 minimum of thymine for different parameters. ΔE is the adiabatic energy gap between the states. The energy interval η for vibrational states search is given in cm^{-1}, # modes denotes the number of vibrational modes included in the calculation, and the entry quanta displays the maximum allowed number of vibrational quanta per mode. Geometries and vibrational frequencies were obtained at the TDDFT/B3-LYP/TZVP level.

ΔE	η	# modes	rate[a]	# quanta	states within interval
8426	0.001	31	0.43×10^6	1	116
8426	0.001	31	0.55×10^8	3	60491
8426	0.001	39	0.16×10^7	1	325
8426	0.001	39	0.61×10^8	3	103601

[a] This rate was calculated for a spin-orbit matrix element of 1 cm^{-1}.
The true rate is obtained multiplying this rate with the calculated sum over squares of SOMEs.

Table S22: Geometry of the ground state of uracil in atomic units obtained at RI-CC2/cc-pVDZ level

1.80276131503938	-3.82523577877818	-0.00001843121476	c
-0.76911959552013	-3.60787322393067	-0.00007500514995	c
-1.94412134408134	-1.10454937651617	0.00002508530838	c
-0.14550597259914	0.88615452904312	0.00017510886307	n
2.48204977900901	0.75797537834155	0.00023770292495	c
3.36151866289513	-1.73799691500085	0.00013053376173	n
-4.22669268030672	-0.64209232037238	-0.00000930583133	o
3.89552706152535	2.59733451753509	0.00037114273740	o
5.27279481407985	-1.92595057138397	0.00017209542869	h
-0.87594766368821	2.67228606501715	0.00025076303206	h
2.76550865539636	-5.65443235453763	-0.00008760001027	h
-1.98531788402312	-5.27108030126895	-0.00019329108878	h

Table S23: Geometry of the ground state of uracil in atomic units obtained at DFT/B3-LYP/TZVP level

-2.31113300958309	1.39616715774855	0.00000000000000	c
-2.14348711943103	-1.21067833133628	0.00000000000000	n
0.04198666450410	2.57568868190690	0.00000000000000	n
0.05832901594390	-2.71679409544589	0.00000000000000	c
2.29446591154163	1.28687122370233	0.00000000000000	c
2.38999898748282	-1.25286105259735	0.00000000000000	c
-4.28057972767846	2.56375432364757	0.00000000000000	o
-0.10057257331357	-5.00568053839637	0.00000000000000	o
3.97167279977125	2.45619603192047	0.00000000000000	h
4.15788368326043	-2.26638067434561	0.00000000000000	h
-0.00535234783703	4.48067410565794	0.00000000000000	h
-3.81090183394734	-2.14783188012697	0.00000000000000	h

Table S24: Geometry of the S_1 state of uracil in atomic units obtained at RI-CC2/cc-pVDZ level

0.33897033221462	1.36132036952789	-0.71354640950436	c
-2.16830967216996	0.27921600085562	-0.55259778778755	c
-2.33291781271658	-2.23250800809978	-0.12483561008593	c
-0.22143039872179	-3.74915347578373	0.21200756656727	n
2.27161351679411	-2.80420926445030	0.25197377565216	c
2.38079163497256	-0.23449154572517	-0.16599513219088	n
-3.85075421208677	1.43897566732052	-0.82824054100883	h
-4.53991708654283	-3.78289851094835	0.06201268861541	o
4.11105733844260	-4.18360201279782	0.62476047658149	o
-0.41352184865411	-5.63002979361522	0.56716080078631	h
4.17622188098919	0.45468528231244	-0.20606788408108	h
0.71559577364017	3.38976059942737	-0.69108040928701	h

Table S25: Geometry of the S_1 state of uracil in atomic units obtained at TDDFT/B3-LYP/TZVP level

-2.30685645238786	1.41474750569193	0.05296826935759	c
-2.18159572835483	-1.23522999124835	0.02356274118783	n
-0.00430519727608	2.57027540360695	0.02310727102924	n
0.07616417244538	-2.58121836814159	0.00024281939633	c
2.33172434917640	1.31986382303649	-0.03307186013577	c
2.33535856478456	-1.33383782934747	-0.02709809491420	c
-4.32794743110461	2.50083798531802	0.09850959646958	o
-0.31199989050728	-5.05430553528401	0.00338934282557	o
3.99957134838786	2.47896719496774	-0.02798008883596	h
4.08097601741691	-2.38280149003647	-0.05354295979744	h
-0.07446779303361	4.47406734992489	0.03231500641158	h
-3.85428936759419	-2.14839585482182	0.06710880159518	h

Table S26: Geometry of the saddle point of the S_2 state of uracil in atomic units obtained at TDDFT/B3-LYP/TZVP level

-2.20749429658053	1.37100286963615	0.05569217144251	c
-2.23217973898031	-1.11245846079492	-0.02781962339649	n
-0.03545389613242	2.61770953539502	0.02963201786877	n
0.12276736838755	-2.79181861132875	-0.00900752043045	c
2.36597021689158	1.32272330919476	-0.24573649850889	c
2.31546881094450	-1.31688136678136	-0.06905116263389	c
-4.35294109330749	2.60396696522070	0.14236736026980	o
-0.29577228257451	-5.06655336413659	0.07732968404052	o
3.99885659777261	2.45780865459851	0.18942443532138	h
4.09012384337911	-2.32896063881337	-0.03536823479804	h
-0.13684899191405	4.51701869970714	-0.04419594012087	h
-3.92723077256800	-1.99709101699514	0.06599157742871	h

Table S27: Geometry of the T_1 state of uracil in atomic units obtained at RI-CC2/cc-pVDZ level

1.91164001968400	-3.84894454808797	0.76085934370093	c
-0.80480063599536	-3.55410211096836	-0.05576329127888	c
-1.92939839894834	-1.06654822108889	0.07178595469496	c
-0.14940202847252	0.86449654246044	0.64216133438314	n
2.43153503217761	0.71567056781175	0.08782439180786	c
3.30666121126855	-1.77911271016009	-0.13529134932617	n
-4.20035084227332	-0.56795061284651	-0.24597887642145	o
3.82104193628791	2.55612524845929	-0.17004733482631	o
5.21906293952542	-1.89260554848371	-0.35009209010192	h
-0.85510646934687	2.65950378661802	0.63044996769175	h
2.84401224282969	-5.68197431665829	0.56296480531994	h
-1.87734509750552	-5.06855912797309	-0.96463511177476	h

Table S28: Geometry of the T_1 state of uracil in atomic units obtained at UDFT/B3-LYP/TZVP level

-2.29888859400814	1.36061278309534	0.07215617701312	c
-2.16276701284828	-1.21508402271527	0.49789521754415	n
0.04374300810531	2.54910427337640	-0.14610644353785	n
0.01968283279884	-2.72066232711477	0.11608197575959	c
2.33158406119494	1.43029204084906	0.48345893525370	c
2.32820358805994	-1.34270917402803	-0.01535364095304	c
-4.26571320924951	2.52642376438801	-0.09652856292563	o
-0.17322983011401	-5.03100799889615	-0.04519031611342	o
4.00174755795880	2.55768961227739	0.16795298656814	h
4.02265006965161	-2.34111978141722	-0.56348200479752	h
-0.08101496350814	4.43779619726310	-0.40068671645239	h
-3.83669298685596	-2.13515894816152	0.52876130404868	h

Table S29: Geometry of the T_2 state of uracil in atomic units obtained at TDDFT/B3-LYP/TZVP level

-2.31402168415616	1.40889962854914	0.05303289442617	c
-2.19405660343462	-1.23110761201354	0.02760629917250	n
-0.00475661712312	2.57004014514727	0.02042948421037	n
0.07486861953609	-2.57596879638068	0.00010440596811	c
2.33470310867718	1.30659532231680	-0.02180246871968	c
2.33847392800987	-1.32192274795215	-0.02727767145607	c
-4.32593550567710	2.51044459021874	0.09795960588131	o
-0.24947669221006	-5.07164514478886	-0.00166030635344	o
4.00528512934441	2.46256973850434	-0.04057139856366	h
4.08739954875657	-2.36781612019096	-0.05399867860222	h
-0.07299898202141	4.47256107494498	0.03452278400068	h
-3.87035234788383	-2.13532211979672	0.06999533962348	h

Table S30: Geometry of the T_3 state of uracil in atomic units obtained at TDDFT/B3-LYP/TZVP level

-2.27010625856786	1.48220303743164	0.05369241781290	c
-2.16523167383146	-1.20970303469149	0.03321659951267	n
-0.01841794261938	2.62139050323485	0.02260360260521	n
0.10404468484096	-2.72916368236613	0.00072365877407	c
2.32609856053794	1.33262666718267	-0.03047277066968	c
2.33041382645002	-1.31651599406667	-0.02820934724408	c
-4.36707486213345	2.49242497721694	0.09861768087399	o
-0.36359736333952	-5.09594630595670	0.00297098476603	o
3.98534697508923	2.50178934133485	-0.03132835485508	h
4.10244742461740	-2.32660391780832	-0.05506826693311	h
-0.06218884820201	4.52618421357117	0.03311790792010	h
-3.84879214346828	-2.13381080613891	0.05567418068061	h

Table S31: Geometry of the ground state of thymine in atomic units obtained at RI-CC2/cc-pVDZ level

1.80467847639010	-3.82768331030142	0.00017256838633	c
-0.77248595387687	-3.63715673109377	0.00009956818093	c
-1.91223731068656	-1.10615996119000	-0.00001345376157	c
-0.13325138697833	0.88607774948266	0.00006043219334	n
2.49742541157605	0.75781269840660	0.00016968217022	c
3.36633735052051	-1.73267815721277	0.00017162516731	n
-2.52517525947582	-5.86967207941727	-0.00011090060169	c
-4.20520534526542	-0.66663501949474	-0.00012031812041	o
3.90557677004676	2.60333217734376	0.00025724699882	o
5.27719578200499	-1.92437168113128	0.00028652361625	h
-0.86707905183507	2.67044871394354	0.00004753420255	h
2.77662425317857	-5.65380172744093	0.00023370848073	h
-1.46082419896370	-7.65950025416043	0.00159308281278	h
-3.76783570463527	-5.82206043476818	1.67202990970417	h
-3.76544811641981	-5.82382518070266	-1.67383435239424	h

Table S32: Geometry of the ground state of thymine in atomic units obtained at DFT/B3-LYP/TZVP level

-2.23345194381764	-3.32810163120920	0.00000000000000	c
0.38017939702073	-3.29625236048306	0.00000000000000	n
-3.27016539530320	-0.92157500401925	0.00000000000000	n
1.99296259447783	-1.18596974418189	0.00000000000000	c
-1.85520701770047	1.26495877007535	0.00000000000000	c
0.69036801164899	1.26082017954084	0.00000000000000	c
-3.49411155287088	-5.24188559899752	0.00000000000000	o
4.27369291323421	-1.47136729027693	0.00000000000000	o
-2.94197801247806	2.99821971796171	0.00000000000000	h
2.27140921473843	3.60937962607961	0.00000000000000	c
-5.17408170746144	-0.85375425066211	0.00000000000000	h
1.22991539582830	-5.00964042662191	0.00000000000000	h
1.09070582901984	5.29909122938744	0.00000000000000	h
3.50320642815582	3.66638762512348	1.65559731857189	h
3.50320642815582	3.66638762512348	-1.65559731857189	h

Table S33: Geometry of the S_1 state of thymine in atomic units obtained at RI-CC2/cc-pVDZ level

0.33048389411507	1.35823498295451	-0.60788074196863	c
-1.99829401997630	0.32372925580859	-0.73053867035561	c
-2.48302784291670	-2.22090104994847	-0.30328930827534	n
-0.56469944559451	-4.01329444491755	0.12845925347989	c
1.80361011676503	-2.92739345546888	0.25505578583550	n
2.36962494693841	-0.35082951276319	0.05984930677219	c
-4.35311019801620	1.56382175445597	-1.28736868505487	o
-1.01129248596558	-6.28737552721796	0.37417760966081	o
0.79802652207934	4.13455280311244	-1.02645337985241	c
-4.25598685339039	-2.93035960172474	-0.53587411844264	h
3.19949428914101	-4.19350611884565	0.64125351240329	h
4.36538369425570	0.14415601534491	-0.14668333048302	h
-0.92800727853156	5.06124499599545	-1.74270164759363	h
1.35496104465238	5.09792261866155	0.73886474406704	h
2.31196958965884	4.43913007824831	-2.42887452606781	h

Table S34: Geometry of the S_1 state of thymine in atomic units obtained at TDDFT/B3-LYP/TZVP level

-0.04039070589645	0.01439055862824	-0.01982087546021	c
2.60544303412630	0.02097588234833	0.00524442668330	n
-1.07751223950249	2.37083392377426	-0.09818629939489	n
4.05120326838163	2.22110713794899	0.03081584451381	c
0.29054343336700	4.64246950149790	-0.11838445250837	c
2.94015736208336	4.55927670710951	-0.03524796673358	c
-1.22710398755174	-1.95193692845040	0.02080188081523	o
6.51352901086336	1.72412652902834	0.10734339978749	o
-0.79457291491620	6.36111119833904	-0.16364397664669	h
4.51336277747687	6.93152147286657	-0.02912754418503	c
-2.98153605512800	2.40014099587789	-0.12994294761555	h
3.44331035796241	-1.68572558412382	0.13124139314972	h
3.29766888633056	8.59425984963975	-0.05305204758712	h
5.70646162694077	7.05469477847028	1.65229766318306	h
5.74944423742660	7.03800338442503	-1.68063666549335	h

Table S35: Geometry of the S_1 state of thymine with rotated methyl group in atomic units obtained at TDDFT/B3-LYP/TZVP level

-0.02713992460535	0.02759497910090	0.01212025126446	c
2.61959662631641	0.01571379867478	0.05152194372558	n
-1.04441199738170	2.39225171478854	0.01614545181694	n
4.08804380984067	2.19889973125920	0.09341254206636	c
0.34192906017852	4.64879292556851	0.05673108724665	c
2.99910827741110	4.54317122127637	0.09593753041347	c
-1.22687475404363	-1.93113093050282	-0.02196514228216	o
6.53960868122775	1.65000270335745	0.12792748463208	o
-0.72686874325581	6.37881745003900	0.04397830107667	h
4.56241390812596	6.92252547490679	0.14506786786053	c
-2.94863780005909	2.43832133761080	-0.01073070806095	h
3.44662051512119	-1.70164935999612	0.04838566168252	h
6.57810832290536	6.50442882288502	0.12893519479538	h
4.17100787994428	8.03915022172185	1.83906608477147	h
4.16004926234997	8.11174925124144	-1.49584624306263	h

Table S36: Geometry of the T_1 state of thymine in atomic units obtained at RI-CC2/cc-pVDZ level

1.72319817829857	-3.81070065882309	0.33444147963110	c
-1.04751040804398	-3.60247394114372	-0.34387701763916	c
-2.19372203297843	-1.12462397459517	-0.25649553148946	c
-0.44358463517930	0.86183706947456	0.22000472614834	n
2.12172647585424	0.76064964484094	-0.39957879520916	c
3.04844219130333	-1.71564588458133	-0.59264027858918	n
-2.49860724661829	-5.83617994946672	-1.23682436566550	c
-4.48300554916687	-0.66040096580886	-0.54530654106213	o
3.46297465935337	2.62564101983094	-0.73621890723532	o
4.95713320713838	-1.79013302125016	-0.84852909721381	h
-1.19525297885639	2.63763729646820	0.15597975326328	h
2.67700977239451	-5.62691621708028	0.06752265026983	h
-1.65236227217059	-6.61387478786286	-2.98658531096922	h
-2.43744005778862	-7.36809460725325	0.18520405639556	h
-4.47548506978080	-5.30760971594959	-1.60218691104771	h

Table S37: Geometry of the T_1 state of thymine in atomic units obtained at UDFT/B3-LYP/TZVP level

-0.00377315968994	0.04362830038441	-0.02010250395846	c
2.55266720959124	0.01551919713913	0.50904097608089	n
-1.05382677559265	2.45350232205105	-0.13741774000178	n
4.20128573030854	2.12531224305435	0.36633841692464	c
0.17287451144048	4.64547777419756	0.60331841889053	c
2.98330012279208	4.53738471101035	0.32121635547238	c
-1.26311054943333	-1.84462689861129	-0.35459438756690	o
6.50062052761457	1.77639226245771	0.32060192216425	o
-0.83038119864252	6.39295024033538	0.27291632347605	h
4.43459574883702	6.89789019984291	0.00181323358093	c
-2.93683766343584	2.45190619215986	-0.45318704615449	h
3.38668640844469	-1.70223729990846	0.46460352664225	h
6.44970774250552	6.51506632641029	-0.13940880950273	h
4.08635400450953	8.18253019041146	1.59451873875864	h
3.81255800829925	7.91739587968477	-1.69673775963332	h

Table S38: Geometry of the saddle point of the T_1 state of thymine in atomic units obtained at UDFT/B3-LYP/TZVP level

0.00318143843632	0.00266600290560	0.00633910844371	c
2.60778527879173	-0.00231206632121	0.00624202889939	n
-1.09162764378399	2.39178851525536	-0.08610589201106	n
4.21278170907640	2.13934326735097	-0.04945785965799	c
0.15347255672025	4.69144423643458	0.00820142739077	c
2.97734947335569	4.54054701230725	-0.06010620958630	c
-1.27388668795042	-1.90412129679246	0.05216048709557	o
6.52004666438358	1.83775606785162	-0.00297905537129	o
-0.80316439858660	6.27071276903433	-0.87718468106522	h
4.49281718333889	6.89428245725166	-0.00563083378742	c
-2.99933270401110	2.34415180453896	-0.14111157176387	h
3.45348054338964	-1.71332441663120	0.06197098194722	h
3.29101879705441	8.56565274057951	0.03208966903147	h
5.73531674188723	6.92796185226133	1.65039155234510	h
5.75191636428707	7.00285457918647	-1.64513068413810	h

Table S39: Geometry of the ground state of 1-methylthymine in atomic units obtained at RI-CC2/cc-pVDZ level

1.80009646109859	-3.79367496258727	-0.00000434755469	c
-0.96041289307839	-3.59768898832893	-0.00005085454695	c
-1.84519808002703	-1.07904910119822	-0.00000705555262	n
-0.46866939786484	1.16223559255944	-0.00003682334017	c
2.15161902225160	0.78039103005411	-0.00012369119249	n
3.19794815147379	-1.61519555813003	-0.00004697737567	c
-2.44984354509549	-5.39788932379239	-0.00002568233492	o
-1.42394490874515	3.28430991839479	0.00001820187420	o
2.94024720500453	-6.39380591975310	0.00018433635829	c
-3.76207866626817	-0.85505767310422	0.00005491374233	h
5.26752080186618	-1.66009065613468	0.00002223952075	h
5.02093369740000	-6.30308861163562	0.00239606878034	h
2.31102894411247	-7.46739294770402	1.67203858880720	h
2.31465350984262	-7.46640880575342	-1.67382602380108	h
3.71025681322392	3.06436102013922	-0.00000310057013	c
5.70600006193744	2.48992557996942	-0.00004039320419	h
3.30313386186607	4.21291831669698	-1.68565847026297	h
3.30301459264579	4.21297360901402	1.68579586372074	h

Table S40: Geometry of the ground state of 1-methylthymine in atomic units obtained at DFT/B3-LYP/TZVP level

-1.10499342051371	-3.19375064961400	0.00000000000000	c
1.50751964338444	-3.20098114528888	0.00000000000000	n
-2.16194884719171	-0.78781505671611	0.00000000000000	n
3.15503209492581	-1.12420399858921	0.00000000000000	c
-0.67389873180636	1.35177277972797	0.00000000000000	c
1.87526284095583	1.32304036536860	0.00000000000000	c
-2.37368436929262	-5.10832099318462	0.00000000000000	o
5.43436146349429	-1.43972144301429	0.00000000000000	o
-1.71596036643682	3.11239834913441	0.00000000000000	h
3.47417486255853	3.65988442030043	0.00000000000000	c
-4.92362130455349	-0.64444199597056	0.00000000000000	c
2.32307976424355	-4.93065197816885	0.00000000000000	h
2.30909964308711	5.36039654033708	0.00000000000000	h
4.70735888980318	3.70671116408920	1.65512637028744	h
4.70735888980318	3.70671116408920	-1.65512637028744	h
-5.47827667240064	1.33443530332988	0.00000000000000	h
-5.68954331792324	-1.57681412984823	-1.66897879197958	h
-5.68954331792324	-1.57681412984823	1.66897879197958	h

Table S41: Geometry of the S_1 state of 1-methylthymine in atomic units obtained at RI-CC2/cc-pVDZ level

1.75694348405518	-3.86302668834292	-0.10573923199763	c
-0.73318493981853	-3.49338152339869	-0.48611186610730	c
-1.80638579187829	-1.11184914764683	-0.68900126258495	n
-0.42808093876766	1.15590289900441	-0.52336738847694	c
2.14499332084592	0.78109709460693	-0.17155511377464	n
3.27099335468673	-1.58712983068312	0.18258473793598	c
-2.69412843607505	-5.35416167892345	-0.77249737470039	o
-1.48894361611972	3.23089154857949	-0.69471834589261	o
2.92913383090123	-6.44563721456626	0.11526006620164	c
-3.70654438907027	-0.90576046072651	-0.90889395822077	h
5.33688497172864	-1.62167454789001	0.05226105451245	h
4.51806091122568	-6.66862085369079	-1.21900997067085	h
3.65693194403028	-6.79518581368055	2.03934017051093	h
1.52243419396860	-7.92431877156596	-0.31624120526742	h
3.72606046963373	3.03030573773633	0.09646420405260	c
5.39382036290413	2.84794459003546	-1.13773603599701	h
2.59946748581980	4.68023269172386	-0.45903429751845	h
4.35460735525122	3.23955622544125	2.07277163327346	h

Table S42: Geometry of the S_1 state of 1-methylthymine in atomic units obtained at TDDFT/B3-LYP/TZVP level

-1.12383228113819	-3.16657136660862	0.01151925881324	c
1.52459780929535	-3.21004885715918	0.01144184937553	n
-2.16757567080027	-0.80808858788471	0.00673978709339	n
3.01886404685071	-1.05192017432135	0.00518098621639	c
-0.71337901536062	1.41404382915236	0.00173388597051	c
1.94010637402881	1.29579606462867	0.00101375639244	c
-2.32323877096305	-5.13190648592296	0.01540624514508	o
5.47474856280943	-1.59688707790376	0.00481531831584	o
-1.74444456963677	3.16630289194807	0.00016873508637	h
3.52613803708395	3.65925974069986	-0.00050484450755	c
-4.92564023856049	-0.67405977804090	0.00322809769054	c
2.32081640226831	-4.94110646413770	0.01517047075686	h
2.31369971766275	5.32504105387864	-0.01017498015490	h
4.73456633353959	3.77581425116575	1.67068272592174	h
4.74687492285587	3.76620887247419	-1.66340281108345	h
-5.47797036331590	1.30427047349682	0.00770806106041	h
-5.69297273097868	-1.59861753784854	-1.67072401111734	h
-5.69649393067223	-1.60529734365243	1.67175890854833	h

Table S43: Geometry of the T_1 state of 1-methylthymine in atomic units obtained at RI-CC2/cc-pVDZ level

1.70317472271263	-3.79443751663497	0.33352932017741	c
-0.93215173175741	-3.59854658290513	-0.33201141109121	c
-1.88248906706653	-1.08790200370039	-0.15367510351754	n
-0.40859850386869	1.07880881477306	-0.48303806986134	c
2.16780549675742	0.72476665528667	0.11625849267273	n
2.97821031637011	-1.46648122311994	1.36419262742017	c
-2.33355532575316	-5.36979046732614	-0.99970890804119	o
-1.27627527971744	3.11561483785489	-1.19838161622194	o
3.13454881191105	-6.17693864033697	-0.08287906722256	c
-3.69767892927891	-0.87250689008700	-0.77282408738826	h
5.02053332522328	-1.53457650968469	1.70170520015803	h
4.69804236805812	-5.87502288424652	-1.44127443157291	h
4.01317371307205	-6.82380931164785	1.70116079112503	h
1.86701685907941	-7.65794481078225	-0.80532548845107	h
3.83751574194105	2.91965749490436	-0.02022528344893	c
5.49823782787563	2.45676846829236	-1.18760505895278	h
2.77483069726809	4.48675013229941	-0.86605020329665	h
4.46583718900752	3.44646906017225	1.89640818740489	h

Table S44: Geometry of the T_1 state of 1-methylthymine in atomic units obtained at UDFT/B3-LYP/TZVP level

-1.05306206368927	-3.17107902223461	0.08422075152883	c
1.54840968385589	-3.23280210901547	-0.14362415380697	n
-2.13265773257050	-0.75852902002173	-0.09250175008783	n
3.18806046084868	-1.13432731758563	0.13770934752788	c
-0.73145943522245	1.31767581316610	-0.87079338498665	c
1.98706676932626	1.26394002606852	-0.14478467527234	c
-2.32166714328922	-5.05930721429700	0.39603930218667	o
5.44885895283895	-1.48703617236577	0.56077493842931	o
-1.73528426900143	3.09536685859662	-0.89433854216408	h
3.37638911502613	3.65298929575272	0.25344223629721	c
-4.88627587915847	-0.59648313923145	0.02248801442588	c
2.33896796310194	-4.95076713512949	0.12267178427826	h
2.36921495433900	4.87264452045715	1.59401563828285	h
5.28146351724811	3.29658866223284	0.94121129853870	h
3.49267664169115	4.72838428156510	-1.51972556551894	h
-5.40475890133369	1.26714669403501	0.72438285926282	h
-5.71539796958287	-0.88032933315739	-1.84908376170583	h
-5.59812429281185	-2.05012254752405	1.28427944409900	h

References

(1) Colarusso, P.; Zhang, K.; Guo, B.; Bernath, P. F. *Chem. Phys. Lett.* **1997**, *269*, 39–48.

Paper 3

Ab initio investigation of the methylation and hydration effects on the electronic spectrum of uracil and thymine

Mihajlo Etinski, and Christel M. Marian

Phys. Chem. Chem. Phys. **12**, (2010) 4915 - 4923

Ab initio investigation of the methylation and hydration effects on the electronic spectra of uracil and thymine†

Mihajlo Etinski and Christel M. Marian*

Received 7th December 2009, Accepted 2nd March 2010
First published as an Advance Article on the web 27th March 2010
DOI: 10.1039/b925677f

In this work we investigated the lowest-lying electronic excitations for a series of methyl-substituted uracil derivatives, *i.e.*, uracil, 1-methyluracil, 3-methyluracil, thymine, 1-methylthymine, 1,3-dimethyluracil, 3-methylthymine, 1,3-dimethylthymine, and their microhydrated complexes by means of coupled cluster singles and approximate doubles (CC2) and density functional theory (DFT) methods. The bulk water environment was mimicked by a combination of microhydration and the conductor-like screening model (COSMO). We find that the shift of the electronic excitation energies due to methylation and hydration depend on the character of the wave function and on the position of the methyl substituent. The lowest-lying singlet and triplet $n \rightarrow \pi^*$ states are insensitive to methylation but are strongly blue-shifted by microhydration and bulk water solvation. The largest red-shift of the first $^1(\pi \rightarrow \pi^*)$ excitation occurs upon methylation at N_1 followed by substitution at C_5 whereas no effect is obtained for a methylation at N_3. For this state, the effects of methylation and hydrogen bonding partially cancel. Upon microhydration with six water molecules, the order of the $^1(n \rightarrow \pi^*)$ and $^1(\pi \rightarrow \pi^*)$ states is reversed in the vertical spectrum. Electrostatic solute–solvent interaction in bulk water leads to a further increase of their energy separation. The $n \rightarrow \pi^*$ states are important intermediates for the triplet formation. Shifting them energetically above the primarily excited $^1(\pi \rightarrow \pi^*)$ state will considerably decrease the triplet quantum yield and thus increase the photostability of the compounds, in agreement with experimental observations.

1 Introduction

In heteroaromatic molecules, we are usually interested in lower-lying excited states that can have $n \rightarrow \pi^*$, $\pi \rightarrow \pi^*$, $\pi \rightarrow \sigma^*$, or Rydberg character. If the energy gap between their potential surfaces is small, non-adiabatic coupling can trigger relaxation to the ground state (photophysics) or chemical transformation (photochemistry).[1–4] In the isolated pyrimidine bases uracil (U) and thymine (T), the S_1 state exhibits $n \rightarrow \pi^*$ character while primary photoexcitation involves the optically bright $^1(\pi \rightarrow \pi^*)$ state (S_2).[5–17] It is common knowledge that substitution effects or hydration can shift electronic states or even change their order. Hence, they can modify the excited-state dynamics of the nucleic acids.[18,19] Replacement of a hydrogen by an electron-donating group in nitrogen-heterocyclic compounds is expected to lead to the blue-shift of an $n \rightarrow \pi^*$ state and the red-shift of a $\pi \rightarrow \pi^*$ state.[1] Indeed, methylation at the N_1 center of pyrimidine bases, for instance, is found to cause a red-shift of the absorption and fluorescence maxima.[20,21] This effect is of particular importance because the N_1 center of T (or U) is attached to a sugar molecule in DNA (or RNA). Furthermore, the electronic energy separation between $n \rightarrow \pi^*$ and $\pi \rightarrow \pi^*$ states can be changed by environment effects. Typically, $n \rightarrow \pi^*$ states are blue-shifted and $\pi \rightarrow \pi^*$ states are red-shifted by hydrogen bonding and solvent polarity.[1] In isoalloxazines that share some structural features with uracil, it has been shown recently that the size of the shift may depend strongly on the electronic structure of the $n \rightarrow \pi^*$ or $\pi \rightarrow \pi^*$ state in question.[22] One key step toward understanding the photo-excited processes of the pyrimidine bases in various environments is thus the determination of the properties of the electronically excited states.

In the gas phase, pump–probe experiments on U and T reveal that the relaxation kinetics following primary photoexcitation has components of femto, pico and nanosecond time scales.[23–29] On the basis of quantum chemical calculations, Matsika[7] suggested a relaxation pathway involving two conical intersections, the first one occurring between the $^1(\pi \rightarrow \pi^*)$ and $^1(n \rightarrow \pi^*)$ potential surfaces and the second one taking place between the intermediate $^1(n \rightarrow \pi^*)$ state and the electronic ground state. Perun *et al.*[9] as well as Merchán *et al.*[10] alternatively proposed direct ultrafast non-radiative decay of the optically bright $^1(\pi \rightarrow \pi^*)$ state to the electronic ground state to be the cause of the (sub)picosecond decay. The reaction coordinate related to the latter mechanism is the twist of the C_5–C_6 bond. In addition, several molecular dynamics simulations were performed.[30–33] All of these studies confirm the decisive role of the C_5–C_6 twist. However, the details of the decay mechanisms vary substantially among these works.

Institute of Theoretical and Computational Chemistry, Heinrich-Heine University Düsseldorf, Düsseldorf, Germany. E-mail: christel.marian@uni-duesseldorf.de

† Electronic supplementary information (ESI) available: The cartesian coordinates and vibrational frequencies of all structures, frontier molecular orbitals and vertical CC2 excitation energies of all chromophores. See DOI: 10.1039/b925677f

Also, the participation of the nearby $^1(n \rightarrow \pi^*)$ state in this process is still under debate. Another possibility considered was the decay of the excited-state population involving a $\pi \rightarrow \sigma^*$ state. Schneider *et al.*[34] examined the photofragmentation of thymine by monitoring the H loss and concluded that there was no evidence for an important role of the $\pi \rightarrow \sigma^*$ state. Similar conclusions based on quantum chemical calculations were recently drawn by González-Vázquez *et al.*[29]

Still there is controversy about the nature of the nanosecond decay. He *et al.*[24] found that the lifetime of the dark state of U derivatives strongly depends on the degree of methylation. They showed that the dark state of T has a lifetime that is an order of magnitude smaller than that of 1,3-dimethylthymine (1,3-DMT). Recently, we proposed the dark state to be the lowest $^3(\pi \rightarrow \pi^*)$ state which is formed *via* the intermediately populated $^1(n \rightarrow \pi^*)$ state.[35]

Also, there is some discussion as to whether the nanosecond decay is quenched in microhydrated clusters. He *et al.*[25] found a lifetime reduction upon gradual microhydration of methyl-substituted uracils and thymines. When more than four water molecules were present, they observed no ion signal, meaning that the relaxation of microhydrated T occurred on the subnanosecond time scale. Their findings are supported by a recent femtosecond pump–probe ionization experiment on thymine.[29] In contrast, Busker *et al.*[28] were able to detect 1-methylthymine (1-MT) and 1-methyluracil (1-MU) water clusters with nanosecond delayed ionization under careful control of the applied water–vapor pressure. They concluded that hydration did not quench the long-lived state.

In the present study we continue our previous examination of the excited states of uracil (U), thymine (T) and 1-methylthymine (1-MT).[35] We extend our study to various methylated uracils and thymines, namely: 1-methyluracil (1-MU), 3-methyluracil (3-MU), 1,3-dimethyluracil (1,3-DMU), 3-methylthymine (3-MT), and 1,3-dimethylthymine (1,3-DMT) (see Fig. 1 for the chemical structures). We will show that the shift of the electronic excitation energy depends on the character of the wave function and on the position of the methyl substituent. This phenomenon is rationalized through a molecular orbital (MO) picture. Furthermore, we will investigate the influence of the solvent environment (microhydration and bulk water) on the excitation energies.

2 Theoretical methods and computational details

All calculations were performed using the TURBOMOLE[36] program. We employed the following electronic structure methods: coupled cluster with approximate treatment of doubles (CC2) and density functional theory (DFT). The CC2 method[37] is an approximation to the coupled-cluster singles and doubles (CCSD) method where singles equations are retained in the original form and the doubles equations are truncated to the first order in the fluctuating potential. We used the resolution-of-identity (RI)[38] CC2 implementation in TURBOMOLE[39] for ground-state minimum searches.[40] RI-CC2 in combination with linear response theory was employed for excited-state optimizations,[41] vertical excitation energies and the calculation of properties.[42] We utilized DFT in connection with the B3-LYP[43] functional for ground-state optimization of the bare molecules and microhydrated complexes. All molecular structures were optimized without symmetry constraints.

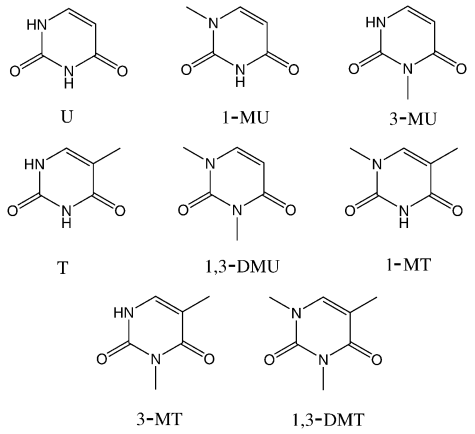

Fig. 1 Chemical structures of the methylated uracils and thymines discussed in this work.

We employed Dunning's[44,45] correlation-consistent basis sets cc-pVDZ (C, N, O: 9s4p1d/3s2p1d; H: 4s1p/2s1p) and aug-cc-pVDZ (C, N, O: 10s5p2d/4s3p2d; H: 5s2p/3s2p) and the standard TZVP (C, N, O: 10s6p1d/4s3p1d; H: 5s1p/3s1p) basis sets from the TURBOMOLE library.[46] Auxiliary basis sets for the RI approximation of the two electron integrals in the CC2 treatments were taken from the TURBOMOLE library.[47]

We determined the ground-state geometries of the methylated uracils and thymines at the RI-CC2/cc-pVDZ and B3-LYP/TZVP levels of theory. The ground states of the corresponding microhydrated complexes were optimized at the B3-LYP/TZVP level. For benchmark purposes, the minimum nuclear arrangement of the smallest water cluster (U + 6 H_2O) was also determined at the RI-CC2/cc-pVDZ level. All excited-state geometries were optimized at the RI-CC2/cc-pVDZ level. Throughout, vertical electronic excitation spectra were calculated at the RI-CC2/aug-cc-pVDZ level. It was shown previously that this combination of method and basis sets represents a good compromise between the cost of the calculation and the accuracy of the results.[12]

In order to compute spectral shifts that are consequences of electrostatic interactions in polar solvents, we used the conductor-like screening model (COSMO)[48,49] at the equilibrium geometries of the microhydated clusters. For the simulation of a bulk water environment we chose a dielectric constant of $\varepsilon = 78$.

3 Results and discussion

After a brief characterization of the most important frontier MOs and the electronic structure of the low-lying excited states we present the effects of methylation and microhydration on the excited-state properties searching for trends and striving for their explanation. Furthermore, the shifts of the vertical excitation energies due to the presence of a dielectric in addition to explicit water molecules, mimicking bulk water environment, are investigated. Finally, the consequences of the substitution and solvation effects on the photophysics of the

pyrimidine bases uracil and thymine will be discussed. The cartesian coordinates of all molecular structures may be found in the ESI.† For the bare chromophores, vibrational frequencies and infrared intensities are also displayed.

3.1 Electronic structure of the excited states

The frontier MOs of all compounds exhibit very similar shapes. Their electron density distributions are shown in Fig. 1 of the ESI.† Representative for all compounds we will analyze here only U and 1,3-DMT. Density distributions (isovalue = 0.03) of the most significant Hartree–Fock orbitals that contribute to the electronic structure of their excited states are presented in Fig. 2. The highest occupied molecular orbital (HOMO) of U is a π-orbital, π_H. Its electron density is distributed over the atoms in positions 1 and 5 of the ring and over the oxygen atoms. The HOMO–1 orbital, π_{H-1}, is a π-orbital as well. Its electron density is spread over the oxygen atoms and the nitrogen atom in position 3. The highest occupied σ-type orbital is HOMO–2. It is predominantly nonbonding with major amplitudes for the lone-pair orbitals at the oxygen atoms, mainly O_4. The lowest unoccupied molecular orbital (LUMO) is a Rydberg-type orbital (R) with diffuse charge distribution centered close to position 6. For the characterization of the electronic structure of the low-lying electronic states the Rydberg orbitals are of no relevance and are therefore not shown in Fig. 2. For the same reason, we denominate the lowest unoccupied π*-orbital with prevailing valence character by π^*_L.

In this work, we will study the lowest three singlet and triplet excited states. The first two singlet and three triplet states of the investigated molecules are of valence type while the third singlet state is of Rydberg type. In uracil, the first singlet state results from an $n_O \rightarrow \pi^*_L$ excitation. The second excited singlet state is a $\pi \rightarrow \pi^*$ state dominated by the $\pi_H \rightarrow \pi^*_L$ configuration. The third singlet excited state has major contributions from $\pi_H \rightarrow R$ excitations. The electronic structure of the lowest triplet state is related to the second excited singlet state while the second triplet state is akin to the first singlet state. The third triplet state is again a $\pi \rightarrow \pi^*$ state and does not have any counterpart among the first three singlet states. The prevailing contribution to its wave function stems from the $\pi_{H-1} \rightarrow \pi^*_L$ configuration. For further details on the electronic structures of the excited states of the other compounds the reader is referred to Tables 1–8 of the ESI.†

3.2 Effect of methylation on the electronic states

The vertical energies of the first three lowest singlet and triplet states computed at the RI-CC2/aug-cc-pVDZ level are presented in Fig. 3. To obtain these results we used ground-state geometries optimized at the B3-LYP/TZVP level. Benchmark data relating to RI-CC2/cc-pVDZ optimized coordinates are provided in Fig. 2 of the ESI.† A detailed comparison of these two data sets shows no major differences in the excitation energies. The nuclear arrangements of the chromophore–water clusters were therefore optimized at the computationally less demanding B3-LYP/TZVP level.

Unexpectedly, methylation causes almost no shift in the $n_O \rightarrow \pi^*_L$ excitation energies. Moreover, the red-shifts of $\pi_H \rightarrow \pi^*_L$ and $\pi_H \rightarrow R$ states are position dependent. Methylation in position 1 (1-MU) produces a shift of −0.26 eV for the $\pi_H \rightarrow \pi^*_L$ transition and of −0.10 eV for the $\pi_H \rightarrow R$ excitation energy with respect to the unsubstituted U. In contrast, no shift of the $\pi_H \rightarrow \pi^*_L$ excitation is found upon methylation in position 3 (3-MU) but again the $\pi_H \rightarrow R$ transition is red-shifted by 0.08 eV. In T (5-methyluracil) the excitation energy of the $\pi \rightarrow \pi^*$ state is red-shifted by 0.14 eV while the relative energy of the $\pi_H \rightarrow R$ state is red shifted by 0.26 eV. Hence, the largest shift of the $\pi_H \rightarrow \pi^*_L$ state absorption occurs when N_1 is methylated and of the $\pi_H \rightarrow R$ transition when C_5 is methylated. Addition of a second methyl group in position 1 (1-MT *vs.* T, and 1,3-DMT *vs.* 3-MT) and 5 (1-MT *vs.* 1-MU, and 3-MT *vs.* 3-MU) causes a further decrease in the excitation energies of the $\pi_H \rightarrow \pi^*_L$ and $\pi_H \rightarrow R$ states. Again we see that a second or third methylation in position 3 has almost no effect (compare 3-MT with 3-MU and 1,3-DMT with 1-MT). It is remarkable that these shifts are additive.

In the triplet manifold, methylation produces smaller shifts. The effects of the methylation on the triplet $\pi_H \rightarrow \pi^*_L$ state are similar to the effects on the second singlet state, as was expected. The smallest shift is produced in position 3. The effect on the triplet $\pi_{H-1} \rightarrow \pi^*_L$ state is more pronounced. Moreover, for the latter state, the largest shift is observed for substitution at N_3. The triplet $n_O \rightarrow \pi^*_L$ state is almost unaffected by methylation.

The position-dependent shifts due to methylation can be rationalized by examining the MOs in Fig. 2. The MOs of the other compounds (compare Fig. 1 of the ESI†) are similar and need not be discussed separately. The n_O orbital has the largest amplitude on the oxygen atoms so addition of a methyl group to the ring cannot markedly disturb its electron density. Comparing the orbital densities of the π^*_L MOs of U and 1,3-DMT (Fig. 2) almost no difference is noticed. In particular, at an isovalue of 0.03 there is no electron density visible on any of the three methyl groups in 1,3-DMT. As a result, methyl substitution in the 1, 3, or 5 position has a negligible effect on the transitions resulting from and $n_O \rightarrow \pi^*_L$ excitation. On the other hand, the π_H orbital has substantial electron density on the ring atoms at positions 1 and 5 but not at 3. Hyperconjugation by the methyl groups in positions 1 and 5 yields antibonding contributions to the π_H MO density and thus leads to an up-shift of its orbital energy enabling easier (and thus less energetic) excitations from this orbital. Since at the same time the accepting MO (π^*_L) is nearly unaffected by methyl substitution (see above), the trend for the $\pi_H \rightarrow \pi^*_L$ transition is dominated by the behavior of the π_H orbital energy. A similar analysis of the substitution effects on the excitation energies of the lowest $^1(\pi_H \rightarrow \pi^*_L)$ state was recently presented by Gustavsson *et al.*[11] Proceeding to the $\pi_H \rightarrow R$ excitation we find no interference between the diffuse charge distribution and the valence densities at the methyl groups in positions 3 and 5. The lowest Rydberg state of 3-MU, T, and 3-MT is thus supposed to experience similar shifts as the corresponding $\pi_H \rightarrow \pi^*_L$ state, in agreement with our findings. The methyl group at the 1-position, on the other hand, leads to a deformation of the Rydberg orbital by a σ^*-type overlap with the in-plane hydrogen and an up-shift of its orbital energy (see Fig. 1 of the ESI for the shape of the Rydberg orbital†).

Hence, the net effect of a methyl group at the 1-position on the $\pi_H \rightarrow R$ transition is small. Excitations from π_{H-1} are lowered in energy when a methyl substituent is introduced at position 3, in agreement with the trends for the $^3(\pi_{H-1} \rightarrow \pi_L^*)$ state. Along the same line of argument, we predict that methylation at the 6-position will lead to a general blue-shift of the low-lying excitations because antibonding interference with the π-like out-of-plane MOs of the methyl group will increase the π_L^* orbital energy.

Methylation, in particular at the 1 and 5 positions, decreases the energy gap between the primarily excited $^1(\pi_H \rightarrow \pi_L^*)$ state and the optically dark $n_O \rightarrow \pi_L^*$ states. In 1-MT (1,5-dimethyluracil) and 1,3-DMT (1,3,5-trimethyluracil) the states lie so close in energy that they are supposed to exhibit strong non-adiabatic interaction which in turn is expected to significantly increase the population of the $n \rightarrow \pi^*$ state. According to Lim,[1] the radiationless decay of the latter state is expected to increase dramatically with vibrational excitation of the out-of-plane bending modes. This might explain the strong dependence of the lifetimes of 1-MU, 1,3-DMU, T and 1,3-DMT on the excitation wavelength observed by He *et al.*[24,25]

For the bare compounds, the effect of methylation on the adiabatic excitation energies of the S_1 and T_1 states was also investigated. The S_1 state has $n_O \rightarrow \pi_L^*$ character whereas T_1 has $\pi_H \rightarrow \pi_L^*$ character. Their geometries are similar to the previously discussed excited-state geometries of U, T and 1-MT.[35] While the S_1 state remains planar, a V-shaped nuclear arrangement is found for T_1. Adiabatic energies related to those states are presented in Table 1. Geometry relaxation in the S_1 state gains about 1 eV of excess energy whereas the T_1 state is stabilized by about 0.6 eV. As was already shown for the vertical excitation energies, methylation has negligible influence on the $^1(n_O \rightarrow \pi_L^*)$ state. Concerning the $^3(\pi_H \rightarrow \pi_L^*)$ state, the shifts of the adiabatic energies caused by methylation are again additive. On the other hand, there is a change with regard to the most influential position of methyl substitution. In the vertical spectrum the largest shift emerges for methylation at position 1 whereas methylation at position 5 produces the largest shift on the adiabatic excitation energy. This reversal of the trend can again be understood by analyzing the MOs. In the T_1 state we observe a substantial elongation of the C_5–C_6 bond. In addition, the methyl groups at the 1- and 5-positions are rotated by 60°. The changes in the orbital densities with respect to the corresponding ground-state distributions are particularly pronounced in the π_H and π_L^* orbitals (compare Figs. 2 and 4). In particular, the antibonding contribution of the electron density at the methyl group at the 1-position is much smaller than at the 5-position. As a consequence, methylation at N_1 produces only slight shifts of the adiabatic T_1 excitation energy.

To our knowledge, there is very little experimental data on absorption maxima or band origins of methylated uracils in the gas phase or in supersonic beams. Clark *et al.*[50] measured vapor spectra and observed absorption maxima at 244 nm for U (corresponding to $\Delta E = 5.08$ eV) and 256 nm for 1,3-DMU (corresponding to $\Delta E = 4.84$ eV). The excitation energy of thymine (4.95 eV) was determined by electron energy loss spectroscopy.[51] Our computed vertical singlet $\pi_H \rightarrow \pi_L^*$ excitation energies of 5.27 eV for U, 5.13 eV for T, and 5.01 eV for 1,3-DMU (Fig. 3) reproduce the trend well, but overestimate the absolute values by about 0.2 eV, in agreement with the outcome of extensive benchmark calculations.[16] We expect our methods to yield $\pi \rightarrow \pi^*$ excitation energies of similar quality for the other compounds as well.

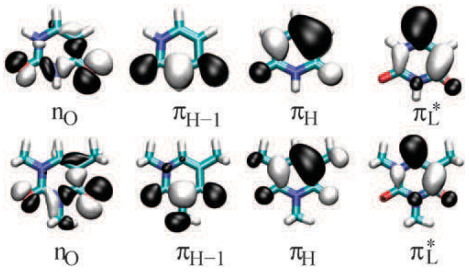

Fig. 2 Important Hartree–Fock orbitals of uracil (upper panel) and 1,3-dimethylthymine (lower panel) at the ground-state geometry. Orbitals are obtained with the aug-cc-pVDZ basis set.

Some time ago, band systems were observed in fluorescence excitation and dispersed fluorescence spectra of jet-cooled uracil derivatives.[52–54] Ito and coworkers[52,53] assigned system I with band origin at 35288 cm^{-1} (U), 33724 cm^{-1} (T), and 35354 cm^{-1} (1,3-DMU) to the $n \rightarrow \pi^*$ transition of the diketo tautomers whereas they attributed the lower-energetic system II with band origin at 30917 cm^{-1} (U) and 31111 cm^{-1} (T) to keto-enol tautomers. Brady *et al.*[54] was able to reproduce system I, but questioned the assignment of these bands to $n \rightarrow \pi^*$ transitions. Our results are rather in favor of the latter interpretation. First of all, the observed band origins of system I (corresponding to 4.38 eV for U, 4.18 eV for T, and 4.38 eV for 1,3-DMU) are much higher than our computed adiabatic energies shown in Table 1. A conservative estimate of the intrinsic errors of our method predicts our computed excitation energies to be too high by at most 0.3 eV. Second, the huge shift of the band origin by 1564 cm^{-1} (0.2 eV) upon methylation at C_5 does not fit the trends observed in our calculations. The measured band origins of system II (corresponding to 3.83 eV for U and 3.86 for T), on the other hand, are in better agreement with our computed adiabatic S_1 excitation energies of the diketo forms and their dependence on the methylation.

3.3 Effect of microhydration on the electronic states

One of us was previously involved in the examination of the effect of microhydration on the vertical excitation spectrum of 1-methylthymine.[28] In that work, microhydration was presented for one to five water molecules and it was found that the order of the lowest two excited singlet states varies with the number of water molecules until these are almost degenerate in the complex containing five water molecules. In the present work we continue that study increasing the number of explicit water molecules to six and at same time taking into account the effect of the methylation.

The optimized ground-state structures of the methylated uracils and thymines with six water molecules are presented in Fig. 5. Starting geometries were generated by placing water molecules around the solute molecule in positions where the

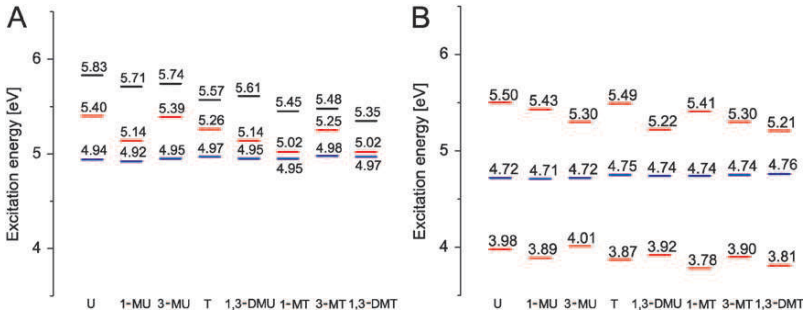

Fig. 3 Vertical excitation spectra of the bare chromophores computed at the RI-CC2/aug-cc-pVDZ level. The ground-state geometries were optimized at the DFT/B3-LYP/TZVP level. ($n \rightarrow \pi^*$ blue; $\pi \rightarrow \pi^*$ red; $\pi \rightarrow R$ black): A singlet states, B triplet states.

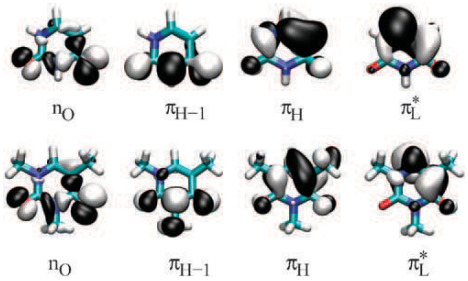

Fig. 4 Important Hartree–Fock orbitals of uracil (upper panel) and 1,3-dimethylthymine (lower panel) at the T_1 minimum. Orbitals are obtained with the aug-cc-pVDZ basis set.

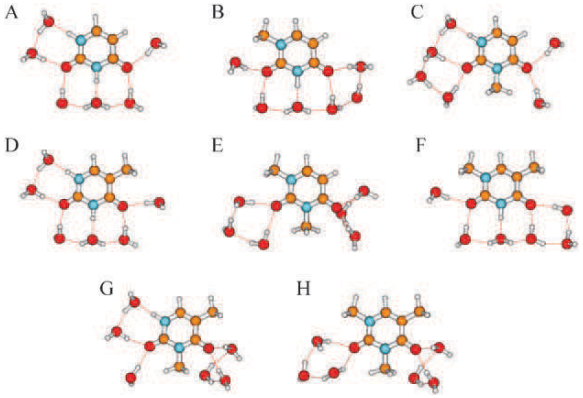

Fig. 5 Ground-state structures optimized at the B3-LYP/TZVP level: A U + $6H_2O$, B 1-MU + $6H_2O$, C 3-MU + $6H_2O$, D T + $6H_2O$, E 1,3-DMU + $6H_2O$, F, 1-MT + $6H_2O$, G 3-MT + $6H_2O$, H 1,3-DMT + $6H_2O$.

formation of hydrogen bonds with the heteroatoms of the compounds were to be expected. Methyl groups are not good hydrogen-bond donors or acceptors and we do not expect that they will contribute to the hydrogen-bonded network. In the water cluster of uracil, we found that all water molecules form hydrogen bonds with the solute. The same is true for thymine. In 1-MU, 3-MU, 1-MT, and 3-MT one water molecule is not bound to the solute molecule. This is a consequence of the methyl group blocking one of the possible hydrogen-bond donors of the pyrimidine ring. In 1,3-DMT, two water molecules are bound exclusively to other water molecules. In fact, the only remaining places for the creation of a hydrogen bond with the solute thymine are the two oxygen atoms. These optimized structures should be understood as possible conformers that can appear in the experiments with water clusters.[25,28,29] Many other conformers of comparable energy will be formed that cannot be investigated exhaustively in the framework of the present study. We expect the chosen cluster conformations to be representative, however.

For benchmark purposes, we optimized the structure of the uracil water cluster at the RI-CC2 level. At this geometry, we obtain excitation energies of 5.08 eV for the S_1 state ($\pi_H \rightarrow \pi_L^*$) and 5.10 eV for the S_2 ($n_O \rightarrow \pi_L^*$) state. Comparison with the results for the corresponding DFT-optimized complex (Fig. 6) shows that the order of states is conserved while the absolute excitation energies are consistently shifted by about 0.15 eV. The same trend was found also for the bare chromophores (see the ESI†). A peculiarity is observed in the case of S_3 at 6.12 eV which has $\pi_{H-1} \rightarrow \pi_L^*$ character at the RI-CC2 geometry whereas it is a Rydberg state in the DFT-optimized complex. The Rydberg state corresponds to the S_4 state at the RI-CC2 geometry, but its energy (6.16 eV) is nearly degenerate. These results justify the use of the less expensive DFT method for the determination of the nuclear arrangements of the microhydrated complexes, but we have to keep in mind that the RI-CC2 single-point energies at these nuclear arrangements are overestimated by about 0.15 eV, in addition to the systematic deviations inherent in the CC2 method.[16]

At the ground-state geometries of the water clusters, we calculated the vertical excitation spectra at the RI-CC2/aug-cc-pVDZ level. They are shown in Fig. 6. The main difference between the spectra of the microhydrated and bare molecules is that the order of the first two singlet states is

Table 1 Adiabatic energies of S_1 and T_1 obtained at the RI-CC2/aug-cc-pVDZ level in eV. (Geometries were optimized at the RI-CC2/cc-pVDZ level.)

State	U	1-MU	3-MU	T	1,3-DMU	1-MT	3-MT	1,3-DMT
S_1 ($n \rightarrow \pi^*$)	3.69	3.67	3.70	3.72	3.69	3.68	3.73	3.70
T_1 ($\pi \rightarrow \pi^*$)	3.21	3.16	3.23	3.07	3.19	3.03	3.09	3.06

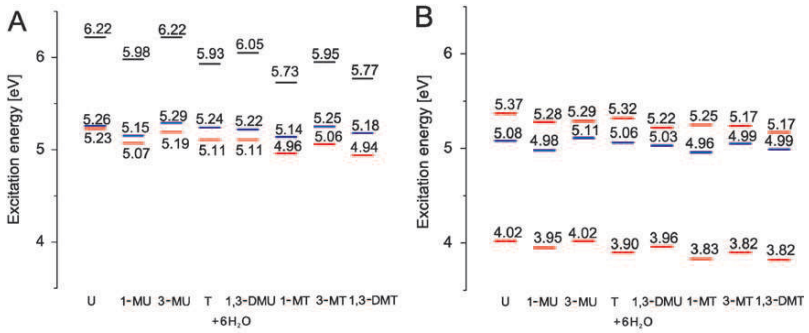

Fig. 6 Vertical excitation spectra of microhydrated complexes with 6 water molecules. ($n \rightarrow \pi^*$ blue; $\pi \rightarrow \pi^*$ red; $\pi \rightarrow \sigma^*$ black): A singlets, B triplets.

changed. Microhydration shifts the singlet $\pi_H \rightarrow \pi_L^*$ state below the $n_O \rightarrow \pi_L^*$ state. That is a consequence of the stabilization of the oxygen lone-pair orbitals and the concomitant destabilization of the $n_O \rightarrow \pi_L^*$ transition through hydrogen bonds. At first sight, no clear trend for the energy shifts due to microhydration can be made out. The stabilization of the $\pi_H \rightarrow \pi_L^*$ excitation appears to be particularly pronounced for those compounds that are unsubstituted at N_1. Methylation and hydration effects thus partially cancel. As a consequence, the variation of the $\pi_H \rightarrow \pi_L^*$ excitation energies is much smaller than in the bare chromophores. The partial cancellation of substitution and hydration effects might also explain the experimentally observed small shifts in the absorption maxima of uridine (1-ribose-uracil) and thymidine (1-deoxyribose thymine) with respect to their parent compounds.[20] Microhydration preferentially destabilizes the Rydberg state, resulting in an increase of the excitation energy of that state by approximately 0.4 eV on the average.

We optimized the S_1 and T_1 states of microhydrated uracil at the RI-CC2/cc-pVDZ level. Interestingly, the S_1 state has $n_O \rightarrow \pi_L^*$ character although it is only the second excited singlet state in the vertical spectrum. T_1 has the same character as in the vertical spectrum, that is $\pi_H \rightarrow \pi_L^*$. In both cases, the C–O bond lengths are extended compared to the corresponding geometries of isolated U and a concomitant contraction of the neighboring bonds in the pyrimidine ring. In the T_1 state, the out-of-plane distortion is less pronounced than in bare U as reflected in a C_2–N_1–C_6–C_5 dihedral angle of 41° (U + 6 H_2O) compared to 46° (U). The blue-shift of the $^1(n_O \rightarrow \pi_L^*)$ state due to microhydration is somewhat smaller at the excited-state geometry (0.22 eV) compared to the shift at the ground-state geometry (0.32 eV) yielding an adiabatic S_1 excitation energy of 4.10 eV for the microhydrated complex. In the triplet case, the effects of geometry relaxation and microhydration are not additive either. The adiabatic excitation energy of the triplet $\pi_H \rightarrow \pi_L^*$ state is shifted by −0.15 eV due to microhydration resulting in a value of 3.39 eV. Comparison with the corresponding values of the bare chromophores in Table 1 shows that the adiabatic energies of both states are higher in the microhydrated environment.

3.4 Excitation energies in aqueous solution

In order to estimate the vertical excitation energies in bulk water we used the dielectric continuum model COSMO in addition to microhydration. The calculated vertical excitation energies are presented in Fig. 7. The effect of the electrostatic solute–solvent interaction on the singlet $\pi_H \rightarrow \pi_L^*$ states was found to be negligible. On the other hand, the $n \rightarrow \pi^*$ states are strongly blue-shifted, in line with their significantly lower dipole moment compared to the electronic ground state (see Tables 1–8 of the ESI†). Due to that differential effect a significant energy gap opens up between the $^1(\pi_H \rightarrow \pi_L^*)$ and $^1(n_O \rightarrow \pi_L^*)$ states in aqueous solution, ranging from 0.29 eV in U to 0.48 eV in 1,3-DMT. Surprisingly, the T_1 state is found to exhibit a significantly lower static dipole moment than its singlet counterpart (see Tables 1–8 of the ESI†). As a consequence, it is slightly blue-shifted by the dielectric continuum. In contrast, the $^3(n_O \rightarrow \pi_L^*)$ states experience blue-shifts of the order of 0.25 eV, in agreement with expectations. The T_3 state is nearly unaffected by the electrostatic solute–solvent interactions and is found to be near degenerate with T_2.

In the literature, several theoretical investigations on the effect of hydration on the vertical excitation energies of uracil have been undertaken. Improta and Barone[55] used TD-DFT in combination with the polarizable continuum model PCM, Zazza *et al.*[56] applied the pertubation matrix method (PMM), Ludwig *et al.*[57] utilized a Monte Carlo/quantum mechanical (MC/QM) approach while Kistler and Matsika[58] employed a combined multi-reference configuration interaction and molecular dynamics approach to model solvent shifts. In Table 2, a selection of previously obtained results are summarized together with our results. Almost all methods give a red-shift of the $\pi \rightarrow \pi^*$ excitation in the interval 0.1–0.2 eV. It is smaller than the value of 0.31 eV that was found experimentally.[59] A recent QM/MM-MD study on the solvent effects on the absorption spectrum of guanine showed that shifts arise both from intrinsic solute–solvent interactions and from nuclear motion effects of the solute.[60] Both effects lead to a red-shift of the absorption maximum on the order of 0.1 eV. The latter effects are not included if a continuum model such as PCM or COSMO is applied at the ground state equilibrium geometry of a microhydrated cluster. In the above mentioned MD simulations of the solvent effects on the uracil absorption by Kistler and Matsika[58] and in the MC/QM simulations by Ludwig *et al.*[57] the solute geometry was kept rigid and thus the nuclear motion effects are neglected as well. Inclusion of these effects is expected to bring the computed solvent shifts into good agreement with the experimental observations.

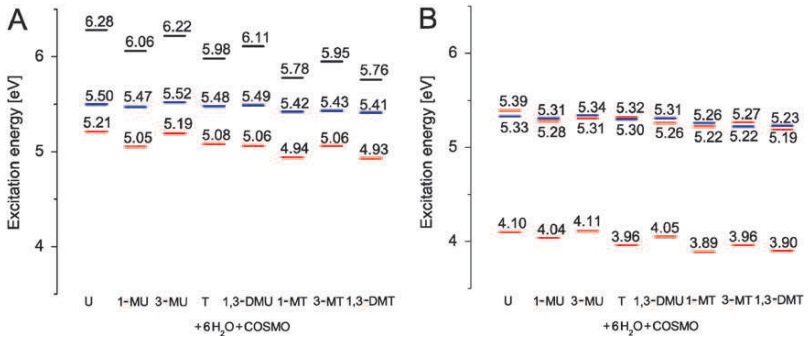

Fig. 7 Vertical excitation spectra of chromphores in aqueous solution. ($n \rightarrow \pi^*$ blue; $\pi \rightarrow \pi^*$ red; $\pi \rightarrow \sigma^*$ black): A singlets, B triplets.

Gustavsson *et al.*[11] measured the absorption spectra of various methylated uracils and thymines in aqueous solution at room temperature. Our computed vertical excitation energies are about 0.40 eV higher than the energetic positions of the experimental absorption maxima of the first bright state of U (4.79 eV), 1-MU (4.64 eV), 3-MU (4.79 eV), T (4.68 eV), 1,3-DMU (4.66 eV) and 1-MT (4.55 eV), but the trends for methylation effects are excellently reproduced by the calculations.

Concerning the blue-shift of the singlet $n_O \rightarrow \pi^*_L$ state, it varies from 0.2 to 0.8 eV depending on the type of calculation. Our value for the microhydrated cluster in the COSMO environment (0.56 eV) is in good agreement with the results of the other approaches that use both explicit water molecules in addition to a continuum model to mimic solution in bulk water (Table 2). These studies show that both hydrogen-bonding and the solvent polarity contribute to the destabilization of the $n_O \rightarrow \pi^*_L$ states. We can roughly estimate the adiabatic excitation energy of the $^1(n_O \rightarrow \pi^*_L)$ state of U in bulk water by adding the electrostatic shifts computed at the ground-state geometry (+0.3 eV) to the adiabatic excitation energy of the microhydrated cluster. If we further assume that the systematic errors of our approach are similar for the vertical and adiabatic excitation energies, an estimated value of about 4.2 eV for the adiabatic excitation energy of the $^1(n_O \rightarrow \pi^*_L)$ state of U in bulk water is obtained. This value is still significantly lower than the typical energy of the pump laser (4.64 eV corresponding to 267 nm) used in many experiments. Although the $^1(\pi_H \rightarrow \pi^*_L)$ state is supposed to be the S_1 state in aqueous solution, it might therefore well be that Hare *et al.*[61] observe the $^1(n \rightarrow \pi^*)$ state as a transient under these conditions.

The relaxation dynamics of a heterocyclic compound critically depends on the order and the energy separation of its $\pi \rightarrow \pi^*$ and $n \rightarrow \pi^*$ states. It is therefore expected that the photophysics of the pyrimidines is significantly changed by methylation and by solvation. A recent dynamics simulation on uracil including solvent effects predicts an ultrafast $^1(\pi_H \rightarrow \pi^*_L)$–$^1(n_O \rightarrow \pi^*_L)$ decay after laser excitation with 10–25% yields, weakly dependent on the solvent.[62] However, these results are deduced from a calculation in a small basis set where the two singlet states are near degenerate (ΔE = 0.007 eV at the Franck–Condon point). Shifting the potential surfaces to a more realistic energy gap (0.193 eV), the quantum yield for internal conversion is reduced to 2–10%. We expect the rate to decrease further if an energy gap of 0.29 eV, corresponding to our value, was used. For the methyl-substituted uracils our calculated energy gap is even larger, increasing to 0.48 eV in 1-MT and 1,3-DMT. Therefore, the branching ratio between the two-step $^1(\pi_H \rightarrow \pi^*_L)$–$^1(n_O \rightarrow \pi^*_L)$ ground-state relaxation and the one-step $^1(\pi_H \rightarrow \pi^*_L)$ ground-state decay is

Table 2 Vertical excitation energy shifts for uracil due to hydration (eV)

Level of theory	S_1 ($n \rightarrow \pi^*$)	S_2 ($\pi \rightarrow \pi^*$)
RI-CC2/aug-cc-pVDZ+6H_2O[a]	+0.32	−0.17
RI-CC2/aug-cc-pVDZ/COSMO	+0.45	−0.16
RI-CC2/aug-cc-pVDZ+6H_2O/COSMO	+0.56	−0.19
QM/MM MCSCF/cc-pVDZ[b]	+0.40	−0.15
QM/MM MRCI1/cc-pVDZ[b]	+0.42	−0.11
QM/MM MRCI2/cc-pVDZ[b]	+0.41	−0.05
MCSCF/PCM/cc-pVDZ[b]	+0.24	−0.16
PMM/TD-B3-LYP/aug-cc-pVTZ[c]	+0.38	−0.18
PMM/TD-PBE0/aug-cc-pVTZ[c]	+0.54	−0.10
PMM/CCSD/aug-cc-pVTZ[c]	+0.34	−0.12
SCRF/CCSD/aug-cc-pVTZ[c]	+0.21	−0.07
MC/QM TD-B3-LYP/6-31G(2p,2d) 300 H_2O (SCP)[d]	+0.80	−0.02
TD-B3LYP/6-31G(2p,2d) PCM[d]	+0.40	−0.04
TD-B3LYP/6-31G(2p,2d) 9H_2O+PCM[d]	+0.62	−0.17
TD-PBE0/6-311+G(2d,2p)/PCM[e]	+0.29	−0.09
TD-PBE0/6-311+G(2d,2p)/PCM + 4H_2O[e]	+0.48	−0.10
Experiment		−0.31[f]

[a] Only microhydration, [b] Ref. 58. [c] Ref. 56. [d] Ref. 57. [e] Ref. 55. [f] Absorption maximum in water,[59]

expected to be smaller in these compounds. The experimental results of Hare *et al.*[61] seem to contradict these conclusions since these authors report a constant branching ratio in all solvents. It should be kept in mind, however, that in this experiment the initially prepared wave packet had a lot of excess energy. It would be interesting to see the outcome for a pump pulse with a longer wavelength.

Recently, we proposed the singlet $n_O \rightarrow \pi^*_L$ state to act as a doorway state for the triplet formation.[35] The strong blue-shift of that state in aqueous solution makes it less accessible for a direct involvement in the relaxation mechanism following the primary photoexcitation of the singlet $\pi \rightarrow \pi^*$ state. Due to the increased energy gap also the vibronic interactions between the triplet $\pi \rightarrow \pi^*$ and $n \rightarrow \pi^*$ states will diminish. In literature, a huge solvent dependence of the triplet quantum yield of uracil derivatives has been reported. Hare *et al.*[61] found the triplet yield of 1-cyclohexyluracil to vary between 0.03 in water and 0.54 in ethyl acetate. The unsubstitued U and T were studied in water and uracil.[63] The ratios of the triplet yields in water and acetonitile (1 : 10) are consistent with the findings of Hare *et al.* Further there is experimental evidence that methylation suppresses triplet formation.[64] In the series U, T, 1,3-DMU, and 1,3-DMT in acetonitrile solution the following triplet quantum yields were reported: U 0.2, T 0.06, 1,3-DMU 0.02, 1,3-DMT $\leq$ 0.004, showing that dimethyl substitution at the nitrogen atoms reduces the triplet yield by roughly a factor of 10. Moreover, methylation at C_5 is seen to have a significant influence on the triplet formation. On a qualitative basis, our trends found for the computed energy gaps explain the experimental observations. However, it is very difficult to predict quantitatively how the change of the vertical electronic energy separation between the $\pi_H \rightarrow \pi^*_L$ and $n_O \rightarrow \pi^*_L$ states will affect the triplet quantum yields. Further dynamical studies including consideration of spin–orbit interaction will be required for this purpose.

4 Summary and conclusion

We have studied the effects of methylation and hydration on the electronic states of uracil and thymine. It was found that singlet and triplet $n \rightarrow \pi^*$ states are insensitive to methylation but are strongly blue-shifted by microhydration and bulk water solvation. The methylation effect is substantial for the lowest $^1(\pi \rightarrow \pi^*)$ and the $^1(\pi \rightarrow R)$ states. It is not an artifact of the calculation, as *e.g.* caused by basis set superposition errors, since the effect is found to be heavily position dependent. For the singlet $\pi_H \rightarrow \pi^*_L$ state the largest red-shift occurs upon methylation at N_1 followed by substitution at C_5 whereas no effect is obtained for a methylation at N_3. A similar but less pronounced effect is found in the corresponding triplet, T_1. In the case of the first Rydberg state, the size of the red-shift depends on the position of the methyl group, too. Here, the most significant shift is observed at the 5-position while substitution at the 1- and 3-positions leads to a smaller, but nearly equal shift. The second triplet state has a different electronic structure. It originates from a $\pi_{H-1} \rightarrow \pi^*_L$ excitation. Its excitation energy is red-shifted markedly in case of a methyl substitution at N_3. Interestingly, successive methylation in different positions produces a shift that is a sum of the individual shifts due to methyl substituents in those positions.

In all compounds, hydrogen bonding leads to a strong blue-shift of $^1(\pi_H \rightarrow R)$. It should thus play only a minor role in the photophysics of the hydrated chromophores. While hydration and methylation effects are found to be additive for the $^1(\pi_H \rightarrow R)$ state this is not the case for $^1(\pi_H \rightarrow \pi^*_L)$. Rather, hydrogen-bonding effects are diminished in the methylated compounds, in particular in those carrying a methyl group at N_1. As a consequence, the strong variation of the $^1(\pi_H \rightarrow \pi^*_L)$ excitation energies observed in the bare chromophores is levelled out to a certain extent. In the microhydrated clusters a preference for methylation at the 1- and 5-positions still exists, though. The solvent polarity has a negligible effect on $^1(\pi_H \rightarrow \pi^*_L)$ and even a slightly destabilizing effect on $^3(\pi_H \rightarrow \pi^*_L)$. In contrast, the singlet and triplet $n \rightarrow \pi^*$ states are strongly destabilized in polar protic solvents.

While $^1(n_O \rightarrow \pi^*_L)$ is the S_1 state in the isolated chromophores, the order of states in the singlet manifold is reversed due to hydrogen bonding with 6 H_2O molecules. In all microhydrated complexes investigated here, the $^1(\pi_H \rightarrow \pi^*_L)$ corresponds to S_1 in the vertical excitation spectrum with the $^1(n_O \rightarrow \pi^*_L)$ state only slightly higher in energy. With regard to the adiabatic excitation energies, the $^1(n_O \rightarrow \pi^*_L)$ state might still represent the global minimum on the S_1 potential surface, as demonstrated for U·6H_2O. However, the electrostatic solute–solvent interaction in bulk water leads to a further increase of the $^1(\pi_H \rightarrow \pi^*_L)$–$^1(n_O \rightarrow \pi^*_L)$ separation. In bulk water, we predict the S_1 state to have $^1(\pi_H \rightarrow \pi^*_L)$ character.

The $n_O \rightarrow \pi^*_L$ states are important for the triplet formation, either directly as transients connecting the optically active $^1(\pi_H \rightarrow \pi^*_L)$ and the $^3(\pi_H \rightarrow \pi^*_L)$ state or indirectly as mediators *via* vibronic interaction. The long-lived T_1 state typically undergoes photochemical addition reactions and is thus a major source of photolesions. Pushing the $n_O \rightarrow \pi^*_L$ state energetically above the primarily excited $^1(\pi_H \rightarrow \pi^*_L)$ state will considerably suppress the triplet formation and hence increase the photostability. Our results are thus in agreement with the experimental finding that the triplet quantum yield diminishes substantially upon substitution at the 1-position and in polar protic solvents.

Acknowledgements

Financial support by the Deutsche Forschungsgemeinschaft through SFB 663 is gratefully acknowledged.

References

1 E. C. Lim, *J. Phys. Chem.*, 1986, **90**, 6770–6777.
2 W. Domcke, D. R. Yarkony and H. Köppel, *Conical Intersections: Electronic Structure, Dynamics and Spectroscopy*, World Scientific, Singapore, 2004.
3 M. Klessinger and J. Michl, *Excited States and Photochemistry of Organic Molecules*, VCH Publishers Inc., New York, 1995.
4 N. J. Turro, V. Ramamurthy and J. C. Scaiano, *Principles of Molecular Photochemistry*, University Science Books, Sausalito CA, 2009.
5 J. Lorentzon, M. P. Fülscher and B. O. Roos, *J. Am. Chem. Soc.*, 1995, **117**, 9265–9273.

6 C. M. Marian, F. Schneider, M. Kleinschmidt and J. Tatchen, *Eur. Phys. J. D*, 2002, **20**, 357–367.
7 S. Matsika, *J. Phys. Chem. A*, 2004, **108**, 7584.
8 M. Z. Zgierski, S. Patchkovskii, T. Fujiwara and E. C. Lim, *J. Phys. Chem. A*, 2005, **109**, 9384–9387.
9 S. Perun, A. L. Sobolewski and W. Domcke, *J. Phys. Chem. A*, 2006, **110**, 13238–13244.
10 M. Merchán, R. González-Luque, T. Climent, L. Serrano-Andrés, E. Rodríguez, M. Reguero and D. Peláez, *J. Phys. Chem. B*, 2006, **110**, 26471–26476.
11 T. Gustavsson, A. Bányász, E. Lazzarotto, D. Markovitsi, G. Scalmani, M. Frisch, V. Barone and R. Improta, *J. Am. Chem. Soc.*, 2006, **128**, 607–619.
12 T. Fleig, S. Knecht and C. Hättig, *J. Phys. Chem. A*, 2007, **111**, 5482–5491.
13 A. Yoshikawa and S. Matsika, *Chem. Phys.*, 2008, **347**, 393–404.
14 G. Zechmann and M. Barbatti, *J. Phys. Chem. A*, 2008, **112**, 8273–8279.
15 E. Epifanovsky, K. Kowalski, P.-D. Fan, M. Valiev, S. Matsika and A. I. Krylov, *J. Phys. Chem. A*, 2008, **112**, 9983–9992.
16 M. Schreiber, M. R. Silva-Junior, S. P. A. Sauer and W. Thiel, *J. Chem. Phys.*, 2008, **128**, 134110.
17 M. R. Silva-Junior, M. Schreiber and W. Thiel, *J. Chem. Phys.*, 2008, **129**, 104103.
18 C. E. Crespo-Hernández, B. Cohen, P. M. Hare and B. Kohler, *Chem. Rev.*, 2004, **104**, 1977–2019.
19 C. T. Middleton, K. de La Harpe, C. Su, Y. K. Law, C. E. Crespo-Hernández and B. Kohler, *Annu. Rev. Phys. Chem.*, 2009, **60**, 217–239.
20 J. W. Longworth, R. O. Rahn and R. G. Shulman, *J. Chem. Phys.*, 1966, **45**, 2930–2939.
21 R. Becker and G. Kogan, *Photochem. Photobiol.*, 1980, **31**, 5–13.
22 S. Salzmann, J. Tatchen and C. M. Marian, *J. Photochem. Photobiol., A*, 2008, **198**, 221–231.
23 H. Kang, K. T. Lee, B. Jung, Y. J. Ko and S. K. Kim, *J. Am. Chem. Soc.*, 2002, **124**, 12958–12959.
24 Y. He, C. Wu and W. Kong, *J. Phys. Chem. A*, 2003, **107**, 5145–5148.
25 Y. He, C. Wu and W. Kong, *J. Phys. Chem. A*, 2004, **108**, 943–949.
26 S. Ullrich, T. Schultz, M. Z. Zgierski and A. Stolow, *Phys. Chem. Chem. Phys.*, 2004, **6**, 2796–2801.
27 C. Canuel, M. Mons, F. Piuzzi, B. Tardivel, I. Dimicoli and M. Elhanine, *J. Chem. Phys.*, 2005, **122**, 074316.
28 M. Busker, M. Nispel, T. Häber, K. Kleinermanns, M. Etinski and T. Fleig, *ChemPhysChem*, 2008, **9**, 1570–1577.
29 J. González-Vázquez, L. González, E. Samoylova and T. Schultz, *Phys. Chem. Chem. Phys.*, 2009, **11**, 3927–3934.
30 H. R. Hudock, B. G. Levine, A. L. Thompson, H. Satzger, D. Townsend, N. Gador, S. Ullrich, A. Stolow and T. J. Martinez, *J. Phys. Chem. A*, 2007, **111**, 8500–8508.
31 Z. Lan, E. Fabiano and W. Thiel, *J. Phys. Chem. B*, 2009, **113**, 3548–3555.
32 D. Asturiol, B. Lasorne, M. A. Robb and L. Blancafort, *J. Phys. Chem. A*, 2009, **113**, 10211–10218.
33 J. J. Szymczak, M. Barbatti, J. T. S. Hoo, J. A. Adkins, T. L. Windus, D. Nachtigallová and H. Lischka, *J. Phys. Chem. A*, 2009, **113**, 12686–12693.
34 M. Schneider, R. Maksimenka, F. J. Buback, T. Kitsopoulis, L. R. Lago and I. Fischer, *Phys. Chem. Chem. Phys.*, 2006, **8**, 3017–3021.
35 M. Etinski, T. Fleig and C. M. Marian, *J. Phys. Chem. A*, 2009, **113**, 11809–11816.
36 R. Ahlrichs, M. Bär, H.-P. Baron, R. Bauernschmitt, S. Böcker, N. Crawford, P. Deglmann, M. Ehrig, K. Eichkorn, S. Elliott, F. Furche, F. Haase, M. Häser, C. Hättig, H. Horn, C. Huber, U. Huniar, M. Kattannek, A. Köhn, C. Kölmel, M. Kollwitz, K. May, P. Nava, C. Ochsenfeld, H. Öhm, H. Patzelt, D. Rappoport, O. Rubner, A. Schäfer, U. Schneider, M. Sierka, O. Treutler, B. Unterreiner, M. von Arnim, F. Weigend, P. Weis and H. Weiss, *TURBOMOLE (Vers. 5.7)*, Universität Karlsruhe, 2004.
37 O. Christiansen, H. Koch and P. Jørgensen, *Chem. Phys. Lett.*, 1995, **243**, 409–418.
38 O. Vahtras, J. Almlöf and M. W. Feyereisen, *Chem. Phys. Lett.*, 1993, **213**, 514–518.
39 C. Hättig and F. Weigend, *J. Chem. Phys.*, 2000, **113**, 5154–5161.
40 C. Hättig, *J. Chem. Phys.*, 2003, **118**, 7751–7761.
41 A. Köhn and C. Hättig, *J. Chem. Phys.*, 2003, **119**, 5021–5036.
42 C. Hättig and A. Köhn, *J. Chem. Phys.*, 2002, **117**, 6939–6951.
43 A. D. Becke, *J. Chem. Phys.*, 1993, **98**, 5648–5652.
44 T. H. J. Dunning, *J. Chem. Phys.*, 1989, **90**, 1007–1023.
45 R. A. Kendall, T. H. J. Dunning and R. J. Harrison, *J. Chem. Phys.*, 1992, **96**, 6796–6806.
46 A. Schäfer, C. Huber and R. Ahlrichs, *J. Chem. Phys.*, 1994, **100**, 5829–5835.
47 F. Weigend, A. Köhn and C. Hättig, *J. Chem. Phys.*, 2002, **116**, 3175.
48 A. Klamt and G. Schüürmann, J. Chem. Soc., *J. Chem. Soc., Perkin Trans. 2*, 1993, 799–805.
49 A. Schäfer, A. Klamt, D. Sattel, J. Lohrenz and F. Eckert, *Phys. Chem. Chem. Phys.*, 2000, **2**, 2187–2193.
50 L. B. Clark, G. G. Peschel and I. Tinoco, Jr., *J. Phys. Chem.*, 1965, **69**, 3615–3618.
51 R. Abouaf, J. Pommier and H. Dunet, *Chem. Phys. Lett.*, 2003, **381**, 486–494.
52 M. Fujii, T. Tamura, N. Mikami and M. Ito, *Chem. Phys. Lett.*, 1986, **126**, 583–587.
53 Y. Tsuchiya, T. Tamura, M. Fujii and M. Ito, *J. Phys. Chem.*, 1988, **92**, 1760–1765.
54 B. B. Brady, L. A. Peteanu and D. H. Levy, *Chem. Phys. Lett.*, 1988, **147**, 538–543.
55 R. Improta and V. Barone, *J. Am. Chem. Soc.*, 2004, **126**, 14320–14321.
56 C. Zazza, A. Amadei, N. Sanna, A. Grandi, G. Chillemi, A. D. Nola, M. D'Amramo and M. Aschi, *Phys. Chem. Chem. Phys.*, 2006, **8**, 1385–1393.
57 V. Ludwig, K. Coutinho and S. Canuto, *Phys. Chem. Chem. Phys.*, 2007, **9**, 4907–4912.
58 K. A. Kistler and S. Matsika, *J. Phys. Chem. A*, 2009, **113**, 12396–12403.
59 L. B. Clark, G. G. Peschel and J. I. Tinoco, *J. Phys. Chem.*, 1965, **69**, 3615–3618.
60 M. Parac, M. Doerr, C. M. Marian and W. Thiel, *J. Comput. Chem.*, 2010, **31**, 90–106.
61 P. M. Hare, C. E. Crespo-Hernández and B. Kohler, *J. Phys. Chem. B*, 2006, **110**, 18641–18650.
62 R. Improta, V. Barone, A. Lami and F. Santoro, *J. Phys. Chem. B*, 2009, **113**, 14491–14503.
63 C. Salet and R. Bensasson, *Photochem. Photobiol.*, 1975, **22**, 231–235.
64 R. S. Becker, R. V. Bensasson and C. Salet, *Photochem. Photobiol.*, 1981, **33**, 115–116.

Supplementary Material (ESI) for PCCP

Ab initio investigation of the methylation and hydration effects on the electronic spectrum of uracil and thymine

Electronic Supplementary Information

Mihajlo Etinski, Christel Marian

February 26, 2010

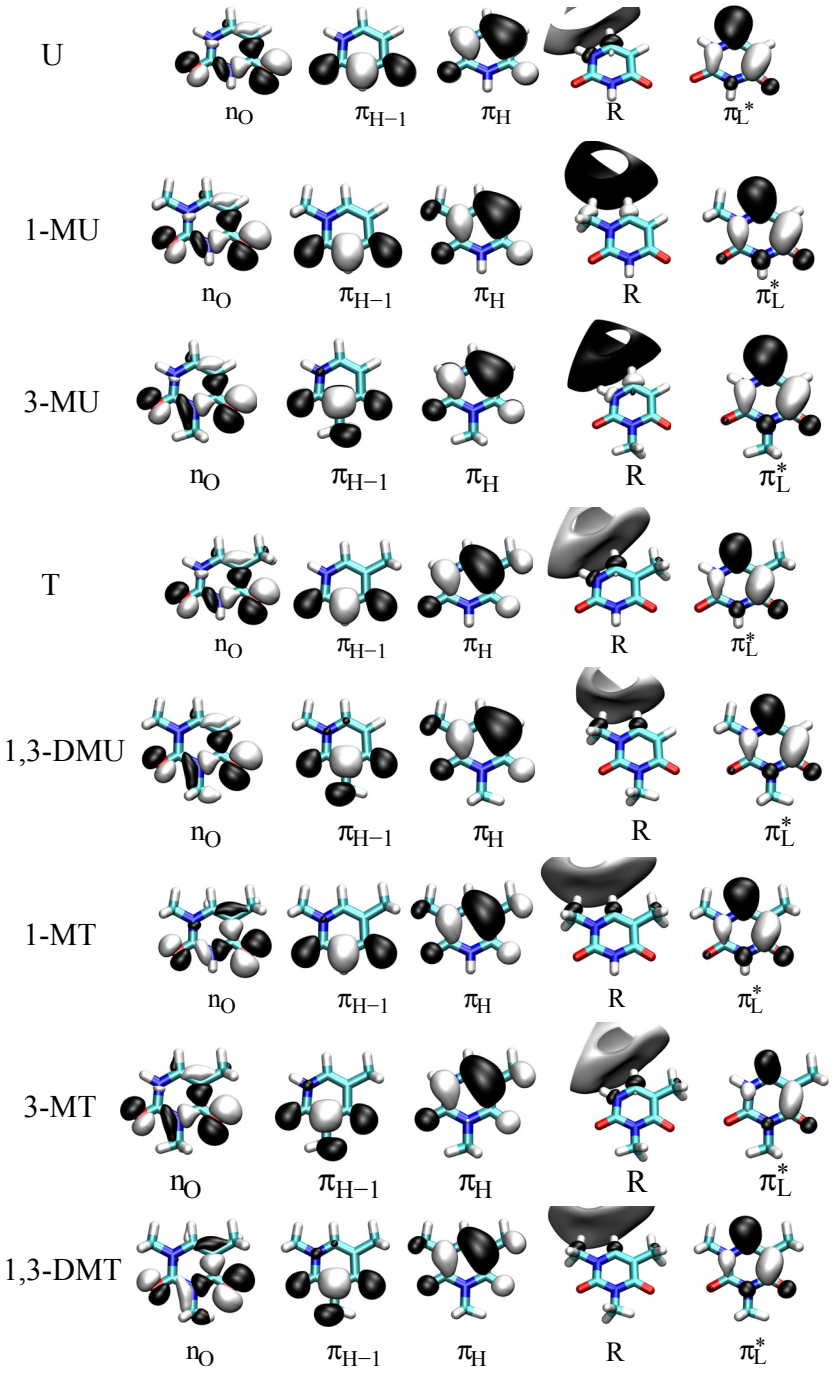

Figure 1: Hartree-Fock orbitals in aug-cc-pVDZ basis

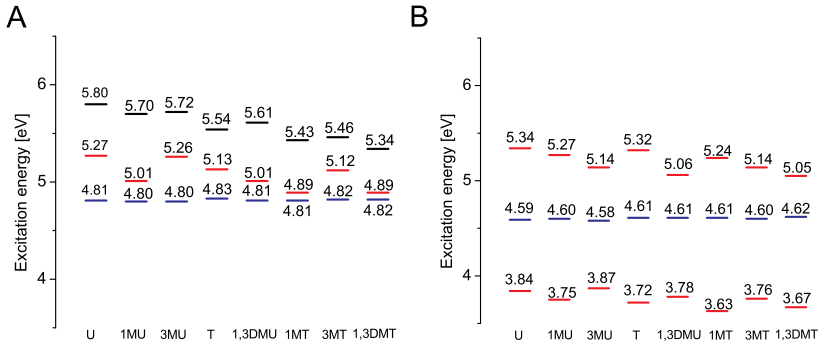

Figure 2: Vertical excitation spectra of the bare chromophores computed at the RI-CC2/aug-cc-pVDZ level. The ground-state geometries were optimized at the RI-CC2/cc-pVDZ level. (n $\rightarrow \pi^*$ blue; $\pi \rightarrow \pi^*$ red; $\pi \rightarrow$R black): A singlet states, B triplet states. For the denomination of the compounds see Figure 1 of the main paper.

For obtaining the results shown in Figure 2 we used ground-state geometries optimized at the RI-CC2/cc-pVDZ level whereas the excitation energies relating to B3-LYP/TZVP optimized coordinates are presented in Figure 3 of the main paper. Similar trends are observed for these two sets of calculations. The $n \rightarrow \pi^*$ and $\pi \rightarrow \pi^*$ state excitation energies are somewhat higher at the DFT-optimized geometries. The main reason for the increase of the computed excitation energy when using DFT-optimized structures is the contraction of the C-O bond lengths. This phenomenon has been discussed in detail in a recent paper.[1] In the Rydberg states, the C-O bond length is of less importance.

References

[1] M. Etinski, T. Fleig and C. M. Marian, *J. Phys. Chem. A*, 2009, **113**, 11809–11816.

Table 1: Excited states of uracil and their character, RI-CC2/aug-cc-pVDZ level. The ground state dipole moment is 4.16 D.

state	transition	energy [eV]	$f(L)$	dipole moment [D]
S_1	$n_O \rightarrow \pi^\star_L$	4.81	$4 \cdot 10^{-6}$	1.53
S_2	$\pi_H \rightarrow \pi^\star_L$	5.27	0.1808	5.36
S_3	$\pi_H \rightarrow$R	5.80	0.0026	5.25
T_1	$\pi_H \rightarrow \pi^\star_L$	3.84		3.60
T_2	$n_O \rightarrow \pi^\star_L$	4.59		1.78
T_3	$\pi_{H-1} \rightarrow \pi^\star_L$	5.34		5.06

Table 2: Excited states of 1-methyluracil and their character, RI-CC2/aug-cc-pVDZ level. The ground state dipole moment is 4.61 D.

state	transition	energy [eV]	$f(L)$	dipole moment [D]
S_1	$n_O \rightarrow \pi^\star_L$	4.80	$1 \cdot 10^{-5}$	1.14
S_2	$\pi_H \rightarrow \pi^\star_L$	5.01	0.2283	6.02
S_3	$\pi_H \rightarrow$R	5.70	0.0217	3.50
T_1	$\pi_H \rightarrow \pi^\star_L$	3.75		4.00
T_2	$n_O \rightarrow \pi^\star_L$	4.60		1.39
T_3	$\pi_{H-1} \rightarrow \pi^\star_L$	5.27		3.24

Table 3: Excited states of 3-methyluracil and their character, RI-CC2/aug-cc-pVDZ level. The ground state dipole moment is 3.46 D.

state	transition	energy [eV]	$f(L)$	dipole moment [D]
S_1	$n_O \rightarrow \pi^\star_L$	4.80	$1 \cdot 10^{-5}$	1.44
S_2	$\pi_H \rightarrow \pi^\star_L$	5.26	0.1291	4.80
S_3	$\pi_H \rightarrow$R	5.72	0.00030	6.35
T_1	$\pi_H \rightarrow \pi^\star_L$	3.87		2.95
T_2	$n_O \rightarrow \pi^\star_L$	4.58		1.63
T_3	$\pi_{H-1} \rightarrow \pi^\star_L$	5.14		2.15

Table 4: Excited states of thymine and their character, RI-CC2/aug-cc-pVDZ level. The ground state dipole moment is 4.09 D.

state	transition	energy [eV]	$f(L)$	dipole moment [D]
S_1	$n_O \rightarrow \pi^\star_L$	4.83	$2 \cdot 10^{-5}$	1.92
S_2	$\pi_H \rightarrow \pi^\star_L$	5.13	0.1814	5.15
S_3	$\pi_H \rightarrow$R	5.54	0.0003	6.31
T_1	$\pi_H \rightarrow \pi^\star_L$	3.72		3.82
T_2	$n_O \rightarrow \pi^\star_L$	4.61		2.21
T_3	$\pi_{H-1} \rightarrow \pi^\star_L$	5.32		6.25

Table 5: Excited states of 1,3-dimethyluracil and their character, RI-CC2/aug-cc-pVDZ level. The ground state dipole moment is 3.97 D.

state	transition	energy [eV]	$f(L)$	dipole moment [D]
S_1	$n_O \rightarrow \pi^\star_L$	4.81	$2 \cdot 10^{-5}$	1.00
S_2	$\pi_H \rightarrow \pi^\star_L$	5.01	0.1873	5.29
S_3	$\pi_H \rightarrow$R	5.61	0.0208	4.29
T_1	$\pi_H \rightarrow \pi^\star_L$	3.78		3.38
T_2	$n_O \rightarrow \pi^\star_L$	4.61		1.18
T_3	$\pi_{H-1} \rightarrow \pi^\star_L$	5.06		4.01

Table 6: Excited states of 1-methylthymine and their character, RI-CC2/aug-cc-pVDZ level. The ground state dipole moment is 4.43 D.

state	transition	energy [eV]	$f(L)$	dipole moment [D]
S_1	$n_O \rightarrow \pi^\star_L$	4.81	$3 \cdot 10^{-5}$	1.53
S_2	$\pi_H \rightarrow \pi^\star_L$	4.89	0.2339	5.70
S_3	$\pi_H \rightarrow$R	5.43	0.0094	2.22
T_1	$\pi_H \rightarrow \pi^\star_L$	3.63		4.05
T_2	$n_O \rightarrow \pi^\star_L$	4.61		1.82
T_3	$\pi_{H-1} \rightarrow \pi^\star_L$	5.24		3.36

Table 7: Excited states of 3-methylthymine and their character, RI-CC2/aug-cc-pVDZ level. The ground state dipole moment is 3.37 D.

state	transition	energy [eV]	$f(L)$	dipole moment [D]
S_1	$n_O \rightarrow \pi^\star_L$	4.82	$4 \cdot 10^{-6}$	1.70
S_2	$\pi_H \rightarrow \pi^\star_L$	5.12	0.1360	4.51
S_3	$\pi_H \rightarrow$R	5.46	0.0005	6.99
T_1	$\pi_H \rightarrow \pi^\star_L$	3.76		3.14
T_2	$n_O \rightarrow \pi^\star_L$	4.60		1.94
T_3	$\pi_{H-1} \rightarrow \pi^\star_L$	5.14		6.90

Table 8: Excited states of 1,3-dimethylthymine and their character, RI-CC2/aug-cc-pVDZ level. The ground state dipole moment is 3.76 D.

state	transition	energy [eV]	$f(L)$	dipole moment [D]
S_1	$n_O \rightarrow \pi^\star_L$	4.82	$2 \cdot 10^{-6}$	1.22
S_2	$\pi_H \rightarrow \pi^\star_L$	4.89	0.1984	5.00
S_3	$\pi_H \rightarrow$R	5.34	0.0091	2.85
T_1	$\pi_H \rightarrow \pi^\star_L$	3.67		3.40
T_2	$n_O \rightarrow \pi^\star_L$	4.62		1.49
T_3	$\pi_{H-1} \rightarrow \pi^\star_L$	5.05		2.50

Table 9: Vibrational spectrum of the uracil ground state at RI-CC2/cc-pVDZ level(unscaled frequencies)

wavenumber [1/cm]	intensity [km/mol]
126.87	0.05
155.15	0.43
374.19	17.83
374.78	29.60
505.87	14.04
522.90	5.88
546.04	2.32
554.01	36.68
688.91	78.57
720.97	1.02
734.78	42.79
760.89	2.20
799.66	55.57
939.52	0.72
962.29	9.46
980.37	5.35
1083.63	5.43
1197.19	94.15
1226.45	0.37
1368.70	6.94
1389.57	45.73
1405.10	60.24
1499.65	100.95
1660.91	12.60
1744.15	386.69
1797.67	587.67
3247.13	3.42
3289.50	1.00
3593.91	63.74
3647.53	114.92

Table 10: Vibrational spectrum of the uracil S_1 state obtained at RI-CC2/cc-pVDZ level (unscaled frequencies)

wavenumber [1/cm]	intensity [km/mol]
44.64	4.16
157.51	1.45
288.28	10.75
302.84	5.31
313.56	50.47
344.23	68.84
472.65	8.89
503.74	3.67
533.81	12.48
548.88	36.69
591.99	38.48
690.98	46.30
718.30	2.33
743.43	44.76
909.93	12.32
970.89	19.03
1012.89	34.69
1105.26	8.82
1150.47	9.38
1276.98	6.88
1307.29	14.44
1405.87	3.40
1426.88	7.63
1451.21	6.33
1631.52	132.31
1777.05	470.40
3255.87	5.64
3275.17	1.24
3627.07	78.00
3629.45	126.46

Table 11: Vibrational spectrum of the uracil T_1 state obtained at RI-CC2/cc-pVDZ level (unscaled frequencies)

wavenumber [1/cm]	intensity [km/mol]
126.55	2.14
158.63	1.03
228.91	2.44
367.47	20.89
460.39	18.79
480.02	8.89
497.54	10.57
530.56	7.06
554.46	37.23
640.59	31.81
683.21	109.17
697.62	2.96
727.46	70.26
762.46	0.28
938.30	4.97
959.28	17.32
1014.62	8.53
1144.59	74.00
1226.79	32.13
1353.70	85.19
1361.39	55.81
1378.64	6.23
1404.58	61.11
1456.89	150.99
1609.48	82.20
1769.32	318.66
3240.73	10.54
3255.24	1.91
3599.47	101.11
3599.65	42.43

Table 12: Vibrational spectrum of the 1-methyluracil ground state at RI-CC2/cc-pVDZ level(unscaled frequencies)

wavenumber [1/cm]	intensity [km/mol]
68.94	0.00
107.92	0.03
147.12	1.17
215.40	3.23
324.39	3.16
375.48	18.86
394.92	7.16
455.76	14.38
522.81	6.59
612.68	1.31
682.79	52.27
712.56	2.00
736.11	40.50
750.33	4.69
790.02	2.41
794.40	43.34
931.22	1.77
964.16	10.15
1037.25	5.54
1147.77	0.15
1153.76	28.34
1205.46	19.60
1234.55	17.77
1342.24	31.88
1369.91	36.96
1392.01	86.29
1448.41	26.93
1467.74	83.31
1469.20	7.76
1516.71	45.47
1659.04	28.11
1743.15	353.55
1769.16	608.71
3098.32	33.81
3196.58	7.88
3218.61	4.47
3236.85	5.25
3284.25	0.68
3589.34	65.08

Table 13: Vibrational spectrum of the 1-methyluracil S_1 state obtained at RI-CC2/cc-pVDZ level (unscaled frequencies)

wavenumber [1/cm]	intensity [km/mol]
65.32	2.08
111.12	0.37
119.73	0.92
237.54	2.55
294.75	2.94
297.69	8.56
332.59	42.29
352.39	11.76
385.95	82.98
433.22	15.42
521.76	9.51
571.73	0.65
577.80	0.98
682.41	27.64
709.96	3.10
737.19	39.62
756.61	5.87
956.75	0.74
1009.87	20.66
1095.01	5.15
1107.81	38.49
1146.63	0.50
1186.04	5.26
1241.11	31.87
1293.04	19.80
1358.50	6.58
1407.66	6.26
1430.62	10.97
1458.08	30.66
1494.05	8.78
1506.65	4.36
1640.43	129.66
1742.03	422.91
3079.37	47.83
3167.55	20.72
3228.63	0.07
3235.73	5.88
3273.02	2.33
3620.61	145.16

Table 14: Vibrational spectrum of the 1-methyluracil T_1 state obtained at RI-CC2/cc-pVDZ level (unscaled frequencies)

wavenumber [1/cm]	intensity [km/mol]
98.46	0.31
108.69	0.09
136.57	2.80
207.74	3.07
261.49	4.44
343.42	0.15
378.64	22.38
438.67	8.37
474.49	10.57
502.67	16.18
568.03	4.29
607.69	15.23
688.02	57.40
700.09	15.59
723.10	69.68
749.53	3.55
784.39	11.41
941.85	2.29
1013.60	12.13
1080.88	20.15
1137.02	2.16
1186.22	23.26
1213.49	88.34
1302.77	73.97
1353.79	31.21
1373.81	93.05
1397.36	2.34
1424.12	114.47
1440.11	67.36
1490.34	14.23
1503.63	32.40
1609.79	81.61
1739.28	268.37
3082.52	35.68
3174.82	14.32
3226.13	10.33
3233.34	0.01
3250.77	3.02
3588.62	69.01

Table 15: Vibrational spectrum of the 3-methyluracil ground state at RI-CC2/cc-pVDZ level(unscaled frequencies)

wavenumber [1/cm]	intensity [km/mol]
84.27	1.42
123.93	4.93
150.14	0.65
208.36	6.07
340.58	5.87
391.57	23.63
397.84	15.60
487.67	4.21
531.29	7.70
565.91	57.93
576.53	8.66
698.65	1.05
717.78	5.98
728.17	21.04
795.68	47.27
854.20	0.41
933.31	0.79
973.45	14.85
1082.59	6.08
1127.84	54.74
1150.52	0.28
1173.08	0.88
1233.91	21.66
1281.22	33.54
1387.02	36.84
1404.46	35.26
1434.13	76.41
1488.77	8.30
1499.71	39.19
1506.27	83.06
1658.82	3.97
1719.25	488.23
1767.61	363.02
3105.52	21.58
3198.82	10.27
3245.75	0.23
3247.40	3.48
3287.69	0.93
3644.52	112.71

Table 16: Vibrational spectrum of the 3-methyluracil S_1 state obtained at RI-CC2/cc-pVDZ level (unscaled frequencies)

wavenumber [1/cm]	intensity [km/mol]
30.23	0.49
92.58	2.31
154.79	0.78
184.33	4.85
299.02	3.91
311.95	4.36
359.30	6.71
371.64	95.63
462.35	3.47
507.38	1.91
549.93	28.52
563.23	17.00
593.08	28.45
687.17	42.43
689.08	1.44
725.10	25.31
777.81	8.70
928.47	1.40
978.18	32.80
1069.41	13.46
1113.32	3.52
1139.61	0.26
1226.56	13.87
1248.31	17.38
1302.00	11.85
1360.41	50.73
1403.20	5.17
1424.53	20.65
1449.13	7.65
1490.11	9.18
1501.99	24.73
1632.38	157.30
1747.21	393.54
3085.06	37.05
3177.45	11.02
3224.41	1.70
3239.73	9.40
3268.78	1.34
3619.81	61.81

Table 17: Vibrational spectrum of the 3-methyluracil T_1 state obtained at RI-CC2/cc-pVDZ level (unscaled frequencies)

wavenumber [1/cm]	intensity [km/mol]
75.24	1.09
109.96	4.43
152.51	1.47
190.91	3.29
243.67	1.39
331.78	6.23
371.97	26.61
451.33	12.34
482.74	2.26
500.06	13.92
557.51	46.47
586.06	65.68
649.75	12.62
690.27	0.89
702.98	3.22
728.88	23.07
835.46	15.67
957.80	9.55
991.78	13.02
1098.45	87.80
1148.53	2.88
1174.17	4.66
1223.96	6.31
1274.33	41.75
1359.98	138.16
1379.97	5.31
1404.94	56.71
1428.16	12.68
1465.93	210.60
1486.57	24.85
1503.25	7.06
1585.63	84.15
1738.29	244.11
3101.50	26.16
3199.33	11.47
3237.42	12.47
3241.59	0.15
3254.11	2.13
3594.13	72.73

Table 18: Vibrational spectrum of the thymine ground state at RI-CC2/cc-pVDZ level(unscaled frequencies)

wavenumber [1/cm]	intensity [km/mol]
102.95	0.00
135.28	0.28
146.84	0.04
270.27	2.82
286.59	0.00
373.67	23.95
377.23	16.65
450.82	14.46
529.10	6.17
554.74	51.59
591.78	1.02
686.47	78.05
732.00	38.07
736.60	3.65
749.66	5.57
792.18	1.68
884.25	16.62
960.48	11.10
1012.80	1.21
1057.52	1.03
1157.52	4.75
1199.75	106.57
1257.74	18.64
1366.62	8.79
1372.94	5.40
1409.02	18.06
1419.17	45.47
1465.17	6.28
1482.45	10.22
1501.72	103.91
1686.84	3.24
1725.42	338.46
1796.72	639.58
3079.24	24.55
3169.09	8.08
3183.30	11.29
3234.65	5.36
3593.93	63.24
3646.27	111.24

Table 19: Vibrational spectrum of the thymine S_1 state obtained at RI-CC2/cc-pVDZ level (unscaled frequencies)

wavenumber [1/cm]	intensity [km/mol]
49.57	2.94
93.00	0.06
153.64	0.35
189.10	7.48
236.51	2.34
303.40	6.95
314.78	0.76
344.20	54.89
368.55	71.18
454.45	7.92
485.18	6.31
550.65	43.21
553.11	12.50
588.70	47.27
692.96	23.90
714.60	3.18
775.58	4.69
908.67	14.46
967.30	6.69
1050.45	2.60
1079.94	1.62
1140.97	31.66
1212.83	43.16
1236.34	1.16
1295.52	10.51
1405.36	0.15
1407.88	10.39
1422.27	3.66
1455.91	14.14
1475.16	6.29
1492.06	6.87
1677.13	99.56
1776.72	516.19
3061.55	42.15
3149.68	18.47
3157.11	15.84
3235.92	5.77
3624.26	68.09
3627.27	130.97

Table 20: Vibrational spectrum of the thymine T_1 state obtained at RI-CC2/cc-pVDZ level (unscaled frequencies)

wavenumber [1/cm]	intensity [km/mol]
74.66	0.54
139.86	1.44
151.53	0.77
180.35	0.65
274.63	5.69
308.52	9.37
376.35	15.57
436.72	19.19
484.44	8.69
546.67	23.84
574.76	5.84
633.49	36.75
678.75	82.78
691.14	4.35
720.99	83.17
738.45	7.80
780.76	5.78
947.21	4.30
972.21	10.12
980.33	0.84
1147.93	61.77
1150.68	69.34
1243.09	7.10
1348.23	116.76
1354.84	13.91
1379.47	26.98
1405.27	56.38
1422.93	1.28
1453.02	47.14
1466.04	13.48
1491.05	85.13
1601.99	89.85
1769.29	346.00
3041.38	13.82
3110.82	10.29
3197.19	1.90
3223.70	11.68
3594.31	71.74
3602.05	71.27

Table 21: Vibrational spectrum of the 1,3-dimethyluracil ground state at RI-CC2/cc-pVDZ level(unscaled frequencies)

wavenumber [1/cm]	intensity [km/mol]
80.55	0.62
106.07	1.17
108.10	1.36
131.49	6.37
188.90	2.05
242.86	0.01
309.76	1.44
355.88	11.52
394.56	20.59
416.45	0.90
469.71	8.16
501.07	11.48
615.16	1.99
676.76	3.55
702.06	0.93
733.21	22.28
790.25	34.67
795.45	1.02
925.17	1.67
933.93	8.57
1010.00	14.95
1081.90	2.48
1144.19	43.25
1147.15	0.30
1150.63	0.23
1177.95	0.16
1265.87	16.50
1279.01	10.48
1350.88	30.91
1386.37	93.63
1420.70	64.35
1451.25	22.20
1468.07	7.99
1472.29	99.04
1492.78	7.94
1498.41	14.88
1518.80	61.79
1656.05	6.00
1719.95	643.33
1738.86	204.90
3097.46	36.67
3101.76	24.86
3195.91	6.37
3196.60	13.34
3217.25	4.79
3235.33	5.38
3239.77	0.48
3282.67	0.65

Table 22: Vibrational spectrum of the 1,3-dimethyluracil S_1 state obtained at RI-CC2/cc-pVDZ level (unscaled frequencies)

wavenumber [1/cm]	intensity [km/mol]
73.04	0.42
87.71	0.31
98.61	0.84
117.59	6.88
158.23	1.79
250.02	0.13
305.99	3.66
314.19	0.10
329.03	4.76
387.50	22.92
405.15	66.34
448.66	11.57
506.45	5.70
561.41	4.84
571.57	3.38
680.08	14.06
687.09	10.58
710.30	6.10
724.25	22.27
921.90	1.27
949.87	0.18
1054.94	21.98
1076.13	5.21
1109.86	13.94
1137.26	15.33
1145.75	0.39
1223.25	41.12
1251.76	7.76
1279.47	13.81
1358.50	18.48
1377.41	55.29
1407.92	14.10
1422.53	10.79
1456.51	31.98
1477.07	12.60
1493.96	8.50
1504.11	8.98
1507.04	1.24
1638.04	127.96
1712.19	372.54
3078.58	68.41
3081.15	19.13
3166.65	21.32
3175.96	12.20
3221.05	10.58
3226.96	0.50
3229.85	0.00
3266.22	1.97

Table 23: Vibrational spectrum of the 1,3-dimethyluracil T_1 state obtained at RI-CC2/cc-pVDZ level (unscaled frequencies)

wavenumber [1/cm]	intensity [km/mol]
72.71	1.26
86.22	0.10
102.39	0.19
112.63	5.18
191.71	3.58
207.18	4.21
275.30	1.84
316.03	2.10
366.74	3.99
382.92	29.83
453.84	5.16
467.77	6.88
499.02	11.96
582.01	5.16
627.73	29.51
672.10	8.07
702.97	2.17
722.48	20.52
786.88	10.27
918.65	12.92
976.75	1.78
1040.81	18.67
1106.49	36.49
1134.91	1.58
1146.02	5.87
1171.40	35.35
1232.30	36.06
1271.90	50.34
1325.84	62.79
1368.33	121.43
1398.53	9.28
1408.42	77.61
1432.24	6.89
1453.41	168.58
1484.04	3.49
1487.33	21.61
1503.13	7.57
1504.92	43.13
1585.90	82.82
1710.62	198.48
3081.65	38.37
3097.79	28.59
3174.07	14.45
3196.23	12.05
3219.56	12.81
3235.58	0.02
3240.88	0.27
3247.37	2.98

Table 24: Vibrational spectrum of the 3-methylthymine ground state at RI-CC2/cc-pVDZ level(unscaled frequencies)

wavenumber [1/cm]	intensity [km/mol]
86.95	1.37
100.96	0.17
123.16	4.39
149.10	0.37
208.72	4.41
265.51	1.69
290.19	0.60
342.51	8.07
394.83	21.57
395.67	11.93
466.49	11.42
497.30	5.55
567.48	77.95
607.90	2.39
666.38	1.40
725.40	15.42
740.88	0.22
796.56	3.76
879.21	16.29
932.86	2.11
982.68	8.84
1056.76	0.81
1059.31	9.09
1137.82	49.47
1150.34	0.33
1223.58	27.11
1269.31	43.94
1284.69	4.21
1368.62	17.46
1405.90	23.05
1412.54	5.45
1435.00	65.46
1464.38	6.60
1482.36	10.15
1488.42	8.12
1498.67	44.83
1508.01	92.32
1673.00	145.63
1713.48	249.31
1766.30	460.75
3078.41	26.60
3104.78	22.54
3168.95	8.32
3181.83	12.07
3198.01	10.46
3234.54	5.71
3244.79	0.27
3642.59	109.33

Table 25: Vibrational spectrum of the 3-methylthymine S_1 state obtained at RI-CC2/cc-pVDZ level (unscaled frequencies)

wavenumber [1/cm]	intensity [km/mol]
64.57	0.05
84.80	0.13
92.00	3.17
111.08	0.87
186.08	3.34
228.85	2.05
239.89	1.66
309.61	12.13
317.50	4.24
361.01	4.58
391.64	78.94
460.98	2.83
474.43	2.98
555.62	40.86
563.90	9.21
588.46	31.45
651.65	2.60
692.47	19.60
742.54	14.16
855.34	4.60
943.82	3.53
1048.06	2.96
1065.40	5.03
1071.39	5.12
1119.10	13.59
1138.42	9.44
1219.12	23.12
1260.13	5.40
1301.04	10.03
1353.00	76.58
1406.01	0.61
1410.05	9.95
1425.19	25.37
1455.77	21.93
1474.54	5.90
1485.18	17.87
1491.97	4.24
1504.72	9.57
1670.00	108.10
1748.27	431.10
3058.93	47.99
3080.68	38.51
3146.54	19.33
3154.53	16.55
3174.57	12.37
3222.65	9.29
3225.71	0.34
3617.64	60.55

Table 26: Vibrational spectrum of the 3-methylthymine T_1 state obtained at RI-CC2/cc-pVDZ level (unscaled frequencies)

wavenumber [1/cm]	intensity [km/mol]
67.84	1.07
79.06	0.21
112.13	5.17
147.84	0.64
175.05	0.47
197.67	2.01
277.92	4.11
311.11	7.79
345.77	7.62
382.88	20.87
448.84	15.19
477.96	4.97
559.82	56.25
588.29	29.23
641.99	10.58
664.32	10.08
700.19	6.74
724.07	26.26
791.11	14.39
904.67	3.13
959.68	0.46
979.41	1.58
1046.42	45.54
1101.44	74.95
1146.11	5.68
1212.29	4.37
1256.68	23.06
1269.03	23.57
1354.45	141.05
1377.74	23.02
1403.98	55.89
1420.74	0.95
1430.28	22.08
1455.25	64.09
1466.97	16.10
1479.99	27.41
1497.01	101.95
1503.76	10.95
1577.97	91.12
1738.99	270.24
3039.56	16.75
3097.12	29.98
3107.56	10.80
3195.25	11.66
3197.94	1.81
3213.96	14.91
3240.94	0.45
3595.07	71.16

Table 27: Vibrational spectrum of the 1-methylthymine ground state at RI-CC2/cc-pVDZ level(unscaled frequencies)

wavenumber [1/cm]	intensity [km/mol]
55.92	0.00
95.85	0.00
126.68	0.09
144.75	0.65
194.73	4.45
259.65	3.24
291.55	0.55
327.37	1.75
378.95	17.76
391.92	3.73
433.09	19.09
509.76	2.50
634.24	1.02
681.22	50.00
697.89	6.62
733.31	36.65
744.06	9.85
767.48	3.27
862.22	3.30
880.54	15.74
1013.98	0.72
1056.06	1.29
1081.52	31.36
1147.10	0.09
1156.35	15.76
1204.66	38.33
1249.30	7.85
1346.82	31.42
1373.72	3.14
1391.50	84.81
1414.77	26.81
1448.45	2.37
1464.63	4.56
1467.82	104.66
1468.99	8.66
1489.73	14.48
1515.52	48.34
1681.90	0.22
1722.90	357.17
1767.30	613.61
3077.09	27.63
3096.08	36.24
3166.04	8.56
3181.18	11.39
3192.46	8.56
3216.54	1.48
3224.19	10.39
3589.63	64.12

Table 28: Vibrational spectrum of the 1-methylthymine S_1 state obtained at RI-CC2/cc-pVDZ level (unscaled frequencies)

wavenumber [1/cm]	intensity [km/mol]
15.86	1.90
85.93	0.12
100.95	0.24
105.42	0.42
188.80	2.43
230.99	2.50
240.35	6.27
294.49	1.99
304.54	2.78
359.04	2.66
373.15	41.28
375.05	109.19
426.98	10.24
484.18	1.04
566.51	0.58
586.38	3.83
685.59	10.88
703.26	7.97
718.79	4.47
839.49	1.26
974.83	1.50
1043.30	11.42
1050.92	0.15
1081.49	3.89
1143.56	2.96
1181.52	1.39
1214.58	50.84
1223.51	55.10
1269.02	4.50
1360.70	3.32
1404.01	0.67
1409.17	6.11
1428.03	14.40
1458.71	39.34
1473.94	6.26
1490.40	8.35
1492.30	7.16
1507.87	4.05
1686.65	89.79
1742.68	477.43
3059.91	44.90
3080.25	45.91
3147.67	19.30
3155.48	15.97
3168.04	20.83
3210.93	8.82
3229.77	0.02
3625.66	148.12

Table 29: Vibrational spectrum of the 1-methylthymine T_1 state obtained at RI-CC2/cc-pVDZ level (unscaled frequencies)

wavenumber [1/cm]	intensity [km/mol]
76.07	0.59
98.45	0.27
111.66	0.03
149.94	1.61
159.80	1.83
243.90	5.10
267.38	4.42
315.93	4.47
345.18	0.81
386.64	17.76
416.46	20.86
468.55	6.80
594.26	13.80
613.35	2.06
657.09	45.65
686.79	7.47
716.97	87.61
726.40	3.81
769.16	7.24
821.82	1.46
971.79	4.14
981.69	0.85
1067.14	19.33
1136.02	46.79
1139.13	10.32
1185.70	25.73
1240.40	31.79
1308.93	143.12
1351.17	7.16
1379.50	86.34
1380.78	12.87
1408.19	41.92
1436.68	71.23
1445.06	1.07
1464.97	8.44
1485.94	24.14
1492.86	15.12
1505.37	53.27
1600.17	90.07
1738.88	294.05
3041.84	15.04
3081.46	37.99
3110.81	11.06
3171.83	15.38
3195.40	2.49
3208.51	10.84
3232.31	0.14
3589.44	70.34

Table 30: Vibrational spectrum of the 1,3-dimethylthymine ground state at RI-CC2/cc-pVDZ level(unscaled frequencies)

wavenumber [1/cm]	intensity [km/mol]
73.79	0.22
92.24	0.27
105.77	1.98
130.44	6.01
145.54	2.27
157.44	0.03
243.96	0.01
262.35	2.36
294.94	0.09
308.72	0.90
360.51	9.89
396.92	22.93
414.02	0.15
449.28	16.52
494.90	4.02
576.47	1.92
660.83	1.98
728.72	17.27
734.97	2.10
765.72	2.83
875.08	14.86
917.26	4.85
976.61	1.82
1047.30	2.41
1055.34	1.04
1068.43	33.60
1101.42	21.82
1146.72	0.20
1150.70	0.32
1198.79	22.93
1280.02	8.36
1302.51	10.17
1355.08	23.01
1388.78	69.47
1412.89	3.57
1415.95	64.93
1448.16	3.41
1463.89	4.73
1467.91	8.94
1472.17	135.90
1488.42	12.51
1492.11	7.59
1499.15	11.62
1517.54	65.09
1668.64	130.50
1709.93	340.24
1735.99	370.96
3076.43	30.01
3095.30	38.64
3101.76	25.98
3166.56	8.72
3179.98	12.25
3192.44	8.40
3196.75	11.70
3215.02	2.29

Table 31: Vibrational spectrum of the 1,3-dimethylthymine S_1 state obtained at RI-CC2/cc-pVDZ level (unscaled frequencies)

wavenumber [1/cm]	intensity [km/mol]
74.45	0.59
87.28	0.66
92.58	0.25
99.16	0.89
110.20	1.35
125.82	6.05
225.00	2.26
235.91	1.96
262.48	0.84
307.71	4.62
313.53	2.56
327.65	4.75
394.11	11.20
416.40	61.53
443.35	11.37
475.33	3.56
565.68	6.06
578.56	3.49
606.85	6.20
686.98	8.37
702.32	5.19
859.36	1.68
947.55	1.03
1021.76	11.56
1047.90	2.10
1070.01	3.79
1079.30	5.31
1098.01	4.86
1137.34	15.24
1145.40	0.38
1203.48	11.93
1256.80	51.54
1305.94	1.10
1347.86	69.98
1373.05	19.91
1406.25	1.73
1413.11	23.27
1422.22	12.43
1460.11	53.90
1473.59	5.26
1477.85	12.46
1491.26	5.42
1493.77	8.53
1505.61	7.85
1507.12	1.45
1673.20	84.06
1717.61	408.28
3057.75	50.25
3077.72	70.14
3079.94	19.37
3144.73	19.83
3153.43	16.80
3165.66	21.14
3173.98	13.18
3202.78	11.00

Table 32: Vibrational spectrum of the 1,3-dimethylthymine T_1 state obtained at RI-CC2/cc-pVDZ level (unscaled frequencies)

wavenumber [1/cm]	intensity [km/mol]
65.66	1.03
76.77	0.11
84.25	0.42
100.35	0.31
124.01	7.93
156.36	0.18
187.74	0.70
247.63	1.96
276.42	4.52
312.92	2.59
329.49	4.72
374.24	6.84
392.01	25.86
431.30	15.88
471.23	5.88
562.61	3.76
625.43	2.67
642.72	25.22
694.54	6.42
719.36	16.13
766.22	5.92
878.72	1.68
947.99	3.10
981.10	1.45
1020.84	3.53
1051.88	58.10
1100.33	32.55
1134.25	3.83
1145.82	5.62
1180.39	26.71
1261.43	10.77
1304.11	17.75
1315.30	166.57
1374.16	82.25
1380.93	15.21
1403.69	70.48
1415.17	4.38
1445.42	1.69
1447.50	100.44
1466.66	9.77
1479.47	27.13
1483.14	3.23
1489.04	34.08
1503.08	5.47
1508.71	62.76
1580.40	97.57
1710.55	222.64
3039.08	18.11
3080.33	40.36
3096.06	32.37
3107.68	11.73
3173.32	14.67
3190.88	2.33
3193.71	12.69
3200.57	14.02

Table 33: Geometry of the ground state of uracil in atomic units obtained at RI-CC2/cc-pVDZ level

1.80276131503938	-3.82523577877818	-0.00001843121476	c
-0.76911959552013	-3.60787322393067	-0.00007500514995	c
-1.94412134408134	-1.10454937651617	0.00002508530838	c
-0.14550597259914	0.88615452904312	0.00017510886307	n
2.48204977900901	0.75797537834155	0.00023770292495	c
3.36151866289513	-1.73799691500085	0.00013053376173	n
-4.22669268030672	-0.64209232037238	-0.00000930583133	o
3.89552706152535	2.59733451753509	0.00037114273740	o
5.27279481407985	-1.92595057138397	0.00017209542869	h
-0.87594766368821	2.67228606501715	0.00025076303206	h
2.76550865539636	-5.65443235453763	-0.00008760001027	h
-1.98531788402312	-5.27108030126895	-0.00019329108878	h

Table 34: Geometry of the S_1 state of uracil in atomic units obtained at RI-CC2/cc-pVDZ level

0.33897033221462	1.36132036952789	-0.71354640950436	c
-2.16830967216996	0.27921600085562	-0.55259778778755	c
-2.33291781271658	-2.23250800809978	-0.12483561008593	c
-0.22143039872179	-3.74915347578373	0.21200756656727	n
2.27161351679411	-2.80420926445030	0.25197377565216	c
2.38079163497256	-0.23449154572517	-0.16599513219088	n
-3.85075421208677	1.43897566732052	-0.82824054100883	h
-4.53991708654283	-3.78289851094835	0.06201268861541	o
4.11105733844260	-4.18360201279782	0.62476047658149	o
-0.41352184865411	-5.63002979361522	0.56716080078631	h
4.17622188098919	0.45468528231244	-0.20606788408108	h
0.71559577364017	3.38976059942737	-0.69108040928701	h

Table 35: Geometry of the T_1 state of uracil in atomic units obtained at RI-CC2/cc-pVDZ level

1.91164001968400	-3.84894454808797	0.76085934370093	c
-0.80480063599536	-3.55410211096836	-0.05576329127888	c
-1.92939839894834	-1.06654822108889	0.07178595469496	c
-0.14940202847252	0.86449654246044	0.64216133438314	n
2.43153503217761	0.71567056781175	0.08782439180786	c
3.30666121126855	-1.77911271016009	-0.13529134932617	n
-4.20035084227332	-0.56795061284651	-0.24597887642145	o
3.82104193628791	2.55612524845929	-0.17004733482631	o
5.21906293952542	-1.89260554848371	-0.35009209010192	h
-0.85510646934687	2.65950378661802	0.63044996769175	h
2.84401224282969	-5.68197431665829	0.56296480531994	h
-1.87734509750552	-5.06855912797309	-0.96463511177476	h

Table 36: Geometry of the ground state of 1-methyluracil in atomic units obtained at RI-CC2/cc-pVDZ level

3.19927492493216	-1.61294411458012	0.00002496572308	n
1.78994513815827	-3.80490875530421	0.00000425774160	c
-0.79562455592143	-3.82574497399391	-0.00005200096061	c
-2.19814316354062	-1.45135065988189	-0.00008777859003	c
-0.57447546404974	0.68307490368417	-0.00007282818888	n
2.05084777304719	0.78296736363196	-0.00000626022137	c
-1.84216337645154	-5.60143284488652	-0.00006587108237	h
-4.51337583495722	-1.18600662462670	-0.00012714570564	o
-1.45042543968538	2.40315870417777	-0.00009288771281	h
3.29104096638268	2.75002496504491	0.00002452016135	o
5.96445752662432	-1.63530129680317	0.00009268440858	c
2.89459639181716	-5.55345191094566	0.00003828359882	h
6.59797914498682	-3.61316638311048	0.00008717986953	h
6.69023167873668	-0.65768880411026	-1.68559838758938	h
6.69017693650958	-0.65777544186486	1.68595990868878	h

Table 37: Geometry of the S_1 state of 1-methyluracil in atomic units obtained at RI-CC2/cc-pVDZ level

2.47284219790390	-1.21883476261733	0.35097373278242	c
1.01471465551930	-3.38649220409950	0.53677103998948	n
-1.63486694404622	-3.40483785631362	0.57155080828315	c
-2.96583384584748	-1.01430645907590	0.74559106965191	c
-1.56362896608391	1.10351097005636	0.54104936098563	c
1.03302848194054	1.02335132300095	0.22110284039145	n
2.33846925714895	-5.81022268346566	0.57477312468215	c
-2.34970005387219	3.68917577919150	0.58742271762857	o
2.06308892529937	2.64930787963247	0.23651621729449	h
4.80586872183922	-1.14431584641531	0.27256638258338	o
-5.01612029820632	-0.94840912581698	0.95565215848534	h
-2.50903283175285	-5.20965661974894	1.07059000464394	h
1.91080736843675	-6.82204050660228	2.34595047606720	h
1.72708949018737	-6.96826125760383	-1.04554565629915	h
4.37369743813411	-5.43050654877564	0.45132462265113	h

Table 38: Geometry of the T_1 state of 1-methyluracil in atomic units obtained at RI-CC2/cc-pVDZ level

3.18157937103570	-1.56546529340471	-0.19908503173766	n
1.86108769455372	-3.51999772934431	-1.41790837067647	c
-0.76419869649515	-3.73351884410390	-0.35948272913945	c
-2.14452357794707	-1.43099959305454	0.11864455759113	c
-0.61257534096132	0.76051054615996	-0.16697665278039	n
2.00000175395557	0.78937301014925	0.24010419890510	c
-1.59042379869529	-5.52567244436657	0.25461851104780	h
-4.41103073072179	-1.26223950584482	0.70653053736305	o
-1.47733853300773	2.41804600240129	0.31348324620631	h
3.16887922497788	2.69172741685061	0.88947741691412	o
5.93152051002599	-1.68861624840196	0.02220804682170	c
2.97584469454787	-5.23712989886609	-1.71340101944579	h
6.45611531560184	-3.32605043424284	1.19458050540891	h
6.78483017450763	-1.89063712563655	-1.86953495447500	h
6.58906488429483	0.07147470583668	0.89977094324186	h

Table 39: Geometry of the ground state of 3-methyluracil in atomic units obtained at RI-CC2/cc-pVDZ level

2.79714164681303	-1.01045026890339	-0.00001791287129	n
1.25389811567673	-3.10246603675422	-0.00016362255182	c
-1.31316486967807	-2.86480407908371	-0.00019078434808	c
-2.46708517483147	-0.35814027765836	-0.00004321799133	c
-0.70637677397164	1.68439222856346	0.00011010194934	n
1.93172230778643	1.48817325204744	0.00012419304869	c
-4.75997781109014	0.08483868394174	-0.00004457760902	o
3.40669124058504	3.28784921728753	0.00024450508516	o
4.70991562415775	-1.18565781259049	-0.00000271805855	h
-1.80814868627959	4.22833202252713	0.00027392507107	c
2.21805379681193	-4.93065827999989	-0.00025498588686	h
-2.55202819089705	-4.51140317880031	-0.00030746949353	h
-0.24216752498826	5.58527638286228	0.00023659189750	h
-3.00170726765816	4.47177526002970	-1.68451421451066	h
-3.00150048836956	4.47165857068938	1.68524425825438	h

Table 40: Geometry of the S_1 state of 3-methyluracil in atomic units obtained at RI-CC2/cc-pVDZ level

2.79138538550787	-1.00126223373660	-0.00546091480648	n
1.31851909173905	-3.19358690560213	-0.19016565115791	c
-1.39057205504203	-2.84124138944154	-0.03995018936935	c
-2.25943674890140	-0.43899347441420	-0.00905220466464	c
-0.72254069131865	1.69010288475517	-0.02080268754906	n
1.95094690981076	1.46013393063429	-0.00297684870678	c
-4.84924166816676	0.36268602110326	0.04531837702526	o
3.36006519094605	3.32488766050975	0.01784991779591	o
4.71074444075797	-1.13048533087093	-0.05950886105723	h
-1.83134024939790	4.22521958412281	0.00101014415586	c
2.26709584373131	-4.97895644865622	0.23324658801925	h
-2.68628389356617	-4.44614134099931	-0.03391910470826	h
-0.24077256896263	5.55844591597488	-0.00295003475465	h
-3.01382116786823	4.51256121809166	-1.68828726474870	h
-2.98979477651223	4.49882248322404	1.70964727142755	h

Table 41: Geometry of the T_1 state of 3-methyluracil in atomic units obtained at RI-CC2/cc-pVDZ level

2.71861610000044	-1.08596160297985	0.30224905701576	n
1.35722643246798	-3.03251202058339	-0.87153392097581	c
-1.36374806596261	-2.81511148066425	-0.06150908122873	c
-2.48008058133044	-0.32704113202667	0.06626659604168	c
-0.72479109306228	1.70273515596575	-0.17078448166096	n
1.85840518654597	1.42577898884371	0.35057184104708	c
-4.77591715712352	0.10511291570904	0.33710668625788	o
3.30560783556969	3.18916083447132	0.80863503575888	o
4.63087739504241	-1.20985161521849	0.51736423640308	h
-1.78782258403116	4.26100948014373	-0.09533836044030	c
2.28988725584137	-4.87643849392636	-0.86047103144193	h
-2.46778964157149	-4.40908405382381	0.65222459141879	h
-0.22121226262804	5.59991182561404	-0.32316126556842	h
-3.16725440752885	4.46425187322566	-1.63282577445189	h
-2.75894842630412	4.59841946280791	1.71529468009731	h

Table 42: Geometry of the ground state of thymine in atomic units obtained at RI-CC2/cc-pVDZ level

1.80467847639010	-3.82768331030142	0.00017256838633	c
-0.77248595387687	-3.63715673109377	0.00009956818093	c
-1.91223731068656	-1.10615996119000	-0.00001345376157	c
-0.13325138697833	0.88607774948266	0.00006043219334	n
2.49742541157605	0.75781269840660	0.00016968217022	c
3.36633735052051	-1.73267815721277	0.00017162516731	n
-2.52517525947582	-5.86967207941727	-0.00011090060169	c
-4.20520534526542	-0.66663501949474	-0.00012031812041	o
3.90557677004676	2.60333217734376	0.00025724699882	o
5.27719578200499	-1.92437168113128	0.00028652361625	h
-0.86707905183507	2.67044871394354	0.00004753420255	h
2.77662425317857	-5.65380172744093	0.00023370848073	h
-1.46082419896370	-7.65950025416043	0.00159308281278	h
-3.76783570463527	-5.82206043476818	1.67202990970417	h
-3.76544811641981	-5.82382518070266	-1.67383435239424	h

Table 43: Geometry of the S_1 state of thymine in atomic units obtained at RI-CC2/cc-pVDZ level

0.33048389411507	1.35823498295451	-0.60788074196863	c
-1.99829401997630	0.32372925580859	-0.73053867035561	c
-2.48302784291670	-2.22090104994847	-0.30328930827534	n
-0.56469944559451	-4.01329444491755	0.12845925347989	c
1.80361011676503	-2.92739345546888	0.25505578583550	n
2.36962494693841	-0.35082951276319	0.05984930677219	c
-4.35311019801620	1.56382175445597	-1.28736868505487	o
-1.01129248596558	-6.28737552721796	0.37417760966081	o
0.79802652207934	4.13455280311244	-1.02645337985241	c
-4.25598685339039	-2.93035960172474	-0.53587411844264	h
3.19949428914101	-4.19350611884565	0.64125351240329	h
4.36538369425570	0.14415601534491	-0.14668333048302	h
-0.92800727853156	5.06124499599545	-1.74270164759363	h
1.35496104465238	5.09792261866155	0.73886474406704	h
2.31196958965884	4.43913007824831	-2.42887452606781	h

Table 44: Geometry of the T_1 state of thymine in atomic units obtained at RI-CC2/cc-pVDZ level

1.72319817829857	-3.81070065882309	0.33444147963110	c
-1.04751040804398	-3.60247394114372	-0.34387701763916	c
-2.19372203297843	-1.12462397459517	-0.25649553148946	c
-0.44358463517930	0.86183706947456	0.22000472614834	n
2.12172647585424	0.76064964484094	-0.39957879520916	c
3.04844219130333	-1.71564588458133	-0.59264027858918	n
-2.49860724661829	-5.83617994946672	-1.23682436566550	c
-4.48300554916687	-0.66040096580886	-0.54530654106213	o
3.46297465935337	2.62564101983094	-0.73621890723532	o
4.95713320713838	-1.79013302125016	-0.84852909721381	h
-1.19525297885639	2.63763729646820	0.15597975326328	h
2.67700977239451	-5.62691621708028	0.06752265026983	h
-1.65236227217059	-6.61387478786286	-2.98658531096922	h
-2.43744005778862	-7.36809460725325	0.18520405639556	h
-4.47548506978080	-5.30760971594959	-1.60218691104771	h

Table 45: Geometry of the ground state of 1,3-dimethyluracil in atomic units obtained at RI-CC2/cc-pVDZ level

3.19487805647921	-1.63418343850067	-0.00000045797039	n
1.80761237791159	-3.83314070846399	-0.00005056092074	c
-0.77514484268780	-3.83912033153101	-0.00005432409450	c
-2.18689302853849	-1.47637497315650	-0.00007207416626	c
-0.60604136361164	0.71676014179638	-0.00003234890558	n
2.03099431564135	0.75178190575228	-0.00005437760932	c
-1.83634731574708	-5.60616582432924	-0.00009455239072	h
-4.51627433945057	-1.29417339675079	-0.00005854152488	o
-1.81535970560174	3.21118575053244	-0.00002312043575	c
3.28754496569621	2.71614246275426	-0.00008784442589	o
5.96001730513952	-1.63045771771152	-0.00003635427253	c
2.91505281614476	-5.58014992074299	-0.00003471686971	h
6.61078640894986	-3.60301813763702	0.00055082927020	h
6.67678034843274	-0.64574511272398	-1.68552567258794	h
6.67675553721488	-0.64473356285251	1.68488789946477	h
-3.86202526192372	2.88043971071654	-0.00004371655041	h
-1.23605125174251	4.27861358688822	1.68778529482087	h
-1.23603947092308	4.27863727623410	-1.68780849509750	h

Table 46: Geometry of the S_1 state of 1,3-dimethyluracil in atomic units obtained at RI-CC2/cc-pVDZ level

3.19657706133500	-0.27959186500231	-0.21380079612269	n
1.72503189379741	-2.47449058566074	-0.03479926925016	c
-0.99952962854711	-2.18726370270642	-0.03607628293705	c
-1.92424136225011	0.12884075893475	-0.56713702772406	c
-0.40673597728440	2.21907393893384	-1.02546243112466	n
2.25347387632616	2.10827612821651	-0.71401584530144	c
-2.24681711280759	-3.79874769134090	0.28525300446282	h
-4.53249601474360	0.84454336962315	-0.74488416007837	o
-1.52659429023360	4.72309154079865	-1.39369739208208	c
3.54841529884353	4.05033623097569	-0.92287981199247	o
5.93733753319334	-0.53896943096926	0.02102154420208	c
2.67052993280888	-4.10885915483510	0.80993409187034	h
6.41719000967623	-1.26363642408884	1.91558679024887	h
6.63746619367226	-1.86926690183019	-1.42125945729460	h
6.78778681513269	1.33156354544335	-0.25809036238614	h
-3.33695894186822	4.49279694254495	-2.39279726366681	h
-1.84924147019142	5.68616080816421	0.42736968612467	h
-0.20696117930998	5.84991486214330	-2.52979747908413	h

Table 47: Geometry of the T_1 state of 1,3-dimethyluracil in atomic units obtained at RI-CC2/cc-pVDZ level

3.16598306624989	-1.62123370548290	-0.19089244236726	n
1.89380635623001	-3.64761615989383	-1.33680049227005	c
-0.75881622851074	-3.76019035894362	-0.34563961701311	c
-2.14936722023074	-1.43137795770768	-0.08439540460184	c
-0.62921373246135	0.77536164333595	-0.40894076587898	n
1.98314897278520	0.76826855968050	0.02121295167338	c
-1.62626065131307	-5.49642960542688	0.36556214485372	h
-4.45534590970225	-1.27788067840425	0.35472445930235	o
-1.87035528369115	3.24485288798938	-0.21901703767695	c
3.17847922641252	2.70430606318817	0.52373859413624	o
5.90772551301192	-1.72380152259630	0.12872969408048	c
3.00670421829344	-5.38882342654781	-1.44647895218452	h
6.39215740128130	-3.34581779339239	1.33868081188091	h
6.83270687835152	-1.94611016103819	-1.72722418542289	h
6.52856405975947	0.05033988587982	1.00334983681971	h
-3.84311390137086	2.98840686231833	-0.80297446532233	h
-1.81551710264107	3.96956411524181	1.73346070217385	h
-0.89243993477409	4.59077974660956	-1.45987686497576	h

Table 48: Geometry of the ground state of 1-methylthymine in atomic units obtained at RI-CC2/cc-pVDZ level

1.80009646109859	-3.79367496258727	-0.00000434755469	c
-0.96041289307839	-3.59768898832893	-0.00005085454695	c
-1.84519808002703	-1.07904910119822	-0.00000705555262	n
-0.46866939786484	1.16223559255944	-0.00003682334017	c
2.15161902225160	0.78039103005411	-0.00012369119249	n
3.19794815147379	-1.61519555813003	-0.00004697737567	c
-2.44984354509549	-5.39788932379239	-0.00002568233492	o
-1.42394490874515	3.28430991839479	0.00001820187420	o
2.94024720500453	-6.39380591975310	0.00018433635829	c
-3.76207866626817	-0.85505767310422	0.00005491374233	h
5.26752080186618	-1.66009065613468	0.00002223952075	h
5.02093369740000	-6.30308861163562	0.00239606878034	h
2.31102894411247	-7.46739294770402	1.67203858880720	h
2.31465350984262	-7.46640880575342	-1.67382602380108	h
3.71025681322392	3.06436102013922	-0.00000310057013	c
5.70600006193744	2.48992557996942	-0.00004039320419	h
3.30313386186607	4.21291831669698	-1.68565847026297	h
3.30301459264579	4.21297360901402	1.68579586372074	h

Table 49: Geometry of the S_1 state of 1-methylthymine in atomic units obtained at RI-CC2/cc-pVDZ level

1.75694348405518	-3.86302668834292	-0.10573923199763	c
-0.73318493981853	-3.49338152339869	-0.48611186610730	c
-1.80638579187829	-1.11184914764683	-0.68900126258495	n
-0.42808093876766	1.15590289900441	-0.52336738847694	c
2.14499332084592	0.78109709460693	-0.17155511377464	n
3.27099335468673	-1.58712983068312	0.18258473793598	c
-2.69412843607505	-5.35416167892345	-0.77249737470039	o
-1.48894361611972	3.23089154857949	-0.69471834589261	o
2.92913383090123	-6.44563721456626	0.11526006620164	c
-3.70654438907027	-0.90576046072651	-0.90889395822077	h
5.33688497172864	-1.62167454789001	0.05226105451245	h
4.51806091122568	-6.66862085369079	-1.21900997067085	h
3.65693194403028	-6.79518581368055	2.03934017051093	h
1.52243419396860	-7.92431877156596	-0.31624120526742	h
3.72606046963373	3.03030573773633	0.09646420405260	c
5.39382036290413	2.84794459003546	-1.13773603599701	h
2.59946748581980	4.68023269172386	-0.45903429751845	h
4.35460735525122	3.23955622544125	2.07277163327346	h

Table 50: Geometry of the T_1 state of 1-methylthymine in atomic units obtained at RI-CC2/cc-pVDZ level

1.70317472271263	-3.79443751663497	0.33352932017741	c
-0.93215173175741	-3.59854658290513	-0.33201141109121	c
-1.88248906706653	-1.08790200370039	-0.15367510351754	n
-0.40859850386869	1.07880881477306	-0.48303806986134	c
2.16780549675742	0.72476665528667	0.11625849267273	n
2.97821031637011	-1.46648122311994	1.36419262742017	c
-2.33355532575316	-5.36979046732614	-0.99970890804119	o
-1.27627527971744	3.11561483785489	-1.19838161622194	o
3.13454881191105	-6.17693864033697	-0.08287906722256	c
-3.69767892927891	-0.87250689008700	-0.77282408738826	h
5.02053332522328	-1.53457650968469	1.70170520015803	h
4.69804236805812	-5.87502288424652	-1.44127443157291	h
4.01317371307205	-6.82380931164785	1.70116079112503	h
1.86701685907941	-7.65794481078225	-0.80532548845107	h
3.83751574194105	2.91965749490436	-0.02022528344893	c
5.49823782787563	2.45676846829236	-1.18760505895278	h
2.77483069726809	4.48675013229941	-0.86605020329665	h
4.46583718900752	3.44646906017225	1.89640818740489	h

Table 51: Geometry of the ground state of 3-methylthymine in atomic units obtained at RI-CC2/cc-pVDZ level

3.14946711210703	-0.41275705147510	0.00053346949426	n
1.60314300851682	-2.51179212560755	0.00140958415783	c
-0.96937282252128	-2.30195248280986	0.00124921144154	c
-2.08734982180744	0.23320972239033	0.00035973314173	c
-0.34570721222286	2.27588782260790	0.00033500638825	n
2.29592248286051	2.08087040978639	0.00013928635212	c
-2.74327282387610	-4.51772348699393	0.00029327420880	c
-4.38966802564336	0.65759343857975	-0.00008416465033	o
3.76557009287884	3.88670422653790	-0.00025869941060	o
5.06175887416944	-0.59390556574169	0.00051315309004	h
-1.45413460732821	4.81670161185104	-0.00007098016509	c
2.57594747970426	-4.33734539341452	0.00211230088294	h
-1.69475477624520	-6.31730809393687	0.00626186646524	h
-3.98973436906758	-4.45604708262536	1.66897110383713	h
-3.97990329689299	-4.46206414379222	-1.67583302886671	h
0.10941609499852	6.17670907488858	-0.00012890643601	h
-2.64848693673059	5.05674041756014	-1.68486820851823	h
-2.64865926039994	5.05709305453598	1.68453341251554	h

Table 52: Geometry of the S_1 state of 3-methylthymine in atomic units obtained at RI-CC2/cc-pVDZ level

3.17079742195367	-0.27302193348822	-0.29815330267392	n
1.74662817815072	-2.48460530986634	-0.03526655230835	c
-0.98016051026892	-2.20386882247723	0.00599917046298	c
-1.87538663038570	0.13188751060959	-0.50769335427706	c
-0.38950081301224	2.25095708014972	-0.98149722940953	n
2.27558476042378	2.12119102903554	-0.79535190476729	c
-2.69868969685729	-4.42928013397127	0.44729660080411	c
-4.50372918285828	0.84871195417280	-0.65242451371758	o
-1.54810589999866	4.74020735023111	-1.31582177379016	c
3.63878654000801	4.00054135942653	-1.07619056144190	o
5.09289704380023	-0.35507881329861	-0.24421194626128	h
2.72213546111375	-4.11722038502498	0.77791587479589	h
-2.21276949474299	-5.41786473456112	2.21945762878087	h
-4.68193741700863	-3.79906348000587	0.59348479279861	h
-2.58069960675278	-5.81405320128446	-1.10968259967018	h
-3.18347103385977	4.56629023400847	-2.59010540400668	h
-2.17008932842736	5.53735639847158	0.50779981858715	h
-0.10310332436763	5.97392205201868	-2.14973163559362	h

Table 53: Geometry of the T_1 state of 3-methylthymine in atomic units obtained at RI-CC2/cc-pVDZ level

3.07612027953311	-0.46956712664860	-0.10158209562820	n
1.69078853921876	-2.40112213160309	1.05654794704982	c
-1.04960707350744	-2.19868307341915	0.27724040565678	c
-2.12466713721060	0.29570597572547	0.00970021622783	c
-0.36844955749579	2.33340138921892	0.22321690173647	n
2.22278670708296	2.03998756795290	-0.22998732646877	c
-2.56328446708613	-4.49026163097253	-0.31841180300075	c
-4.41073262364906	0.74500757026330	-0.35982897891141	o
3.68346218195969	3.78976485574302	-0.70110359598302	o
4.99286903090337	-0.59928596413905	-0.26450758462516	h
-1.41074323720271	4.89165899253447	0.02469872355864	c
2.59907285143407	-4.26083052004204	1.01265779979170	h
-1.69551991620561	-5.56046311672936	-1.89463409229413	h
-2.60683414511113	-5.78457145826451	1.32442751534212	h
-4.50585712658759	-3.95520030063839	-0.82819705361124	h
0.10862386266246	6.23145724198106	0.46600631307883	h
-2.13363176327004	5.26042096304816	-1.89438367225566	h
-2.98206711724819	5.07452360020470	1.36834155010402	h

Table 54: Geometry of the ground state of 1,3-dimethythymine in atomic units obtained at RI-CC2/cc-pVDZ level

3.22022206759642	-1.61810362002763	-0.00036295455137	c
1.81064727119988	-3.78582386899000	-0.00048404588510	c
-0.94679032023300	-3.59783569447014	-0.00062241852478	c
-1.89724306989047	-1.08086387292953	-0.00037438737916	n
-0.45891780010703	1.13343895425780	-0.00023298438301	c
2.16054066682242	0.76455570691268	-0.00032429416619	n
2.94147168502109	-6.39101399589123	0.00004586806911	c
-2.38242656770763	-5.44897201431080	-0.00065979676045	o
-1.39985228212658	3.26888875090063	-0.00000171837400	o
3.70477503887431	3.05787140425583	-0.00005976413685	c
-4.64332219668209	-0.70096525529496	-0.00001531400698	c
5.28976399329761	-1.66098549764283	-0.00013287715343	h
5.02276566837948	-6.30560134205046	0.00215572096999	h
2.30760150318596	-7.46168378088604	1.67187640694232	h
2.31112281874473	-7.46178875510787	-1.67308907979160	h
5.70343888482066	2.49198838852881	-0.00016360892074	h
3.29070762561144	4.20463655321774	-1.68523495035336	h
3.29077150203346	4.20427717117211	1.68538338703080	h
-5.50784205485698	-2.58544729299901	0.00003041658681	h
-5.20703008134354	0.37524313585782	1.68741160714135	h
-5.20751307875564	0.37534246677784	-1.68727949189804	h

Table 55: Geometry of the S_1 state of 1,3-dimethythymine in atomic units obtained at RI-CC2/cc-pVDZ level

3.34423783187624	-1.57387095394669	-0.21715014902200	c
1.81084748725883	-3.84318437414594	-0.02189692910309	c
-0.71196323270138	-3.48344812619288	-0.02761937419443	c
-1.87022946091366	-1.12661190343336	-0.12360101241250	n
-0.44524730237160	1.12983408144647	0.02112965593496	c
2.14984982404813	0.77826811879935	-0.03025078689677	n
2.99788039927517	-6.42846624317660	0.03320579781754	c
-2.62049701060881	-5.42820549236140	0.07706692092673	o
-1.51623457814315	3.21182391030306	0.15001386979725	o
3.73786763083025	3.03888516512866	0.01433484559948	c
-4.61909295760209	-0.89387343193003	0.08374731684139	c
5.36726203269419	-1.58043475172154	0.22831302463228	h
4.37542085490132	-6.59437391738315	1.59219022670765	h
1.54029438865189	-7.89454146302391	0.31276914762834	h
3.99781149094855	-6.85200204814555	-1.74920687780790	h
4.96882521375446	3.00215167821869	1.69625438804492	h
4.91963957320500	3.09492177700918	-1.70040717175835	h
2.49393935692247	4.69689997842814	0.08140530644834	h
-5.49192926328418	-2.53683239600133	-0.84828353574838	h
-5.22858010614451	-0.81432230715085	2.07645746901502	h
-5.18112855721669	0.86314246902952	-0.86502378066685	h

Table 56: Geometry of the T_1 state of 1,3-dimethythymine in atomic units obtained at RI-CC2/cc-pVDZ level

3.08020666545311	-1.48329741794633	-1.27091819037057	c
1.65080608387439	-3.79349648666961	-0.43159514805397	c
-1.04752643959361	-3.57802473381045	-0.10833420846736	c
-1.98500138771968	-1.05175193163846	-0.30519870268449	n
-0.48071008873980	1.06520793790759	0.19459718708529	c
2.15094604587869	0.67605937161420	-0.05528142202139	n
2.98573593359227	-6.19674936521245	0.15585288377319	c
-2.50965154158843	-5.38542141292416	0.29253818337726	o
-1.37640949502193	3.13405763585407	0.78786245662715	o
3.79291380557765	2.87081495165712	0.28881786438992	c
-4.71610618190924	-0.65962730159544	-0.05987439844398	c
5.14888430875660	-1.58331734783496	-1.34033922315504	h
4.35146916999977	-5.92300054202723	1.71842462844205	h
1.61478665374569	-7.66810942493160	0.68616671394871	h
4.09377364912200	-6.84539070670200	-1.49577712158644	h
5.50653123725664	2.27613547681779	1.30784332991358	h
4.33160637758893	3.66663660817401	-1.56264253785227	h
2.75470260369881	4.29992905347564	1.37406537711483	h
-5.64730906619838	-2.40228879953969	-0.68781180273935	h
-5.24997142993222	-0.26299488729608	1.91478006616045	h
-5.27547768682413	0.95411918657795	-1.23971179184900	h

Table 57: Geometry of the ground state of uracil+6H_2O in atomic units obtained at B3-LYP/TZVP level

0.20775884851906	0.07356579155689	-0.18583725755595	c
2.75542656646271	0.10921949251565	-0.19811629007736	c
4.03859892217919	2.51096456750382	0.00629832362615	c
2.47420371902501	4.61753899695527	0.15520149844033	n
-0.11053574465878	4.57728725441861	0.22576607900870	c
-1.19899088309171	2.23234253650130	0.02031314468237	n
6.36186758772745	2.77053202076443	0.05824039529974	o
-1.38753555221199	6.52412865946944	0.46335435492745	o
-6.63055983955597	6.95545586622821	0.80914828039623	o
9.00724360991960	6.99577752979754	2.05290005228129	o
4.72764593062309	9.24819415812061	0.14150201239204	o
8.51358529778579	-2.15556066874047	-0.64607132120292	o
-0.87538501512077	-1.65503881545369	-0.32183443716260	h
3.88169731440990	-1.58581930395065	-0.35063123190850	h
-3.14625791358345	2.11419872139255	0.01974447169321	h
3.34198635143741	6.41335240655113	0.17657017055059	h
8.31411874756676	5.42477734454378	1.37462718886730	h
10.73896919940333	7.06974102153183	1.50503217469076	h
-4.78861984406421	7.04296999717046	0.66436416403294	h
-7.29613759519175	8.36520472949074	-0.12609321276769	h
3.69267987909263	10.41679414157753	1.11742788545413	h
6.37118575633656	9.04764912702211	0.95511483657746	h
8.13755958991254	-0.37460833792154	-0.37862988217304	h
9.70320907796294	-2.20237014313860	-2.02008454003956	h
-6.50546066361992	1.89185213680599	0.08268688030569	o
-7.02129164240121	3.66258065824330	0.31717875458856	h
-7.63277931910630	1.16945339093923	-1.14637121845757	h
0.40472472700385	11.29178694357122	2.32454676673698	o
-0.08505558793455	11.42865246078496	4.07056677275929	h
-0.36490414885324	9.73742231222933	1.70199668381254	h

Table 58: Geometry of the ground state of 1-methyluracil+6H_2O in atomic units obtained at B3-LYP/TZVP level

-0.13705077365498	-4.46526820248801	-1.97764871973731	c
-1.53514374077158	-2.74050498921006	-0.72679637497714	c
-0.29504036018351	-0.93641550883741	0.90115733093591	c
2.30979072704645	-1.18486327893064	1.03750186475539	n
3.74777551572894	-2.89345747733471	-0.26218631044655	c
2.44103401805596	-4.58749405244288	-1.78589389627164	n
-1.38676989239756	0.72811225798093	2.11936408403053	o
6.07172406092344	-2.94731547305762	-0.12926131374754	o
3.91464129262494	-6.45039841266624	-3.22723162348765	c
4.84811318968798	2.03128248591896	4.03156988585176	o
0.96441838226472	5.34405083402967	4.31130784034817	o
8.96397011915433	-7.58444833527424	0.09225067595407	o
-5.44221724373955	3.92340282814047	1.11962899815226	o
-2.49175008253470	8.29114488651116	1.47413528447037	o
-3.56346923311232	-2.66965447885093	-0.91828835902092	h
3.31219612059476	0.09305525068295	2.22427372370098	h
-0.98444707282478	-5.85282132263140	-3.21689113554248	h
2.60513352465221	-7.57175684317764	-4.34606815050119	h
5.23692887565364	-5.48695971546975	-4.47694007252918	h
4.98130663570882	-7.67327007437414	-1.96170692409485	h
10.08178286744034	-7.75958128551867	1.51585748166401	h
8.30125818352243	-5.87764602189238	0.18864698738966	h
6.57182336741404	2.31851365509659	3.46102973446611	h
3.93593170412064	3.63674371219051	4.18018900144553	h
-0.01284654143582	3.84043057226858	3.93687667986748	h
0.10737261809811	6.68566026156295	3.38250974137547	h
-6.72760252462060	3.74526380143916	2.39496064139433	h
-4.19199545506852	2.60845545355365	1.47363361378550	h
-3.70007394970101	6.91016533878569	1.22486684252013	h
-2.32693216618152	9.11873916576614	-0.13561226109581	h
9.39636890893124	0.98688007365715	1.59625637733187	o
10.29864364969004	1.71596514656351	0.19682053239570	h
8.43886980127959	-0.42692717565059	0.90937033623703	h

Table 59: Geometry of the ground state of 3-methyluracil+6H_2O in atomic units obtained at B3-LYP/TZVP level

3.31737502599818	-2.97301667966542	1.70472941814529	c
0.84103925007676	-3.42932963963523	2.29437281036969	n
-1.09559815725935	-2.01709935976916	1.34804983138934	c
-0.68497793014013	-0.05140518321719	-0.21681232242397	c
1.86694401003919	0.60890645048335	-0.90523885070932	c
3.78264726459327	-0.91247870947746	0.15553666487175	n
2.40939997894637	2.37655056117788	-2.32372751961804	o
6.44726152339651	-0.38097473471977	-0.43095819545051	c
5.04120916532578	-4.32531896485262	2.50128006511140	o
6.75818034520726	4.88189128462177	-4.48600526315331	o
-2.26401332702036	4.54728968456235	-4.08044625795563	o
4.38323766993921	-9.10057088831958	5.31500689059719	o
-0.32711362672314	-7.33775437642017	5.56816193852855	o
9.98371522879333	-4.69696031358476	4.46477348638454	o
0.45109793381607	-4.89199289366533	3.54873973385240	h
-2.20119763076544	1.06731358090840	-1.00189405526455	h
-2.96468863848893	-2.60052373410256	1.93586766503370	h
6.56795866639185	1.41288912783034	-1.41076687613714	h
7.52635298370910	-0.29862297533339	1.31732668035003	h
7.21750892211933	-1.86992898636115	-1.62870206610260	h
-2.36741634091562	4.61227799999399	-5.89470339717469	h
-0.52486978677291	4.08908652186659	-3.70355232131826	h
4.82233705304750	-7.77466337525243	4.12618422434292	h
5.64680629644812	-8.93072875174180	6.65615436728338	h
11.06958745893924	-5.37004794050526	3.16951267684176	h
8.36586312036673	-4.37365553567294	3.64341370762852	h
6.70183079038571	6.63387095171079	-4.00137341698454	h
5.15242277559096	4.18155393266305	-3.94693458984485	h
1.30596256509135	-8.24949356308166	5.73531225740997	h
-0.98677590661986	-7.14188600611683	7.25107289363387	h
8.34655685469292	-7.71363859571859	8.48347004102239	o
9.63932883752764	-8.67320190630909	9.32654964138259	h
9.20653783343126	-6.62053866053222	7.26210367035799	h

Table 60: Geometry of the ground state of thymine+6H_2O in atomic units obtained at B3-LYP/TZVP level

-0.01100761848085	0.03118286725459	-0.00997088909594	n
2.57875544097952	0.03770633955610	-0.00899851473635	c
3.96745557049116	2.18098747204169	-0.01335197066473	c
2.59622820128255	4.56294073365719	-0.02478899290225	c
-0.01879516108975	4.39657489158725	-0.08414573546729	n
-1.39892252959417	2.21222961058877	-0.02017343434104	c
3.62470704296005	6.66049172086266	0.01592446062030	o
-3.74086439085501	2.21128100853809	0.03001734678422	o
-2.65327560534475	8.80640072725248	-0.54309931488339	o
1.33500851874032	11.20328511865171	1.78788701666162	o
-6.85422764875447	6.38698002872555	1.50523763982058	o
-6.92610542147003	-1.95163824625216	0.37172955257205	o
-2.57633147627910	-4.62874432443094	0.12237689066391	o
8.61243122575779	8.82581220552308	0.03045730613765	o
3.43567326735110	-1.81936099469630	0.01267819041805	h
6.79904135875267	2.21640785946487	0.01761054209331	c
-0.95859397884207	-1.67504914337654	0.00550470370375	h
-1.04227632244809	6.10208921717744	-0.23197886359168	h
2.34732328691296	9.76413458583503	1.23798674244444	h
2.39313755440965	12.66942002018615	1.59910460126961	h
-5.99724889924823	-0.35932379466824	0.20393993211774	h
-8.37069690503042	-1.83238710429059	-0.72557053131239	h
-4.26765718113707	8.60466230273994	0.31961233521538	h
-1.67594631666172	10.12421672474679	0.29815973854320	h
6.98428490627409	7.97692948754943	0.03003272357724	h
8.74841891138506	9.58464484213980	-1.61619024863917	h
-4.35093198823132	-4.07641202345145	0.20947321128351	h
-2.50680011691415	-5.97679307545862	-1.09528337514503	h
-7.32078774899183	6.14943615513953	3.24666878303059	h
-5.93994797643887	4.86443405656278	1.01394973568473	h
7.55505142416379	0.29890653412917	0.00301739640611	h
7.55117208451496	3.22810020357646	-1.61653984491027	h
7.51910469992414	3.18769559767972	1.69041094079048	h

Table 61: Geometry of the ground state of 1,3dimethyluracil+6H_2O in atomic units obtained at B3-LYP/TZVP level

0.17848931754453	-3.40158859983297	1.68800448752252	c
-1.64131596298701	-1.71802795698958	0.56142165727877	c
-0.62468574541251	0.30562757081940	-0.81897450735801	n
1.91945734560409	0.90317178832349	-0.88645061317851	c
3.54887948803791	-0.78949552593377	0.27165446842966	n
2.65937797592769	-2.88968517552567	1.50026081935222	c
-3.94508073912187	-1.96946719810034	0.76164286242022	o
-2.38745472647133	1.94390569633612	-2.22095742157526	c
2.72682050650705	2.82182716674335	-1.91290294862128	o
6.26226942881613	-0.22789863136363	0.16236375914580	c
-0.50869091908837	-5.06209725348995	2.65065232803669	h
-8.39144894022867	-2.16556877664229	-2.22547619114407	o
7.00105933515903	6.02255414121792	-2.46616995105556	o
-5.02179387351447	-7.27049881281418	0.39918679809951	o
0.52685919025057	7.00779634031569	-5.28681056933811	o
5.54245914134818	8.03048657980176	-7.20420419723974	o
-4.37499573235832	-5.08360426025836	-4.81344854268691	o
4.08934985467439	-4.09834807338692	2.31858332710626	h
7.27688889016328	-1.78464025982836	1.03805817094383	h
6.86989317221313	-0.02375366325129	-1.79254851291066	h
6.68557664166552	1.51806953273564	1.16864959843081	h
-3.90196939854341	0.76378802909446	-2.94230819289825	h
-3.16020560073961	3.40078738870011	-0.98530946840167	h
-1.39681775050866	2.82978869508840	-3.78006843193929	h
-4.36662846263778	-6.24173075510544	-3.39406574154698	h
-5.91852388277037	-4.13219067493347	-4.56498536306417	h
-6.76899311242895	-7.77464314847687	0.48549226225057	h
-5.01239720023606	-5.48350021862656	0.82843408009159	h
5.56532753398407	4.91230143490389	-2.15938156249546	h
6.80568110219452	7.41273502333984	-1.30683851661482	h
1.97210120399603	7.53014577286327	-6.29501870720182	h
1.24247561724518	5.84285093935866	-4.08080392303295	h
-9.53693057256830	-0.76099906382045	-2.37403033210482	h
-7.07595509682456	-1.64940492378533	-1.05438349767858	h
6.37011919411720	7.31167627771102	-8.65384744418247	h
6.37438851940230	7.31395351925287	-5.72102835127612	h

Table 62: Geometry of the ground state of 1-methylthymine+6H_2O in atomic units obtained at B3-LYP/TZVP level

-1.44625145301301	-0.62074483935181	-0.03778731782524	n
-0.07338752142000	1.56941625292619	0.02315120868794	c
2.52482965316527	1.27970133340476	0.07634187598565	n
3.59816433353045	-1.08576413424905	0.06085828545232	c
2.25396907599734	-3.25655583245909	0.02470569160883	c
-0.48421438271682	-3.05218953596134	0.02497160468317	c
-1.06048083691332	3.68054752762267	0.02696109498873	o
4.08943258880553	3.57297270512440	0.14372273255123	c
3.44305651233888	-5.82749985603096	0.01520486252309	c
-1.93320104523483	-4.88253229776341	0.08427418303227	o
-6.50870563443338	-0.15305050460989	-0.44541805122299	o
-7.14198578707571	-4.52721505495767	2.12327136656684	o
-6.26126987761248	4.99446999062398	0.81861273760195	o
-3.16712552027675	-10.03822968396557	-0.54186663589811	o
0.88558100933269	8.66985947284277	1.37065149994670	o
-3.44132788001463	-0.42132300327349	-0.16832307222115	h
5.64302538333086	-1.09727176228965	0.08924479491851	h
5.49741475047387	-5.69307999128709	0.10877451946501	h
2.78557945690987	-6.95340658672232	1.61529818437402	h
2.94290546828938	-6.87084982702046	-1.69631438694076	h
6.06396454648176	3.00517713905372	0.15315284896804	h
3.71692835551723	4.74014312175989	-1.50974633448731	h
3.67885827463470	4.68756561098421	1.82334614119852	h
-5.38113028409535	-4.80433650064784	1.69674466992908	h
-7.94172931712397	-6.15670156219601	1.78950612548910	h
-7.28894327421277	-1.56291636636749	0.47703331532199	h
-7.07312324593050	1.44910365827217	0.25952897210998	h
-4.47588791180891	4.68640253748512	0.48652488961268	h
-6.83048384484169	6.08591580289772	-0.52106291393525	h
-2.50362981084732	-8.32415239669131	-0.38797549329982	h
-2.91908307672929	-10.51213035863850	-2.28004190603862	h
-0.34636209383675	9.62455698993157	2.30721744841796	h
0.04205853726307	7.11162111749101	0.90080112934498	h
-8.20043274523463	-9.65265727293228	1.06177138566157	o
-6.47860628689332	-10.01826884390634	0.48896243817188	h
-8.50494566829859	-10.76753546769608	2.46588765565475	h

Table 63: Geometry of the ground state of 3-methylthymine+6H_2O in atomic units obtained at B3-LYP/TZVP level

3.64422902673796	-0.58915796046853	0.28349100881177	c
2.96463883110200	-2.40863492631315	1.98724377925835	n
0.52460128201728	-3.16750508491528	2.35787108723969	c
-1.43802349301295	-2.13323371362658	1.09854409529688	c
-0.88152814993953	-0.13191440965491	-0.68868811567437	c
1.66311575778261	0.51700421803761	-1.02837763679494	n
-4.13234457748212	-2.93616653072640	1.44441138304283	c
-2.53411595445175	0.99297246018260	-1.89382711089316	o
2.22658348099607	2.43021463803532	-2.97125335347930	c
5.87209499407408	0.00964299533255	-0.04835362228038	o
10.24909737720142	-2.18629268873618	2.13895735531876	o
9.44224249246397	3.67084657875004	-2.00367365062396	o
-3.88588622504048	3.87659400745773	-6.22895220665086	o
6.76298834085126	-4.64766737997755	4.92492703380163	o
-5.37517063570895	-1.75768477423624	-5.75242435206366	o
-0.60345170705598	-0.06607005519701	-8.32679573422793	o
4.38551139462440	-3.20869060915189	3.06463483186750	h
0.28784895639901	-4.66267078719062	3.73225097591228	h
1.67877252673398	1.69939263255281	-4.81976457766377	h
1.16257674709739	4.14208503297546	-2.55923770484835	h
4.23021393320589	2.84145128725707	-2.91964534924538	h
-1.89078311369595	-1.24475777695086	-7.76688358139531	h
-1.49045130720743	1.53443779360781	-8.28258852685925	h
-6.20746111295765	-0.39818223287211	-6.63884709257042	h
-4.72344100689191	-0.93968727251599	-4.24622709029708	h
-4.18127798392981	5.66442321017768	-6.08096250658705	h
-3.31191122980779	3.29722086708990	-4.58059222884021	h
-5.31489000893390	-1.34027250794163	2.00604199059011	h
-4.91803688921652	-3.68150492078916	-0.31410441835020	h
-4.27768749903452	-4.39895764055905	2.88951185359576	h
9.72390312468294	3.15716509101273	-3.72560229425317	h
8.13804203824122	2.54450802552789	-1.38406540295683	h
11.62692377109716	-1.01713675641093	2.33329589977661	h
8.94113179745638	-1.29633664953514	1.19473061976196	h
8.33277858443138	-3.94421773505794	4.21977084996564	h
6.93592341898159	-4.59952473538910	6.73447120178750	h

Table 64: Geometry of the ground state of 1,3dimethylthymine+6H_2O in atomic units obtained at B3-LYP/TZVP level

3.03530875278916	-2.39879091206728	2.06287009398612	c
0.60929188646876	-3.13604234632587	2.31396318645218	c
-1.27301594184477	-1.89520046725856	0.75786156742643	c
-0.39622372084718	-0.08105458228314	-0.94706136316907	n
2.10183542963071	0.70023851435267	-1.13099448278665	c
3.79742014924442	-0.53923413370751	0.42275097904936	n
-3.55188499193935	-2.37700421509539	0.88244316857125	o
-2.26629560453031	1.04524536808912	-2.67795265831364	c
2.79454846730262	2.37428895783591	-2.57721970859911	o
6.46265522911241	0.21355082896030	0.25286124725520	c
-8.46626933106025	-2.22270257436469	-1.30410394636005	o
6.84786943207557	6.14472724634545	-2.95245816435014	o
5.04925477528836	8.60761560112675	-7.34119778281254	o
-4.96756898030737	-7.38200517153488	-0.85229991373907	o
1.77515826416818	8.18974948435423	-3.06995055555841	o
-5.27091129321603	-4.04063724303246	-5.40793457806604	o
-0.22758200147863	-5.16751878273422	4.10284015943465	c
4.53481614122252	-3.24297436731624	3.16691846355625	h
7.54138577973149	-0.93000584912758	1.57516618890231	h
7.16992064355321	-0.09944290935856	-1.65518439158086	h
6.68776937682563	2.20434447463749	0.72276055797479	h
-3.25024377288897	-0.46762078493248	-3.67303994519737	h
-3.61057372725354	2.17972007265683	-1.60635125029607	h
-1.26255391725852	2.23240105705794	-4.01055259170263	h
-4.86144952224512	-5.49435601532461	-4.36864008188484	h
-6.76268061116765	-3.36432297046149	-4.58732656380863	h
-6.75822438671467	-7.67899979973192	-0.70040957747568	h
-4.68739326644961	-5.80073671772475	0.03556485088509	h
5.88902111938084	4.58672690580294	-3.05987806735307	h
5.58260513006481	7.30878451607835	-2.29778725358013	h
2.33180649864633	8.62144623063036	-4.77005828337086	h
1.40740699865627	6.40350827050022	-3.15081984793882	h
-9.66697206256088	-0.93915572937437	-0.83980668084738	h
-6.90648371987246	-1.83127763248807	-0.41587932138283	h
5.33246332049825	7.97368438976008	-9.02025084563180	h
6.19919092914230	7.69573747457423	-6.22363529837477	h
-1.63408049352387	-4.44628574821918	5.43041072371758	h
-1.10368377811526	-6.73482771327852	3.08363179541174	h
1.37084107815854	-5.90127437921210	5.17619343105264	h

Table 65: Geometry of the ground state of uracil+6H_2O in atomic units obtained at RI-CC2/cc-pVDZ level

0.23692480981438	0.05576598148804	-0.07498313408757	c
2.82264907336489	0.12050370870882	-0.03261556142092	c
4.07378861650596	2.55671445687344	0.11662256501894	c
2.46941611589819	4.65520053103928	0.12379944840583	n
-0.13253270134293	4.58921362171002	0.13121545931984	c
-1.20344278143533	2.21529053912459	0.00944468886697	n
6.42715292757197	2.85187439339721	0.23967063739002	o
-1.45154726592058	6.55873016249886	0.24372358241806	o
-6.65608725195599	6.73469749238877	1.07819323832713	o
8.81010841601509	7.22931441293897	2.21050490660456	o
4.65705321615838	9.19729525954321	-0.19413682021329	o
8.33440140189478	-2.20504490986321	-0.34709990718092	o
-0.83712509325709	-1.70875264947070	-0.16114905534333	h
3.98927320801713	-1.57973582940308	-0.07450721842173	h
-3.17740640110477	2.07913333536771	-0.04060972370896	h
3.33166059880634	6.49144048575337	0.02703202342620	h
8.12014632176078	5.60024992389316	1.66217465808295	h
10.21098346581279	7.45197793438629	1.05463199294309	h
-4.81494628483581	6.84902279296351	0.88601598750950	h
-7.26036784842638	7.87627882608585	-0.21656505249308	h
3.54356512399200	10.24766529331347	0.85218012783704	h
6.18495589828943	8.92366850848644	0.82652669126646	h
8.04555156775454	-0.43330007522215	0.07641348031509	h
8.42901071451564	-2.10973800536472	-2.17047959626843	h
-6.38146017608209	1.77521076491644	-0.07812149893912	o
-6.84510248506503	3.51097640845396	0.44162850337373	h
-7.06028033318493	1.67412384643212	-1.77440881609085	h
0.54985246295512	11.05183835217842	2.41380969325795	o
0.54775465276973	10.47247288940412	4.14886879748809	h
-0.30902375610839	9.66129437179458	1.54958249595566	h

Table 66: Geometry of the S_1 state of uracil+6H_2O in atomic units obtained at RI-CC2/cc-pVDZ level

0.13753994197352	-0.03378175112134	0.02079904816826	c
2.84145639841666	0.09728018089448	-0.22452401673673	c
3.85402225029866	2.43568827208900	-0.41460487882597	c
2.45158774708917	4.66239224106747	-0.33272181653378	n
-0.14606518479180	4.58147321890922	0.03157761220368	c
-1.20382244572652	2.24061361226901	0.18555774141812	n
6.48689362638243	3.10438322818994	-0.70387552350906	o
-1.41304344899608	6.60297433169741	0.19265470459190	o
-6.53569159000147	7.04533533231374	1.13147683782802	o
8.49029051027716	6.68785175975168	2.99592879279212	o
5.02829146985114	9.06815285963085	-0.28306418536396	o
8.52448234479389	-1.12697297883361	-1.35031502472631	o
-0.94127669312485	-1.76894025587674	0.28649065746396	h
4.03869625082451	-1.57739418293837	-0.30264104211645	h
-3.16212691340916	2.16817168952160	0.38977338871043	h
3.37318347573987	6.43880148158998	-0.44407518638621	h
7.98104278986957	5.12147624188406	2.17386390604722	h
10.02750767580052	7.10624109751613	2.09373339374818	h
-4.69044379705560	7.00611171281471	0.91738500533929	h
-7.07402561044779	7.93152015080401	-0.37574361068381	h
3.73034839266194	10.14496074611448	0.50819271750723	h
6.16457094680377	8.64777782331636	1.11417002013655	h
9.57648047940572	-0.22185557297952	-0.15807669952048	h
8.50108283624989	0.02768380035678	-2.77222040887144	h
-6.46714311345280	1.94166129437781	0.66100967954946	o
-6.83771829383460	3.74621723368920	0.96783756867508	h
-7.18457858495776	1.67360514769181	-1.00082309358541	h
0.77308702459023	11.08547811561825	1.84100440509342	o
0.70655144399943	10.73111491946350	3.63480987820094	h
-0.15211520846849	9.63872086067443	1.13768700476890	h

Table 67: Geometry of the T_1 state of uracil+$6H_2O$ in atomic units obtained at RI-CC2/cc-pVDZ level

0.08773872419271	0.29109553531883	-1.51176348237959	c
2.80447415889115	0.28092610994330	-0.66067336322638	c
4.04760787265428	2.68590397441205	-0.36599074226878	c
2.48594946455019	4.81090908204393	-0.55254966028251	n
-0.09820866664332	4.67040585232282	-0.13888670885711	c
-1.19734746042445	2.31687132857104	-0.38953629826773	n
6.38826848850807	2.91305679319921	0.04523533170141	o
-1.37368487346487	6.58279165100326	0.43697517127482	o
-6.61108892000997	6.88016487928839	1.31857710423743	o
8.74182996541381	7.28969937448729	2.15903248891270	o
4.70584040774010	9.39880607466151	-0.38960871757121	o
8.03442717541909	-2.29792075824363	0.54592556715542	o
-0.97361969990782	-1.48221357779816	-1.52508934724430	h
3.83308377772126	-1.41608354651984	-0.07535969356056	h
-3.16004559863216	2.21112929221348	-0.15243151513557	h
3.33867084234793	6.63659717646667	-0.47157499945464	h
8.07506665881304	5.67616393301062	1.55217704102700	h
10.22815602708458	7.50665702053519	1.11429117411020	h
-4.76907251521734	6.94446722706024	1.14503597309066	h
-7.16838675192954	7.99865358683354	-0.01700442812130	h
3.58897920774260	10.34964696196752	0.74500384938032	h
6.20597370145785	9.03720162196049	0.64164377379846	h
7.86118173349222	-0.46409158978043	0.57434927962548	h
8.45984771263475	-2.58420904035877	-1.20920315741128	h
-6.38535435985333	1.88970359093203	0.18164344427118	o
-6.83012544482953	3.62588431557353	0.70420384099943	h
-7.23995672869273	1.72391089453474	-1.42766597779129	h
0.77405928851166	11.00931771799872	2.64922375676063	o
1.02767543745781	10.36379629206014	4.34224464835416	h
-0.14190401720634	9.62230839586122	1.84372114315563	h

Paper 4

Overruling the energy gap law: Fast triplet formation in 6-azauracil

Mihajlo Etinski, and Christel M. Marian

Phys. Chem. Chem. Phys., *submitted*

Overruling the energy gap law: Fast triplet formation in 6-azauracil†

Mihajlo Etinski,[a] and Christel M. Marian*[a]

Received Xth XXXXXXXXXX 20XX, Accepted Xth XXXXXXXXX 20XX
First published on the web Xth XXXXXXXXXX 200X
DOI: 10.1039/b000000x

The photophysical properties of 6-azauracil were studied by means of *ab initio* quantum chemical methods. On the basis of our calculations we propose here the following mechanism for the lack of fluorescence and the high triplet quantum yield that was observed experimentally after irradiation of this compound with UV light [Kobayashi *et al., J. Phys. Chem. A*, 2008, **112**, 13308]. Multiple potential energy surface crossings between excited singlet states of $\pi \rightarrow \pi^*$ and $n \rightarrow \pi^*$ character lead to an ultrafast transfer of the S_2 ($^1\pi \rightarrow \pi^*$) population to the lower-lying S_1 ($^1n \rightarrow \pi^*$) state. This state acts as a doorway state from which the T_1 ($^3\pi \rightarrow \pi^*$) state is formed approximately within 125 ps in the isolated 6-azauracil and within 30 ps in acetonitrile solution according to our calculations. The enhancement of the $S_1 \rightsquigarrow T_1$ intersystem crossing in acetonitrile solution is noteworthy as it goes along with an increased adiabatic energy gap between the interacting states. Blue shift of the S_1 potential energy surface by about 0.2 eV in this polar, aprotic environment places the intersection between the S_1 and T_1 potentials close to the S_1 minimum, thus increasing the overlap of the vibrational wavefunctions and consequently speeding up the spin-forbidden nonradiative transition.

1 Introduction

Nucleic acid bases are the main chromophores for the absorption of UV radiation at wavelengths below 300 nm in DNA and RNA. After excitation they essentially relax to the ground state on an ultrafast timescale[1] although the formation of a long-lived dark state in uracil and thymine was observed[2–8] and a significant triplet state yield in aprotic solvents was obtained[5,9].

On the other hand it is known that isomers of nucleic acids or their analogs can have drastically different properties[1]. A well-known example is the different photophysical behavior of 2-aminopurine and adenine (6-aminopurine)[10]. The shift of amino group from position 6 to position 2 increases the lifetime of the excited state by three orders of magnitude.[1,11,12] The different excited-state deactivation characteristics of the two isomeric forms were attributed to the differing energetic accessibility of a conical intersection between the primarily excited $\pi \rightarrow \pi^*$ state and the electronic ground state along a puckering coordinate.[13] Another example is the fluorescence decay of two amino-substituted uracils, 5-aminouracil and 6-aminouracil.[14] While 6-aminouracil exhibits similar characteristics as the parent uracil molecule, 5-aminouracil behaves fundamentally different. The decays are globally slower and depend strongly on the wavelength of the laser irradiation.

Recently, Kobayashi et al.[15,16] investigated the photophysical behavior of 6-azauracil, a compound in which a nitrogen atom has been substituted for the CH group in 6-position of uracil. They showed that this compound exhibits remarkably different relaxation dynamics from uracil. After excitation to the first bright state with 248 nm radiation, 6-azauracil in acetonitrile solution does not relax to the ground state by internal conversion (IC) nor does it fluoresce. Instead, the lowest triplet state is populated by intersystem crossing (ISC) with a quantum yield of unity. Irradiation of the molecule with laser light of longer wavelength (308 nm) still leads predominantly to a population of the T_1 state but in addition weak fluorescence is observed. Those results demonstrate that aza-substitution of uracil in 6-position substantially increases the triplet quantum yield and inhibits the ultrafast internal conversion to the ground state. Spin and energy transfer from the T_1 state to molecular oxygen is efficient, making 6-azauracil a powerful type II photosensitizer. It is thus not surprising that 6-azauracil is used as antiviral drug[17] and growth inhibitor for many microorganisms[18].

Kobayashi et al.[15] offer two possible explanations for the effect of aza-substitution on the dynamics: acceleration of the ISC rate by introducing an N atom, thus enhancing the spin-orbit coupling (SOC), or alternatively, an increase of the rigidity of the C_5-N_6 double bond that would prohibit the ultrafast relaxation along the twisting mode of that bond. In the related pyrimidine bases uracil, thymine, and cytosine the twist of the corresponding C_5-C_6 bond in the $^1(\pi \rightarrow \pi^*)$ state had been

† Electronic Supplementary Information (ESI) available: [Cartesian coordinates and harmonic vibrational frequencies of all optimized structures.] See DOI: 10.1039/b000000x/

[a] *Heinrich-Heine-University Düsseldorf, Institute of Theoretical and Computational Chemistry, Universitätsstraße 1, 40225 Düsseldorf, Germany. Fax: +49 211 8113466; Tel: +49 211 8113209; E-mail: Christel.Marian@uni-duesseldorf.de*

‡ Dedicated to Prof. Karl Kleinermanns on the occasion of his 60th birthday.

identified as the decisive coordinate leading to an energetically easily accesible conical intersection.[19–23] The purpose of the present paper is to elucidate the photorelaxation mechanisms of 6-azauracil. Using *ab initio* quantum chemical methods, we have computed energy profiles along pathways connecting the minimum geometries of the most important electronic states and have determined ISC rates for several processes. These data can be directly compared to the results of our recent theoretical study on uracil, thymine, and 1-methylthymine where it was found that ISC from the S_1 to the T_1 state is a fast process.[24]

2 Theoretical methods and computational details

All calculations were performed using the following programs: Turbomole[25] for geometry optimization and electronic excitation energies, MRCI[26] in combination with SPOCK[27,28] for obtaining spin-orbit matrix elements, SNF[29] for the numerical determination of vibrational frequencies in harmonic approximation and VIBES[30] for calculating intersystem crossing rates. The predominatly employed electronic structure method is coupled cluster with approximate treatment of doubles (CC2).[31] We used the resolution-of-identity (RI) CC2 implementation in Turbomole for ground state optimizations.[32–34] RI-CC2 in combination with linear response theory was utilized for excited-state optimizations and the determination of vertical excitation energies.[35,36] It was shown that the CC2 method gives good vertical excitation energies for nucleic acid bases.[37] All geometries were optimized without symmetry constraints. In order to calculate spectral shifts that are consequencies of electrostatic interactions in polar solvents, we used the conductor-like screening model (COSMO)[38,39].

We employed Dunning's[40,41] correlation-consistent basis sets cc-pVDZ (C, N, O: 9s4p1d/3s2p1d; H: 4s1p/2s1p) for the geometry optimization and calculation of spin-orbit coupling matrix elements (SOCMEs). Recent benchmark calculations performed in our laboratory had shown that this type of basis set yields satisfactory geometry parameters for the ground and excited-state minima of the nucleic acid bases whereas augmentation of the basis set by diffuse functions is required for obtaining accurate excitation energies.[24,37] Unless otherwise noted, we therefore employed Dunning's aug-cc-pVTZ basis (C, N, O: 11s6p3d2f/5s4p3d2f; H: 6s3p2d/4s3p2d) for the calculation of excitation energies. Auxiliary basis sets for the RI approximation of the two-electron integrals in the CC2 treatments were taken from the Turbomole[42].

SOCMEs were computed with the SPOCK program[27,28] using the one-center mean-field approximation[43,44] to the Breit-Pauli Hamiltonian. This effective one-electron operator treats the expensive two-electron terms of the full Breit-Pauli Hamiltonian in a Fock-like manner. This approximation typically reproduces results within 5% of the full treatment[45,46]. The underlying spin-orbit free electronic wavefunctions were obtained by the combined density functional theory / multireference configuration interaction (DFT/MRCI) method.[26] In all electronic structure calculations only valence electrons were correlated. Experience has shown that the combination of CC2 geometries and DFT/MRCI SOMEs yields reliable results at manageable costs[24].

Intersystem crossing rates were calculated between the lowest vibrational level of the initial electronic state and the vibrational manifold of the final electronic state using a time-independent approach in the framework of the Condon approximation as is described elsewhere[47]. In order to obtain rates, Franck-Condon (FC) overlaps were calculated only with vibrational levels that are present in a selected energy interval around the energy level of initial state. After careful tests an interval width of 1 cm^{-1} was chosen. To speed up the calculations, highly excited vibrational states with more than 7 quanta per normal mode were excluded.

3 Results and discussion

3.1 Ground-state geometry and vertical excitation energies

The ground state minimum structure was found to be planar. Bond lengths obtained from this optimization are presented in Figure 1(a) together with DFT/B3-LYP/6-31G(d,p) bond lengths from Kobayashi et al.[15] (in parentheses) and data from crystallographic analysis[48] (in square brackets). Comparing the CC2 and DFT results it is seen that the CC2 method gives slightly longer bonds as was previously noticed for uracil[24]. The largest difference are found for C–N bonds, namely 0.02 Å. Improvement of the basis set is expected to lead to a slight bond contraction[37]. Since we have been searching for excited-state minimum structures as well, for which the computational expense increases significantly when employing the larger aug-cc-pVTZ basis set, we nevertheless decided to stand by the cc-pVDZ level. DFT/B3-LYP appears to be less sensitive with respect to the basis set size and gives bond lengths that are closer to the experimental ones but it should be kept in mind that in the crystal intermolecular hydrogen bonds are formed and stacking effects are present. Comparing the bond lengths of 6-azauracil and uracil, optimized at the same level of calculation,[24] we see that the N_6 substitution does not affect the C–O bonds whereas the ring bonds are slightly perturbed. The cartesian coordinates of the minimum and the vibrational spectrum in harmonic approximation are given in the Electronic Supplementary Information (ESI)†.

The vertical absorption spectrum of the few lowest sin-

Fig. 1 Local minimum structures of the ground- and excited-state potential energy surfaces. (a) Ground state, in parentheses data from reference [J. Phys. Chem. A 2008. 112. 13308], in square brackets cristallographic data from reference [Acta Cryst. 1974 B30 1430] ; (b) S_1 ($n \rightarrow \pi^*$) ; (c) S_2 ($\pi \rightarrow \pi^*$) ; (d) T_1 ($\pi \rightarrow \pi^*$) ; All bond lengths are in Å

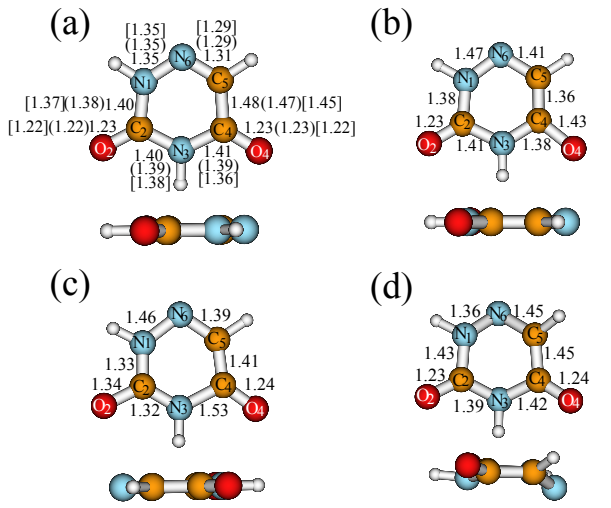

glet and triplet states in vacuum and acetonitrile ($\varepsilon = 38$) is presented in Table 1 together with scaled TDDFT/B3-LYP/6-31G(d,p) excitation energies and experimental data from Kobayashi et al.[15] Although the virtual orbital with the lowest energy is a Rydberg-type orbital in the aug-cc-pVTZ basis, Rydberg states are not observed among the first five singlet and triplet states states. The first Rydberg state in the FC region is the sixth singlet state, 6.68 eV above the electronic ground state. In the graphical representation of the electron densities of the most important frontier orbitals (Figure 2) we therefore omitted the Rydberg-type orbitals and denominate the lowest unoccupied valence molecular orbital by LUMO.

As in uracil, single excitation of an electron from the highest occupied molecular orbital (HOMO) to the LUMO yields the lowest triplet state (T_1) but only the second excited singlet state (S_2) in the vertical absorption spectrum. Due to the addition of a nitrogen atom in the ring, more $n \rightarrow \pi^*$ states are present than in uracil. Figure 2 shows that the electron density from the N_6 lone-pair orbitals contributes to the n orbitals HOMO–2 and HOMO–3. In the FC region the $n \rightarrow \pi^*$ comprise the S_1 and S_3 states and two low-lying triplet states, T_2 and T_3. The fourth triplet state has $^3(\pi \rightarrow \pi^*)$ character and originates from the HOMO–1 $\rightarrow$ LUMO excitation. Energetically it is located very close to the first bright state in the gas phase whereas the corresponding singlet state (S_4) is found at significantly higher energy in the FC region. It will be seen later, however, that the order of the electronic states depends

Fig. 2 Selected Hartree-Fock ground-state orbitals at the S_0, S_1, S_2 , and T_1 minimum geometries (from top to bottom)

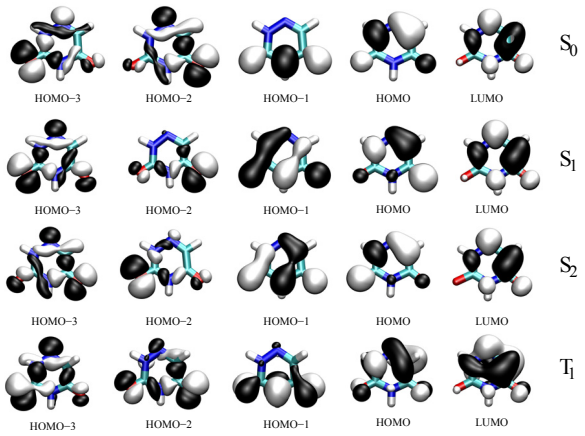

strongly on the molecular geometry.

Comparison with experimentally determined absorption maxima is possible for 6-azauracil in acetonitrile solution. We see from Table 1 that acetonitrile as a solvent induces different spectral shifts on different electronic transitions. Because of the small change in charge density upon HOMO $\rightarrow$ LUMO excitation, almost no spectral shift is observed for the T_1 and S_2 states. The computed vertical excitation energy of the S_2 state (4.92 eV) compares very favorably with the measured maximum of the absorption peak in acetonitrile (38610 cm^{-1} corresponding to 4.79 eV)[15]. The ($n \rightarrow \pi^*$) excitations, on the other hand, are accompanied by a transfer of electron density from the oxygen atoms to the ring, thus reducing the electric dipole moment in the excited state. As a consequence, all ($n \rightarrow \pi^*$) states (T_2, T_3, S_1, S_3) are blue shifted in the presence of a polar solvent. The rather untypical blue shift of the second ($\pi \rightarrow \pi^*$) states (T_4 and S_4) can be explained by the difference between the electron densities of the involed orbitals, too (see Figure 2). In the HOMO–1 the π-electron density resides predominantly on the O_2, N_3, and O_4 centers, whereas in the LUMO the largest orbital amplitudes are found at C_4, C_5, N_6, and N_1. Kobayashi et al.[15] assign a broad plateau on the short wavelength tail of the first absorption band at about 5.4 eV to the second $^1(\pi \rightarrow \pi^*)$ transition. We do not find any optically bright vertical transition in this energy regime, but will present an alternative explanation of this feature later on (Section 3.3). Instead, we attribute the second absorption band at with maximum around 200 nm (6.2 eV) to the HOMO–1 $\rightarrow$ LUMO ($S_0 \rightarrow S_4$) transition which is found at 5.92 eV in our calculated singlet excitation spectrum.

Despite the significant blue shift of the $n \rightarrow \pi^*$ states, the order of the singlet and triplet states is not changed by the solvent. That fact is exploited later on when we construct

relaxation paths for the chromophore in acetonitrile solution by shifting the potential energy profiles computed for vacuum conditions. In polar protic solvents such as water we expect the spectral shifts to be substantially more pronounced. Recent work in our laboratory on hydration effects on uracil and thymine derivatives revealed large differential effects of hydrogen bonding and solvent polarity on the excited states, pushing the first singlet $n \rightarrow \pi^*$ state of uracil energetically above the first $\pi \rightarrow \pi^*$ singlet.[49]

3.2 Excited-state properties

We optimized the nuclear geometry of the first two excited singlet states and the lowest triplet state. The cartesian coordinates of the minima and the harmonic vibrational frequencies are displayed in the ESI. Attempts to find the minimum of the second triplet state were not successful but it can be assumed that its minimum nuclear arrangement is similar to the one in the corresponding singlet $n \rightarrow \pi^*$ state. Bond lengths are presented in Figure 1. A sketch of the vertical excitation spectrum computed at the ground- and excited-state geometries is shown in Figure 3 while adiabatic excitation energies are compiled in Table 2.

Fig. 3 Vertical electronic spectrum at different minimum geometries. All energies in eV relative to the ground state. Left columns : singlet state; right columns : triplet states. Color scheme: ($n \rightarrow \pi^*$) red; ($\pi \rightarrow \pi^*$) blue; ground state black

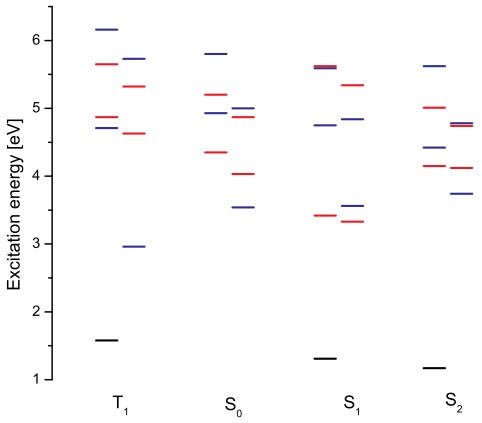

The global minimum on the first excited singlet potential energy surface (PES) is found for a state with $n \rightarrow \pi^*$ character. Note that the HOMO–2 has lost its contributions from the lone-pair at the N_6 center whereas HOMO–1 is more delocalized than at the ground-state geometry (Figure 2). The minimum geometry of S_1 is planar. Its is characterized by a significant increase of the C_4-O_4 bond length from 1.23 Å to 1.43 Å and a rearrangement of the single and double bonds in the ring. The N_1-N_6 bond is elongated by 0.12 Å reflecting its single bond character. The same is true for the C_5-N_6 bond which is changed by 0.10 Å. On the other hand, the C_4-C_5 bond is reduced by 0.12 Å obtaining a double bond character. These geometry changes produce a stabilization of the lowest $^1(n \rightarrow \pi^*)$ and $^3(n \rightarrow \pi^*)$ states while the second $^1(n \rightarrow \pi^*)$ and $^3(n \rightarrow \pi^*)$ states are destabilized. In contrast, the geometry changes appear to have a small effect on the $\pi \rightarrow \pi^*$ singlet and triplet states, except for the T_1 state that comes to lie above the lowest $n \rightarrow \pi^*$ states (S_1 and T_2) at the S_1 minimum. However, closer inspection of the S_2 wavefunction reveals considerable contributions of the HOMO–1 → LUMO configuration. We will discuss the effect of this wavefunction mixing in more detail in Section 3.3.

Table 2 Adiabatic energies of singlet and triplet states obtained at the RI-CC2/cc-pVDZ level

Molecule	Excitation energy/eV		
	$S_1(n \rightarrow \pi^*)$	$S_2(\pi \rightarrow \pi^*)$	$T_1(\pi \rightarrow \pi^*)$
6-azauracil	3.57	4.58	2.95
uracil	3.88		3.24

Although the CC2 optimization of the lowest optically bright $^1(\pi \rightarrow \pi^*)$ state failed in uracil, it was possible to optimize that state in 6-azauracil. The nuclear arrangement at the S_2 minimum remains planar with a stretched ring conformation. The N_1–N_6 and the opposite N_3–C_4 bonds become single bonds. In addition, the C_2–O_2 is elongated by 0.10 Å whereas the neighboring N_1–C_2 and C_2–N_3 bonds gain partial double bond character. The geometry relaxation on the S_2 PES is accompanied by a switch of the energetic order of the n orbitals (HOMO–2 and HOMO–3, see Figure 2). Thereby, the electronic structure that is associated to the S_1 and T_2 states in the FC region is destabilized to an extent that these $n \rightarrow \pi^*$ states are located energetically above the optically bright singlet state at the S_2 minimum. In turn, the electronic structures diabatically related to the S_3 and T_3 states in the FC region are greatly stabilized and lie below the first $^1(\pi \rightarrow \pi^*)$ state at the S_2 minimum. The consequences of this behavior on the photophysics of 6-azauracil will be discussed in more detail in the next section. Interestingly, we find that the S_2 minimum geometry is quite unfavorable for the T_1 state although both states result formally from a HOMO → LUMO excitation.

The reverse is not true at the T_1 geometry. Actually, here the $^1(\pi \rightarrow \pi^*)$ electronic structure corresponds to the lowest excited singlet state. Optimization of the T_1 state yields a V-shaped nuclear arrangement folded along the N_3-N_6 axis (see Figure 1). The C_5-N_6 bond is elongated by 0.14 Å with respect to its ground-state equilibrium value and becomes a single bond. The loss of planarity leads to a substantial increase

of the ground-state energy by about 1.6 eV. The $n \rightarrow \pi^*$ states are destabilized, too, but to a smaller extent. The S_2 state is almost unaffected. In contrast, there is a pronounced destabilization of the second singlet and triplet $\pi \rightarrow \pi^*$ states.

Comparing the adiabatic excitation energies of the S_1 and T_1 states of 6-azauracil with the corresponding data in uracil (Table 2) it is seen that the minima of both states are lowered by about 0.3 eV upon substitution of the C_6-H group by an N atom.

3.3 Excited-state relaxation and triplet-state formation

In order to understand the relaxation mechanisms following the photoexcitation of the first bright state of 6-azauracil, we calculated energy profiles along linearly interpolated paths between stationary points of the PESs. As noted earlier, the influence of acenonitrile on the electronic vertial excitation energies is sensible but not substantial. We can expect the $n \rightarrow \pi^*$ states to be shifted upward by about 0.2 eV and the lowest $\pi \rightarrow \pi^*$ states to be almost unaffected.

Fig. 4 Single-point calculations along a linearly interpolated path between the FC point (RC = 0) and the S_2 minimum (RC = 10) and extended on both sides.

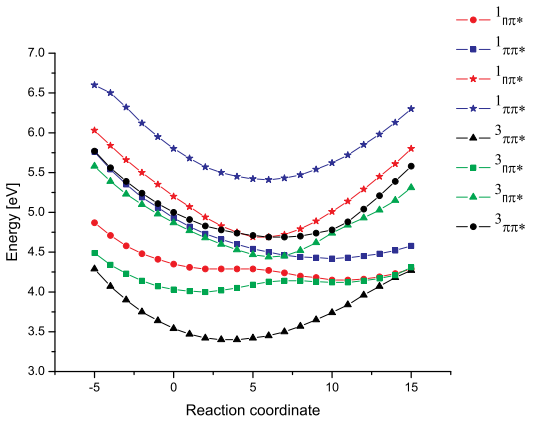

Figure 4 displays the energy profiles of the excited states along the linearly interpolated path (LIP) from the S_0 geometry toward the minimum of the S_2 state (RC = 10). The reaction coordinate (RC) was extrapolated on both sides using the coordinate displacement increments from linear interpolation. It is seen that a barrierless path exists starting at the FC point (RC = 0) on the S_2 PES and leading toward the $^1(\pi \rightarrow \pi^*)$ minimum (RC = 10). From the discussion of the geometry relaxation effects on the energetic ordering of the $n \rightarrow \pi^*$ states in the previous section we had anticipated several intersections of the excited PESs. Indeed, about half way between the FC point and the S_2 minimum (close to RC = 6) we find an avoided crossing between the first and the second singlet and triplet $n \rightarrow \pi^*$ states. It is known that in the vicinity of an avoided crossing most probably a conical intersection exists.[50] However, more important for the photophysics of 6-azauracil is the fact that the upper and lower branches of the two $^1(n \rightarrow \pi^*)$ states bracket the $^1(\pi \rightarrow \pi^*)$ surface. Hence, we can expect to find conical intersections between the $^1(\pi \rightarrow \pi^*)$ and $^1(n \rightarrow \pi^*)$ states close to this relaxation path, thus enabling ultrafast decay of the $^1(\pi \rightarrow \pi^*)$ population by internal conversion (IC) to the S_1 state. We have refrained from computing IC rates since a perturbational treatment of nonadiabatic coupling is not valid when conical intersections are found in close proximity to the minimum of the bright state. A dynamical treatment appears to be more appropriate in this case. From the results of excited-state dynamics simulations on other pyrimidine bases[21–23] the decay from the S_2 to the S_1 PES is estimated to occur on the subpicosecond time scale. This has to be compared with the fluorescence lifetime of the S_2 state for which we obtain a value of 160 ns in the isolated chromophore. It is thus clear that the fluorescence from the optically bright state will be quenched by ultrafast IC to the S_1 state. This nonradiative decay mechanism should also be operative in acetonitrile since the blue shift of the $n \rightarrow \pi^*$ states is much smaller than the energy difference between the S_2 and S_1 minima. In fact, due to the decreased energy gap, IC is expected to be even faster in acetonitrile solution.

According to El-Sayed rules[51] spin-orbit coupling is expected to be large between $\pi \rightarrow \pi^*$ states on the one hand and $n \rightarrow \pi^*$ states on the other hand whereas spin-orbit interaction is expected to be small between $^1(\pi \rightarrow \pi^*)$ and $^3(\pi \rightarrow \pi^*)$ states or between $^1(n \rightarrow \pi^*)$ and $^3(n \rightarrow \pi^*)$ states. This supposition is indeed comfirmed by our calculations, as the numerical values displayed in Table 3 show. Due to the random orientation of the molecule in the space-fixed coordinate system it is not meaningful to analyze the matrix elements of the individual components of the spin-orbit coupling Hamiltonian. Instead we will focus on the sum of the squared $\hat{\mathcal{H}}_{SO,x}$, $\hat{\mathcal{H}}_{SO,y}$, and $\hat{\mathcal{H}}_{SO,z}$ matrix elements. The $^3(n \rightarrow \pi^*)$ PESs run nearly parallel to the $^1(n \rightarrow \pi^*)$ ones. It is thus not surprising to find avoided crossings between the two $^3(n \rightarrow \pi^*)$ states as well. The change of their electronic characters along the LIP is clearly reflected in the large variation of the SOCMEs between the S_2 state and T_2 state close to the S_2 minimum (RC = 0) displayed in Figure 5. In the Condon approximation employing the SOCMEs computed at the S_2 minimum, a rate of 1.5×10^{10} s^{-1} is obtained for the $S_2 \rightsquigarrow T_2$ ISC under vacuum conditions and of 0.6×10^{10} in acetonitrile solution. Because of the large variation of coupling matrix elements with the nuclear geometry parameters these rates have to be considered only as rough estimates, however. In principle, the VIBES program allows to go beyond the Condon approximation. Nevertheless, we

have refrained from adding Herzberg-Teller-type corrections. While it is clear that the spin-forbidden nonradiative depletion of the S_2 population is at least two orders of magnitude faster than the radiative fluorescence decay, it will not be able to compete with the even faster $S_2 \rightsquigarrow S_1$ internal conversion.

Table 3 Spin-orbit matrix elements calculated at the respective singlet minimum geometry

Component	Spin-orbit matrix element/cm^{-1}		
	$S_1 \rightsquigarrow T_1$	$S_2 \rightsquigarrow T_2$	$S_2 \rightsquigarrow T_3$
$\hat{H}_{SO,x}$	-33.56	10.22	12.02
$\hat{H}_{SO,y}$	36.44	19.97	31.91
$\hat{H}_{SO,z}$	0.22	0.01	0.01
$\sum_i \lvert\hat{H}_{SO,i}\rvert^2$	2454.20	503.25	1162.73

Fig. 5 Sum of the squared spin-orbit matrix element components computed along the linearly interpolated reaction path connecting the S_2 minimum geometry (RC = 0) and the S_1 minimum geometry (RC = 10).

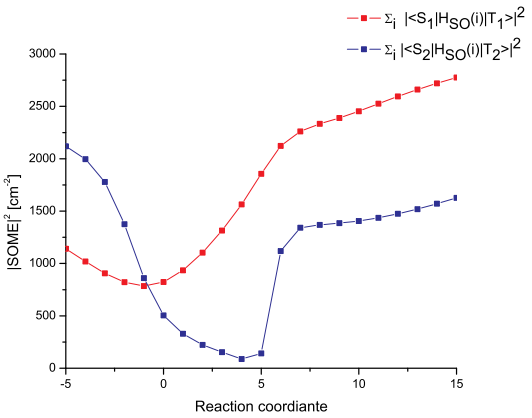

Energy profiles along a LIP between the S_2 minimum (RC = 0) and the S_1 minimum (RC = 10) are shown in Figure 6. The aforementioned avoided crossings between the first and second $n \rightarrow \pi^*$ states of singlet and triplet multiplicity are clearly visible in this graph. Along this path, we also find indications of an avoided crossing or conical intersection between the two $^1(\pi \rightarrow \pi^*)$ states corresponding to HOMO–1 → LUMO and HOMO → LUMO excitations, respectively. The strange shape of the experimental absorption spectrum of 6-azauracil with a long tail at the high-energy side of the first absorption band and a shoulder around 5.4 eV is most presumably caused by the strong nonadibatic coupling between these two bright states and nonvertical transitions to the crossing area.

Fig. 6 Single-point calculations along a linearly interpolated path between the S_2 minimum (RC = 0) and the S_1 minimum (RC = 10) and extended on both sides.

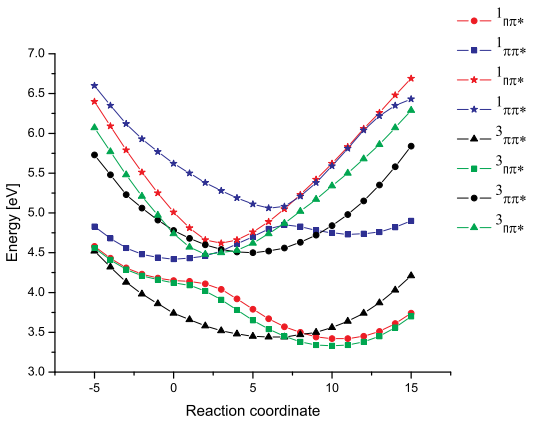

Kobayashi et al.[15] did not observe any fluorescence of 6-azauracil in acetonitrile solution after 248 nm light excitation, close to the S_2 absorption maximum. This means that the excited singlet population is quantitatively depleted by nonradiative processes. On the other hand, when exciting with 308 nm laser light (corresponding to an excitation energy of 4.02 eV), weak fluorescence with emission maximum at 420 nm and quantum yield of $\Phi_F = 4 \times 10^{-3}$ was measured. At present, we do not have an explanation for this fluorescence.

Fig. 7 Single-point calculations along a linearly interpolated path between the S_1 minimum (RC = 0) and the T_1 minimum (RC = 10) and extended on both sides.

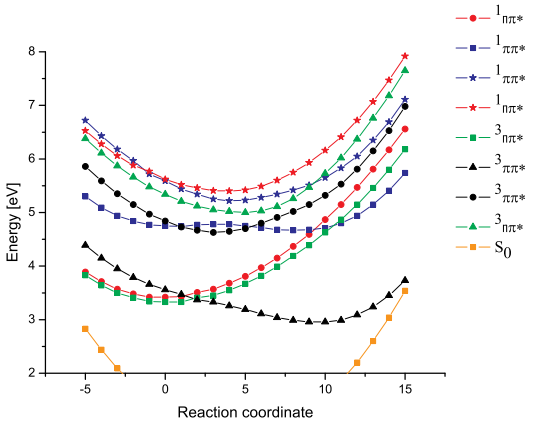

Figure 7 represents a LIP from the S_1 minimum towards

the T_1 minimum. Close to the S_1 minimum an intersection with the T_1 state occurs. ISC $S_1 \rightsquigarrow T_1$ is thus expected to be efficient, provided that the electronic spin-orbit coupling (SOC) is sizable. Indeed, this is the case (see Table 3) since the transition is allowed according to El Sayed's rules[51]. In the vicinity of the S_1 minimum the variation of the SOCMEs is small (compare Figure 5) and we may assume the Condon approximation to be valid. For the isolated 6-azauracil a sum of squared SOCMEs of 2454 cm^{-2} is obtained at an adiabatic energy difference of 4961 cm^{-1} yielding an ISC rate of 0.8×10^{10} s^{-1}. The rate constant in acetonitrile solution was computed using the same SOCMEs but employing energy-shifted PESs ($\Delta E_{adia} = 6815$ cm^{-1}), resulting in an enhanced ISC rate of 2.9×10^{10} s^{-1}. According to the energy gap law[52] it is generally assumed that the rate of a non-radiative transition between two states is particularly large if the energy difference between the states is small. At first sight it is therefore counter-intuitive that the rate for the $S_1 \rightsquigarrow T_1$ transition increases when the $^1(n \rightarrow \pi^*)$ state is blue-shifted in acetonitrile solution. However, a close look at Figure 7 reveals a significant coordinate displacement between the S_1 and T_1 minima and a crossing of the PESs along the LIP connecting them. A vertical shift of the $^1(n \rightarrow \pi^*)$ PES by about 0.2 eV brings the crossing between the S_1 and T_1 PESs close to the minimum of the S_1 state. In this way, the spatial overlap between the $v = 0$ wave function of the S_1 state and the energetically degenerate vibrational wave functions of the T_1 state is maximized. Furthermore, the vibrational density of states at the energy of the initial state is larger in solution.

In contrast, SOCMEs between the T_1 state and the S_0 state are negligibly small. In solution, where the excess energy of the solute is readily dissipated to the surrounding solvent molecules, the T_1 state is thus expected to be long-lived with respect to unimolecular decay, in agreement with experimental findings[15]. This might be different for an isolated 6-azauracil molecule in a supersonic jet. Here, the internal energy of the vibrationally hot triplet state might be sufficient to reach the intersection between the T_1 and S_0 PESs located roughly 0.5 eV above the T_1 minimum as indicated in Fig. 7.

4 Summary and conclusion

We have studied the photophysical properties of 6-azauracil, an analog of uracil in which an N atom is substitued for the CH group in position 6, by means of *ab initio* quantum chemical methods. The presence of a third heteroatom with nonbonding electrons in the six-membered ring increases the number of $n \rightarrow \pi^*$ states in the singlet and triplet spectrum and leads to various conical intersections between the low-lying electronic states.

Experimentally, the triplet yield of 6-azauracil was found to be 1.0 in acetonitrile[15] to be contrasted with a much lower triplet yield of 0.2 for the uracil analog in the same solvent[5]. Kobayashi et al. proposed that the effect of the aza-substitution is caused by the acceleration of the ISC due to increased spin-orbit interaction between the S_1 and T_1 states. Our present calculations and comparison with the results of our former work on uracil[24] show, however, that the SOCMEs are of similar size in both molecules. The second mechanism suggested to cause a major difference between uracil and 6-azauracil referred to the rigidity of the C_5–N_6 bond that prevents the ultrafast depletion of the $^1(\pi \rightarrow \pi^*)$ population via a conical intersection with the ground state. This idea cannot be ruled out but we do not find indications supporting this assumption.

We propose here an alternative explanation. Multiple potential energy surface crossings between excited singlet states of $\pi \rightarrow \pi^*$and $n \rightarrow \pi^*$character give reason to suggest that the primary S_2 ($^1\pi \rightarrow \pi^*$) population generated by irradiation of the molecule with UV light is transferred nearly quantitatively to the lower-lying S_1 $^1(n \rightarrow \pi^*)$ state. This state acts as a doorway state from which the T_1 ($^3\pi \rightarrow \pi^*$) state is formed approximately within 125 picoseconds in the isolated 6-azauracil and within 30 picoseconds in acetonirile solution according to our calculations. The enhancement of the $S_1 \rightsquigarrow T_1$ ISC process in acetonitrile solution is remarkable as it goes along with an increase of the adiabatic energy difference between these states. It is caused a more favorable vibrational overlap between the vibrationally cold S_1 state and the excited vibrational levels of the significantly discplaced T_1 potential. Spectroscopic experiments on the transient species with femtosecond time resolution in solvents with varying polarity could be of great help verifying or disproving our proposed mechanism.

5 Acknowlegments

This work has been supported by the Deutsche Forschungsgemeinschaft through SFB 663/C1. We would like to thank Prof. Karl Kleinermanns for many stimulating discussions on the nature of the long-lived dark states of pyrimidine bases.

References

1 C. E. Crespo-Hernandez, B. Cohen, P. M. Hare and B. Kohler, *Chem. Rev.*, 2004, **104**, 1977–2019.
2 Y. He, C. Wu and W. Kong, *J. Phys. Chem. A*, 2003, **107**, 5143–5148.
3 Y. He, C. Wu and W. Kong, *J. Phys. Chem. A*, 2004, **108**, 943–949.
4 M. Busker, M. Nispel, T. Häber, K. Kleinermanns, M. Etinski and T. Fleig, *Chem. Phys. Chem.*, 2008, **9**, 1570–1577.
5 P. M. Hare, C. E. Crespo-Hernandez and B. Kohler, *J. Phys. Chem. B*, 2006, **110**, 18641–18650.
6 P. M. Hare, C. E. Crespo-Hernandez and B. Kohler, *PNAS*, 2007, **104**, 435–440.
7 W.-M. Kwok, C. Ma and D. L. Phillips, *J. Am. Chem. Soc.*, 2008, **130**, 5131–5139.
8 J. González-Vázquez, L. González, E. Samoylova and T. Schultz, *Phys. Chem. Chem. Phys.*, 2009, **11**, 3927–3934.

9 S. M. Bishop, M. Malone, D. Philips, A. W. Parker and M. C. R. Symons, *J. Chem. Soc., Chem. Commun.*, 1994, 871–872.
10 S. K. Pal, J. Peon and A. H. Zewail, *Chem. Phys. Lett.*, 2002, **363**, 57–63.
11 C. Canuel, M. Mons, F. Piuzzi, B. Tardivel, I. Dimicoli and M. Elhanine, *J. Chem. Phys.*, 2005, **122**, 074316.
12 R. K. Neely, S. W. Magennis, D. T. F. Dryden and A. C. Jones, *J. Chem. Phys. B*, 2004, **108**, 17606–17610.
13 K. A. Seefeld, C. Plützer, D. Löwenich, T. Häber, R. Linder, K. Kleinermanns, J. Tatchen and C. M. Marian, *Phys. Chem. Chem. Phys.*, 2005, **7**, 3021–3026.
14 Á. Bányász, T. Gustavsson, E. Keszei, R. Improta and D. Markovitsi, *Photochem. Photobiol. Sci.*, 2008, **7**, 765–768.
15 T. Kobayashi, Y. Harada, T. Suzuki and T. Ichimura, *J. Phys. Chem. A*, 2008, **112**, 13308–13315.
16 T. Kobayashi, H. Kuramochi, Y. Harada, T. Suzuki and T. Ichimura, *J. Phys. Chem. A*, 2009, **113**, 12088–12093.
17 E. D. Clercq, *Antivir. Res.*, 2005, **67**, 56–75.
18 F. Exinger and F. Lacroute, *Curr. Genet.*, 1992, **22**, 9–11.
19 S. Perun, A. L. Sobolewski and W. Domcke, *J. Phys. Chem. A*, 2006, **110**, 13238–13244.
20 A. Yoshikawa and S. Matsika, *Chem. Phys.*, 2008, **347**, 393–404.
21 H. R. Hudock, B. G. Levine, A. L. Thompson, H. Satzger, D. Townsend, N. Gador, S. Ullrich, A. Stolow and T. J. Martinez, *J. Phys. Chem. A*, 2007, **111**, 8500–8508.
22 G. Zechmann and M. Barbatti, *J. Phys. Chem. A*, 2008, **112**, 8273–8279.
23 Z. Lan, E. Fabiano and W. Thiel, *J. Phys. Chem. B*, 2009, **113**, 3548–3555.
24 M. Etinski, T. Fleig and C. M. Marian, *J. Phys. Chem. A*, 2009, **113**, 11809–11816.
25 R. Ahlrichs, M. Bär, H.-P. Baron, R. Bauernschmitt, S. Böcker, N. Crawford, P. Deglmann, M. Ehrig, K. Eichkorn, S. Elliott, F. Furche, F. Haase, M. Häser, C. Hättig, H. Horn, C. Huber, U. Huniar, M.Kattannek, A. Köhn, C. Kölmel, M. Kollwitz, K. May, P. Nava, C. Ochsenfeld, H. Öhm, H. Patzelt, D. Rappoport, O. Rubner, A. Schäfer, U. Schneider, M. Sierka, O. Treutler, B. Unterreiner, M. von Arnim, F. Weigend, P. Weis and H. Weiss, *TURBOMOLE (Vers. 5.7)*, Universität Karlsruhe, 2004.
26 S. Grimme and M. Waletzke, *J. Chem. Phys.*, 1999, **111**, 5645–5655.
27 M. Kleinschmidt, J. Tatchen and C. M. Marian, *J. Comp. Chem.*, 2002, **23**, 824–833.
28 M. Kleinschmidt and C. M. Marian, *Chem. Phys.*, 2005, **311**, 71–79.
29 J. Neugebauer, M. Reiher, C. Kind and B. A. Hess, *J. Comp. Chem.*, 2002, **23**, 895–910.
30 J. Tatchen, VIBES, Universität Düsseldorf, 2005.
31 O. Christiansen, H.Koch and P. Jørgensen, *Chem. Phys. Lett.*, 1995, **243**, 409.
32 O. Vahtras, J. Almlöf and M. W. Feyereisen, *Chem. Phys. Lett.*, 1993, **213**, 514–518.
33 C. Hättig and F. Weigend, *J. Chem. Phys.*, 2000, **113**, 5154.
34 C. Hättig, *J. Chem. Phys.*, 2003, **118**, 7751.
35 A. Köhn and C. Hättig, *J. Chem. Phys.*, 2003, **119**, 5021–5036.
36 C. Hättig and A. Köhn, *J. Chem. Phys.*, 2002, **117**, 6939.
37 T. Fleig, S. Knecht and C. Hättig, *J. Phys. Chem. A*, 2007, **111**, 5482.
38 A. Klamt and G. Schürmann, *J. Chem. Soc., Perkin Trans.*, 1993, **2**, 799.
39 A. Schäfer, A. Klamt, D. Sattel, J. Lohrenz and F. Eckert, *Phys. Chem. Chem. Phys.*, 2000, **2**, 2187.
40 T. H. J. Dunning, *J. Chem. Phys.*, 1989, **90**, 1007.
41 R. A. Kendall, T. H. J. Dunning and R. J. Harrison, *J. Chem. Phys.*, 1992, **9**, 6796.
42 F. Weigend, A. Köhn and C. Hättig, *J. Chem. Phys.*, 2002, **116**, 3175.
43 B. A. Hess, C. M. Marian, U. Wahlgren and O. Gropen, *Chem. Phys. Lett.*, 1996, **251**, 365.
44 AMFI is an atomic spin-orbit integral program written by B. Schimmelpfennig, University of Stockholm, 1996.
45 J. Tatchen and C. M. Marian, *Chem. Phys. Lett.*, 1999, **313**, 351–357.
46 D. Danovich, C. M. Marian, T. Neuheuser, S. D. Peyerimhoff and S. Shaik, *J. Phys. Chem. A*, 1998, **102**, 5923–5936.
47 J. Tatchen, N. Gilka and C. M. Marian, *Phys. Chem. Chem. Phys.*, 2007, **9**, 5209–5221.
48 P. Singh and D. J. Hodgson, *Acta. Cryst.*, 1974, **B30**, 1430–1435.
49 M. Etinski and C. M. Marian, *Phys. Chem. Chem. Phys.*, 2010, **14**, published online.
50 D. G. Truhlar and C. A. Mead, *Phys. Rev. A*, 2003, **68**, 032501.
51 M. A. El-Sayed, *Acc. Chem. Res.*, 1968, **1**, 8–16.
52 R. Englman and J. Jortner, *Mol. Phys.*, 1970, **18**, 145–164.

Table 1 Vertical excitation spectrum of the ground state.

State	Excitation	Oscillator strength	Excitation energy/eV			
			RI-CC2/aug-cc-pVTZ[a]	RI-CC2/aug-cc-pVTZ[b]	TDDFT/6-31G(d,p)[c]	Experiment[d]
$S_1(n \rightarrow \pi^*)$	(HOMO-2 → LUMO)	0.0005	4.35	4.60	4.10	
$S_2(\pi \rightarrow \pi^*)$	(HOMO → LUMO)	0.1529	4.93	4.92	4.70	4.79
$S_3(n \rightarrow \pi^*)$	(HOMO-3 → LUMO)	0.0026	5.20	5.43	4.71	
$S_4(\pi \rightarrow \pi^*)$	(HOMO-1 → LUMO)	0.0540	5.80	5.92	5.39	5.41
$T_1(\pi \rightarrow \pi^*)$	(HOMO → LUMO)		3.54	3.56	3.00	
$T_2(n \rightarrow \pi^*)$	(HOMO-2 → LUMO)		4.03	4.25	3.56	
$T_3(n \rightarrow \pi^*)$	(HOMO-3 → LUMO)		4.87	5.09	4.32	
$T_4(\pi \rightarrow \pi^*)$	(HOMO-1 → LUMO)		5.00	5.12	4.22	

[a] In vacuum

[b] Polarizable continuum model mimicking acetonitrile solution

[c] Ref. [15]. Polarizable continuum model mimicking acetonitrile solution. The excitation energies, obtained with the B3-LYP functional, were scaled by 0.95.

[d] Ref. [15]. Maximum of absorption peak in acetonitrile.

Overruling the energy gap law: Fast triplet formation in 6-azauracil

Electronic Supplementary Information

Mihajlo Etinski and Christel Marian

Heinrich-Heine-University Düsseldorf,
Institute of Theoretical and Computational Chemistry
Universitätsstraße 1, 40225 Düsseldorf, Germany.
Fax: +49 211 8113466; Tel: +49 211 8113209
E-mail: Christel.Marian@uni-duesseldorf.de

April 1, 2010

Table 1: Vibrational spectrum of the ground state state obtained at RI-CC2/cc-pVDZ level (unscaled frequencies). Wavenumbers ν are given in cm^{-1}, intensities I in km/mol.

ν	I
126	0.97
145	1.19
368	20.81
392	6.66
506	4.92
521	21.15
543	8.62
607	44.99
704	133.41
725	18.89
732	8.89
744	1.50
886	19.27
971	26.96
1003	7.12
1127	25.28
1237	29.31
1338	33.74
1365	10.22
1406	87.14
1439	54.04
1581	14.24
1733	286.99
1798	518.09
3263	0.09
3584	67.76
3631	118.88

Table 2: Vibrational spectrum of the S_1 state state obtained at RI-CC2/cc-pVDZ level (unscaled frequencies). Wavenumbers ν are given in cm^{-1}, intensities I in km/mol.

ν	I
103	0.63
183	0.06
302	5.86
314	5.06
409	69.32
472	13.38
494	3.15
546	9.07
589	12.46
656	79.88
681	23.19
695	1.25
768	45.28
915	17.94
968	20.72
1021	32.62
1107	3.98
1169	5.44
1260	0.92
1297	3.91
1429	8.24
1435	1.14
1602	211.85
1770	388.46
3279	5.00
3601	75.72
3619	157.15

Table 3: Vibrational spectrum of the S_2 state state obtained at RI-CC2/cc-pVDZ level (unscaled frequencies). Wavenumbers ν are given in cm^{-1}, intensities I in km/mol.

ν	I
43	0.56
194	1.19
310	11.88
355	10.44
371	24.51
488	22.71
501	21.60
511	2.31
563	0.10
627	55.30
670	50.46
696	121.51
703	60.51
813	11.11
895	8.09
928	487.40
1084	31.89
1100	0.60
1225	61.10
1269	46.71
1371	149.71
1408	24.64
1616	68.50
1737	232.91
3236	1.28
3583	205.26
3595	99.77

Table 4: Vibrational spectrum of the T_1 state state obtained at RI-CC2/cc-pVDZ level (unscaled frequencies). Wavenumbers ν are given in cm^{-1}, intensities I in km/mol.

ν	I
127	1.83
155	1.25
224	2.32
364	18.19
436	8.95
481	12.02
513	15.41
520	10.48
573	10.73
660	132.04
692	10.34
712	84.28
729	10.92
950	28.09
977	9.36
1013	12.06
1206	40.27
1245	3.64
1323	145.94
1358	1.12
1396	110.36
1424	60.12
1637	113.46
1769	280.24
3260	1.67
3557	69.07
3596	78.38

Table 5: Cartesian coordinates/bohr of the ground state minimum obtained at RI-CC2/cc-pVDZ level

-1.74610099736496	-2.22240265834325	0.00449565927163	c
1.04380765341883	-2.32412964268841	-0.00234588751951	c
2.11572577304878	0.10751366537799	-0.00119438050326	n
0.82956298515604	2.41214101722268	0.00553295218914	c
-1.79204276381764	2.06387091765626	0.01355038214799	n
-3.09282819734742	-0.14023042659925	0.01202440802523	n
1.83958958452372	4.49581537459581	0.00484352223484	o
2.32658155756143	-4.26488628454951	-0.00851159800297	o
-2.79455216344083	-4.00208925911174	0.00333103347986	h
-2.86851142686696	3.65789742855908	0.01819485140458	h
4.04389471091239	0.21864498496745	-0.00677148077657	h

Table 6: Cartesian coordinates/bohr of the S_1 state obtained at RI-CC2/cc-pVDZ level

-1.70942743306936	-2.28862676386382	0.01171803574604	c
0.85186934253273	-2.18433362413726	0.00304030842125	c
2.11879899612192	0.08546595015361	0.00540273369754	n
0.81137827666896	2.40924641302505	0.01350208669795	c
-1.77960155935168	2.06066459904651	0.02315894080454	n
-3.21179872531814	-0.09522472029197	0.02304793827355	n
1.89301875972419	4.46794230004381	0.01235157021997	o
2.63879617184379	-4.20210264894317	-0.00908114690792	o
-2.73969468817620	-4.07409795610917	0.01066363238671	h
-2.80045655928674	3.69613248188546	0.02979266612826	h
4.04302727571830	0.15860473290155	-0.00452307249332	h

Table 7: Cartesian coordinates/bohr of the S_2 state obtained at RI-CC2/cc-pVDZ level

-1.71827507408612	-2.24397766518739	0.01233487758568	c
0.94769711480994	-2.43280073654303	0.00179277976845	c
2.13383170529868	0.19901431998794	0.00433266655245	n
0.74490682054897	2.27973110212464	0.01359962671832	c
-1.76229403339219	2.12172237235798	0.02286910927231	n
-3.31854266039105	-0.16204656007902	0.02398871968691	n
1.74363854174153	4.60190904005255	0.01450380274673	o
2.44222912958946	-4.24743837997651	-0.00897205844489	o
-2.76104184321613	-4.03251594913419	0.01150692493834	h
-2.73262450517248	3.79305171030558	0.02980335552034	h
4.05821674617707	0.35482825420333	-0.00325525027252	h

Table 8: Cartesian coordinates/bohr of the T_1 state obtained at RI-CC2/cc-pVDZ level

-1.70543259811873	-2.22687115289721	0.05256993108285	c
1.03026286184038	-2.31744010721149	0.09054337463554	c
2.09747813119421	0.12995182046546	0.37693092483039	n
0.77876402984206	2.34280092007962	-0.13161907485166	c
-1.89425265511141	2.01206264772269	-0.09336157908310	n
-3.12399577475616	-0.03071173985523	0.88344339396988	n
1.72120608700431	4.42655751619203	-0.49253711953501	o
2.36524653906037	-4.21703605018496	-0.19608731641017	o
-2.77917281453484	-3.78287057822387	-0.77974663553158	h
-2.84376858923679	3.68819780655726	0.07914263401925	h
4.01715552887198	0.25434139281412	0.23008822353881	h